Revealing Structural and Spin-state Dependent Reactivity of Single Atom Catalysts (SACs) with Systematically Improvable Computational Tools

by

Haojun Jia (贾皓钧)

B.S. Physics
Jilin University (吉林大学), 2019

Submitted to the Department of Chemistry
in Partial Fulfillment of the Requirements for the Degree of

DOCTOR OF PHILOSOPHY IN CHEMISTRY

at the

MASSACHUSETTS INSTITUTE OF TECHNOLOGY

May 2024

Authored by: _____
Haojun Jia
Department of Chemistry
May 3, 2024

Certified by: _____
Heather J. Kulik
Associate Professor of Chemical Engineering and Chemistry
Thesis Supervisor

Accepted by: _____
Adam Willard
Professor of Chemistry
Graduate Officer

This doctoral thesis has been examined by a Committee of the Department of Chemistry as follows:

Professor Adam Willard..…….
Thesis Committee Chair
Professor of Chemistry

Professor Heather J. Kulik…..……...
Thesis Supervisor
Associate Professor of Chemical Engineering
Associate Professor of Chemistry

Professor Jianshu Cao……..……..
Thesis Committee Member
Professor of Chemistry

Revealing Structural and Spin-state Dependent Reactivity of Single Atom Catalysts (SACs) with Systematically improvable Computational Tools

by

Haojun Jia

Submitted to the Department of Chemistry on May 3 in Partial Fulfillment of the Requirements for the Degree of Doctor of Philosophy in Chemistry

ABSTRACT

Efficient catalysts are essential for advancing energy conversion and storage technologies, particularly for challenging reactions such as methane-to-methanol conversion and the oxygen reduction reaction (ORR) important for fuel cells. Single-atom catalysts (SACs), particularly doped graphitic catalysts, have emerged as a promising class of materials. SACs combine the advantages of homogeneous and heterogeneous catalysts, offering tunable active sites and scalability. However, understanding the relationship between the structure of SAC active sites and their reactivity remains challenging due to the limitations of experimental characterizations. Computational modeling provides atomic-level insights into SAC active site configurations and the impact of the metal's local environment on their properties and catalytic activity. This thesis presents a combined effort utilizing computational methods to explore the design and optimization of SACs for methane-to-methanol conversion and the ORR.

In this thesis, we use range-separated hybrid density functional theory (DFT) to compare the energetics and structure of the direct metal-coordinating environment in the presence of 2p (i.e., N or O) and 3p (i.e., P or S) dopants and with increasing finite graphene model flake size to mimic differences in local rigidity. While metal–ligand bond lengths in SACs are significantly shorter than those in transition metal complexes, they remain longer than SAC mimic macrocyclic complexes. Consequently, we observe SACs to simultaneously favor the formation of the metal–oxo while also allowing for methanol release. This reactivity is different from what has been observed for large sets of square planar model homogeneous catalysts. Moreover, modulating the coordination environment near single metal sites by means of codopants, we carry out a large-scale virtual high-throughput screening (VHTS) of transition metal (i.e., Mn, Fe, Co, and Ru) SACs codoped with various elements (i.e., N, O, P, and S) in numerous spin and oxidation (i.e., M(II)/M(III)) states for the challenging conversion of methane to methanol. We identify that the ground-state preference is metal- and oxidation-state-dependent. We observe a weak negative correlation between the oxo formation energy ($\Delta E(oxo)$) and the energy of hydrogen atom transfer ($\Delta E(HAT)$), thanks to the high variability in the coordination environment. Therefore, codoped SACs demonstrate flexible tunability that disrupts linear free energy relationships in a manner similar to that of homogeneous catalysts without losing the scalability of heterogeneous catalysts. Further exploration focuses on codoped Fe and Ru-based SACs for ORR using VHTS and machine learning (ML). The ML models demonstrate superior accuracy in predicting reaction energetics compared to traditional scaling relationships. The findings validate codoping as a powerful strategy for tuning the properties of SACs to achieve enhanced ORR performance. Promising catalyst candidates are proposed for experimental validation, showcasing the potential of SACs in overcoming limitations in catalyst design for challenging reactions and provides valuable insights for the rational design of high-performance ORR catalysts.

Thesis supervisor:	Heather J. Kulik
Title:	Professor of Chemical Engineering and Chemistry

Acknowledgements

As I conclude this thesis journey, I want to take this opportunity to express my deepest gratitude to all the people who supported me along the way.

First and foremost, I would like to acknowledge my Ph.D. advisor, Prof. Heather J. Kulik, for her continued guidance and support throughout my Ph.D. Without her mentorship, this thesis would almost be impossible. She has been an invaluable resource, offering insightful research and career advice. As I look back at my five years in the lab, I am particularly grateful for her mentorship, which significantly improved my ability to think logically, take feedback constructively, and refine my work additionally. Her scientific insights and guidance on conducting and presenting research, collaborating with fellow scholars, and navigating the chemistry world have been incredibly inspiring. I deeply appreciate the flexibility and encouragement she consistently provided. Additionally, her influence extends beyond the academic work and I have learned so much from her as a person: her efficient and structured working style, her kindness, friendliness, and her support for her students during challenging times. I could not have imagined having a better advisor and mentor for my Ph.D.

I also want to extend my sincere appreciation to my thesis committee members Prof. Adam Willard and Prof. Jianshu Cao for their guidance and valuable feedback on my research throughout my Ph.D. They have always fostered a growth environment where I could confidently present my work and learn about various strategies and approaches. Through their enthusiasm and appreciation of my work, I walk out of each annual meeting feeling energized and prepared to tackle the next steps in my research. I am also grateful for the insightful questions they posed during my oral exam, which deepened my understanding of my research. Furthermore, I appreciate their continued guidance and support as I embarked on my career.

My colleagues have been my teachers and so I would like to express my deepest gratitude to all Kulik group members, both alumni and current members, for their unwavering support, advice, assistance and scientific insights. Especially, I would like to thank Dr. Chenru Duan, who pioneered the “machine learning workflow for chemical discovery”, taught me so much about science, coding and machine learning models. Throughout the more than four years I've spent with Chenru, I've cherished every interaction and collaboration with him. Each exchange and joint effort brings me profound joy. Not only has he deepened my understanding of science and enhanced my project management skills, but he also fosters a positive work environment that keeps me motivated and content. I would like to thank Aditya Nandy, from whom I learned reaction mechanism, electronic structure theory, software management skills and so on. I had lots of discussions with Aditya Nandy who sat with me over a Zoom call to discuss the results and teach to me patiently when I was first and second Ph.D. student during the pandemic. I would also like to thank Prof. Mingjie Liu, from whom I learned literally all my initial knowledge on SACs. She provided me valuable perspectives and advice on research directions. I would like to thank Ilia Kevlishvili, Prof. Fang Liu, Prof. Zhongyue Yang, Prof. Shuwen Yue, Yeongsu Cho, Ralf Meyer and Clorice Reinhardt for their valuable discussions and advice on the career path. A couple of other graduate students I enjoyed collaborating with throughout my Ph.D. include Husain Adamji, Gianmarco Terrones, Daniel Chu, Changhwan Oh, Xiao Huang, David Kastner and Vyshnavi Vennelakanti. Lastly, I would like to thank Prof. Kit Bowen, Prof. Yanming Ma, Prof. Xiaochun

Wang and Prof. Defang Duan, Prof. LA Svyatkin who led me towards the road of scientific discovery back in my undergrad.

As an international student, there are always extra bits needed to deal with. I would like to thank administration people in Chemistry Education Office, especially Jennifer Weisman, who are always available to offer support to the best that they can.

I would also like to express my sincere gratitude to my friends, without whose support my Ph.D. is impossible. Although it is impossible to express my gratitude in a paragraph to all of you, here is a modest attempt: I would like to thank my friends at MIT and Boston, especially Hao Yan & Jiawen Dai, Jian Jing, Xinrong Gu, Chenru Duan, Hongbin Xu, Xiao Huang, Luyang Zhang, Jizheng Luan and so on for making my Ph.D. more interesting and full of fun. I will never forget the time the time we spent together for playing poker, drinking, hiking together. I really want to thank our secret "Yezibang": Yanzhen Zhao, Hongfei Ge and Yuxuan Wu for their help on hard times of my Ph.D. and my life. I would also like to thank some old friends, Zihan Zhang, Zihao Hua, Zhaotian Yang and so on. I am also extremely grateful for opportunity of serving for the whole Chinese community at MIT as co-president of the MIT Chinese Student and Scholar Association (MIT CSSA) 2022-2023 with Xinyi Gu. Lastly, I want to thank myself.

Finally, I would like to thank my incredible support from family. 感谢我的家庭对我无条件的爱和支持。我深爱的父母、爷爷奶奶、姥爷姥姥。我身在海外七年，五年不没有回国，爷爷、姥爷和姥姥在国内新冠时期短短一个月内相继离开，未曾见到最后一面。我是老一辈带大的，跟他们有着浓烈而独特的情感。我时常在脑海中回想起来美国前，我与爷爷在小区门口最后道别的场景：当车子启动后，爷爷快步追着车子走，我清晰的记得他不舍的眼光。我从未想过那会是我们最后一面。我也十分感谢我姐&姐夫（杨文婷&徐耀林）从小对我支持和帮助。最后，父母对我的爱，我甚至不知道怎么用语言表述，我亏欠你们的太多，我永远爱你们！

Over the past year, one of the most asked questions is: why do you want to have a startup? There are many reasons, but the ultimate reason is: My intrinsic curiosity for physical science and passion to push the upper limits of engineering have driven me towards deep tech entrepreneurship. I'm launching a startup to carry on this momentum to the next chapter of my life. Finally, a sentence from Peking Opera for myself:

"看前面，黑洞洞，定是那贼巢穴，待俺赶上前去，杀他个干干净净，有道是：不入虎穴，焉得虎子!"

Table of Contents

Chapter 1: Introduction

This chapter has been partially adapted from 'H. Jia, A. Nandy, M. Liu, and H. J. Kulik, "Modeling the roles of rigidity and dopants in single-atom methane-to-methanol catalysts", *J. Mater. Chem. A* **2022**, 10, 6193-6203.'

and

'H. Jia, C. Duan, I. Kevlishvili, A. Nandy, M. Liu, and H. J. Kulik, "Computational Discovery of Codoped Single Atom Catalysts for Methane-to-Methanol Conversion", *ACS Catal.* **2024**, *14*, 2992−3005.'

1.1. Catalysts Design for Methane-to-Methanol Conversion

Methane (CH_4), the second most prominent greenhouse gas (GHG), contributes to approximately 16−20% of global GHG emissions[1]. With over half of the methane emission arising from human activities, such as leaks from refineries, coal mines, and landfill sites[2, 3], its impact on the environment has become a pressing concern. Moreover, methane's potency in trapping heat is 86 times that of carbon dioxide (CO_2) over 20 years[4], underscoring the urgency of finding effective solutions to mitigate its impact. Currently, the primary method for addressing methane emissions involves direct combustion through flaring; however, this approach is criticized for its inefficiency in harnessing the energy potential of methane. Not only does flaring contribute to environmental concerns by releasing CO_2, but it also represents a wasted opportunity to utilize methane as a valuable energy resource. Converting methane to valuable chemicals (e.g., methanol) emerges as a key strategy to reduce methane emissions and has great environmental significance and economic value. However, the direct conversion of methane-to-methanol is particularly challenging due to the high energy required to activate the strong C–H bonds of methane together with the thermodynamic favorability of methanol overoxidation to CO_2[5, 6], which requires efficient catalyst to lower the energy barrier for the conversion reaction.

The optimal catalysts for methane-to-methanol conversion need to satisfy numerous criteria, driving an exhaustive search of catalytic materials [7, 8]. Enzymes with mononuclear Fe active sites (e.g., Fe(II) in TauD[9-11]) have demonstrated the capability to selectively oxidize the substrates with strong C–H bonds. This observation has motivated bioinspired design[12-14] of synthetic systems, including both homogeneous[15-18] and heterogeneous[19-21] catalysts, aiming for more energy-efficient direct methane-to-methanol conversion. Despite substantial progress, no synthetic catalyst to date has been able to simultaneously achieve as high activity and selectivity

as the enzymes. This gap has prompted an extended search for alternative catalysts with the objective of achieving a comparable catalytic efficiency to enzymatic systems for direct methane-to-methanol conversion.

1.2. Single-Atom Catalysts: A New Frontier in Catalysis

Single-atom catalysts (SACs), [22-29] with isolated metal atoms dispersed on solid supports, have recently emerged as a captivating frontier, attracting intensive research attention. SACs have the promise to combine the scalability of heterogeneous catalysts and the high atom economy of homogeneous catalysts[30, 31], offering significant opportunities for atom-economical utilization of metal resources[32-34]. Their unique electronic structures and unsaturated coordination environments within the active metal center have demonstrated enhanced catalytic activity across various reactions[35, 36]. Among different classes of SACs, N-doped graphene SACs[26, 29, 37], featuring an isolated metal atom embedded in a graphitic carbon material, more closely resemble their homogeneous counterparts compared to others. For instance, the Fe–N_4 active site in Fe-SACs exhibits an analogy to hemes[36, 38-40], where Fe atom is coordinated to four nitrogen atoms.

Experimentally synthesizing SACs conditions (e.g., Harsh pyrolysis condition)[37, 41] generate variable active sites, and trends in active site dependence are difficult to deconvolute via experiment, due to challenges in controlling active site arrangement. Although synthesis conditions can cause the active site properties to vary, the metal is believed to bind at single vacancy (SV) or double vacancy (DV) graphene sites to form the single atom site. Some or all of the metal-coordinating atoms are replaced with various coordinating atoms in the case of graphene doping, among which N-doped graphene flakes[36, 41-45] are common supports used to make M-N-C SACs. Although SACs have well-defined structures, the understanding of the reactivity-structure relationship is challenging[36]. For example, different configurations of the same element[44, 46] (e.g.,

pyridinic vs. pyrrolic N) can lead to distinct SAC reactivity. In addition, distinct coordinating atom identities have different metal ligand bond length which can tune the strength of ligand field and then determine the catalytic performance[47-55].

Various characterization techniques, including Mössbauer spectroscopy[35, 36], high-angle annular dark-field scanning transmission electron microscopy (HAADF-STEM)[56, 57], X-ray absorption near-edge spectroscopy (XANES), and extended X-ray absorption fine structure (EXAFS)[58, 59], have been employed to investigate the structure and reactivity of SACs. These experimental analyses have revealed that both the support and coordination environment of SACs are essential in determining their catalytic reactivity[41, 51]. Similar to biological enzymes or transition metal complexes (TMCs), the spin state and oxidation state significantly influence the reactivity of SACs[48, 60], making it challenging to assess reactivity trends due to the difficulty of experiments to precisely capture the oxidation/spin states[35, 44].

1.3. Computational Catalyst Discovery with Density Functional Theory

Although SACs exhibit attractive properties for catalysis, unravelling the catalytic mechanisms of SACs through experimental means faces significant challenges. The degree of applicability of structure-property relationships derived from homogeneous or heterogeneous catalysts to predict the reactivity of SACs remains an outstanding question. Due to the lack of precise control over active site configuration in the synthesis of SACs, deciphering the relationship between the coordination structure of the active site and the catalytic performance is challenging via experiment[35, 36]. Low site density and short-lived, variable SAC active sites[61, 62] fundamentally challenge many experimental techniques that bulk average over all sites, which limits the analysis of individual active sites. The synthesis of SACs under harsh pyrolysis conditions results in a distribution of active sites[37, 41] and significant variations of the local coordination environment,

posing fundamental challenges for most experimental characterization techniques, even for the highest-resolution spectroscopic techniquues[63, 64]. In contrast, first-principles modeling with density functional theory (DFT) has been a powerful tool for designing new SACs[65, 66] and obtaining mechanistic insights[67-69] into their catalytic activities[70-74] with atomic precision. Computational modeling enables us to study active site configurations on SACs with atomic precision, and correspondingly elucidates the effects of metal-local environment variation in SACs.

However, it is challenging to study SACs with conventional computational modeling using density functional theory (DFT). The trade-offs between representing the system as an infinite model simulated with periodic boundary conditions (PBCs) versus as a finite model flake have to be considered to simulate SACs. PBCs naturally reproduce the translational symmetry of crystals[75], and thus are typically used to describe an infinite bulk crystal. However, the higher cost of exact exchange in plane wave PBC calculations typically motivates the use of generalized-gradient approximation (GGAs) that can be sensitive to delocalization error[76], especially for embedded transition metal atoms[23, 76-80]. Additionally, PBCs may enforce unnecessary symmetry and rigidity to the metal-local environment in disordered SACs, which are known to contain curvature[53]. Finite models[81], conversely, are more tractable for higher-cost methods (e.g., range-separated GGA hybrid functionals) that suffer less from delocalization error. The extent to which finite size effects can influence predictions of SAC properties remains unclear[23, 82].

DFT calculations have been used to provide insights into the catalytic mechanism of single iron atoms supported on nitrogen-doped graphene (Fe-N-C) for the electrochemical CO_2 reduction reaction (CO_2RR).[83-87] However, the inherent limitations of DFT functionals have led to diverging conclusions regarding the rate-limiting step and the effect of the active site environment on

catalytic activity. To resolve controversies in DFT calculations and achieve a quantitative understanding of electrocatalytic mechanisms, high-level coupled-cluster singles and doubles with perturbative triples (CCSD(T)) methods[88-90] are employed to simulate thermodynamics of Fe–N–C catalyzed CO_2 to CO reduction step[91], which accurately predict experimental observables like CO binding energy, onset potential, and potential of maximal Faradaic efficiency for the Fe–N–C active site.

1.4. Engineering Coordination Environment to Tune Activity and Selectivity

In recent years, SACs have been extensively studied[26, 33, 92], demonstrating remarkable catalytic performance and stability compared to traditional nanoparticle-based catalysts[93-96]. The unsaturated coordination environments and unique electronic structures of SACs have led to improved catalytic performance across a wide range of reactions[35, 36] and show promising potential for applications in energy storage and conversion[97, 98]. Recent experimental studies have demonstrated the significant potential of various codoping configurations for the ORR, including N/S and N/P codopants in the first coordination sphere[51-53, 99], as well as configurations with N in the first and P or S in the second coordination sphere[54, 100]. The results indicated that engineering the coordination environment metal center can modulate the structural and electronic properties, which further alter the energetics of reactions and catalytic performance. However, the investigation of codoped SACs, incorporating two or more heteroatoms into the catalyst structure, still requires further exploration.

The wide range of coordination configurations, enabled by various choices of the type and heterogeneity of coordination elements (i.e., N, O, P, and S), further allows for tuning the design and hence the structure-property relationship of SACs. This vast chemical space offers unparalleled control over the structure-property relationship of SACs. Precise manipulation of the

coordination sphere surrounding the central metal atom is crucial to unlocking the full potential of SACs and achieving desired catalytic activity and selectivity. Ingeniously adjusting the coordination environment allows for fine-tuning the electronic structure and reactivity of the metal center, thus enhancing the catalytic performance[51, 52]. Therefore, engineering the coordination environment near single metal sites by means of codopant[51-54, 60], from the first coordination sphere to the second or even further, would be a rational approach to establish structure-property relationships and design efficient SACs with optimal electronic structure for catalytic applications.

1.5. Utilizing High-throughput Virtual Screening and Machine Learning for Catalysts discovery

The discovery of new and improved catalysts is of paramount importance for driving advancements in various fields, including chemical synthesis, energy conversion, and environmental remediation. However, the traditional approach of experimental trial-and-error can be time-consuming and resource-intensive. The combination of high-throughput virtual screening (HTVS) [48, 101-107] and machine learning (ML)[8, 108-111] holds great promise in tackling combinatorial challenges and accelerating material development. HTVS facilitates rapid evaluation of an extensive library of catalyst candidates and identification of promising compounds, allowing for rapid exploration of chemical l space. ML algorithms can analyze this data, identifying relationships between catalyst structure and desired properties. HTVS often employs ML, which has emerged as a promising alternative strategy to address the limitations of scaling relationships and accelerate catalyst discovery and optimization. ML models have proven superior to scaling relationships by predicting reaction energetics with higher accuracy.[112-116] These models achieve this high performance by leveraging the power of data-driven approaches, learning from vast amounts of experimental and computational data, to capture intricate patterns and relationships that may not be apparent through traditional computational methods. Furthermore, ML models can

incorporate a wide range of features, including structural, electronic, and compositional information, thereby enabling a more comprehensive understanding of the factors influencing catalytic activity and stability.[116-118] Because of the advantages they provide, HTVS and ML can be leveraged to accelerate the rational design of SACs and other catalytic materials, expediting the discovery of novel catalysts with enhanced performance for catalytic reactions. Moreover, these approaches can be leveraged to elucidate the structure-reactivity relationships of SACs and to investigate the role of structural change in catalytic reactions.

1.6. Thesis Outline

In this thesis, we mainly employ first principle computational modeling to design and optimize SACs for catalytic applications and experimental collaborations on other chemical materials. The second chapter discusses the use of range-separated hybrid DFT to compare the energetics and structure of the metal-coordinating environment in SACs with 2p (N or O) and 3p (P or S) dopants, as well as the effect of increasing graphene model flake size. The third chapter describe a large-scale virtual high-throughput screening (VHTS) of transition metal (Mn, Fe, Co, and Ru) SACs codoped with various elements (N, O, P, and S) to explore the impact of codoping various elements on methane-to-methanol conversion. The fourth chapter focus on codoped Fe and Ru-based SACs for ORR using VHTS and machine learning (ML) models. We compare the accuracy of ML models in predicting reaction energetics to traditional scaling relationships. The fifth chapter discusses computational modeling on nitrous oxide adsorption and activation in metal-organic frameworks with coordinatively unsaturated metal centers. The sixth chapter focus on enhanced mechanics in the interpenetrating polymetal–organic cages networks with incorporating endohedral alkyl chain. The seventh chapter provides an outlook for future research directions stemming from this thesis.

Chapter 2: Modeling the roles of rigidity and dopants in single-atom methane-to-methanol catalysts

This chapter has been partially adapted from 'H. Jia, A. Nandy, M. Liu, and H. J. Kulik, "Modeling the roles of rigidity and dopants in single-atom methane-to-methanol catalysts", *J. Mater. Chem. A* **2022**, 10, 6193-6203.'

2.1. Introduction

Single-atom catalysts (SACs) are emergent catalysts that contain isolated single metal atoms dispersed on supports, which are frequently graphitic[22-28]. SACs capture the inherent advantages of both homogeneous and heterogeneous catalysts by combining active site tunability with scalability[30, 31]. Nevertheless, the applicability of structure–property relationships derived from homogeneous or heterogeneous catalysts to predict the reactivity of SACs remains an outstanding question. Low site density and the short-lived, variable nature of SAC active sites[63, 64] fundamentally challenge many experimental techniques that bulk average over all sites, which limits the analysis of individual active sites. The harsh pyrolysis conditions used for SAC synthesis generate a distribution of active sites.[37, 41] Due to a lack of control over active site configuration, relationships between the structure of the SAC active site and the catalytic activity are challenging to deconvolute via experiment.[35, 36] Moreover, because the sub-nm scale can challenge even the highest-resolution spectroscopic probes that are sensitive to local variations in chemical environment[63, 64], the structures, reactivity, and selectivity of SACs are poorly understood from an experimental perspective. Computational modeling enables us to study active site configurations of SACs with atomic precision and can elucidate the effects of metal-local environment variation in SACs.

In doped graphene SACs, some or all of the metal-coordinating atoms are substituted with different atoms that lead to formation of vacancies (e.g., a double vacancy) where the metal atom can bind to form the SAC active site.[119] N-doped graphene, generated with nitrogen dopants, is the most common example of a support used in SACs.[36, 41-45] The identity of the coordinating atom alone, however, does not govern structure–property relationships, as different hybridization environments of the same element (e.g., pyridinic N vs. pyrrolic N) can lead to distinct SAC

reactivity.[30, 44] Similarly, different coordinating atom identities provide distinct ligand field strengths which could influence SAC properties and catalysis[47-52, 54, 55, 120].

The properties that make SACs attractive also make them challenging to study with conventional computational modeling using density functional theory (DFT). The trade-offs between representing the system as an infinite model simulated with periodic boundary conditions (PBCs) versus as a finite model flake must be considered when simulating SACs. PBCs naturally reproduce the extended nature of crystalline materials.[121, 122] However, the higher cost of exact exchange in plane wave PBC calculations typically motivates the use of generalized-gradient approximation (GGA) functionals that can be sensitive to delocalization error[123, 124], especially for the localized *d* orbitals of embedded transition-metal atoms.[23, 77, 78, 80, 123, 125] Additionally, PBCs may enforce unnecessary symmetry and rigidity to the metal-local environment in disordered SACs, which are known to exhibit curvature.[120] Finite models[81], conversely, are more tractable for higher-cost methods (e.g., range-separated GGA hybrid functionals) that suffer less from delocalization error. The extent to which finite-size effects can influence predictions of SAC properties remains unclear[23, 82].

Using computation to understand structure–activity relationships in SACs is important because are of the highest interest in catalyzing challenging reactions where only homogeneous catalysts have been successful. Strategies for SAC design require understanding which aspects of homogeneous catalysts can be preserved in an extended, heterogeneous catalyst. Two recent studies on molecular 14-membered pyridinic macrocycles, which are the smallest synthesized SAC mimics, show promise for the oxygen reduction reaction (ORR) in fuel cells[58, 126]. C–H bond activation[127-131] (e.g., for methane-to-methanol conversion) remains an outstanding challenge due to the high bond dissociation energy in methane. The activity, selectivity and stability must be

address for scalable C–H activation catalyst design[47, 48, 71, 132, 133]. Although many earth-abundant mid-row 3*d* transition-metal complexes (TMCs) have been demonstrated as homogeneous catalysts, the reactivity and selectivity in direct methane-to-methanol conversion under mild conditions of these TMCs is still very limited[133, 134]. Previous studies[36, 135-137] show that SACs can activate inert C–H bonds, but the differences in reactivity for C–H bond activation between SACs and TMCs remains unknown.

In this work, we investigate the effects of local structure on SAC reactivity for the challenging reaction of partial oxidation of methane to methanol. First, we calculate stability and structural properties of increasingly large SAC models to establish a benchmark of using finite models to simulate periodic graphene systems. We carry out a comprehensive structural study, comparing the metal–ligand bond lengths of 5- or 6-membered ring SACs, 14-membered macrocycles that most closely represent SACs, and octahedral TMCs for a range of candidate dopant atoms. Finally, we compare reaction energetics for methane-to-methanol conversion in SAC models to those that have been previously observed for TMCs[48] to understand the role the rigid graphitic environment can play in tuning SAC reactivity in comparison to analogous TMCs.

2.2. Model Systems

We studied two possible Fe(II) finite graphitic SAC models with identical metal-coordinating atoms of one of four elements (i.e., N, O, P, and S) in 5- or 6-membered rings within the graphene model (Figure 2.1). First, we obtained a 58-atom graphene flake model from a data set of structures[138] that were optimized using density functional tight binding. We used this initial model to construct a so-called FeX_4C_{10} SAC model (where X = N, O, P, or S) with the chemical formula $C_{36}X_4H_{16}Fe$ that corresponds to all metal-coordinating atoms in 6-membered rings, i.e.,

pyridinic N for X = N. To construct this SAC model, we created a divacancy in the center of the graphene sheet and replaced the four nearest carbon atoms with a given metal-coordinating atom and placed an Fe atom in the middle of the divacancy (Appendix Figure A2.1). To study the size dependence of 6-membered ring SACs, we built model systems from increasingly large flakes ranging from 58 to 398 atoms, with all starting structures derived from the same database[138].

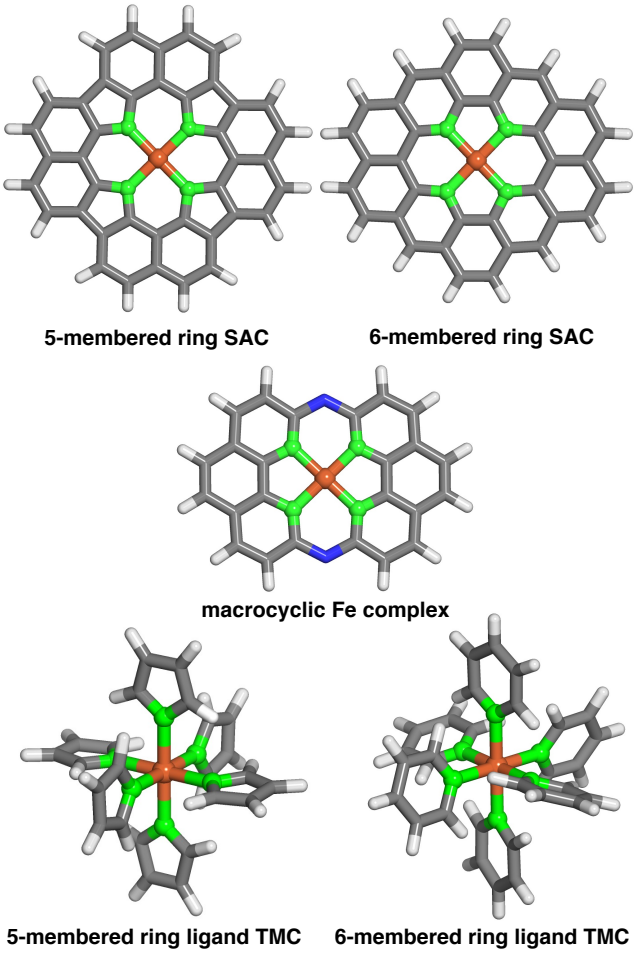

Figure 2.1. Atomic structures of 5- and 6-membered ring SACs, a fourteen-membered macrocyclic Fe complex, 5- and 6-membered ring ligand TMCs with different coordinating atoms shown in green (N, O, P and S). The representative structures are shown in the ball-and-stick representation colored as follows: Fe in brown, N in blue, C in gray, and H in white.

Next, we studied a FeX_4C_{12} compound (i.e., chemical formula $C_{40}X_4H_{16}Fe$), where all metal-coordinating atoms were in 5-membered rings (i.e., pyrrolic N for X = N, Figure 2.1). We

built the initial $C_{46}H_{16}$ structure in Avogadro v1.2.0[139], and formed the SAC model by removing two C atoms from the center and replacing the inward-facing C atoms of the remaining 5-membered rings with the metal-coordinating atoms (Appendix Figure A2.1). This model was not studied in flakes of increasing radius due to ambiguities associated with the fact that formation of a five-membered ring requires formation of a likely unstable neighboring eight-membered ring in an otherwise defect-free model.

To understand the relationship between SACs and analogous molecular species, we also studied a recently experimentally characterized[58] 14-membered macrocyclic Fe(II) complex (Figure 2.1). The 14-membered macrocyclic structure has been synthesized and characterized[58] for the case of X = N, and we also study it by replacing N with the other three dopants (i.e., $C_{24}X_4H_{12}N_2Fe$, where X = N, O, P, or S) we study in the SAC models. To build all molecules, we either worked directly from the experimental crystal structure[58] of $C_{24}N_4H_{12}N_2Fe$ or by replacing the relevant dopant atoms. Finally, as a further point of comparison, we also constructed homoleptic mononuclear octahedral transition-metal complexes (TMCs) with monodentate ligands that are considerably more flexible than the other systems studied (Figure 2.1). Initial structures of these TMCs with five- or six-membered ligands, i.e., N-coordinating pyrrole and pyridine, O-coordinating furan and 4H-pyran, P-coordinating phosphole and phosphinine, and S-coordinating thiophene and 4H-thiopyran, ligands were built using the molSimplify toolkit[140] with both ligand force-field pre-optimization and trained metal–ligand bond length features enabled[141].

2.3. Computational Details

Gas-phase geometry optimizations and single-point energy calculations were performed using density functional theory (DFT) with a developer version of the GPU-accelerated electronic structure code TeraChem v1.9[142]. The range-separated hybrid functional ωPBEh[143] (default ω =

0.2 $bohr^{-1}$) was employed for all calculations with the LACVP* composite basis set, which consists of a LANL2DZ effective core potential[144, 145] for transition metals and the 6-31G* basis for all other atoms. The ωPBEh functional was chosen to avoid unphysical HOMO–LUMO gap closing that has been observed in larger systems with global hybrids[146, 147]. All singlet spin state calculations were carried out in a spin-restricted formalism, while other calculations (i.e., metal-hydroxo intermediates) were carried out in a spin-unrestricted formalism that employed level shifting[148] of 1.0 for majority-spin virtual orbitals and 0.1 Ha for minority-spin virtual orbitals to enable the convergence of the self-consistent field (SCF). The default SCF convergence threshold of $3x10^{-5}$ Ha for the direct inversion of the iterative subspace (DIIS) error was applied. We focus on singlet states to isolate the effect of angular distortion on catalyst energetics in SACs in comparison to a prior data set of molecular complexes that showed angular distortion had no effect. While for these catalysts, intermediate spin energetics are generally more favorable, trends in dopant-specific energetics are preserved (Appendix Tables A2.1– A2.3).

Geometry optimizations were carried out with the translation-rotation-internal coordinate (TRIC)[149] optimizer, using default tolerances of 4.5×10^{-4} hartree/bohr for the maximum gradient, and 1×10^{-6} hartree for the change in SCF energy between steps. In the constrained calculations, the position of each atom in the SAC model along the z-direction was kept fixed to maintain a planar geometry. Converged unrestricted (i.e., metal-hydroxo) calculations were removed from the data set following established protocols[48, 101, 110] if: i) the expectation value of the S^2 operator, $\langle S^2 \rangle$, deviated from its expected value of $S(S+1)$ by > 1 μ_B^2 or ii) the Mulliken spin density on the metal differed from the spin multiplicity by > 1 μ_B.

For the four classes of systems studied, complexes were simulated with iron assumed to be in a formal Fe(II) oxidation state when no catalytic ligand was present, meaning that the total

charge of the overall model could vary. We simulated N- and P-coordinating 5-membered (6-membered) ring SAC models with net charges of -2 (+2), but all O- and S-coordinating SAC models with both 5-membered and 6-membered rings were simulated with a net charge of +2 to satisfy the octet rule (Appendix Table A2.4). We simulated all 14-membered macrocycles with a +2 net charge (Appendix Table A2.4). The formal charges assigned to the TMC ligands were neutral, except for pyrrole and phospholide, which were assigned a -1 charge (Appendix Table A2.4).

For catalytic intermediates of SAC models, the resting state SACs (i.e., square-planar Fe(II) complexes) were optimized first. An oxygen atom was added to these SACs at a distance of 1.65 Å, after which the geometry of the metal-oxo intermediate was optimized. Following the procedure developed in Ref. [48], the optimized metal-oxo intermediate was used as the starting point for the metal-hydroxo species, which was generated by adding an H atom and re-optimizing in a doublet spin state. That metal-hydroxo structure was then used to generate the methanol-bound singlet intermediate by adding a methyl group to the optimized metal-hydroxo structures using an in-house Python script.

To determine the relative stability of SAC models, we computed the complexation energies of SACs, E(SAC), relative to the bare, doped flake model, E(flake), and a gas-phase low-spin Fe(II) ion, E(Fe(II)). The complexation energy, indicates the relative stabilization energy that the flake provides to the metal and is evaluated as follows:

$$\mathrm{E(complexation)} = \mathrm{E(SAC)} - \mathrm{E(flake)} - \mathrm{E\big(Fe(II)\big)} \qquad (1)$$

In addition, we carry out an analysis on scaled metal−ligand bond lengths, d_{rel}(Fe−X), evaluated relative to the sum of covalent radii of each ligand element, X, with iron:

$$d_{\mathrm{rel}}(\mathrm{Fe–X}) = \frac{d(\mathrm{Fe–X})}{r_{\mathrm{Fe}} + r_{\mathrm{X}}} \qquad (2)$$

2.4. Results and Discussion

2.4A. Size Effects of Graphene Flakes on SAC Properties

Simulating SACs requires consideration of the trade-offs between representing the system as an infinite model simulated with periodic boundary conditions (PBCs) versus as a finite (i.e., flake) model. Thus, we first aim to understand the approach to an asymptotic limit in model flakes that can be systematically increased in size (i.e., with 6-membered rings coordinating the metal). We focus on evaluating the effect of model size on both overall and local geometric properties as well as the stability (i.e., complexation energy). To determine the size effects of graphene flakes on SAC properties, we study six sizes of doped 6-membered ring graphene flakes ranging from a minimal model that is 13.6 Å in size ($C_{36}X_4H_{16}Fe$, where X = N, O, P, or S) to a larger, 35.0-Å model ($C_{346}X_4H_{46}Fe$, Appendix Figure A2.2). We estimate the size of the flake models by the distance between the most distant H atoms prior to optimization. After full geometry optimization, we observe that the SACs with 2*p* coordinating elements (i.e., N and O) remain planar, while SACs with 3*p* coordinating elements (i.e., P and S) become distorted. For smaller flake sizes, complexation energies (see Computational Details) are less favorable, and they generally approach asymptotic limits with a flake size of 186 carbon atoms (i.e., 225 atoms total), after which they no longer change significantly (Figure 2.2). For all flake sizes, the relative stability (i.e., N > P > S > O) is unchanged, but the absolute stability, especially of O- and S-doped models, is somewhat more sensitive to model size (Figure 2.2).

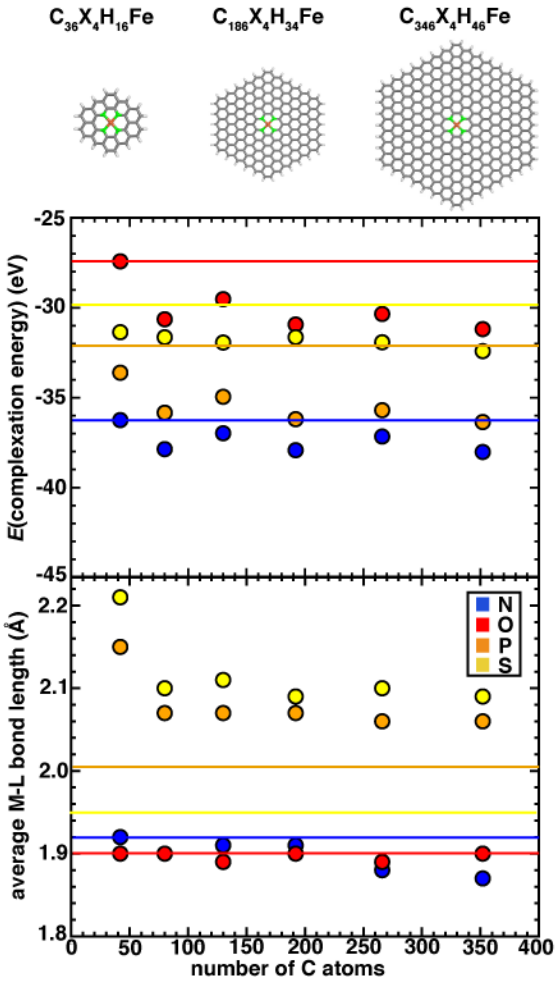

Figure 2.2. The complexation energy (in eV) and average M–L bond length (in Å) of increasingly large Fe SACs with N, O, P and S-doped graphene flakes. The z-constrained optimization results are shown as the corresponding horizontal lines. Three sizes of representative SACs ($C_{36}X_4H_{16}Fe$, $C_{186}X_4H_{34}Fe$ and $C_{346}X_4H_{46}Fe$) are shown at top. The structures are shown in stick representation colored as follows: Fe in brown, dopant coordinating atoms in green, C in gray, and H in white. Here, the number of C atoms refers to all atoms in the flake prior to insertion of the vacancy and placement of the dopants and iron.

Since the observed sensitivity of absolute complexation energies has some sensitivity to graphene flake size, we next investigated whether these changes were associated with differences in structure with increasing size of the model. When no constraints are applied during geometry optimization, the SACs with 2*p* (e.g., N and O) coordinating elements remained planar regardless of model size, whereas SACs with 3*p* (e.g., P and S) coordinating elements are distorted in a

manner that is sensitive to the size of the model (Figure 2.2). While complexation energies were sensitive to model size for both 2*p* and 3*p* elements, we aimed to separately determine if the distortion observed in 3*p*-coordinating SAC models also depends on model size. We first quantify the global distortion of these models by measuring the distance between the centers of mass of planar and distorted structures. We divide this measure by the size of the SAC model to estimate the size-independent degree of distortion. For all 3*p*-coordinating SACs, we observe decreased flake distortion with larger graphene models, which is consistent with expectations that larger model sizes should constrain and reduce the degree of distortion (Appendix Figure A2.3 and Table A2.5).

Although all 3*p*-coordinating SACs exhibit out-of-plane distortion, P-coordinating SACs are more distorted than corresponding S-coordinating SACs for the same model size (Appendix Figure A2.3 and Table A2.5). This observation is surprising because it occurs despite only minor differences in covalent radii between P and S (1.07 and 1.05 Å, respectively). Since the center-of-mass-measured distortion may be influenced by metal-distal carbon atoms, we also measured the metal-local root-mean-square deviation (RMSD) of the metal and four coordinating atoms of P- and S-doped SACs with increasingly large models. We observe that the local RMSD values between the optimized and initial structures of the metal and the four metal-coordinating atoms of P- and S-doped SACs decrease when the flakes become larger, suggesting that increasing model size indeed leads to more constrained metal coordination (Appendix Figure A2.4). Thus, observations of flake distortion based on the overall out-of-plane bending and local-RMSD based measures indicates that distortion decreases with increasing model size.

On the basis of the observation of the noticeable distortion, we aimed to understand its impact on the metal–ligand bond lengths of the increasingly large SACs because metal–ligand

bond lengths are critical for understanding spin states[150] and catalytic properties[47, 48]. We thus also analyzed the metal–ligand bond lengths of the increasingly large SAC models (Figure 2.2 and Appendix Table A2.6). Consistent with the effects of reduced distortion for larger graphene models, we observe a general trend that metal–ligand bond lengths reduce with increasing SAC size (e.g., from 2.21 Å for the smallest $C_{36}S_4H_{16}Fe$ to 2.09 Å for the largest $C_{346}S_4H_{46}Fe$). Thus, in terms of electronic effects of these shortened bond lengths, we can expect that metal sites in increasingly large SACs experience stronger ligand fields (i.e., due to shorter metal–ligand bond lengths). Nevertheless, despite these model-size-dependent trends, relative bond lengths (S > P >> N ~ O) are qualitatively preserved across all flake sizes (Figure 2.2). Furthermore, in contrast to complexation energies, we observe fast convergence for metal–ligand bond lengths with size of SAC models from the second-smallest (i.e., $C_{74}X_4H_{22}Fe$) flake onward, where changes in bond lengths are observed only for 3*p* elements or between the smallest and larger models (Figure 2.2).

While quantitative differences are apparent for the smallest model sizes, qualitative trends in dopant-dependent complexation energies and bond lengths hold for all model sizes (Figure 2.2). Thus, in order to aid comparison to macrocycles (i.e., 14-membered rings), TMCs, and alternative coordination within 5-membered-ring-coordinating SAC models, our subsequent analysis focuses on the smallest (i.e., $C_{36}X_4H_{16}Fe$) 6-membered ring SAC model. We note that this means that the finite-size effects cannot be disregarded, but we expect the qualitative comparison of dopant-dependent SAC properties will hold.

2.4B. Structural Comparisons of SAC Models and Molecular Complexes

Despite evident structural similarities of SACs and single-site homogeneous catalysts, the relationship to similarities in their catalytic activities is only partially understood.[58, 126, 151] We thus first investigate the structural role that the rigid graphitic environment plays in altering the metal-

local environment in SACs in comparison to homogeneous catalysts. To isolate the effect of graphene rigidity on SAC structural properties, we compare the metal–ligand bond lengths of three distinct systems: i) finite models of SACs, ii) a recently synthesized[58] rigid molecular complex believed to represent the local coordination environment in SACs, and iii) mononuclear octahedral transition-metal complexes (TMCs, Figure 2.1).

The covalent radius of 2*p* dopants (i.e., N and O) is smaller than that of 3*p* dopants (i.e., P and S), but the graphitic environment always constrains the metal–ligand bond distance to be equivalent in comparison to molecular catalysts with low-denticity ligands. Nevertheless, a competing effect observed in the 3*p*-doped SACs (see Sec. 4a) is that the metal and its coordinating atoms are distorted out of the plane (Appendix Figure A2.5). To further isolate the effect of this distortion, we compare unconstrained 5- and 6-membered ring SAC models with constrained geometry optimizations in which we fix all atoms to lie in the same plane (i.e., the xy plane). As should be expected, applying this constraint leads to even shorter metal–ligand bond lengths in 3*p*-doped SAC models relative to the corresponding unconstrained structures (Figure 2.3 and Appendix Table A2.7). Thus, the unfavorable SAC distortion that occurs is compensated for by lowering the degree of metal–ligand bond compression that is highly unfavorable when all atoms are constrained to lie in the same plane. For the smaller 2*p* dopants, the degree of compression is small enough that no distortion out of the plane is observed (Appendix Figure A2.6).

Focusing on the 3*p*-coordinating SACs, 5-membered ring SACs exhibit more severe distortion relative to 6-membered ring SACs, likely due to the ability of this structure to accommodate larger dopant–dopant distances upon distortion (Appendix Table A2.8). Specifically comparing the individual 3*p* dopants, we observe a slight increase in distortion for P-coordinating

SAC models relative to S-coordinating models (i.e., 5- or 6-membered ring SACs), consistent with the somewhat larger covalent radius of P than S (Appendix Table A2.9).

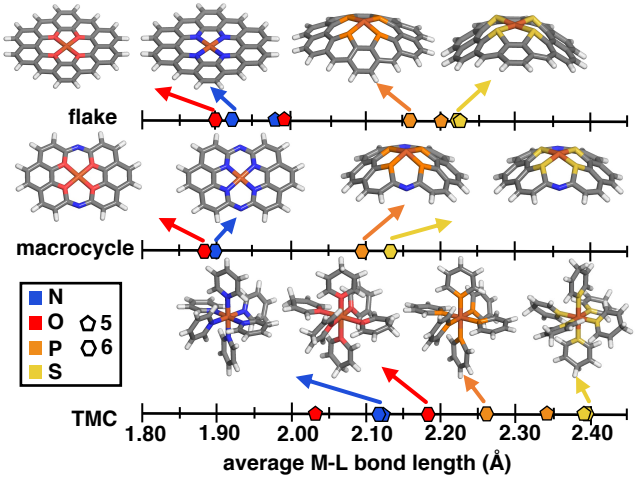

Figure 2.3. Comparison of Fe-dopant bond lengths between N, O, P and S-doped graphene Fe SAC models (top), 14-membered macrocyclic complexes (middle) and transition-metal complexes (TMCs, bottom). Representative SAC, macrocyclic, and TMC compounds are shown in stick representation colored as follows: Fe in brown, N in blue, O in red, P in orange, S in yellow, C in gray, and H in white. Bond lengths for 5-membered ring complexes and SACs are shown as pentagon symbols and 6-membered ring complexes and SACs are shown as hexagons. Only six-membered ring structures are shown in insets.

To put the distortion and compression of the bond lengths in SACs in perspective, we compare them to TMC bond lengths. The metal–ligand bond lengths of freely optimized SAC models span a large, 0.32 Å range, from 1.89 Å in O-doped 6-membered ring SACs to 2.21 Å for S-doped 6-membered ring SACs (Figure 2.3 and Appendix Table A2.7). When the ligands can move freely in mononuclear octahedral TMCs, we observe both longer overall bonds and a somewhat larger range (0.35 Å) from O-coordinating furan (2.03 Å) to S-coordinating thiophene (2.38 Å). Thus, the SAC metal–ligand bond length is significantly compressed for all dopants in comparison to analogous TMCs by around 0.1 to 0.2 Å. The 14-membered macrocyclic complexes have very similar structural characteristics to the SACs due to the comparable rigidity. The O-doped 14-membered macrocyclic complexes have equivalently short metal–ligand bonds (i.e.,

1.88 Å) to those in the SACs, and the structure is even less accommodating of the larger dopants, with the longest observed metal–ligand bond length in the S-coordinating model (i.e., 2.12 Å) corresponding to both shorter bond lengths and smaller overall range (i.e., 0.24 Å) of dopant-dependent bond lengths than for either SACs or TMCs. The fact that the metal–ligand bonds of the 14-membered macrocycle more closely resemble that of our SACs than TMCs is expected, given previous observations of similarities in activity between SACs and the macrocycle[58].

As a specific example, metal–ligand bonds in TMCs with 5- and 6-membered ring ligands (e.g., 2.03 Å and 2.17 Å for furan and 4H-pyran) are consistently longer than those in analogous 5- and 6-membered ring SACs (e.g., 1.99 Å and 1.89 Å for O-doped 5- and 6-membered ring SACs). The shorter bond lengths of SACs (e.g., 1.92 Å in an N-doped 6-membered ring SAC and 2.11 Å in a pyridine TMC) indicate the influence of SAC rigidity on the active site. To quantify this effect on more equal footing between 2*p* and 3*p* dopants, we analyze scaled metal−ligand bond lengths, d_{rel}(Fe−X), relative to the sum of covalent radii of each ligand element, X, with iron (Appendix Table A2.9). Using spin-state-dependent definitions of covalent radii[150], a d_{rel}(Fe−X) of around 0.90–0.95 is typical for a low-spin TMC. The d_{rel}(Fe−X) values are significantly shorter than this value in all SACs and 14-membered macrocycles, especially for the cases with 3*p*-coordination (Appendix Table A2.10). The 3*p*-coordinating 14-membered macrocycles have more compressed metal–ligand bonds (e.g., d_{rel}: 0.78 in the S-doped macrocycle) compared to equivalent SACs (e.g., d_{rel}: 0.87 and 0.89 in 5- and 6-membered ring SACs). Both absolute bond lengths and their trends are fairly insensitive to exchange-correlation functional, and most DFT functionals predict experimental bond lengths of transition metal complexes well.[152] To validate this expectation, we compare our optimized bond lengths to those of the crystal structure of the 14-

membered macrocycles and confirm the metal-ligand bond lengths are in good agreement (i.e., within around 0.05 Å).

Motivated by quantitative structural differences among 5- and 6-membered ring SACs and 14-membered macrocycles, we estimate the relative stability of these coordination environments (i.e., by computing the complexation energies). While all structures form favorably relative to the chosen reference in our energetic evaluation, we find that N-doped SACs and N-doped 14-membered macrocycles have the most favorable complexation energies of the systems studied. Due to the less crowded metal-coordination environment, complexation energies of 5-membered ring SACs are more favorable than the corresponding 6-membered ring SACs with the same coordinating atoms (Appendix Table A2.11). The complexation energy in the distorted 3*p*-coordinating SACs is up to 1.5 eV more favorable than the constrained case (Appendix Table A2.11). Overall, the coordination atom type and local chemical environment (i.e., five-membered or six-membered rings and degree of rigidity) both significantly influence the metal–ligand bond lengths and corresponding complexation energy of the systems. Constraining 3*p*-coordinating SACs to be planar reduces metal–ligand bond lengths in a manner that is likely unrealistic for 3*p* dopants, potentially leading to poor models of the structural environment in simulations that naturally enforce such constraint (e.g., in calculations with PBCs).

2.4C. Relating Structural and Catalytic Properties of SACs

SACs with Fe(II) centers bear strong similarity to single-site homogeneous and biological catalysts capable of challenging reactions such as selective partial methane oxidation to methanol. To understand the relationship between catalytic properties of SACs and homogeneous counterparts for partial methane oxidation, we compare SAC reaction energetics to those from 385 LS Fe(II) TMCs studied previously[48]. For consistency with this prior work[48], we evaluate the

reaction energetics for the radical rebound mechanism[153] of methane-to-methanol conversion on both fully optimized and partially constrained SAC models. In brief, to follow the radical rebound mechanism[153] we start from the resting state structure (**1**) and form a high-valent terminal Fe(IV)=O (**2**) via two-electron oxidation (Figure 2.4). We evaluate the oxo formation energy, ΔE(oxo), using the common oxidant nitrous oxide, N_2O,[154, 155] as the oxygen atom source

$$\Delta E(\text{oxo}) = E(\mathbf{2}) - E(\mathbf{1}) + E(N_2) - E(N_2O) \qquad (3)$$

Since we primarily focus on reaction thermodynamics, alternative oxygen atom sources could be equivalently used in eqn. 3 with the only effect of rigidly shifting all relative energies. Next, the Fe(IV)=O catalyzes hydrogen atom transfer (HAT) from methane to form methyl radical. We calculate the ΔE(HAT) energy as

$$\Delta E(\text{HAT}) = E(\mathbf{3}) - E(\mathbf{2}) + E(CH_3\bullet) - E(CH_4) \qquad (4)$$

where (**3**) is the Fe(III)−OH intermediate formed after abstraction of a hydrogen from methane to form methyl radical (Figure 2.4). Recombination of the methyl radical with the iron-hydroxo in the radical rebound step forms a metal-bound methanol intermediate (**4**). We calculate the ΔE(rebound) energy as

$$\Delta E(\text{rebound}) = E(\mathbf{4}) - E(\mathbf{3}) - E(CH_3\bullet) \qquad (5)$$

To complete the catalytic cycle, the SAC must then release the methanol and return to the resting state (**1**, see Figure 2.4). We compute the energetics of methanol release, ΔE(release), as

$$\Delta E(\text{release}) = E(\mathbf{1}) + E(CH_3OH) - E(\mathbf{4}) \qquad (6)$$

For the above formal oxidation states, we confirmed we converged to these states in our calculations by carrying out Mulliken spin density analysis (Appendix Table A2.12). The closed shell calculations ensure that a nominal Fe(IV)=O intermediate is studied during oxo formation, as determined by the total charge in the system. For the open shell Fe(III)−OH species, the spin is

localized on the metal (Appendix Table A2.12). These observations were corroborated by natural bonding orbital analysis that confirmed that changes in the coordinating atoms (e.g., N vs O or S) did not dramatically change the degree of charge localized on the metal (Appendix Table A2.13). We also confirmed that formation of the metal-oxo was generally more favorable than oxygen addition to the organic coordinating atoms, except in the case of P-doped structures that could form a μ-oxo not feasible in the presence of the metal (Appendix Table A2.14). While the present work allows us to evaluate the radical rebound mechanism, we have not addressed the well-known selectivity challenges for methane to methanol conversion.[156, 157] Future work should also address whether favorable methanol activation could in fact be a limiting factor in SACs or if the scaling relationship can be broken between activation on methane versus methanol.

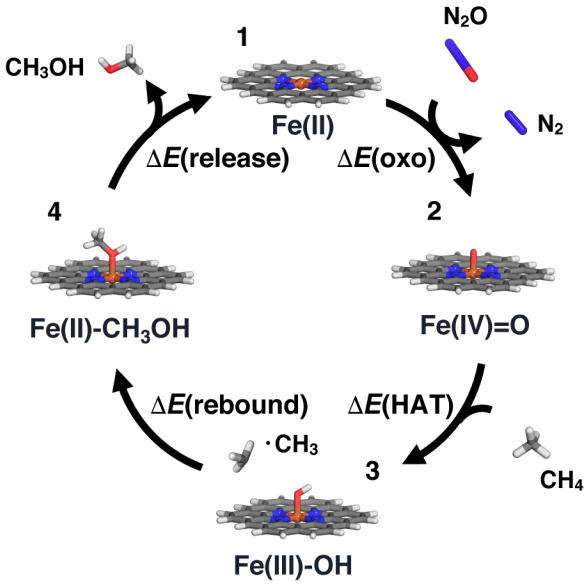

Figure 2.4. Catalytic cycle for the radical rebound mechanism for conversion of methane to methanol. From the resting state (**1**, top) in oxidation state II, the cycle proceeds clockwise: iron−oxo (**2**, right) formation with an N_2O oxidant, hydrogen atom transfer to form an iron−hydroxo complex (**3**, bottom), and rebound to form a methanol-bound intermediate (**4**, left). A representative N-doped 6-membered ring graphene Fe SAC model is shown in stick representation colored as follows: Fe in brown, N in blue, O in red, C in gray, and H in white.

Following our observations of differences in the stability of distorted and constrained 3*p*-

doped SACs, we would expect such constraints to also alter catalytic properties. In addition, the nature of the surrounding coordination environment (i.e., 5-membered vs 6-membered rings), and the elements coordinating the metal are expected to also play a role in determining catalytic properties. Although for N- and O-doped 5- and 6-membered ring SAC models, constraints did not have any effect on the resting state structure and thus were not expected to influence reaction energetics, we do observe some differences between constrained and unconstrained structures (Figure 2.5 and Appendix Table A2.7). These differences in 2*p*-coordinated SACs arise due to distortion favored in the reaction intermediates that were absent in the resting state (e.g., especially the metal-oxo, Figure 2.5). When unconstrained, the metal-oxo, -hydroxo, and methanol-bound intermediates all exhibit out-of-plane metal distortion of around 5–10°, consistent with prior results[47] (Appendix Figure A2.6). Because this distortion is generally largest for the metal-oxo, this intermediate is most strongly destabilized for constrained SACs, which in turn influences both oxo formation and hydrogen atom transfer energetics (Figure 2.5).

The distortion observed in unconstrained P- and S-doped SAC models was expected to have a much more noticeable effect on the reaction coordinate because it affected resting state energetics. Indeed, while some intermediates are similar in energy (e.g., the methanol-bound intermediate in S-coordinating 5-membered ring SACs) with and without constraints, the likely rate-limiting steps of oxo formation and HAT are more favorable in the structures that allow for distortion with 3*p*-coordinating SACS (Figure 2.5). We attribute the differences in energetics to differences in the bond lengths rather than angles because the distortion largely moves the metal out of the plane simultaneously with the dopants. This observation is also consistent with our prior studies[48] that suggest bond length was most important for tuning singlet Fe(II) reaction thermodynamics in TMCs. Overall, our analysis suggests that the freely optimized SACs with 3*p*

dopants (e.g., P-doped, five-membered ring SACs) are competitive with more well studied N-doped SACs because methanol release energetics are relatively favorable without strongly destabilizing oxo or HAT formation (Figure 2.5). We focus here on LS states to isolate the effect of angular distortion on catalyst energetics in SACs in comparison to this prior data set. We observe general trends are preserved (e.g., for Fe/N systems with five-membered versus six-membered rings) if we had instead computed IS energetics (Appendix Tables A2.1– A2.3).

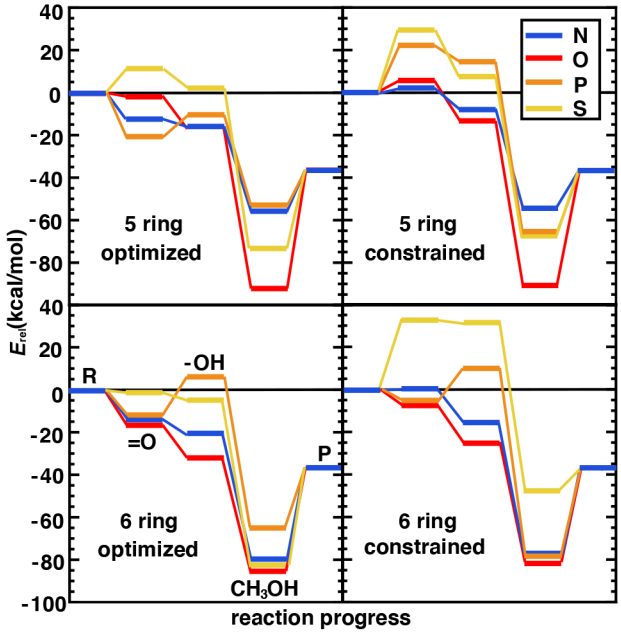

Figure 2.5. Reaction energetics (E_{rel}, in kcal/mol) for the N (in blue), O (in red), P (in orange), and S (in yellow) doped 5- and 6- membered ring graphene model SACs with full geometry optimization (left) or constrained optimization (right). The intermediates are labeled in the bottom left pane: the reactant (R), the oxo intermediate (=O), the hydroxo intermediate (−OH), the methanol-bound intermediate (CH_3OH), and the product (P). N-doped system in blue, O-doped system in red, P-doped system in orange, S-doped system in yellow, respectively.

We next compare the catalytic performance of these SAC models with the set of previously studied TMCs[48]. The TMCs from our previous study have four coordinating minimal model ligands in a square pyramidal geometry constrained to specific metal–ligand bond lengths that correspond to both slightly stretched and compressed bonds with respect to their equilibrium

values (i.e., by around 0.2 Å) along with out-of-plane distortions (i.e., the dihedral of the metal with three ligand atoms) of the metal coordination environment. In comparison to these TMCs, we had observed that the SAC structure compresses the metal–ligand bond length to the lower end of the range or even shorter (see Sec. 4b). In combination with the distinct local environment around the metal-coordinating atoms, SAC models exhibit significantly different energetics from those of the TMCs. Generally, SAC models exhibit more thermoneutral ΔE(oxo) while displaying comparable ΔE(HAT) and ΔE(release) to TMCs from prior work (Figure 2.6). These observations are not strongly sensitive to the choice of hybrid DFT exchange-correlation functional, instead suggesting distinct reactivity between the SAC models and TMCs (Appendix Figures A2.7– A2.8).

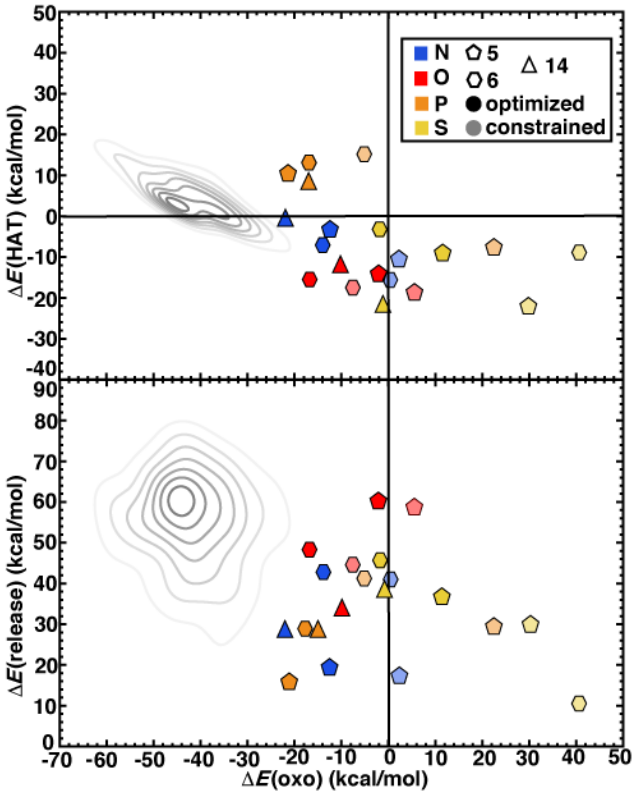

Figure 2.6. ΔE(oxo) vs ΔE(HAT) (top) and ΔE(oxo) vs ΔE(release) (bottom) reaction energies (in kcal/mol) of representative TMCs from prior work[48] compared to 5-membered (pentagons) and 6-membered (hexagons) ring SAC models, and 14-membered macrocyclic Fe complexes (triangles). The SACs and macrocycles are colored by the metal-coordinating atoms in the ligands, as indicated in inset legend. The TMCs from prior work are the full LS Fe(II) subset from the square pyramidal constrained (SQ) set of Ref. [48]. The kernel density estimates of the distributions for the TMC set are colored in gray and shown as contour lines with decreasing saturation in 7

evenly spaced levels. The SACs are distinguished by full geometry optimization (opaque) and constrained optimization (translucent).

Despite distinct reaction energetics for SACs and TMCs with common metal-coordinating atoms, there are some notable cases where the two types of catalysts have comparable properties (Appendix Figures A2.9– A2.10). Several O-doped SACs behave similarly to the square pyramidal Fe(II) TMCs with O-atom coordination in a somewhat stretched (i.e., 10° out-of-plane distortion and 2.2 Å bond distance) structure (Appendix Figure A2.10). This correspondence in energetics does not coincide with correspondence in structure, as the SAC has significantly more compressed metal–ligand bonds (1.9 Å). Somewhat surprisingly, we find more comparable reaction energies between SACs and TMCs in tetragonal equilibrium geometries from prior work[48] which contain axial ligands that are not present in our SAC models (Appendix Figure A2.11). Because the distal axial ligand tends to make oxo formation more favorable relative to that for compounds in the more structurally equivalent square planar set, the energetics of these TMCs coincide more with the SACs (Appendix Figures A2.12– A2.13). Overall, SACs increase the favorability for oxo formation, which we attribute to rigidity from the graphene flake strengthening the ligand field and stabilizing a high-valent metal-oxo without requiring the presence of an axial ligand common to TMCs and biological catalysts.

Next, we return to the energetics for the 14-membered macrocycle, which we would expect to behave more comparably to SAC models than to TMCs, despite also being a molecular complex. Reaction energetics are largely consistent between the macrocycles and the 6-membered ring SAC models, although some small differences are observed (Figure 2.6). For the 14-membered macrocycle in comparison to SACs, the relative position of N-doped and P-doped models in terms of their $\Delta E(oxo)$ vs $\Delta E(HAT)$ favorability is altered (Figure 2.6). This reversal of 2*p*- and 3*p*-

doped favorability is not observed for the O- and S-doped cases (Figure 2.6). Overall, the N-doped 14-membered macrocycles exhibit more favorable oxo formation energy than the corresponding N-coordinating 6-membered ring SAC model. We attribute the differences between the two N-doped catalysts to be due to the shorter metal–ligand bond length of the 14-membered macrocycle (1.88 Å) relative to the 6-membered ring SAC model (1.92 Å) in the metal-oxo intermediate along with a larger out-of-plane distortion (19° vs 11°, Appendix Figure A2.14). Structures for the P-doped cases are more comparable, leading to similar energetics and explaining the change in relative favorability (Appendix Figure A2.14 and Table A2.7).

The results compared here focus on reaction energetics due to scaling relations between the reaction thermodynamics and kinetic barriers in this work. Nevertheless, we selected representative favorable N-doped SACs for follow up analysis of the barriers as well (Appendix Figures A2.15– A2.16). From this analysis, we confirm that favorable thermodynamics for N-doped SACs in five-membered rings indeed corresponds to relatively modest barrier heights for oxo formation and HAT (Appendix Figure A2.15– A2.16). This observation supports our focus on more computationally affordable reaction energetics in our large-scale screen.

2.5. Conclusions

While single-atom catalysts (SACs) consisting of metal atoms embedded in doped graphene represent promising catalysts, the extent to which design principles derived from homogeneous or heterogeneous catalysts, such as the applicability of scaling relations, can be extended to SACs remains largely unknown. Here, we focused on understanding the relationship between SAC structure and tradeoffs in key reaction steps in the selective partial oxidation of methane to methanol via a radical rebound mechanism at single Fe(II) sites.

After confirming that qualitative conclusions about the dopant-dependent structural and stability properties on model SACs were invariant to model size, we carried out a systematic comparison of SACs to TMCs and macrocyclic mimics of SACs using range-separated hybrid DFT. We observed differences in the degree of distortion around the Fe(II) metal center depending on the dopant type. In the resting state, we observed that 2*p*-coordinating species favored planar structures, whereas significant distortion was observed with 3*p* dopants. We attributed this difference to differences in the relative covalent radii of these dopants, where the penalty for forming a very short metal–dopant bond in the 3*p* cases was so large that distortion of the graphitic substrate was preferred. In comparison to transition-metal complexes, SAC model metal–ligand bond lengths were considerably shorter, corresponding to a stronger ligand field, and recently characterized macrocyclic complexes exhibited the shortest metal–ligand bond lengths. Even with this significant compression in the bonding environment, P-doped SACs had energetics competitive with more well studied N-doped systems, with favorable methanol release and exothermic oxo formation. These steps were less favorable if we constrained the structures to be planar. Combined with our observations of model-size-dependent distortion at the metal center, these observations suggest that processing of doped graphitic catalysts that influences flexibility around the catalytic active site should influence reactivity.

Overall, analysis of the doped graphitic SAC reaction energetics indicated distinct energetics for most SAC models in comparison to prior work on TMCs, with SACs having more thermoneutral ΔE(oxo) while displaying comparable ΔE(HAT) and ΔE(release) to TMCs. While we attribute this effect to differences in ligand field, we observed that a set of TMCs with an axial ligand that is absent in our SAC models had more comparable oxo formation energetics. Overall, these results highlight the potential of SACs for altering the energetics of methane-to-methanol

conversion by constraining metal–ligand bond distances to values distinct from those typically accessed by more flexible homogeneous catalysts.

Chapter 3: Computational discovery of codoped single atom catalysts for methane-to-methanol conversion

This chapter has been partially adapted from ‘H. Jia, C. Duan, I. Kevlishvili, A. Nandy, M. Liu, and H. J. Kulik, "Computational Discovery of Codoped Single Atom Catalysts for Methane-to-Methanol Conversion", *ACS Catal.* **2024**, *14*, 2992−3005.’

3.1. Introduction

Methane, the second-most prominent greenhouse gas (GHG), contributes to approximately 16−20% of global GHG emissions[1]. Converting methane to valuable chemicals (e.g., methanol) is seen as a key strategy to reduce methane emissions and therefore has great environmental significance and potential economic value. However, the direct conversion of methane to methanol is particularly challenging due to the high energy required to activate the strong C–H bonds of methane, which requires an efficient catalyst to lower the energy barrier, together with the thermodynamic favorability of methanol overoxidation to CO_2[5, 6]. The optimal catalysts for methane-to-methanol conversion need to satisfy numerous criteria, driving an exhaustive search of catalytic materials[7, 8]. Enzymes (e.g., Fe(II) active sites in TauD[9-11]) have demonstrated the capability to selectively oxidize substrates with strong C–H bonds and motivated bioinspired design[12-14] of synthetic systems, including both homogeneous[15-18, 129, 130] and heterogeneous[19-21] catalysts, for direct methane-to-methanol conversion. Although there has been substantial progress, no synthetic catalyst can simultaneously achieve as high activity and selectivity as enzymes, motivating a more extensive search for alternative catalysts.

Single-atom catalysts[22-29] (SACs), with isolated metal atoms dispersed on solid supports, have recently emerged as a captivating frontier, attracting intense research attention, although only limited study of SACs for direct methane-to-methanol conversion[92, 158-161] has so far been reported. SACs have the promise to combine the scalability of heterogeneous catalysts and the high atom economy of homogeneous catalysts[30, 31], offering significant opportunities for atom-economical utilization of metals[32-34]. Their unique electronic structure and unsaturated coordination environments have led to enhanced catalytic activity across numerous reactions[35, 36]. Among different classes of SACs, N-doped graphene SACs[26, 29, 37], featuring an isolated metal atom

embedded in a graphitic material, more closely resemble their homogeneous counterparts compared to others. For instance, the Fe–N_4 active site in Fe-SACs are viewed as analogous to hemes[36, 38-40], where the Fe center is also coordinated to four nitrogen atoms, and molecular analogues have been developed to these SACs[162].

Although SACs exhibit attractive properties for catalysis, unraveling the catalytic mechanisms of SACs through experimental means faces significant challenges. The synthesis of SACs under harsh pyrolysis conditions results in a distribution of active sites[37, 41, 52, 54, 163] and significant variation of the local coordination environment[51, 53, 163], posing fundamental challenges for most characterization techniques, even for the highest-resolution spectroscopic techniques[63, 64]. Similar to biological enzymes or transition metal complexes (TMCs), the spin state and oxidation state significantly influence the reactivity of SACs[48, 60], making it challenging to assess reactivity trends due to the difficulty of experiments that precisely identify the oxidation/spin states during catalysis[35, 44]. To overcome these limits, first-principles modeling with density functional theory (DFT) has been a powerful tool for designing new SACs[65, 66] and obtaining mechanistic insights[67-69, 137, 164-167] into their catalytic activities[70-74, 168] with atomic precision. These DFT simulations[137, 166] have revealed that both the support and coordination environment of SACs are essential in determining their catalytic reactivity, consistent with the conclusions drawn from experimental characterization[41, 51]. Thus, gaining a comprehensive understanding of the correlation between the structure and catalytic performance holds the key to achieving the rational design of SACs for targeted reactions at the atomic scale. Additionally, high-throughput virtual screening (HTVS)[48, 101-105] facilitates evaluation of an extensive library of catalyst candidates and the identification of promising ones. These approaches can be leveraged to elucidate the structure–

reactivity relationships[65, 66] of SACs and to investigate the role of structural change in catalytic reactions.

SACs with open-shell metal centers resemble single-site homogeneous and biological catalysts capable of catalyzing reactions such as C−H activation. The wide range of coordination configurations, enabled by various choices of the type and heterogeneity of coordination elements (i.e., N, O, P, and S), further allows for tuning the design and hence the structure–property relationship of SACs. Our previous work[29] investigated the rigid graphitic environment of SACs with N, O, P, and S coordination environments and compared them to homogeneous analogues for methane-to-methanol conversion, finding that differences in dopant sizes had major impacts on the structure and energetic properties of SACs. Further manipulation of the coordination sphere around the metal atom is paramount to unlocking the full potential of SACs and tailoring their catalytic activity and selectivity by fine-tuning the electronic structure and reactivity of the metal center, thus enhancing the catalytic performance[51, 52]. Therefore, engineering the coordination environment near single metal sites by means of codopants[51-54, 60, 169] would be a way to design efficient SACs with optimal electronic structure for catalytic applications. Several codoping studies (e.g., N/S codopants in the first coordination sphere[52, 53], N/P codopants in the first coordination sphere[51], and N in first with P in the second coordination sphere configuration[54]) have been reported experimentally and shown significant potential for the oxygen reduction reaction (ORR), but the effect of codoping on methane-to-methanol conversion has not yet been reported.

In this work, we employ a VHTS approach to explore 2,048 transition metal (i.e., Mn, Fe, Co, and Ru) SACs codoped with various elements (i.e., N, O, P, and S) for the challenging conversion of methane to methanol. Initially, we investigate the global trends in spin state ordering and catalytic reaction energetics of the whole methane-to-methanol reaction cycle. Next, we focus

on relationships between metal or codopant identity and reaction energetics, considering period dependence and coordination effects through the comparison of *3d* and *4d* codoped SACs (e.g., Fe and Ru). In particular, best-trade-off catalyst candidates are identified along the ΔE(oxo) and ΔE(HAT) reaction energetics Pareto frontier. Finally, comprehensive characterization of the complete kinetic reaction coordinate validates the best-performing codoped SACs.

3.2. Model Systems

We modeled SACs with various metal-coordinating atoms (i.e., N, O, P, and S) in vacancies formed in 5- and 6-membered rings (Figure 3.1). The sizes of the 5- and 6-membered ring graphitic SAC systems investigated in this work are 59 and 61 atoms, respectively. Previous studies[29] have shown that even though finite-size effects of SAC flake models are not negligible, the qualitative trends and comparison of dopant-dependent SAC properties will hold and DFT modeling of finite-size SACs permits the use of accurate (i.e., hybrid) DFT functionals that are cost-prohibitive when using periodic boundary conditions. To generate an expanded chemical space of SACs that are likely to be synthetically accessible by codoping the first and second coordination spheres, we define the local coordination environment of a SAC using three criteria: 1) the metal center; 2) the first coordination sphere atom identities (i.e., up to two dopant atom identities); 3) the second coordination sphere, which can contain dopants that are located in the smallest possible ring that contains all four metal-coordinating atoms (Figure 3.1).

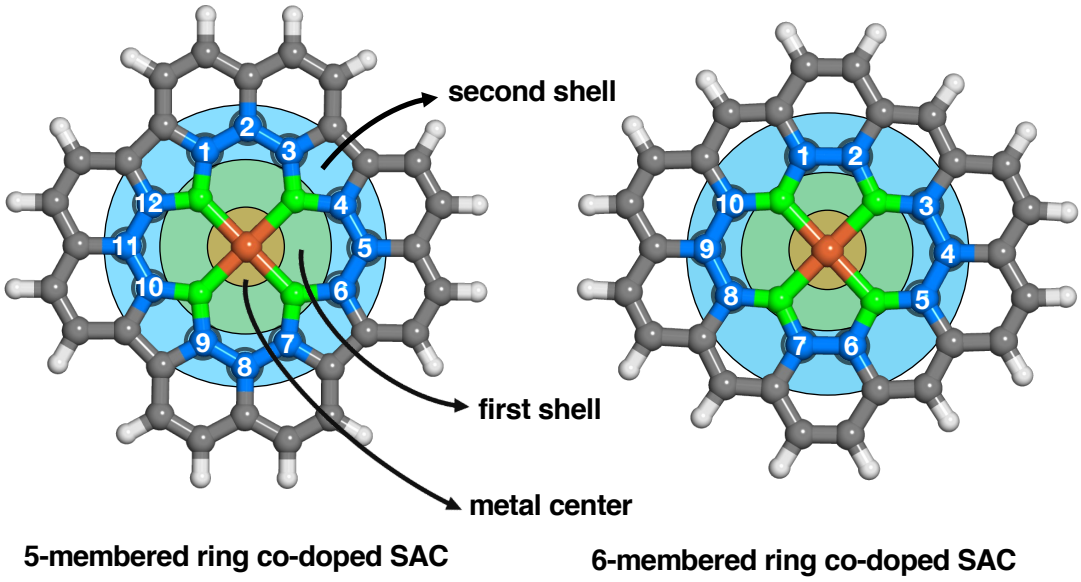

Figure 3.1. Schematic of the first and second coodination shells in the equatorial plane of 5- and 6-membered ring SACs. Regions of the SACs used to classify the local coordination environment are designated as metal center in orange, first coordination sphere in green and second coordination sphere in light blue. Numbers are used as labels for the position of dopants in the second coordination sphere. There are twelve and ten possible dopant positions in the second coordination sphere for 5- and 6-membered ring SACs, respectively. The structures are shown in the ball-and-stick representation and colored as follows: metal (Mn, Fe, Co, and Ru) in orange, C in gray, and H in white.

We investigate two distinct codoped SACs configurations: codoping only in the first coordination sphere or also codoping the second coordination sphere (e.g., atoms directly connected to the first coordination sphere). For any given dopant configuration, we used up to two distinct atoms. First, we codoped the first coordination sphere without doping any atoms in the second coordination sphere. This results in four distinct positional dopant configurations for each of the 6 atom combinations (e.g., NO, NP, NS, OS, OP, PS) for each 5- and 6-membered ring SAC, resulting in 48 total arrangements (Appendix Figures A3.1 and A3.2). The naming scheme for codoping in the first coordination sphere is ring size (e.g., 6-membered), metal and oxidation state (e.g., Fe(II)), and the identity and number of the dopants in the first coordination sphere (e.g.,

N_2O_2) along with any designation of symmetry (e.g., cis or trans) for the dopants where relevant (e.g., 6-membered Fe(II)(trans N_2O_2)). In the 6-membered ring SAC, the four dopants in the first coordination sphere of 6-membered rings is not symmetric (e.g., NOON and NNOO are inequivalent), but these modestly inequivalent variations were ignored due to their limited effect on energetics (Appendix Table A3.1). For the second approach, we fixed the first coordination sphere to contain four N atoms, and codoped the second coordination sphere with two atoms that have the same identity (i.e., 2 N atoms, 2 O atoms, 2 P atoms, or 2 S atoms), following the doping reported in the experimental literature that tends to favor up to two unique elements and typically around two additional codopants in the second coordination sphere[54, 170]. The naming scheme for codoping in both the first and second coordination spheres is ring size (e.g., 6-membered), metal and oxidation state (e.g., Fe(II)), positions for dopant in the second coordination sphere (e.g., 6 and 13 to make 6-13, see Figure 3.1), and the identity and number of the dopants in first (e.g., N_4) and second coordination sphere (e.g., S_2) for a configuration such as 6-membered Ru(III)(6-13 N_4-S_2). We initially imposed an additional restriction that for atoms to be considered in the second sphere they had to be nearest neighbors to the first-coordination sphere dopants. We then expanded this definition, as motivated by experimental studies[60], to also include three types of bridging configurations (i.e., 5-membered Fe(II)(2-5 N_4-X_2), 5-membered Fe(II)(2-8 N_4-X_2), and 6-membered Fe(II)(4-9 N_4-X_2), where X is any co-dopant, see Appendix Figures A3.3 and A3.4). We repeated this for the 5- and 6-membered ring SAC models, resulting in 9 (11) distinct geometries for codoped 5-membered (6-membered) ring SAC models for a total of 80 arrangements (Appendix Figures A3.3 and A3.4).

In total, the 128 distinct codoped configurations combined with four metals in two oxidation states produces 2,048 transition-metal SACs in up to two spin states. After data filtering,

our final codoped SAC dataset consists of over 700 catalysts (see Computational Details). From this dataset, we identify strategies to engineer dopant configuration types and metal identities to tune catalyst energetics and discover optimal catalysts that can simultaneously activate methane and release methanol.

3.3. Reaction Mechanism

We calculate the reaction energetics of methane-to-methanol conversion by codoped SACs with four metals (M = Mn, Fe, Co, and Ru) in two oxidation states (i.e., M(II)/M(III)) in their corresponding spin states (Appendix Table A3.2). As in prior work[8, 29, 48], we compute energetics for the radical rebound mechanism[153] for methane-to-methanol conversion starting from the resting state structure (**1**). In this mechanism, we form a high-valent terminal M(IV/V)=oxo (**2**) via two-electron metal oxidation by nitrous oxide[154, 155], a common oxidant (Figure 3.2). The oxo formation energy, ΔE(oxo), is computed as

$$\Delta E(\text{oxo}) = E(\mathbf{2}) - E(\mathbf{1}) + E(N_2) - E(N_2O) \qquad (1)$$

Upon oxo formation, the metal formal oxidation state changes from M(II/III) to M(IV/V). Since we compute reaction energetics, an alternative oxidant choice would rigidly shift absolute reaction energetics but not influence relative catalyst energetics.

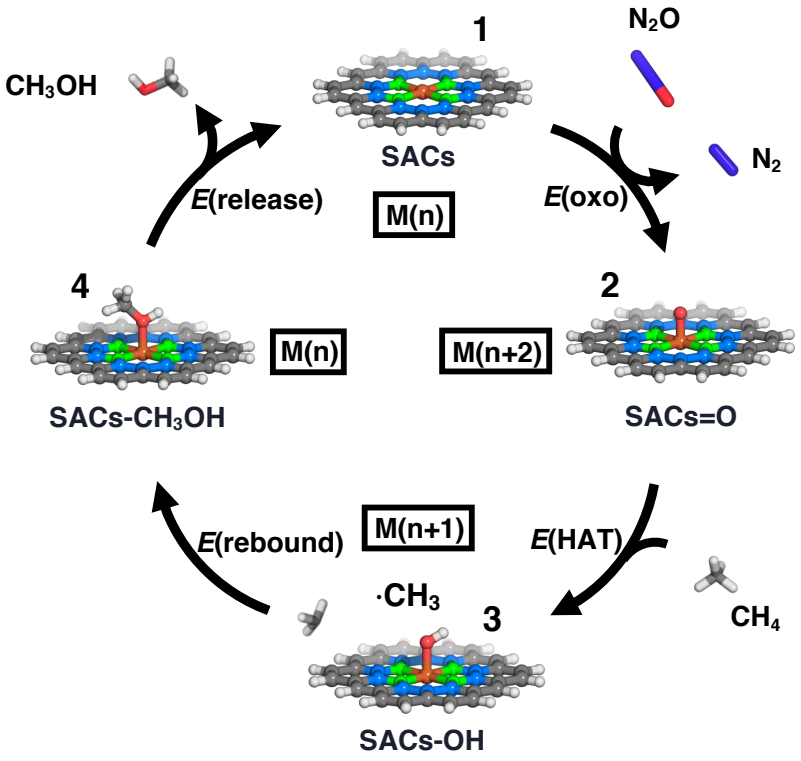

Figure 3.2. Catalytic cycle for the partial oxidation of methane to methanol. The catalytic cycle proceeds clockwise: from the resting state (**1**, top) in oxidation state n = II/III, metal−oxo (**2**, right) formation with an N_2O oxidant, followed by HAT to form a metal−hydroxyl complex (**3**, bottom), and rebound to form a methanol-bound intermediate (**4**, left). The structures are shown in the ball-and-stick representation colored as follows: metal center in orange, oxygen in red, nitrogen in dark blue, first coordination sphere dopant sites in green, second coordination sphere dopant sites in light blue, C in gray, and H in white.

After oxo formation, the high-valent M(IV/V)=O intermediate catalyzes hydrogen atom transfer (HAT) by abstracting a hydrogen atom from methane to form an M(III/IV)−OH intermediate (**3**) and a methyl radical (Figure 3.2). The reaction energy for the HAT step, ΔE(HAT), is calculated as:

$$\Delta E(HAT) = E(\mathbf{3}) - E(\mathbf{2}) + E(CH_3\bullet) - E(CH_4) \qquad (2)$$

Following the HAT step, the recombination of the methyl radical with the M(III/IV)−OH intermediate in the radical rebound step forms a metal-bound methanol intermediate (**4**). We calculate the ΔE(rebound) energy as:

$$\Delta E(\text{rebound}) = E(\mathbf{4}) - E(\mathbf{3}) - E(CH_3\bullet) \qquad (3)$$

To complete the catalytic cycle, CH_3OH is released from the catalyst to return it to the resting state (**1**). ΔE(release), is calculated as:

$$\Delta E(\text{release}) = E(\mathbf{1}) + E(CH_3OH) - E(\mathbf{4}) \qquad (4)$$

All intermediates were investigated in low-spin (LS) states and intermediate-spin (IS) states for both the M(II/III) resting states and the M(IV/V)=O intermediates (see Computational Details).

3.4. Computational Details

We performed all gas-phase geometry optimizations using density functional theory (DFT) with a development version of the GPU-accelerated electronic structure code TeraChem v1.9.[142] We chose the range-separated hybrid functional ωPBEh[171] (default ω = 0.2 bohr^{-1}) to avoid the unphysical HOMO–LUMO gap closing that occurs in larger systems with global hybrid functionals.[146, 147] The LACVP* composite basis set was employed throughout our work, which consists of a LANL2DZ effective core potential[144, 145] for metals and the 6-31G* basis for all other atoms. We confirmed that reaction energetics are not strongly sensitive to our omission of semi-empirical dispersion, choice of functional (i.e., B3LYP global hybrid versus range-separated hybrid ωPBEh), and basis set size (i.e., def2-TZVP vs LACVP*, Appendix Figure A3.5). We carried out closed-shell singlet calculations in a spin-restricted formalism and all other calculations in a spin-unrestricted formalism that employed level shifting[148] of 0.25 Ha for both majority- and minority-spin virtual orbitals to enable the convergence of the self-consistent field (SCF). We used the default SCF convergence threshold of 3x10^{-5} hartree for the direct inversion of the iterative subspace (DIIS) error. We carried out geometry optimizations in the translation-rotation-internal coordinate (TRIC)[172] optimizer, with default tolerances for the maximum gradient of 4.5×10^{-4} hartree/bohr and the energy difference between steps of 1×10^{-6} hartree.

We simulated SAC systems with four transition metals (i.e., Mn, Fe, Co, and Ru) in two resting state oxidation states (i.e., II and III). Therefore, the total charge of the overall systems could vary, depending on the metal oxidation state and coordination environment. Following the same approach as our previous work[29], we simulated N and P coordinating atoms with a net -1 (0) charge for 5-membered (6-membered) ring SAC models. In contrast to the charge of N and P coordinating atoms, we simulated both O and S coordinating atoms with 0 charge in models for both 5-membered and 6-membered ring SACs. When there are an odd number of O or S coordinating atoms in 6-membered rings, we treated the flake model with +1 charge to satisfy the octet rule (Appendix Table A3.3). When we have a second coordinating shell dopant (i.e., N, O, P and S), all substitutions are made without altering net charge. All the catalytic intermediates were examined in both low-spin (LS) and intermediate-spin (IS) configurations, with the spin states being determined based on those that are applicable to both the resting state M(II/III) and the oxidized M(IV/V)=O intermediate. Specifically, this corresponds to LS singlet/IS triplet for $3d^2$ Mn(V)=O, LS doublet/IS quartet for $3d^3$ Mn(IV)=O/ Fe(V)=O or $3d^5$ Co(IV)=O or $4d^3$ Ru(V)=O, and LS singlet/IS triplet for $3d^4$ Fe(IV)=O/Co(V)=O or $4d^4$ Ru(IV)=O (Appendix Table A3.2).

For the oxo intermediate in methane-to-methanol catalysis generated at SAC active sites, initial geometries were constructed using molSimplify[140], which uses OpenBabel[173] as a backend. We first optimized the LS state oxo intermediate with the metal-oxo bond distance set to 1.65 Å. After optimizing the metal-oxo intermediate, we geometry optimized the corresponding resting state SACs by removing the oxygen atom. Following the procedure developed in our previous work[48], we also generated the metal-hydroxo intermediate using the metal-oxo intermediate as a starting point by adding an H atom to the optimized metal-oxo intermediate (Appendix Figure A3.6). The methanol-bound intermediates were generated in a similar fashion by adding a methyl

group to the optimized metal-hydroxo intermediates using an in-house Python script (Appendix Figure A3.6).[29] All IS SAC intermediates were optimized from the corresponding pre-optimized LS structures (Appendix Table A3.2).

All job submissions were automated by the job manager in molSimplify with a 72-hour wall time per run cutoff and a maximum of five resubmissions for each job.[174] If one intermediate optimization was not successful, the following downstream intermediate optimizations were not carried out. Converged structures were removed from the data set following established protocols[29, 48] if: 1) the expectation value of the S^2 operator, $\langle S^2 \rangle$, deviated from its expected value of $S(S+1)$ by > 1; 2) the Mulliken spin density on the metal and oxygen differed from the spin multiplicity by > 1 μ_B; or 3) the oxo moiety inserted into metal-coordinating bonds or deviated from the initial structure by a root-mean-square deviation (RMSD) > 0.6 Å. After all of these checks, the total number of converged and successful codoped SACs was 720 (Appendix Table A3.4).

We used ORCA v5.0.1[175] to calculate the transition states (TSes) and barrier heights of our best-performing codoped SACs because TeraChem does not support analytical Hessians. The TSes and barrier heights for the oxo formation and HAT step were modeled with the climbing image nudged elastic band (CI-NEB) method and bond length scan, respectively, followed by partitioned rational-function optimization (P-RFO) to locate transition state structures starting from a computed Hessian. For the bond length scan of the HAT step, the distance between the hydroxyl hydrogen and the methyl radical carbon was scanned from 2.0 to 1.0 Å in 0.1 Å decrements while fixing the distance between the metal-oxo oxygen and the methyl radical carbon atom and letting all other atoms relax. Then, the maxima obtained from NEB calculations and the bond length scan

served as initial guesses for P-RFO calculations to locate the TS structures. TS identities were confirmed through frequency calculations (i.e., by the presence of a single imaginary frequency).

3.5. Results and Discussion

3.5A. Global trends in spin state ordering and reaction energetics

Identification of the ground spin state of catalytic intermediates in the radical rebound methane-to-methanol catalytic cycle provides insight into reactivity trends and determines whether the process is spin-allowed or spin-forbidden. We first evaluate the broad trends of spin splitting energies, $\Delta E_{I\text{-}L}$ = E(IS)-E(LS), for the resting state, metal−oxo, metal−hydroxo, and methanol-bound intermediates of codoped Mn, Fe, Co and Ru SACs (Figure 3.3). The ground state of codoped SACs varies significantly depending on the nature of the (co)dopants but is most sensitive to the metal and oxidation state. The resting state SAC structures for some metal/oxidation state combinations, Mn(II/III), Fe(II), Co(III) and Ru(II), have an IS ground state, whereas Fe(III), Co(II) and Ru(III) SACs have ground spin states that depend on the codopant configuration. For Fe(II) codoped SACs, all four reaction intermediates mostly have IS ground states (Figure 3.3). For the codoped SACs with most other metals, e.g., Mn(II/III), Fe(III), and Co(III), we find that most catalytic intermediates also have IS ground states although there are numerous exceptions (Appendix Figures A3.7– A3.10). However, there is no consistent typical ground spin state for all intermediates in SACs with Co(II) and Ru(II/III) metal centers (Appendix Figures A3.11– A3.13). For Mn(IV)=O, Ru(III)-OH, Ru(IV)-OH, Ru(III)-methanol SACs intermediates, the LS is predominantly the ground state (Appendix Figures A3.7, A3.12, and A3.13). Thus, codoped SAC structures are likely to exist in both IS and LS states, potentially requiring spin-crossover for the most favorable catalyst energetics in Ru or Co(II), but IS states are the most likely ground states across the entire catalytic cycle for Mn(III) and Fe(II) codoped SACs.

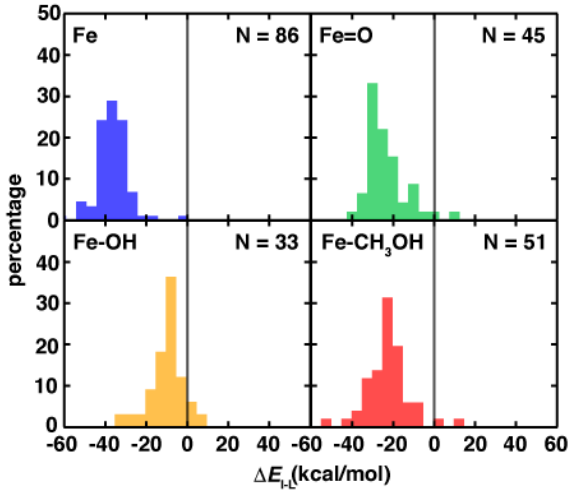

Figure 3.3. Histograms (bin width: 20 kcal/mol) of spin-splitting energies (ΔE_{I-L} = E(IS)-E(LS)) for the resting state in blue (Fe, top left), metal−oxo in green (Fe=O, top right), metal−hydroxyl complex in orange (Fe-OH, bottom left), and methanol-bound intermediate in red (Fe-CH_3OH, bottom right) of Fe(II) codoped SACs. The total number of species used to compute each histogram is indicated in the top right corner of each panel. Zero axes are shown on all plots as solid black lines, with compounds on the left of the line favoring IS states and those on the right of the line favoring LS states.

We next investigated the trends in ΔE(oxo) and ΔE(HAT) reaction energetics across the codoped SACs data set in both LS and IS states. Over the codoped SACs set, we obtain a wide range of ΔE(oxo) (ca. 140 kcal/mol) reaction energies (Figure 3.4 and Appendix Figure A3.14). We observe distinct reaction energetics depending on the metal identity, oxidation state, and spin state, with LS Mn(II), IS Mn(II) and LS Fe(II) SACs most favorably forming metal-oxo species. Conversely, LS Co(II) SACs exclusively disfavor forming oxo intermediates, which is in agreement with generalization of the oxo wall theory to these square pyramidal coordination geometries[176]. However, there is no conclusive trend in ΔE(oxo) favorability for IS Fe(II) and IS Co(II) SACs. Over the same data set, ΔE(HAT) spans a narrower range (ca. 100 kcal/mol) than ΔE(oxo) and shows reduced metal dependence. The most energetically favorable candidates for ΔE(HAT) are LS Fe(II) and IS Co(II) codoped SACs, while the ΔE(HAT) reaction energetics are not typically favorable (i.e., $\Delta E > 0$) for other metal and spin states (Figure 3.4). We thus find LS

Fe(II) codoped SACs are ideal candidates for direct methane-to-methanol conversion because LS Fe(II) codoped SACs have more favorable ΔE(HAT) (i.e., around 25 kcal/mol) while the ΔE(oxo) reaction energy is similar to IS Fe(II) codoped SACs. Nevertheless, although LS Fe(II) codoped SACs have favorable reaction energies, they are less likely to be the ground spin state for many intermediates during the reaction cycle. This observation underscores the challenges in discovering an optimal SAC for methane-to-methanol conversion.

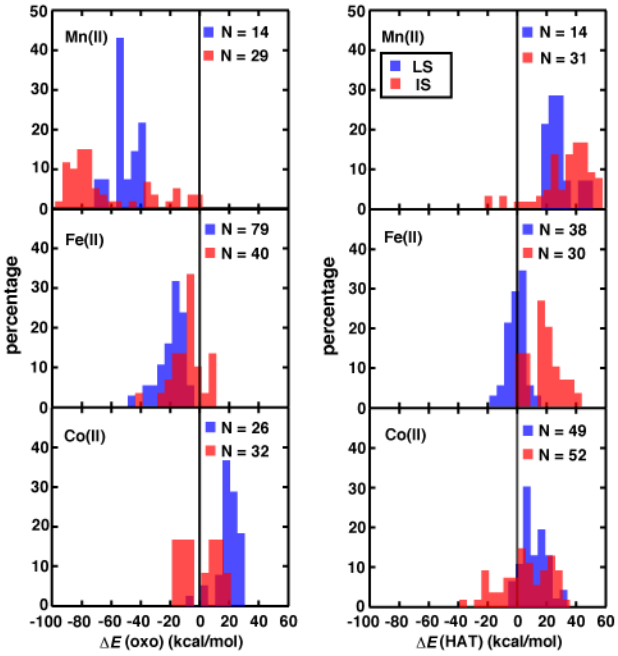

Figure 3.4. Percentage histograms (bin width: 20 kcal/mol) of ΔE(oxo) (left) and ΔE(HAT) (right) of codoped SACs grouped by metal (from top to bottom, Mn(II), Fe(II), and Co(II), colored by spin state (i.e., LS in blue and IS in red). The ΔE(HAT) values are for ferromagnetically coupled hydrogen atom transfer. The total number of intermediates used to compute each histogram is indicated in the top right corner of each panel. The percentage is normalized separately for each spin state. Zero axes are shown on all plots as solid black lines.

Next, we evaluated the oxidation state (i.e., Fe(II) vs Fe(III)) influence on ΔE(oxo) and ΔE(HAT) reaction energetics for the codoped SACs (Appendix Figures A3.14 and A3.15). Here, we focus on investigating Fe-based SACs due to their favorable reaction energetics. Both the

ΔE(oxo) and ΔE(HAT) of LS Fe(III) codoped SACs are less favorable than those of LS Fe(II), whereas the ΔE(oxo) and ΔE(HAT) energetics of IS Fe(II) and IS Fe(III) codoped SACs are similar. This observation is consistent with our prior study[48] suggesting the benefit of having a stronger Fe(III) oxidant is outweighed by more favorable ΔE(oxo) for Fe(II) without much penalty on ΔE(HAT) energetics relative to Fe(III). Our study here expands on that earlier observation to suggest that the benefit for HAT is indeed minimal for Fe(III) SACs.

Continuing through the reaction cycle to rebound, we observe that over the codoped SACs data set, ΔE(rebound) is predominantly favorable. The energetics nevertheless span a wide range from weakly (ca. 0 kcal/mol) to strongly (ca. −140 kcal/mol) exothermic (Appendix Figure A3.16). We observe near-zero rebound energetics for cases where N atoms codoped in the first and second coordination spheres, while several specific cases of SACs formed by M(III) metals with codopants in the first and second coordination spheres are strongly exothermic (i.e., −140 kcal/mol, Appendix Table A3.5). In general, the ΔE(rebound) values of codoped SACs show less metal dependence than ΔE(oxo) and ΔE(HAT). The ΔE(rebound) energetics of Mn, Fe and Ru codoped SACs show strong spin state dependency, with LS codoped SACs of these metals more near-zero energetics than that of their IS counterparts. Conversely, no strong spin state dependency is observed for Co codoped SACs. In terms of oxidation state dependence, we only observe significant dependence for Ru codoped SACS, which we attribute to the highly diverse coordination environment and geometries in this study that make it difficult to isolate any specific effect of oxidation state (Appendix Figure A3.16).

In addition to oxo formation, HAT and rebound, the energetics of the release step could be unfavorable, leading to lack of conversion of methane to methanol by not allowing turnover or through overoxidation. Thus, we also compared broad trends in release energetics. We observe

that all ΔE(release) energetics are unfavorable for the codoped SACs, with a wide range from weakly (ca. 2-3 kcal/mol) to strongly (ca. 90 kcal/mol) unfavorable values (Appendix Figure A3.17 and Table S6). The ΔE(release) energetics of codoped SACs vary significantly depending on the nature of dopants near the metal but are most sensitive to the metal identities. We observed the strongest penalty for releasing methanol for cases with only codopants in the first coordination sphere, whereas the interaction is weakened when SACs are also codoped in their second coordination sphere (i.e., 4 N in the first coordination sphere and 2 other dopants in the second coordination sphere, Appendix Table A3.6). The ΔE(release) values of Mn and Fe codoped SACs span a wide range (~ 10–90 kcal/mol), with strong oxidation and spin state dependence. In particular, we find ΔE(release) is more unfavorable for the higher oxidation state LS/IS Fe(III) and LS Mn(III) SACs, consistent with our previous observation on molecular catalysts[48], but the same trend is not observed for IS Mn(III) SACs (Appendix Figure A3.17). On the other hand, the distributions of ΔE(release) energetics of Co and Ru codoped SACs are much narrower, ranging from 10 to 40 kcal/mol. Perhaps due to this reduced variation, we also do not observe any oxidation- and spin-state-dependent trends for Co and Ru codoped SACs (Appendix Figure A3.17). In terms of optimizing SACs for release, Ru codoped SACs with more thermoneutral ΔE(release) values show promise as candidate catalysts for methane-to-methanol. Overall, both Fe and Ru SACs appear to offer the best trade-offs for all reaction steps, whereas Co or Mn catalysts destabilize oxo or HAT intermediates, respectively.

3.5B. Period trends in codoped transition metal SACs

Although less earth abundant than *3d* transition metals, *4d* transition metals often form catalysts with superior catalytic performance (e.g., Ru for water oxidation[177, 178] or

hydrogenation[179]) compared to *3d* transition metal catalysts. A compounding consideration is that according to hard-soft acid-base (HSAB) theory[180, 181], 4*d* metals should prefer to be coordinated by softer 3*p* ligands whereas 3*d* metals prefer 2*p* ligands. Thus, we need to investigate both metal and ligand period effects simultaneously to understand changes in catalytic activity.

To investigate the impact of *3d* vs. *4d* period trends (i.e., Fe(II) vs Ru(II)) on reaction energetics in codoped transition metal SACs, we focused on the ΔE(oxo) and ΔE(HAT) reaction step energetics of both LS and IS Fe(II) and Ru(II) codoped SACs. The ΔE(oxo) and ΔE(HAT) reaction energetics of LS Fe(II) are both better than IS Fe(II) SACs; ΔE(HAT) energetics are more favorable for LS Ru(II) SACs than IS Ru(II) counterparts while ΔE(oxo) values are comparable (Appendix Figure A3.18). Comparing the LS Fe(II) and Ru(II) codoped SACs, we observe that ΔE(oxo) is less favorable (by ca. 10 kcal/mol) for LS Fe than for LS Ru. Conversely, ΔE(HAT) is more favorable for LS Fe (by ca. 15 kcal/mol). For IS SACs counterparts, this trend is even stronger, with ΔE(oxo) significantly less favorable in Fe codoped SACs than in Ru codoped SACs (by ca. 20 kcal/mol) while ΔE(HAT) is more favorable for Fe than in Ru codoped SACs (by ca. 20 kcal/mol). These energetic trends suggest that the combination of the confined active site with the more diffuse orbitals of the Ru center leads to more favorable formation of the oxidized metal-oxo, at the cost of worsened HAT performance. Nevertheless, individual catalysts can deviate significantly from this average trend, motivating our comparison of both Ru and Fe SAC catalytic cycles (see Sec. 5d).

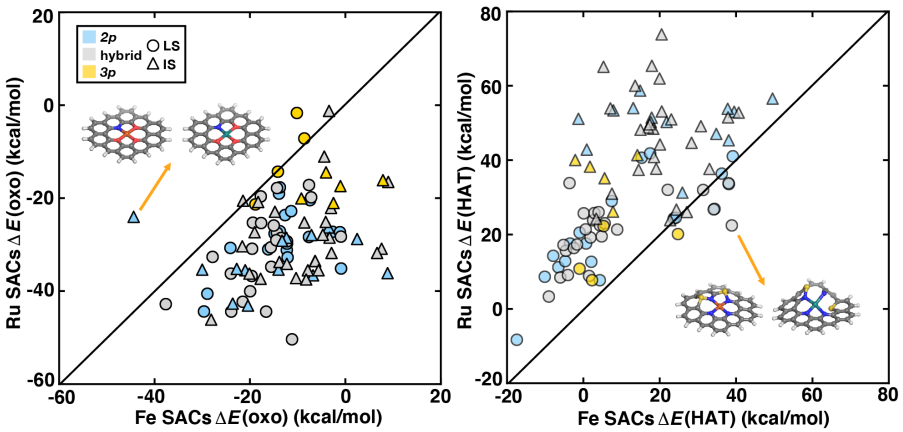

Figure 3.5. Parity plots of ΔE(oxo) (left) and ΔE(HAT) (right) reaction energies (in kcal/mol) between codoped Fe SACs and Ru SACs under the same flake and oxidation state conditions. Data are colored by coordination environment (*2p* in blue, a combination of *2p* and *3p* in gray and *3p* in yellow) and distinguished by spin state (LS in circles and IS in triangles) as indicated in the legend. Two outliers of codoped SACs are shown in the parity plot: IS 6-membered Ru(II)(N_1O_3) SACs vs IS 6-membered Fe(II)(N_1O_3) SACs (left) and LS 6-membered Ru(III)(**6-8** N_4-S_2) SACs vs LS 6-membered Fe(III)(**6-8** N_4-S_2) SACs (right). Atoms are colored as follows: brown for Fe, dark teal for Ru, blue for N, red for O, yellow for S, gray for C, and white for H.

In order to understand the period dependence and coordination environment effects (*2p*, a combination of *2p* and *3p*, and *3p*) on reaction energetics, we evaluate variations with dopant atoms for ΔE(oxo) and ΔE(HAT) of Fe and Ru codoped SACs with the same coordination environment (Figure 3.5). Overall, the *3p* (i.e., P or S) dopants in codoped SACs make ΔE(HAT) more favorable but ΔE(oxo) less favorable relative to *2p* elements (i.e., N or O) in codoped SACs (Appendix Figure A3.19). This trend holds for Ru or Fe but is subtler than the earlier observation that ΔE(oxo) energetics on Fe codoped SACs are less favorable than Ru codoped SACs while ΔE(HAT) energetics on Ru codoped SACs are less favorable than Fe SACs (Appendix Figure A3.19). For the outliers to these general observations, e.g., LS 6-membered Ru(III)(6-8 N_4-S_2) SACs versus LS 6-membered Fe(III)(6-8 N_4-S_2) SACs, we identify that the inclusion of S dopants in the second coordination sphere induces distinct graphene flake distortion for Fe vs. Ru (Figure 3.5). This distortion occurs in opposing directions between the LS 6-membered Ru(III)(6-8 N_4-S_2) SACs and the LS 6-membered Fe(III)(6-8 N_4-S_2) SACs. The trend in increasing HAT favorability for 3*p*

dopants is similar to those that have been previously observed for Fe(II) complexes for methane-to-methanol conversion[182]. Nevertheless, in other cases, the origin appears more electronic in nature, such as a 6-membered Fe(II)(N_1O_3) SAC where oxo formation is more favorable for Fe(II) than Ru(II), despite a weaker ligand field (Figure 3.5). Overall, both electronic and structural differences in 2p and 3p dopants play a role in relative energetics of SAC catalysts, but the metal dependence (i.e., 3*d* vs 4*d*) is stronger than the dependence on coordination environment (i.e., 2*p* vs 3*p*).

3.5C. Reaction energetics tradeoffs of codoped transition metal SACs

Often in HTVS for heterogeneous catalysts, linear free energy relationships (LFERs) are leveraged to correlate energetics of individual intermediates to the holistic catalytic activity[71, 73]. The ΔE(oxo) and ΔE(HAT) reaction energies typically have a strong negative correlation (i.e., a negative slope LFER) for heterogeneous catalysts, while the LFER is known to be weak in homogeneous catalysts[48]. In light of the extensive utilization of LFERs to simplify a complex catalytic cycle into a single representative descriptor, we aimed to determine whether a diverse chemical space of codoped transition metal SACs follow established LFERs[71, 183] for the radical rebound mechanism of direct methane-to-methanol conversion by comparing trends in the four metals (i.e., Mn, Fe, Co, and Ru, see Computational Details). Over our codoped SACs dataset, we observe a relatively weak global negative correlation between ΔE(oxo) and ΔE(HAT) (Figure 3.6, Appendix Figure A3.20). This lack of global correlation motivates determination of metal- and spin-state-dependent LFERs.

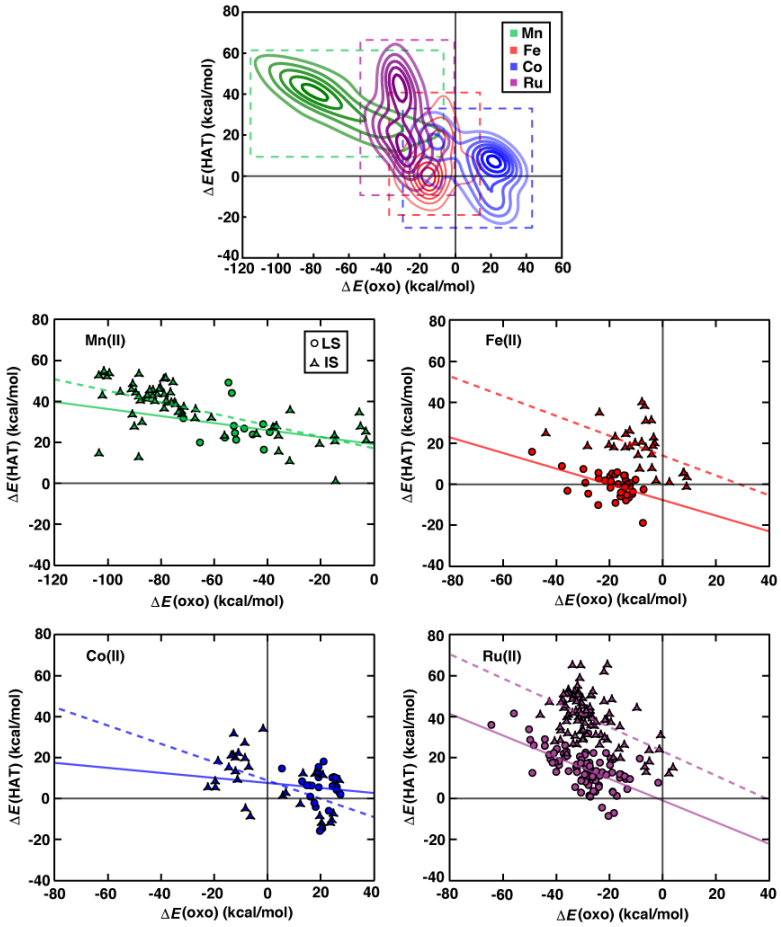

Figure 3.6. ΔE(oxo) vs. ΔE(HAT) reaction energies (in kcal/mol) of codoped M(II) SACs shown as metal-dependent Gaussian kernel density estimates (KDEs, top) and explicit data points for the Mn(II) (middle left), Fe(II) (middle, right), Co(II) (bottom, left), and Ru(II) (bottom, right) panes. The KDEs and explicit data points are colored by metal identities (Mn in green, Fe in red, Co in blue, and Ru in purple). The KDEs of the distributions for the codoped SACs are shown as contour lines with decreasing saturation in 10 evenly spaced levels. Dashed colored outlines in the KDEs correspond to the ranges of ΔE(oxo) and ΔE(HAT) of Mn, Fe, Co and Ru codoped SACs. Explicit data points are distinguished by spin state (LS in circles and IS in triangles) as indicated in the legend. The solid lines are linear fits for the LS codoped SACs and dashed lines are equivalent fits for IS systems. Zero axes are shown on all plots as solid black lines.

Indeed, we observe the degree of correlation between the ΔE(oxo) and ΔE(HAT) reaction energetics to vary by metal and spin state. In particular, IS Mn(II) codoped SACs exhibit the strongest correlation between the two reaction energies among all codoped SACs (Pearson's r = -0.67, Figure 3.6 and Appendix Table A3.7). Notably, this correlation is accompanied by a shallow

slope of -0.28, indicating that the formation of stable Mn-oxo SACs does not correspond to a significant reduction in favorability for HAT. Nevertheless, all IS Mn(II) codoped SACs have unfavorable ΔE(HAT) reaction energetics, with relatively high values in the range of 20–40 kcal/mol (Figure 3.6). In contrast, the LS Co(II) codoped SACs show among the weakest correlation between ΔE(oxo) and ΔE(HAT) reaction energetics (Pearson's r = -0.08) and relatively little trade-off between the two steps (slope of -0.12, Figure 3.6 and Appendix Table A3.7). The observations on codoped SACs of weakened LFERs is consistent with our previous observations for transition metal complexes[48], including metal- and spin-specific trends such as the weak correlation for LS Co. We attribute the weak correlation between ΔE(oxo) and ΔE(HAT) in codoped SACs to the high variation of the coordination environment (i.e., both material composition and geometric configurations).

Beyond metal identity, SACs with different spin states show significantly different behavior in terms of the slope and intercept for a linear fit (Appendix Table A3.7). Among all metal and oxidation state combinations, those with a low-spin d^6 electron configuration, i.e., LS Fe(II) and LS Co(III), most likely form codoped SACs with both favorable (i.e., $\Delta E < 0$) oxo and HAT energetics thanks to a modest trade-off in the two reaction energies (Figure 3.6 and Appendix Figure A3.20). Therefore, codoped SACs have flexible tunability that allows for disrupting LFERs as in homogeneous catalysts.

3.5D. Catalytic cycles of codoped SACs with the best energetic trade-offs

Despite weak LFERs, all SAC catalyst candidates have at least some trade-off in reaction energetics between multiple steps in the radical-rebound mechanism. Here, we first consider the trade-off of reaction energetics between ΔE(HAT) and ΔE(oxo), which are the potential rate-limiting steps in the catalytic cycle for methane-to-methanol conversion[153]. The best catalysts

should have an optimal trade-off between ΔE(oxo) and ΔE(HAT) reaction energetics (i.e., not favoring one too strongly at the cost of disfavoring the other). We thus define a Pareto front consisting of the catalysts with the best trade-off between ΔE(oxo) and ΔE(HAT) reaction energies. Based on the Pareto frontier, we identify six total catalyst candidate SACs: four lying on the Pareto frontier of ΔE(oxo) and ΔE(HAT) (**A**: LS 5-membered Mn(III)(O_3P_1), **B**: LS 5-membered Fe(II)(**6-11** N_4-S_2), **C**: IS 6-membered Fe(II)(cis N_2O_2) and **E**: LS 6-membered Fe(II)(**14-15** N_4-P_2)) and the two next closest catalysts to the Pareto frontier (**D**: LS 5-membered Ru(II)(**14-16** N_4-N_2) and **F**: LS 6-membered Co(II)-(cis O_2P_2)), for direct methane-to-methanol conversion. Surprisingly, despite average trends indicating favorable formation of metal-oxos by Ru catalysts, the best Ru-based codoped SAC (i.e., **D**) does not reach the Pareto frontier spanned by the *3d* transition metal SACs, reinforcing the greater potential of light, earth-abundant transition metal SACs for direct methane-to-methanol conversion (Figure 3.7). We find Fe(II)-based codoped SACs are most likely to be favorable (i.e., both ΔE(oxo) and ΔE(HAT) < 0) compared to SACs with other metal centers. In comparison to **A** or **F**, which have extremely favorable reaction energetics for either ΔE(oxo) or ΔE(HAT) and unfavorable reaction energetics on the other, the Fe(II)-based codoped SACs along the Pareto front display more moderate tradeoffs. If Brønsted−Evans−Polanyi (BEP) relations[74, 184] hold, one would ideally minimize (ΔE(oxo) + ΔE(HAT)) to achieve the optimal balance between ΔE(oxo) and ΔE(HAT) reaction energetics (Appendix Table A3.8). Based on this criterion, we can conclude that **A** and **C** provide an optimal trade-off between ΔE(oxo) and ΔE(HAT) (Appendix Table A3.8). Importantly, **C** is spin-allowed in catalytic cycle of methane-to-methanol reaction (i.e., the resting state and all intermediates have the same ground-state spin) (Appendix Tables A3.9 and A3.10).

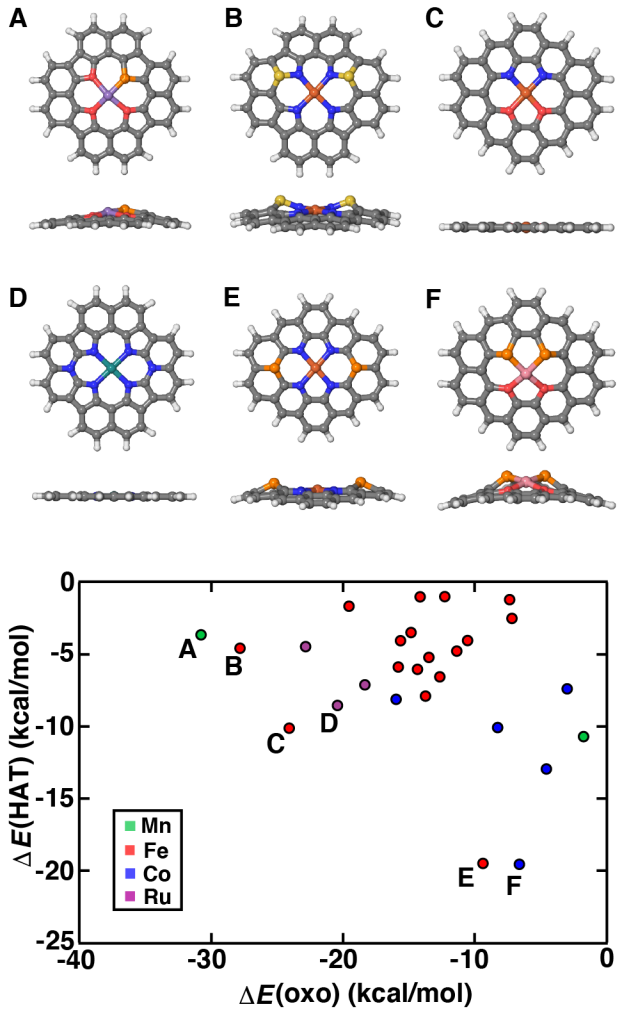

Figure 3.7. Examples of the best-trade-off catalysts (top) across codoped SACs dataset are indicated by letters A–F. The ΔE(oxo) vs. ΔE(HAT) reaction energies (in kcal/mol) of the best performing catalysts (bottom) are colored by metal identities (Mn in green, Fe in red, Co in blue, and Ru in purple). Only SACs with both energetically favorable ΔE(oxo) and ΔE(HAT) reaction energetics are shown. On top (from left to right) are the codoped SACs from **A**: LS 5-membered Mn(III)(O_3P_1) SAC, **B**: LS 5-membered Fe(II)(**6-11** N_4-S_2) SAC, **C**: IS 6-membered Fe(II)(cis N_2O_2) SAC, **D**: LS 5-membered Ru(II)(**14-16** N_4-N_2) SAC, **E**: LS 6-membered Fe(II)(**14-15** N_4-P_2) SAC, and **F**: LS 6-membered Co(II)-(cis O_2P_2) SAC. Atoms are colored as follows: purple for Mn, brown for Fe, pink for Co, dark teal for Ru, blue for N, red for O, orange for P, yellow for S, gray for C, and white for H.

Next, we proceed to compare the catalytic performance of the Fe(II) SAC **C**, which has two N and two O atoms codoped in the first coordination sphere, with the pure N-doped SAC models. The N-doped SACs from our previous study[29] have four N atoms coordinating in the first

coordination sphere with 5- or 6-membered ring structures. These N-doped SACs have similar ΔE(oxo) energetics (i.e., ca. -10 kcal/mol) along with favorable ΔE(HAT) (i.e., -3.4 kcal/mol for 5-membered ring and -6.8 kcal/mol for 6-membered ring N-doped SACs). In comparison to the pure N-doped SACs in our previous study[29], we observe that introducing O dopants with N dopants in the first coordination sphere of SACs, as in the candidate **C**, leads to significant improvements in both ΔE(oxo) and ΔE(HAT) reaction energetics (i.e., by > 5 kcal/mol). This observation can be ascribed to the electronic environment created by multiple dopants, which cannot be accessed by a single dopant element. On the basis of this analysis, employing N/O codopants in the first coordination sphere may provide an approach to improve catalytic performance of these materials for methane-to-methanol conversion.

To validate our best-trade-off codoped SACs designs, we now characterize the full reaction coordinate, i.e., with both transition states (TS) and reaction intermediates, of the selected codoped SACs for the radical rebound mechanism of methane-to-methanol conversion. Here, we focus our analysis on the codoped SACs: **A**, **C**, **D** and **E** after omitting **B** and **F** because we were unable to fully converge the pathway for oxo formation on these SACs with CI-NEB. Of these four remaining catalysts, all have favorable reaction energetics, and **C** is in its ground spin state. As the ΔE(oxo) and ΔE(HAT) steps play crucial roles as potential rate-limiting steps in the catalytic cycle of methane-to-methanol conversion, we calculate kinetics properties associated with oxo formation and HAT with NEB and potential energy scans, respectively (see Computational Details). The radical rebound step has been shown to be nearly barrierless and not involved in the turnover-determining transition state (TDTS) in our previous work[8], and so we do not attempt to compute a barrier for it.

We observe comparatively low oxo formation barriers of 17.3 kcal/mol for **C** and 4.0 kcal/mol for **D**, indicating relatively facile formation of metal-oxo species for C–H bond activation in methane (Figure 3.8). In contrast, the oxo formation barriers of **A** and **E** are considerably higher (i.e., 31.3 kcal/mol and 26.7 kcal/mol, respectively), which is also noteworthy that both activation energies are relatively similarly high even though they were on the opposite ends of the Pareto front in terms of oxo formation energetic favorability (Figure 3.8). Among the four selected codoped SACs, the HAT barrier of ground state **C** exhibits the lowest HAT barrier energy at 14.7 kcal/mol, followed by **D** with a moderate barrier of 21.6 kcal/mol. Compared to the **C** and **D** systems, **E** has a higher HAT barrier energy of 39.0 kcal/mol indicating that it requires more energy for HAT and is unlikely to be a proficient catalyst for direct methane-to-methanol conversion. The **A** SAC has the highest HAT barrier energy at 44.5 kcal/mol, making it the most energetically demanding for the HAT process and unlikely to feasibly catalyze HAT, even when accounting for uncertainty due to error in the DFT functional (Appendix Table A3.11). Comparing these energetics, we observe at most a qualitative BEP relationship in the HAT step: the most favorable SAC in terms of reaction energetics, **C**, has the lowest kinetic barrier while the most unfavorable SAC, **A**, has the highest kinetic barrier. There are, however, exceptions for **D** and **E**, where the kinetic barriers are drastically different although their energetics are similar (Appendix Figure A3.21). This observation, which we ascribe to the diverse chemistry of the metal, oxidation state, spin state, and coordination environment combinations we included in this study, highlights the importance of explicit evaluation of kinetic barriers in identifying favorable SACs.

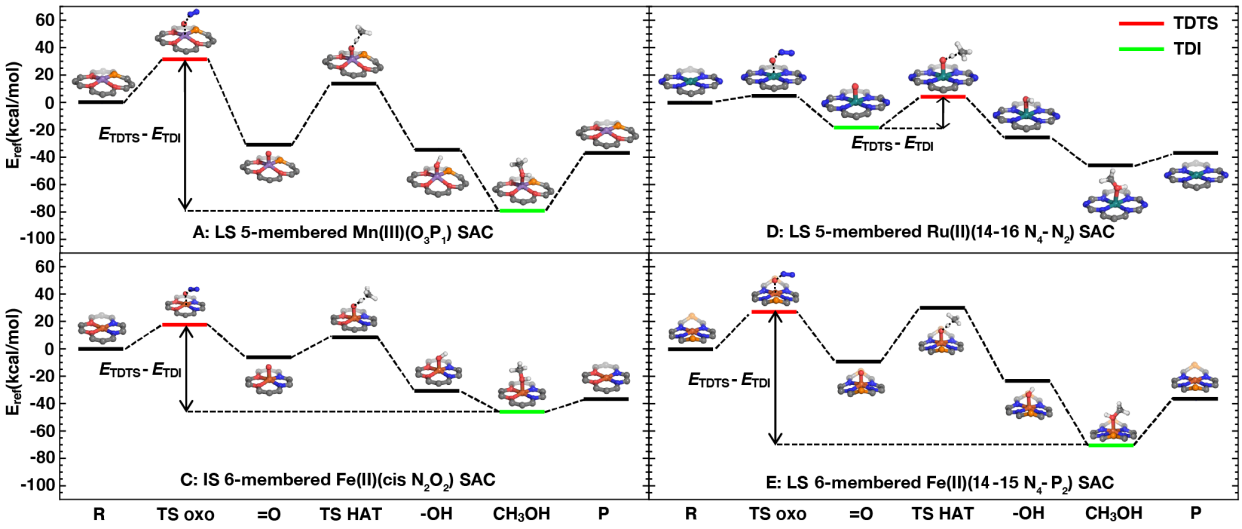

Figure 3.8. Full energy landscapes (E_{rel} in kcal/mol) of the four best-trade-off codoped SACs with **A**: LS 5-membered Mn(III)(O_3P_1) (top left), **C**: IS 6-membered Fe(II)(cis N_2O_2) (bottom left), **D**: LS 5-membered Ru(II)(**14-16** N_4-N_2) (top right), and **E**: LS 6-membered Fe(II)(**14-15** N_4-P_2) (bottom right). The reaction coordinates are labeled with intermediates: the reactants (R), the TS of oxo formation (TS oxo), the metal-oxo intermediate (=O), the TS of HAT (TS HAT), the metal hydroxyl intermediate (−OH), the methanol-bound intermediate (CH_3OH), and the product (P). The turnover-determining TS (TDTS) and turnover-determining intermediate (TDI) are shown inset along with the energy differences between the TDTS and TDI (E_{TDTS} - E_{TDI}) that governs efficiency of catalysis. The TDTS and TDI are labeled with red and green, respectively. Atoms are colored as follows: purple for Mn, brown for Fe, dark teal for Ru, blue for N, red for O, orange for P, gray for C, and white for H.

Next, we employed the energetic span model to estimate the catalytic turnover frequency (TOF) of the four selected codoped SACs. We observe that **A**, **C** and **E** share a common TDTS associated with the oxo formation step (Figure 3.8, Appendix Table A3.12). Additionally, the turnover-determining intermediate (TDI) for those three codoped SACs is the methanol-bound intermediate. However, as for **D**, the TDTS associated with the TS HAT and the TDI is the metal-oxo intermediate due to moderate methanol release energetics. The energetic span (δE) differs significantly among the four codoped SACs with a wide variation of 60 kcal/mol. This range extends from 21.6 kcal/mol in **D** (i.e., likely to catalyze C–H activation) to 73.3 kcal/mol in **A** (i.e., unlikely to catalyze C–H activation), resulting in a large 37 order of magnitude difference in the

computed catalyst TOFs (Appendix Table A3.12). Interestingly, **D** was one catalyst that was not on the Pareto front, only close to it, but our kinetic analysis highlights its superior performance, emphasizing the limited predictive capabilities of a reaction-energetics-only screen in SACs. Full kinetic screening of candidates might therefore reveal even better SAC candidates that are not on the reaction energetics Pareto front. Furthermore, our investigation reveals that the relative energetics and energy spans associated with methane oxidation for our selected codoped SACs, **C** and **D**, are comparable to the computed energy spans reported in macrocyclic molecular complexes[8] and metal−organic framework nodes[155, 185, 186]. Given the favorable reaction energetics, kinetics, and TOF of **C** and **D**, we conclude that **C** and **D** are the most promising codoped SACs for methane-to-methanol conversion and merit further experimental exploration.

3.6. Conclusions

Using a high-throughput virtual screening (HTVS) approach, we investigated 2,048 codoped transition metal (i.e., Mn, Fe, Co, and Ru) SACs in numerous spin and oxidation states for the challenging conversion of methane to methanol. Here, we focused on modulating the coordination environment by doping in both the first and second coordination spheres, to design efficient SACs and alter the catalytic properties for direct methane-to-methanol conversion. To determine the ground spin state of catalytic intermediates of SACs, we first explored the impact of the influence of metal/oxidation state in SACs. We found that SACs can have either IS or LS ground states in the catalytic cycle depending on the transition metal center. Next, we evaluated the relationship of the energetics of oxo formation and HAT steps in codoped transition metal SACs. Across our codoped SACs dataset, we observed a relatively weak negative correlation between $\Delta E(oxo)$ and $\Delta E(HAT)$. We attribute the weak correlation to the significant variation of the coordination environment among these SAC catalysts, especially the structural variation in the

first coordination sphere. The ΔE(release) energetics are endothermic for the codoped SACs, with a wide-spread range for Fe and Mn codoped SACs but are quite narrow for Co and Ru codoped SACs. We expect the flexible tunability demonstrated here, which allows disruption of LFERs as in molecular catalysts, should combine with the stability and scalability of SAC catalysts in general to benefit from the advantages of both homogeneous and heterogeneous catalysts. In order to understand the periodic trends and coordination environment effects on reaction energetics, we compared Fe and Ru reaction energetics and found Ru formed more stable metal-oxos, while Fe HAT energetics were more favorable. Conversely, ΔE(HAT) energetics in LS Ru codoped SACs are less favorable than those in all LS Fe SACs, and most IS Ru systems exhibit far less favorability than IS Fe systems.

Finally, we considered the trade-off between ΔE(HAT) and ΔE(oxo) and identified catalyst candidates along the ΔE(oxo) and ΔE(HAT) Pareto frontier through reaction energetics assessments. Owing to weak BEP relations over this set, we found that points close to but not on the Pareto frontier had superior kinetic properties. Our kinetic analysis on the best-trade-off subset of SACs results recommended that the following two codoped SACs hold great promise for methane-to-methanol conversion: **C**: IS 6-membered Fe(II)(cis N_2O_2) SAC and **D**: LS 5-membered Ru(II)(**14-16** N_4-N_2) SAC. Overall, our analysis of codoped SACs indicated the performance of SAC active sites is strongly influenced by both first and second coordination sphere element identities as well as by the local geometric structures they favor. By strategically engineering the local coordination environment, not just in the first coordination sphere but also the second, there are untapped opportunities to fine-tune the energetics of the HAT and oxo formation steps that normally are expected to have a steep tradeoff. Among the codoped SACs

studied, we identify SAC candidates with promising reaction energetics, kinetics and turnover frequencies for methane-to-methanol catalysis, warranting further experimental exploration.

Chapter 4: Computational discovery of Fe/Ru single atom catalysts for oxygen reduction reaction by DFT and machine learning

4.1. Introduction

The oxygen reduction reaction (ORR) is a crucial electrochemical process in a range of energy conversion and storage technologies from fuel cells to metal-air batteries.[187-190] The efficiency and performance of practical devices for these processes require high catalytic activity and stability of catalysts to overcome the intrinsically sluggish kinetics of ORR.[191] Despite its importance, optimization of catalysts for ORR presents significant challenges.[192] Noble metal-based ORR catalysts, such as Pt/C-based electrocatalysts,[193-195] have been well-developed and show good activity.[195, 196] However, the high cost, scarcity, and long-term stability issues of Pt-based catalysts cannot meet the increasing demand and greatly hinder large-scale commercial applications.[197, 198] The importance of ORR thus calls for deeper understanding of its mechanisms and development of novel catalysts, which would unlock new possibilities for energy conversion technologies.

Single-atom catalysts (SACs),[22-29] featuring isolated metal atoms dispersed on solid supports, have emerged as a promising class of catalysts for a wide range of electrochemical reactions due to their unique electronic and geometric properties,[35, 36] as well as their high metal atom economy.[32-34] Compared to traditional nanoparticle-based catalysts,[93-96] the unsaturated coordination environments and unique electronic structures of SACs have led to improved catalytic performance and shown promising potential for applications in ORR.[54, 97, 98, 199] Experimental studies have demonstrated the significant potential of doped graphitic SACs with various codoping configurations for ORR, including N/S and N/P codopants in the first coordination sphere,[51-53, 99] as well as configurations with N in the first and P or S in the second coordination sphere.[54, 100] However, codoped SACs, in which two or more heteroatoms are incorporated into the catalyst structure, still require further investigation and better guidance for

both computational design and experimental synthesis efforts. Our previous work[106] investigated the co-doping effect (e.g., NO, NP, NS, OS, OP, PS) with a wide range of coordination configurations of SACs for methane-to-methanol conversion, which shares many intermediates (i.e., oxo intermediates and hydroxo intermediates) with ORR. The results indicated that engineering the coordination environment near single metal sites can modulate the structural and electronic properties, which alters the energetics of reactions and catalytic performance. Therefore, manipulating the coordination sphere around the metal atom through codoping would be a rational approach to establish structure-property relationships and design efficient SACs for ORR applications as well.

Scaling relationships[113, 200, 201] computed with density functional theory (DFT), have become a crucial tool in computational catalysis for understanding the principles governing catalytic activity and selectivity.[70-74, 168] However, emerging catalysts, such as SACs, may deviate from the established scaling relationships for ORR,[202, 203] which presents a critical bottleneck in catalyst development. To overcome these limitations, the combination of virtual high-throughput screening (VHTS)[48, 102, 104-107] and machine learning (ML)[8, 108-111, 174] holds great promise in tackling challenges and accelerating material development. VHTS facilitates rapid evaluation of an extensive library of catalyst candidates and identification of promising compounds. ML models, learning from vast experimental and computational data, can predict reaction energetics with higher accuracy[112-116] than scaling relationships by capturing intricate patterns and incorporating a wide range of features.[116-118] Leveraging VHTS and ML can accelerate the rational design of SACs and other catalytic materials, expediting the discovery of novel catalysts with enhanced performance for ORR.

In this work, we employ VHTS and ML to investigate the potential of codoped SACs with Fe and Ru centers for optimizing ORR reaction energetics. We identify promising candidates for ORR and assess the applicability of conventional scaling relationships to these systems. Our ML models trained on this VHTS data predict the reaction energetics and catalytic performance of codoped SACs with higher accuracy than traditional scaling relationships. Our findings highlight the potential of codoping as a powerful strategy to tune the properties of SACs and overcome the limitations of traditional catalyst design approaches. We propose promising codoped SAC candidates for experimental validation and provide guidelines for the rational design of high-performance ORR catalysts.

4.2. Reaction Mechanism

We calculate the reaction energetics of ORR for Fe and Ru co-doped SACs in two oxidation states (i.e., M(II)/M(III)). All the catalytic intermediates were examined in both low-spin (LS) and intermediate-spin (IS), with the spin states being determined based on those that are accessible for both the resting state M(II/III) and the oxidized M(IV/V)=O intermediate. Specifically, these spin states correspond to LS doublet/IS quartet for $3d^3$ Fe(V)=O or $4d^3$ Ru(V)=O and LS singlet/IS triplet for $3d^4$ Fe(IV)=O or $4d^4$ Ru(IV)=O.

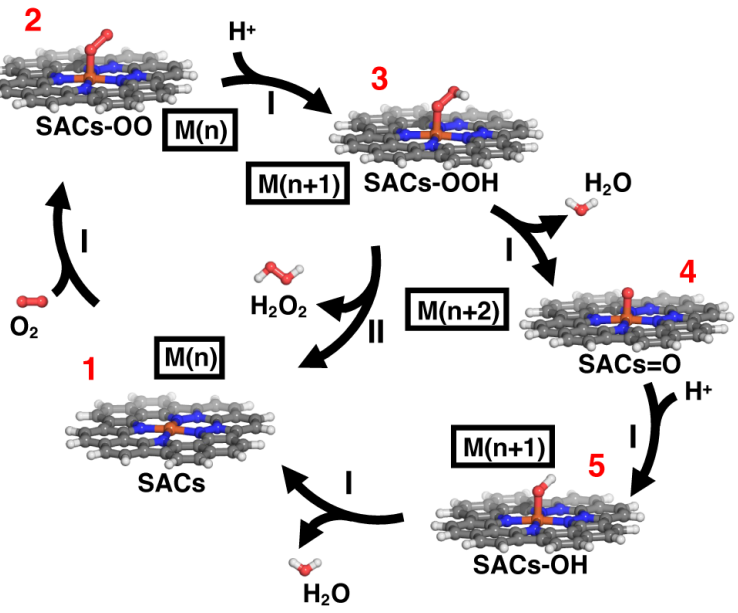

Figure 4.1. Catalytic cycle for ORR on a codoped Fe SAC in acid aqueous condition. The catalytic cycle proceeds clockwise: from the resting state (**1**) in oxidation state n = II/III, SACs−OO (**2**) formation with O_2 oxidant, followed by a SACs−OOH intermediate (**3**), water release to form a SACs=O intermediate (**4**), and formed a SACs−OH intermediate (**5**). Paths I and II follow four-electron reduction and two-electron reduction pathways, respectively. The structures are shown in the ball-and-stick representation colored as follows: Fe in orange, oxygen in red, nitrogen in blue, C in gray, and H in white.

The preferred pathway and the overall efficiency of the ORR depend on a few factors, such as the catalyst material, surface structure, electrolyte composition, and operating conditions.[201, 204-207] The reaction scheme of O_2 reduction in acidic aqueous conditions is believed to follow two possible pathways: the direct four-electron pathway (path I), where O_2 is reduced directly to H_2O, and the indirect two-electron pathway (path II), which involves the formation of H_2O_2 as an intermediate (Figure 4.1).[208, 209]

Due to the higher selectivity and efficiency of the four-electron pathway[112], we primarily focus on path I. The catalytic cycle for ORR starts from the resting state structure (**1**). The first

step is the adsorption of O_2 onto the metal center of the SAC, the energy of which can be computed as follows:

$$\Delta E(\mathbf{1} \rightarrow \mathbf{2}) = E(\mathbf{2}) - E(\mathbf{1}) - E(O_2) \qquad (1)$$

After the formation of the SACs−OO (**2**) M(II/III) intermediate, adsorbed O_2 receives the first electron from an external source along with a proton (e.g., from H_2O dissociation) to form the SACs−OOH intermediate (**3**) in an M(III/IV) oxidation state. While the proton source can be accounted for a number of ways, we compute the reaction energy for this step as:

$$\Delta E(\mathbf{2} \rightarrow \mathbf{3}) = E(\mathbf{3}) - E(\mathbf{2}) - \frac{1}{2}E(H_2) \qquad (2)$$

For the path I mechanism, the SACs−OOH intermediate (**3**) receives a second electron and releases OH^- in the form of H_2O to form an oxo intermediate (**4**, SACs=O), with a reaction energy computed as follows:

$$\Delta E(\mathbf{3} \rightarrow \mathbf{4}) = E(\mathbf{4}) - E(\mathbf{3}) - E(H_2O) + \frac{1}{2}E(H_2) \qquad (3)$$

This species has a metal center nominally in an M(IV/V) oxidation state. In the final step of the path I reaction, the SACs=O intermediate (**4**) accepts the third electron and a proton to form SACs−OH intermediate (**5**) in the M(III/IV) oxidation state. The reaction energy for this step is calculated as:

$$\Delta E(\mathbf{4} \rightarrow \mathbf{5}) = E(\mathbf{5}) - E(\mathbf{4}) - \frac{1}{2}E(H_2) \qquad (4)$$

To complete the catalytic cycle, the SACs−OH intermediate (**5**) gains the fourth electron to desorb OH^- to H_2O and the catalyst returns it to the resting state (**1**). We calculate the reaction energy in this step as:

$$\Delta E(\mathbf{5} \rightarrow \mathbf{1}) = E(\mathbf{1}) - E(\mathbf{5}) + E(H_2O) - \frac{1}{2}E(H_2) \qquad (5)$$

In addition to the reaction energetics, a key descriptor that is often used to describe ORR is the binding energy of the reaction intermediates (i.e., SACs=O, SACs-OH, SACs-OOH) to the metal sites of the SACs. The binding energies of the reaction intermediates (ΔE(OOH), ΔE(oxo), and ΔE(OH)) are calculated using the following equations:

$$\Delta E(OOH) = E(\mathbf{3}) - E(\mathbf{1}) - 2E(H_2O) + \frac{3}{2}E(H_2) \quad (6)$$

$$\Delta E(O) = E(\mathbf{4}) - E(\mathbf{1}) - E(H_2O) + E(H_2) \quad (7)$$

$$\Delta E(OH) = E(\mathbf{5}) - E(\mathbf{1}) - E(H_2O) + \frac{1}{2}E(H_2) \quad (8)$$

In all cases throughout, the energy of H_2O and H_2 are computed in the gas phase, and these choices for balancing each reaction are motivated by prior observations of errors in DFT for computing oxygen energetics.[201, 204]

4.3. Computational Details

All gas-phase geometry optimizations and single-point energy calculations were performed using density functional theory (DFT) with a development version of the GPU-accelerated electronic structure code TeraChem v1.9.[142] The range-separated hybrid functional ωPBEh[171] (default $\omega = 0.2$ bohr^{-1}) was employed for all calculations throughout our work with the LACVP* composite basis set, which consists of a LANL2DZ effective core potential[144, 145] for Fe and Ru and the 6-31G* basis for all other atoms. The choice of the ωPBEh functional was made to prevent the occurrence of the unphysical HOMO-LUMO gap closing observed in larger systems when using global hybrid functionals.[146, 147]

All closed shell singlet calculations were carried out in a spin-restricted formalism and all other calculations were in a spin-unrestricted formalism that employed level shifting[148] of 0.25 Ha for both majority and minority spin virtual orbitals to enable the convergence of the self-consistent field (SCF). The default SCF convergence threshold of 3×10^{-5} hartree for the direct inversion of

the iterative subspace (DIIS) error was employed. All geometry optimizations were carried out using the translation-rotation-internal coordinate (TRIC)[172] optimizer with default tolerances: a maximum gradient of 4.5×10^{-4} hartree/bohr and an energy difference between steps of 1×10^{-6} hartree.

The initial 412 Fe and 497 Ru codoped SACs each from a possible unique 512 configurations were adapted from the optimized codoped SACs dataset of our prior work (Appendix Table A4.1).[106] Any prior calculations that did not pass checks for quality in geometric or electronic structure were discarded in prior work and thus were not used here. We first optimized the low spin (LS) state oxo intermediate with the M=O bond distance initially placed at 1.65 Å. The initial metal-hydroxo intermediate was generated using the optimized metal-oxo intermediate as a starting point, to which an H atom was added to the oxygen atom (Appendix Figure A4.1). In a similar fashion, the metal-superhydroxo intermediate was initialized by adding a hydroxyl group to the optimized metal-oxo intermediates (Appendix Figure A4.1). After optimizing the metal-hydroxo and metal-superhydroxo intermediate, the corresponding metal-O_2 intermediate and resting state were optimized by removing the hydrogen atom and hydroxyl group, respectively. All intermediate spin (IS) SAC intermediates were optimized from the corresponding pre-optimized LS structures (Appendix Table A4.2).

All job submissions were automated through the job manager in molSimplify[140], with a 72-hour wall time per run cutoff and a maximum five resubmissions allowed for each job.[174] If an intermediate optimization failed, subsequent downstream intermediate optimizations were not executed. The converged structures were excluded from the dataset based on established protocols[29, 48, 106] if: 1) the expectation value of the S^2 operator, $\langle S^2 \rangle$, deviated from the expected value of $S(S+1)$ by > 1; 2) the sum of the Mulliken spin density on the metal and oxygen differed

from the spin multiplicity by > 1 μ_B; or 3) geometric deviations indicated by the oxo moiety inserting itself into metal-coordinating atom bonds or the structure differed from the corresponding initial structure by a root-mean-square deviation (RMSD) > 0.6 Å.

4.4. Results and Discussion

4.4A. Scaling relationship of codoped Fe/Ru SACs

The correlations between binding energies of reaction intermediates on a catalyst surface, which are known as scaling relationships,[113, 200, 201] have become an important concept in computational catalysis. Scaling relationships can be leveraged to discover and optimize catalysts by identifying the key descriptors that determine catalytic performance. For the rational design of SACs tailored for the ORR at the atomic scale, a comprehensive understanding of structure-performance relationships is crucial, allowing the identification and fine-tuning of the critical descriptors that determine their catalytic activity. Scaling relationships between the binding energies of OOH*, O*, and OH* intermediates in ORR typically exhibit strong positive linear correlations for heterogeneous catalysts.[7, 72-74, 210-214] Nonetheless, emerging catalysts like SACs may diverge from established scaling relationships for ORR.[202, 203] Given the widespread application of scaling relationships to simplify complex catalytic cycles into single descriptors, we aimed to determine whether a diverse chemical space of codoped transition metal SACs follows established scaling relationships [71, 183] for ORR, particularly concerning the period dependence (i.e., Fe/Ru).

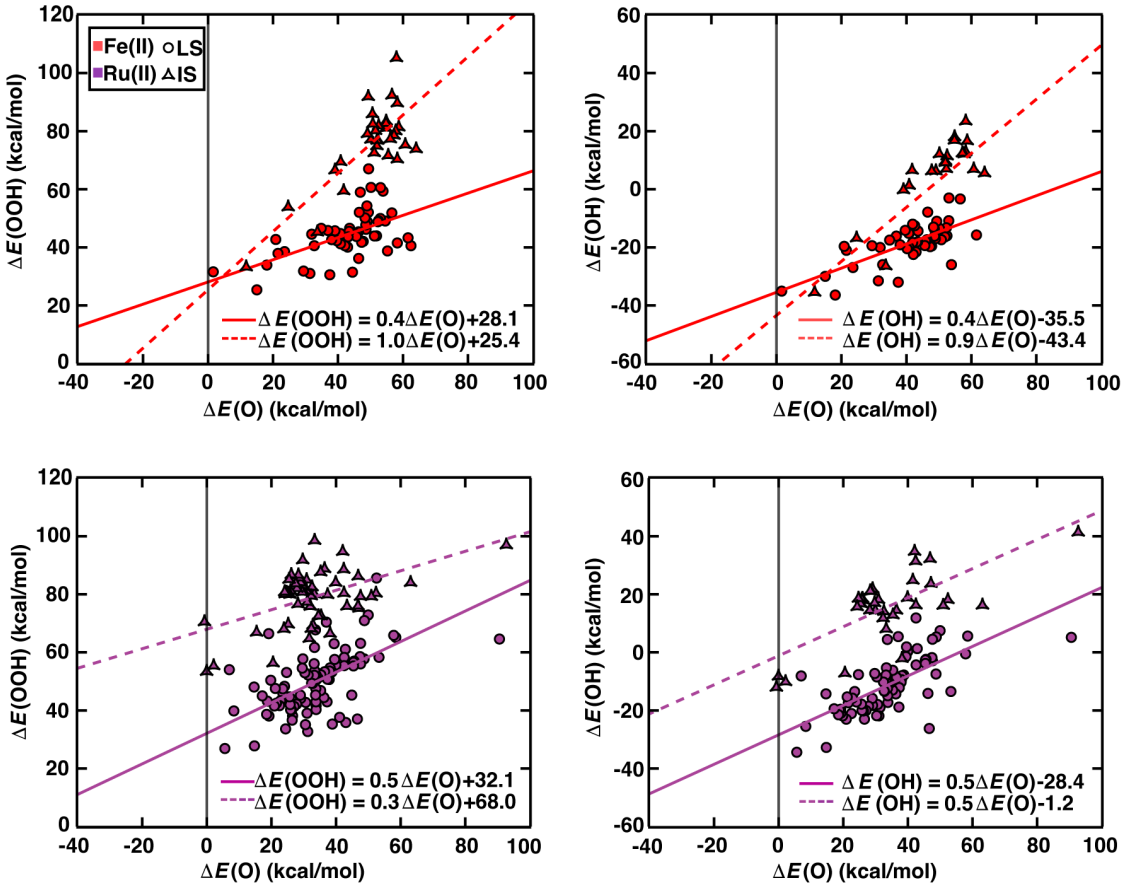

Figure 4.2. Scaling relationships for the binding energies (in kcal/mol) on the metal(II) sites of the codoped SACs with ΔE(O) as a descriptor. The data points are colored by metal identities (Fe in red and Ru in purple). The four panes illustrate Fe(II) ΔE(O) vs. ΔE(OOH) energetics (top left), Fe(II) ΔE(O) vs. ΔE(OH) energetics (top right), Ru(II) ΔE(O) vs. ΔE(OOH) energetics (bottom left), and Ru(II) ΔE(O) vs. ΔE(OH) energetics (bottom right). Data point shapes indicate spin state (LS as circles and IS as triangles). The solid lines are linear fits for the LS codoped SACs and the dashed lines are equivalent fits for IS systems. Zero axes are shown on all plots as solid black lines.

Over the codoped Fe/Ru SACs dataset, we observe that the binding energies ΔE(OOH), ΔE(O), and ΔE(OH) are positively correlated intermediate (Figure 4.2). These linear scaling relationships originate from the fact that all the adsorbates bind to the metal active site through an oxygen atom. We first assess the impact of a 3d vs. 4d metal (i.e., Fe(II) vs. Ru(II)) on the scaling relationships of ΔE(O) vs. ΔE(OOH) and ΔE(O) vs. ΔE(OH) reaction energetics in codoped SACs. For ΔE(O) vs. ΔE(OOH) energetics, both LS codoped Fe(II) SACs and LS codoped Ru(II) SACs

show comparable scaling relationships (Appendix Table A4.3 SLinear fits). In LS codoped Fe(II) SAC systems, ΔE(OH) exhibits a linear scaling relation with ΔE(O) with a Pearson's r of 0.70, which is similar to the equivalent linear scaling relationship in LS codoped Ru(II) SACs (Appendix Table A4.3) with a Pearson's r of 0.69. To investigate the impact of spin states (i.e., LS vs. IS) on scaling relationships there isn codoped transition metal SACs, we focused on the ΔE(O) vs. ΔE(OOH) and ΔE(O) vs. ΔE(OH) reaction energetics of both LS and IS Fe(II) and Ru(II) codoped SACs. The Ru(II) codoped SACs exhibit comparable scaling relationships (i.e., similar slope) for ΔE(O) vs. ΔE(OOH) and ΔE(O) vs. ΔE(OH) reaction energies; however, the IS systems show a steeper slope than their LS counterparts in codoped Fe(II) SACs.

For both LS codoped Fe and Ru SACs, the ΔE(O) vs. ΔE(OH) scaling relationship has a slope close to that of heterogeneous catalysts of various metals on the (111) surface (i.e., a slope near 0.5).[201] In comparison to SACs with the same coordination environment but different metal identities, the slope of ΔE(O) vs. ΔE(OH) in LS Fe(II) systems is comparable with the slope in TM@C_2N SACs, while the correlation between these energies in codoped SACs (Pearso''s r of 0.56) is weaker than that of TM@C_2N SACs (R^2 of 0.86).[112] This relatively weak correlation in codoped Fe/Ru SAC systems is due to high variation of the coordination environment (i.e., atom identities and geometry) resulting in increased scatter relative to scaling relationships obtained for TM@C_2N SACs.[112] In addition, weaker linear correlations are observed for codoped SACs inthere isS state than their LS state for both metals. The large deviation from linear scaling relationships owing to the varied local coordination geometry and metal spin state makes codoped SACs more tunable, indicating they can achieve superior catalytic performance through orthogonal adjustment of binding energies.

4.4B. Machine learning models on predicting reaction energetics

The molecular representations used in this work are revised autocorrelations (RACs),[215] which have been successfully applied for building structure–property relationships in transition metal complexes[101, 174, 216] and metal-organic frameworks.[217-219] RACs are based on the graph representation of a chemical system and can be calculated from heuristic atomic properties (e.g., nuclear charge, Pauling electronegativity, topology etc.) of atoms on a graph. Several types of ML models are trained in this work: random forest (RF), linear regression, Gaussian process regression (GPR) and recursive feature addition Gaussian process regression (RFA GPR) are built as surrogates for DFT calculations. Our goal is using ML models to make direct predictions on energetics of the ORR catalytic intermediates (e.g., ΔE(O), ΔE(OH), and ΔE(OOH)) based on the 2D connectivity of SACs. In this way, we aim to efficiently discover codoped SACs for ORR without high-cost quantum chemistry calculations.

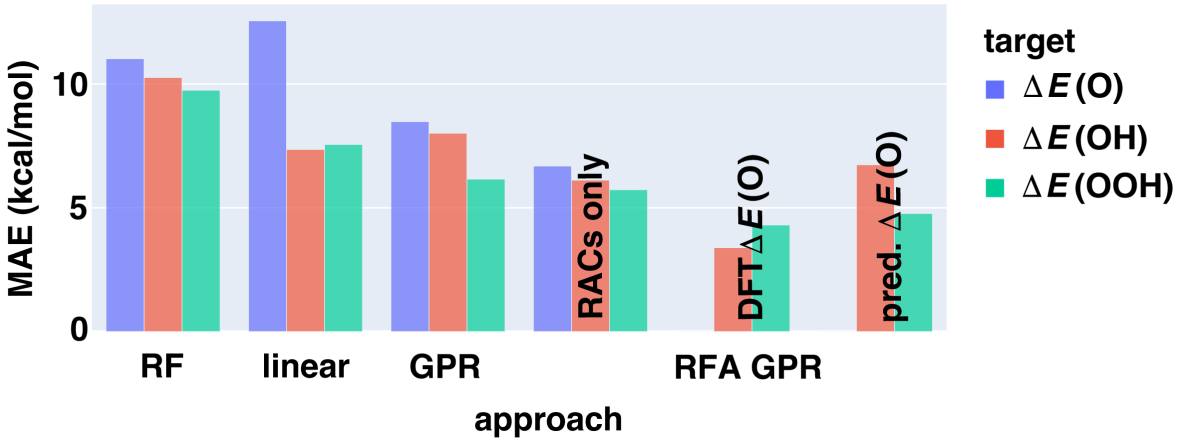

Figure 4.3. Comparison of different ML models in predicting ΔE(O), ΔE(OH), and ΔE(OOH) energetics, evaluated using the mean absolute error (MAE) in kcal/mol. The random forest (RF), linear regression, and Gaussian process regression (GPR) models utilize only the RACs as the feature set. For the recursive feature addition Gaussian process regression (RFA GPR), three different feature sets are employed: (1) RACs, (2) RACs combined with DFT-calculated ΔE(O) values, and (3) RACs combined with RFA GPR-predicted ΔE(O) values.

In our exploration of various ML models for predicting ΔE(O), ΔE(OH), and ΔE(OOH) energetics, we find that feature selection plays a critical role in model performance. Using a set of features marked as important (with a threshold of 0.02) by RF, the GPR model outperforms other approaches, including RF and linear regression models (Figure 4.3). To improve the GPR model performance, we employ recursive feature addition Gaussian process regression (RFA GPR) to predict ΔE(O), ΔE(OH), and ΔE(OOH) energetics based on RACs. The RFA GPR model significantly outperform the traditional GPR model by 2~3 kcal/mol. The RFA GPR's ability to iteratively add relevant features and update the model allows it to capture the most predictive descriptors for these energetic quantities. To further enhance the predictive capabilities of the RFA GPR model for ΔE(OH) and ΔE(OOH), we employed two approaches that leveraged ΔE(O) as a feature: (1) combining RFA GPR with DFT-calculated ΔE(O) values, and (2) combining RFA GPR-predicted ΔE(O) values. Our results show leveraging ΔE(O) as a feature significantly enhanced the predictive capabilities of RFA GPR, particularly in forecasting ΔE(OH) and ΔE(OOH). Even substituting DFT-calculated ΔE(O) with RFA GPR-predicted ΔE(O) values resulted in a noticeable improvement in the accuracy of ΔE(OH) and ΔE(OOH) predictions. Notably, the RFA GPR model demonstrated superior performance compared to some codoped SACs (i.e., IS Fe(II) codoped SACs and IS Ru(II) codoped SACs, Appendix Table A4.3 Table SLinear fits) due to the linear scaling relationships, which have traditionally been utilized as a baseline approach for computational catalyst discovery. By going beyond the limitations of scaling relationships, the RFA GPR model achieved higher accuracy in its energetics predictions.

4.4C. *Exploring 0.28 million triple-doped SACs with machine learning*

The RFA GPR model, which incorporates the predicted ΔE(O) and RACs as input features, exhibited superior predictive capabilities compared to conventional linear scaling relationships.

To fully exploit the potential of this RFA GPR model for the discovery of highly active codoped SACs for ORR, we aim to explore an expanded chemical space through an extensive computational screening approach.

The expanded chemical space is constructed based on codoped Fe/Ru SACs, where their explicit DFT-level catalytic properties were obtained and used during RFA GPR model training. Specifically, we employed a random selection process to choose a single C atom within the SACs flake, subsequently substituting this selected C atom with one of alternative atoms (i.e., N, O, P or S), which results in a new triple-doped SAC. This doping strategy introduces additional structural and electronic modifications to the local environment of the active metal site, potentially altering the catalytic properties. Through this systematic approach, we effectively generate a diverse set of 69,526 distinct codoped SAC geometries within our expanded chemical space for subsequent screening. Together with the metal, oxidation state, and spin state variation, we assemble a new space of 0.28 million triple-doped SAC.

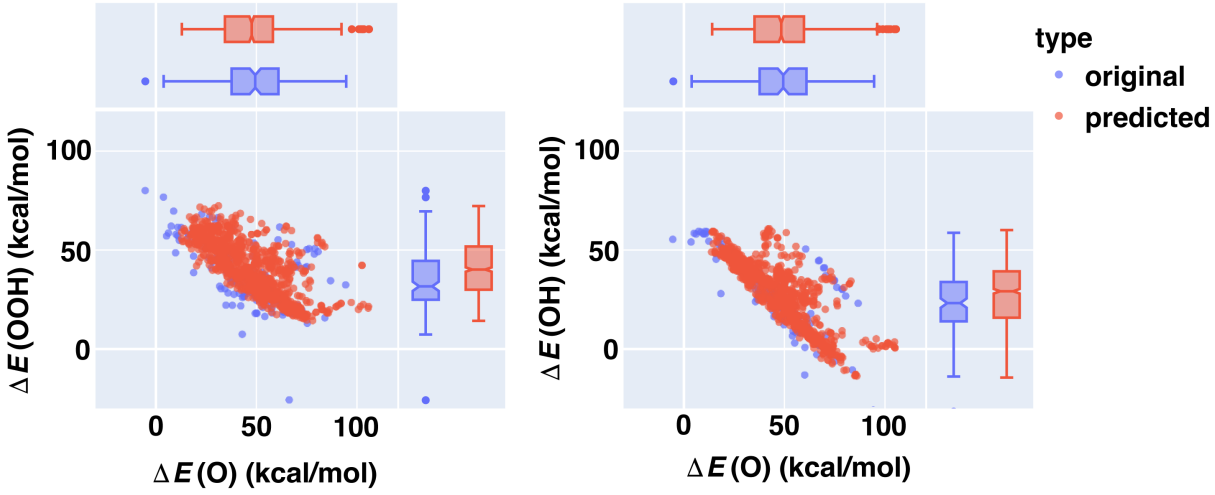

Figure 4.4. The ΔE(O) vs. ΔE(OOH) energetics (left) and ΔE(O) vs. ΔE(OH) energetics (right) for the expanded chemical space of codoped Fe/Ru SACs. The explicit data points are colored by data types (original in blue and predicted in red).

Next, we applied the RFA GPR to make predictions across the expanded chemical space of triple-doped SACs. Specifically, we aimed to identify promising candidates that could potentially exhibit improved catalytic performance for the ORR. The ORR involves a series of elementary steps, with the binding energies of reaction intermediates such as OOH and OH playing a critical role in determining the overall catalytic activity. Our results indicated that the expanded chemical space, obtained through the random triple-doping strategy, did not significantly extend the catalytic performance beyond the original space for both the $\Delta E(O)$ vs. $\Delta E(OOH)$ and $\Delta E(O)$ vs. $\Delta E(OH)$ reaction energetics (Figure 4.4). This suggests that the introduction of heteroatom dopants outside the first and second coordination sphere may not substantially modify the local metal environment to further tune the catalytic activity for the ORR. While the triple-doping approach provided a diverse set of structures, the electronic and geometric perturbations induced by the heteroatom substitutions were not sufficient to further extend the catalytic capability of Fe/Ru SAC systems. These results underscore the complexity inherent in optimizing catalytic systems and highlight the necessity for further refinement in our approach to uncovering novel catalysts with enhanced performance characteristics.

4.5. Conclusions

In conclusion, this study demonstrates the potential of codoped SACs with Fe and Ru centers for optimizing the ORR energetics. Through VHTS and ML techniques, we explored a vast chemical space of codoped SAC structures and identified promising candidates exhibiting enhanced ORR catalytic performance. Our results show that codoping significantly influences the electronic and geometric properties of SACs, enabling tunable catalytic activity and stability The ML models trained on the VHTS data outperformed conventional scaling relationships in accurately predicting reaction energetics and catalytic performance metrics. This highlights the

efficacy of combining computational screening and machine learning approaches for rational catalyst design and discovery. The promising codoped SAC candidates identified in this work warrant experimental validation and offer exciting opportunities for developing high-performance, cost-effective ORR catalysts. Furthermore, our findings provide valuable insights into the fundamental factors governing the catalytic behavior of codoped SACs. The ability to precisely control the dopant type, concentration, and local coordination environment through codoping emerges as a powerful strategy for tuning the electronic structure and catalytic properties of SACs. This knowledge can guide future efforts in designing tailored SACs for various energy conversion and storage applications beyond ORR. In summary, this study paves the way for the rational development of advanced SAC-based catalysts through computational screening and machine learning techniques. The proposed codoped SAC candidates hold great promise for overcoming the limitations of traditional noble metal catalysts and enabling more sustainable and efficient energy technologies.

Chapter 5: Benchmarking nitrous oxide adsorption and activation in metal–organic frameworks bearing coordinatively unsaturated metal centers

This chapter has been partially adapted partially from ‘T. A. Pitt, H. Jia, T. J. Azbell, M. E. Zick, A. Nandy, H. J. Kulik, and P. J. Milner "Benchmarking Nitrous Oxide Adsorption and Activation in Metal-Organic Frameworks Bearing Coordinatively Unsaturated Metal Centers", Journal of Materials Chemistry C, *J. Mater. Chem. C*, **2024**, 12, 3164-3174.’

5.1. Introduction

N_2O is the third most prevalent anthropogenic greenhouse gas after CO_2 and CH_4, accounting for 6% of the total effective radiative forcing from 1960 to 2019.[220] Although CO_2 and CH_4 are present in higher concentrations in the atmosphere, the global warming potential of N_2O (265) is far greater (1 and 28 for CO_2 and CH_4, respectively) and its atmospheric lifetime (116 years) is far longer (1 and 12 years for CO_2 and CH_4, respectively).[221] Over the last four decades, global anthropogenic emissions of N_2O have increased by 30%.[222] Up to 87% of this increase derives from agriculture and nitrogen additions to soils. In nature, the sources of these emissions (i.e., farmlands) are diffuse, in contrast to point sources of N_2O emissions such as adipic and nitric acid manufacturing.[223] Diffuse emissions are currently largely uncontrolled, except for preventative measures such as the use of more efficient fertilizers.[224, 225] At point sources, N_2O can be catalytically destroyed, but regulations requiring this practice have not been globally adopted.[226] Thus, the majority of human-caused N_2O emissions are currently unabated, leading to a current estimated rate of increase in atmospheric N_2O concentration of 2% per decade.[220] In addition to its global warming potential, N_2O was found to be the dominant ozone-depleting substance emitted in the 21st century,[223] underscoring the urgency of curtailing N_2O emissions. The environmental effects of anthropogenic N_2O emissions and its long atmospheric lifetime necessitate the development of new materials for N_2O capture.

Selectively capturing gases from diffuse sources such as air is a unique challenge that requires specially designed sorbents. Metal-organic frameworks (MOFs) are an emerging class of materials that have drawn significant interest for their potential applications in greenhouse gas capture,[227] separations,[228] catalysis,[229] and beyond.[230] They are crystalline, highly porous materials formed by connecting metal secondary building units (SBU) with multitopic organic linkers.

MOFs have been designed to selectively bind CO_2 and CH_4 based on a range of strong binding pathways, including electrostatic interactions,[231, 232] chemical reactivity,[233-235] hydrogen bonding,[236] and more. In contrast, only a small number of largely unrelated MOFs have been studied for N_2O capture to date.[237-243] The presence of Lewis acidic open metal sites has been shown to enhance N_2O binding;[238] however, a general lack of structure-property trends informing the design of new materials hinders improvements in N_2O capture in porous materials.

Herein, we present a structure-activity study of N_2O adsorption in MOFs, with the purpose of identifying features that contribute to strong binding and high uptake. Through a combined experimental and computational analysis, we clarify the effects of the ligand field and metal identity on N_2O adsorption at Lewis acidic open-metal-sites in the M_2Cl_2(btdd) (M= Mn, Co, Ni, Cu; btdd^{2-} = bis(1,2,3-triazolo[4,5-b],[4',5'-i])dibenzo[1,4]dioxin)[244, 245] and M_2(dobdc) (M = Mg, Mn, Fe, Co, Ni, Cu, Zn; dobdc^{4-} = 2,5-dioxido-1,4-benzenedicarboxylate) series of MOFs.[231, 246, 247] From this analysis, we identify the M_2(dobdc) series, particularly Mg_2(dobdc) and Ni_2(dobdc), as promising adsorbents that display strong binding and record-setting N_2O adsorption capacities.

Beyond reducing its environmental impact, N_2O capture is incentivized by the opportunity to utilize it as a cheap, abundant, and potent oxidant in organic synthesis.[248-250] As a kinetically inert molecule, transition metal catalysts and/or high temperatures and pressures are required to facilitate N_2O activation. Thus, MOFs and zeolites containing unsaturated Fe(II) sites have been explored as catalysts for N_2O functionalization.[251-255] In particular, Fe_2(dobdc) has been demonstrated to catalyze C–H oxidation of hydrocarbons using N_2O as an oxidant.[254, 256, 257] Bearing strong similarities to enzymatic iron-based catalysts,[258, 259] this occurs through a 2 e^- transfer from Fe(II) to the oxygen of N_2O, cleaving the N–O bond and forming an Fe(IV)–oxo intermediate, followed by σ-attack and H atom abstraction by the Fe(IV)–oxo and radical rebound

to generate the oxidized product.[256] Herein, DFT calculations support that N_2O activation is also thermodynamically favorable in Mn_2(dobdc), and we map out an approximate reaction coordinate for this process using the climbing-image nudged elastic band method (CI-NEB). While computation results suggest that this reaction is kinetically limited in Mn_2(dobdc), our work motivates further study of N_2O activation in related Mn-based MOFs. Overall, our findings stimulate the development of new framework materials for selective N_2O capture and conversion to mitigate its environmentally destructive impact.

5.2. Computational Details

Gas-phase geometry optimizations of MOF cluster models in this work were geometry optimized with density functional theory (DFT) using ORCA v4.0.1.2.[260] The B3LYP[261] global hybrid functional with the empirical D3 dispersion correction[262, 263] incorporating the default Becke-Johnson damping was used for all models. Scalar relativistic effects were incorporated by using the zero-order regular approximation (ZORA)[264] with defaults applied in ORCA. All metal ions in oxidation state +2 (from Mn(II) to Zn(II)) were modeled with the ZORA-def2-TZVPP[265] basis, with all remaining atoms treated with a ZORA-def2-SVP basis. We constrained O atoms in linkers and allowed all other atoms to relax. All calculations made use of the resolution of identity (RI) and chain of sphere (COSX) approximations[266] for acceleration. We considered two types of spin flips (i.e., at the central metal or in one edge metal) in broken symmetry DFT (BS-DFT)[267] of the system containing three identical metals. Geometry optimizations were carried out using default tolerances of 3×10^{-4} hartree/bohr for the maximum gradient and 5×10^{-6} hartree for the self-consistent field (SCF) energy change between steps. The transition state (TS) and barrier heights for the oxo formation step were modeled with the climbing image nudged elastic band (CI-NEB) method[268]. The initial and final states were frozen from prior geometry optimizations and

contain M–O and O–N bond lengths, respectively, of 2.52 Å and 1.19 Å for the N_2O adduct and 1.62 Å and 2.98 Å for the Mn–oxo species. We mapped the reaction coordinate between these states with CI-NEB using 10 total images.

5.3. Results and Discussion

5.3A. N_2O adsorption analysis

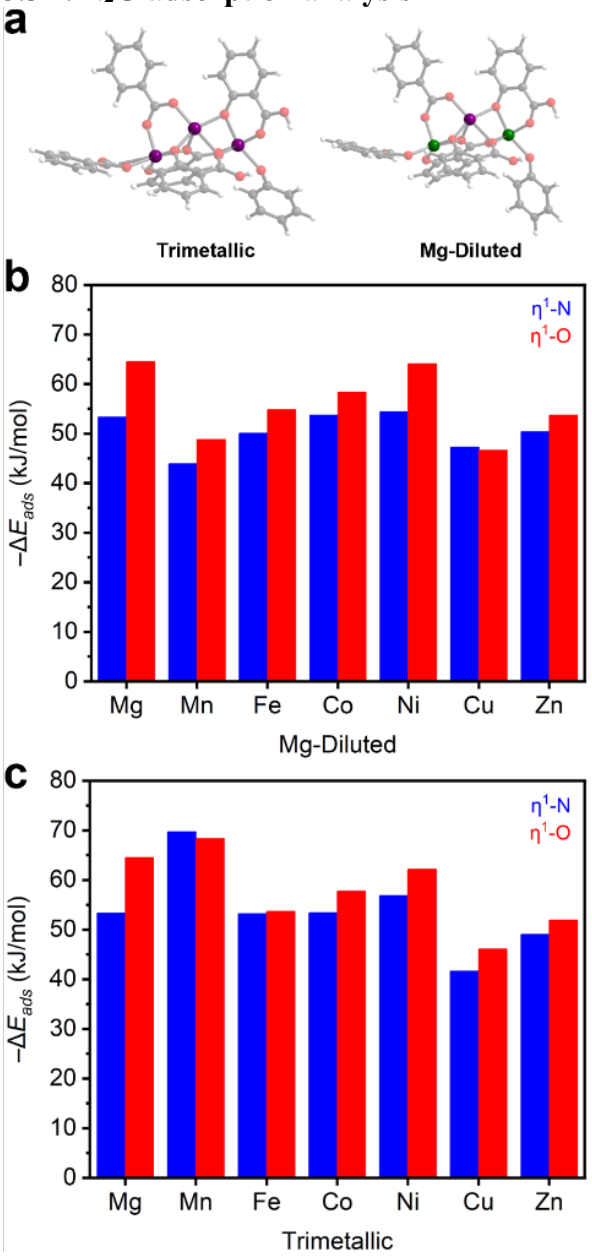

Figure 5.1. a) Trimetallic (left) and Mg-diluted (right) cluster models of M_2(dobdc). Purple, green, grey, red, and white spheres represent metal, magnesium, carbon, oxygen, and hydrogen atoms, respectively. DFT-calculated negative adsorption energies ($-\Delta E_{ads}$) of η^1-N (blue) and η^1-O (red) coordinated N_2O in the b) Mg-diluted and c) trimetallic systems.

In our calculations, trimetallic cluster models were generated to approximately study the one-dimensional SBU structure (Figure 5.1a). Similar cluster models have been used to evaluate N_2O reduction in Fe_2(dobdc).[256, 269] For each member of the M_2(dobdc) series, excluding Mg_2(dobdc) for redundancy, two types of cluster models were simulated: a trimetallic system and a Mg-diluted system. In the Mg-diluted models, both edge metal ions were replaced with Mg(II) ions. The purpose of including the Mg-diluted systems is to simulate only one open-shell metal center and decouple adsorption energetics from the potential influence of metal-metal coupling on N_2O adsorption. All systems are neutral with all M(II) ions in the high-spin state where applicable (Appendix Table A5.1).

The adsorption energy of η^1-N ($\Delta E_{ads}(\eta^1\text{-N})$) and η^1-O ($\Delta E_{ads}(\eta^1\text{-O})$) coordinated N_2O in the pure metal and Mg-diluted M_2(dobdc) clusters was evaluated as follows:

$$\Delta E_{ads}(\eta^1\text{-N}) = E\left(M^{(n+2)}\text{-}N_2O\right) - E(M^n) - E(N_2O) \quad (1)$$

$$\Delta E_{ads}(\eta^1\text{-O}) = E\left(M^{(n+2)}\text{-}ON_2\right) - E(M^n) - E(N_2O) \quad (2)$$

$E(M^{(n+2)}\text{–}N_2O)$ is the energy of the pure metal or Mg-diluted M_2(dobdc) cluster model with η^1-N coordinated N_2O, $E(M^{(n+2)}\text{–}ON_2)$ is the energy of the cluster with η^1-O coordinated N_2O, $E(M^n)$ is the energy of the bare cluster, and $E(N_2O)$ is the energy of an N_2O molecule in the gas phase.

The energies of adsorption ($-\Delta E_{ads}$) for both η^1-N and η^1-O coordinated N_2O adducts in the model clusters were first calculated (Figure 5.1b–c, Appendix Table A5.2). In both the trimetallic and Mg-diluted models, η^1-O coordinated N_2O is slightly more stabilized (2–10

kJ/mol) than η^1-N coordinated N_2O. This aligns with the approximately 60%/40% η^1-O/η^1-N population split determined from neutron diffraction data collected on N_2O-dosed Fe_2(dobdc).[254] The calculated formation energies of N_2O adducts in the Mg-diluted series (Figure 5.1b) approximately match the trend observed experimentally: Cu ≈ Mn < Fe ≈ Zn < Co < Ni ≈ Mg. However, some divergence is noted in the trimetallic systems (Figure 5.1c): the Mn-based trimetallic system binds N_2O considerably more strongly than the equivalent Mg-diluted model, suggesting multiple metal effects that require consideration of metal-metal coupling (see below). Additionally, η^1-N coordination to Mn_2(dobdc) is slightly more favorable than η^1-O in the trimetallic model.

Across the series, the model systems reveal that η^1-O and η^1-N adducts of N_2O are bent, with bond angles and M–N_2O distances in agreement with those solved from the neutron diffraction data in Fe_2(dobdc) (Appendix Table A5.3), the only definitively characterized structure of N_2O bound to a metal center within a MOF reported to date.[254] In the DFT-calculated structure, η^1-N coordinated N_2O exhibits a typical bond angle of 115–123° (122° in N_2O–Fe_2(dobdc)), whereas η^1-O coordinated N_2O exhibits slightly smaller bond angles ranging from 105–120° (117° in N_2O–Fe_2(dobdc)). Bond lengths of η^1-N and η^1-O coordinated N_2O (2.25–2.57 Å and 2.27–2.54 Å, respectively) vary over only a narrow range. These models reinforce that N_2O binding across the M_2(dobdc) series is primarily based on electrostatic interactions rather than π-backbonding, which would be expected to lead to linear η^1-N (V, Cu, Ru, Rh) or side-on η^2-N,N (Co, Ni) interactions with N_2O.[270-276]

It should be noted that N_2O adsorption has been modelled previously in a small variety of other open metal site MOFs. The Fe(II)- and Cu(II)-based paddlewheel nodes in M_3(btc)$_2$ (btc^{2-} = benzene-1,3,5-tricarboxylate) MOFs show bent η^1-N and η^1-O coordination modes for N_2O.[277]

Likewise, N_2O adducts have been modelled in many derivatives of the trinuclear carboxylate-bridged, oxygen-centered nodes ($M_3(\mu_3\text{-}O)(RCOO)_6$, M = V, Cr, Mn, Fe, Co, Ni) common among MOFs such as MIL-100, MIL-101, and MIL-127.[278] The calculated binding of η^1-N coordinated N_2O at V centers is linear, but other adducts are bent, with similar bond angles and bond lengths as calculated in the M_2(dobdc) series herein. In the Kuratowski-type SBU of Cu-MFU-4*l* (MFU = Metal-Organic Framework Ulm-University), DFT calculations support an approximately linear η^1-N coordinated N_2O molecule, indicating possible π-backbonding from the Cu(I) centers.[238] Overall, these findings support that N_2O is predicted to bind in a bent fashion at all but the most electron-rich metal centers in MOFs.

5.3B. BS-DFT with two spin flip configurations

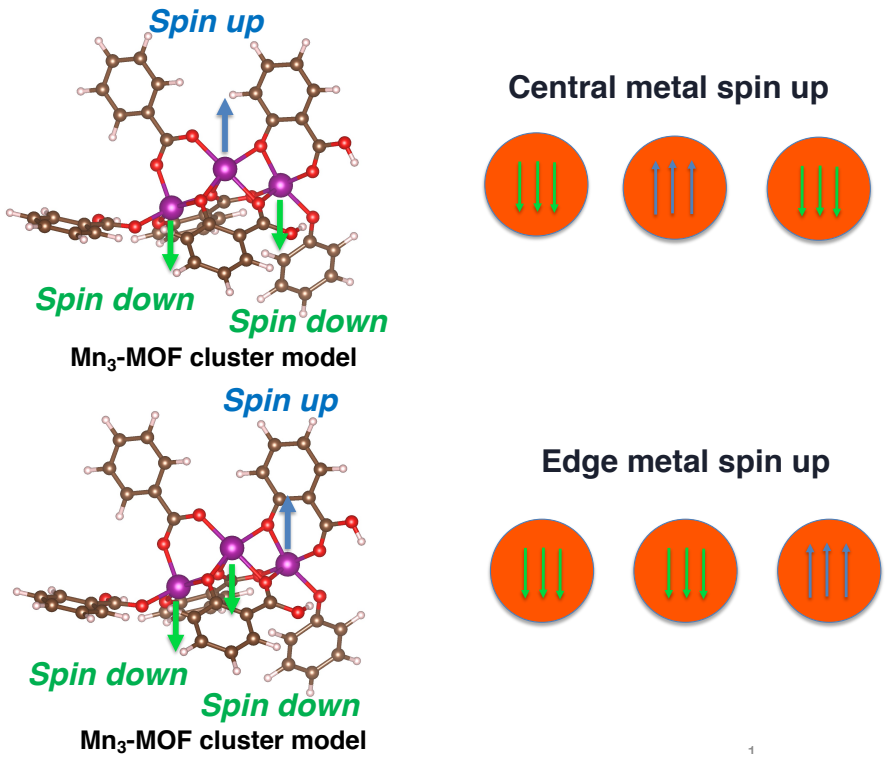

Figure 5.2. Structures for two spin flip configurations (the central metal and the edge metal) of MOF-74 cluster and corresponding HS electron configuration of Mn_3-MOF system.

A notable exception to the trends outlined above is the trimetallic Mn cluster, in which η^1-N coordinated N_2O is nearly linear (172°), suggesting that π-backbonding occurs from the Mn *d* orbitals into the π* orbital of N_2O, which has previously been invoked in linear η^1-N V, Cu, Ru, and Rh adducts of N_2O to justify the unusual stability of those complexes.[270, 272-274, 276] Consistently, the Mn–N bond length (1.95 Å) is considerably shorter than in other models (Appendix Figure A5.1). These characteristics are distinct from the equivalent Mg-diluted cluster, suggesting that metal-metal coupling may affect the binding mode of N_2O in these calculations. We thus evaluated N_2O binding in the open-shell trimetallic systems (Mn through Cu) using broken-symmetry density functional theory (BS-DFT) with two spin flip configurations (i.e., in the central metal or in one edge metal) to quantify the metal-metal coupling and to extract coupling constants (Figure 5.2). To ensure that the BS-DFT calculations converged to the desired states, the spin density was visually inspected (Appendix Figure A5.2).

The energy of M(IV)–oxo formation (ΔE_f ($M^{(n+2)}$-oxo)) in the pure metal and Mg-diluted M_2(dobdc) cluster models was evaluated as follows:

$$\Delta E_f\left(M^{(n+2)}\text{–oxo}\right) = E\left(M^{(n+2)}\text{–oxo}\right) + E(N_2) - E(M^n) - E(N_2O) \qquad (3)$$

$E(M^{(n+2)}$–oxo) is the energy of the oxo-containing pure metal or Mg-diluted M_2(dobdc) cluster, $E(M^n)$ is the energy of the bare cluster, $E(N_2)$ is the energy of an N_2 molecule in the gas phase, and $E(N_2O)$ is the energy of an N_2O molecule in the gas phase. In particular, the energetic difference in the trimetallic Mn system in comparison to the dilute case indicates especially strong metal-metal coupling (Appendix Table A5.4). From this data, we calculated strong magnetic coupling along the SBU chains in the trimetallic Mn system ($J = 314.27\ cm^{-1}$), which becomes even stronger after N_2O binding regardless of the coordination mode ($J = 857.47\ cm^{-1}$ for η^1-N, $J = 857.47\ cm^{-1}$ for η^1-O). Consistently, prior first principles studies support that Mn_2(dobdc) exhibits

antiferromagnetic coupling below approximately 27 K.[279, 280] Adsorbate-induced changes in magnetic coupling are also precedented in the M_2(dobdc) series; for example, in Fe_2(dobdc), the ferromagnetic exchange strength along the SBU chains is attenuated by interaction with weak adsorbates (e.g., CH_4, $-\Delta H_{ads}$ = 20 kJ/mol), and the coupling becomes antiferromagnetic upon interaction with strong adsorbates (e.g., C_2H_2, $-\Delta H_{ads}$ = 47 kJ/mol).[281] Our results point to an additional stabilization of the N_2O adducts of Mn_2(dobdc) related to enhanced metal coupling, possibly leading to greater π-backbonding from Mn to N_2O and favoring linear η^1-N coordination. Above 27 K, however, this effect is no longer expected to significantly contribute to the adsorption interactions as the spins become randomly oriented. Consistently, the experimental binding enthalpies do not show enhanced adsorption in Mn_2(dobdc) relative to other MOFs in the series. Nevertheless, if a suitable Mn-based open-metal-site MOF with a higher Neel temperature were to be identified, this feature could potentially be leveraged to enhance N_2O binding.

5.3C. Evaluating N_2O activation in the M_2(dobdc) series

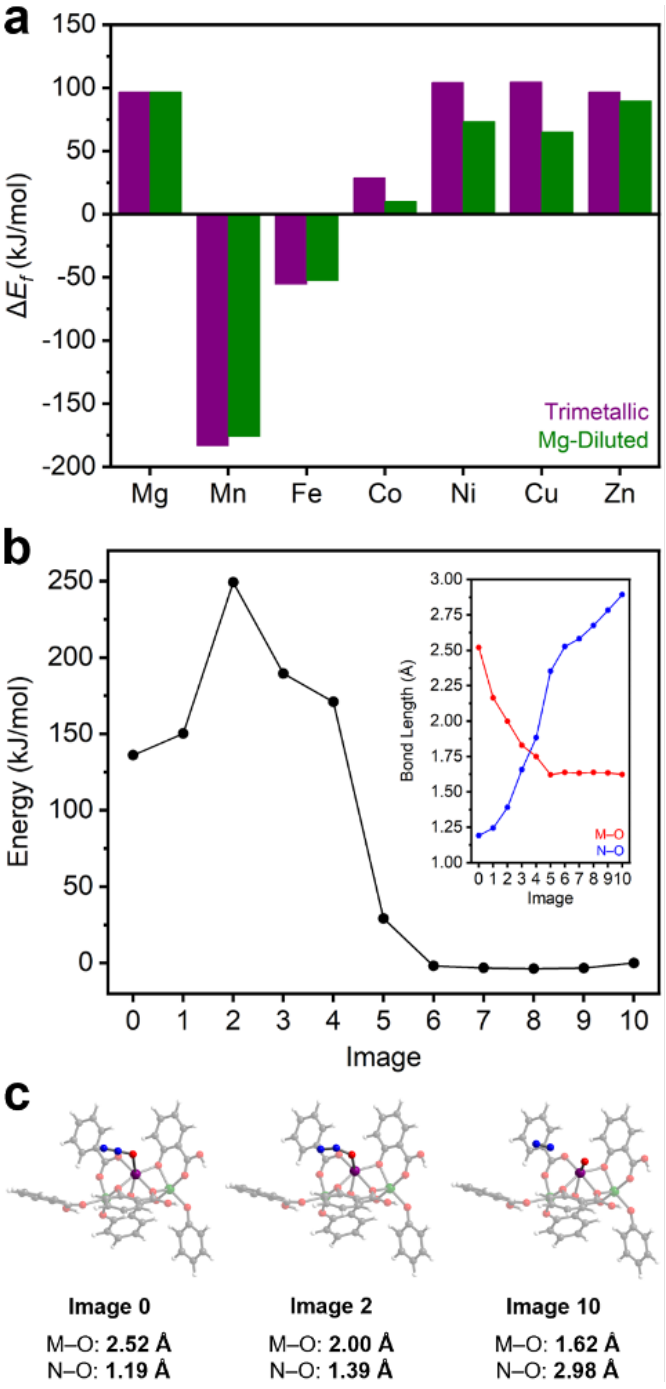

Figure 5.3. a) DFT-calculated energies of M–oxo formation (ΔE_f) in the trimetallic (purple) and Mg-diluted (grey) models of M_2(dobdc). b) CI-NEB-calculated approximate reaction coordinate of Mn–oxo formation from η^1-O coordinated N_2O in the Mg-diluted system. Inset: M–O (red) and N–O (blue) bond lengths vs. image number. c) Structures of the initial (left), transition (center), and final (right) states. Purple, green, blue, grey, red, and white spheres represent manganese, magnesium, nitrogen, carbon, oxygen, and hydrogen atoms, respectively.

N_2O activation to form M(IV)-oxo species and N_2 in MOFs has been principally studied in Fe_2(dobdc) and other Fe(II)-based frameworks.[254-256, 269, 282, 283] Unfortunately, Fe(II)-based systems are prohibitively air sensitive for practical applications. Identifying more air-stable materials capable of N_2O activation would be a significant step towards utilizing N_2O as a green oxidant. As such, the same cluster models were used to calculate the favorability of M(IV)-oxo formation in the remainder of the M_2(dobdc) series and determine if this reactivity is unique to the Fe analogue (Appendix Table A5.5-A5.6). DFT calculations with both the trimetallic and Mg-diluted cluster model series show that, in addition to Fe_2(dobdc), M(IV)-oxo formation is thermodynamically favorable ($\Delta E_f < 0$ kJ/mol) in Mn_2(dobdc) (Figure 5.3a). Indeed, M(IV)-oxo formation is calculated to be significantly more thermodynamically favorable in Mn_2(dobdc) (−183.1 and −176.1 kJ/mol for trimetallic and Mg-diluted systems, respectively) than in Fe_2(dobdc) (−55.5 and −52.7 kJ/mol for trimetallic and Mg-diluted systems, respectively). In contrast, metal-oxo formation is endothermic in the Mg, Co, Ni, Cu, and Zn analogues, ruling out these materials as potential catalysts for N_2O activation. Precedent for this reactivity in Mn-based systems is found in manganese oxides, which catalyze the decomposition of N_2O[284] and the oxidation of 1-butene at high temperatures.[285] Likewise, Mn-substituted polyoxometalates have been shown to activate N_2O and catalyze the epoxidation of alkenes,[286, 287] and Mn-substituted zeolites catalyze N_2O decomposition as well.[288, 289]

To determine the potential viability of N_2O activation by Mn_2(dobdc), an approximate reaction coordinate for this process was modelled using the CI-NEB method to generate (Figure 5.3b). The η^1-O coordinated N_2O adduct of the Mg-diluted Mn_2(dobdc) cluster model was used as the initial state, and the Mn(IV)–oxo-containing Mg-diluted cluster was used as the final state. During N_2O activation, the Mn(IV)–oxo bond is formed and the O–N bond is broken, forming N_2

(Appendix Figure A5.3). From the initial state, the M–O bond length shrinks significantly and is matched by a substantial lengthening of the O–N bond. During this transition, the energy of the system rises sharply early on, after which it falls to roughly the energy of the final state. Likewise, a constant M–O bond length, consistent with Mn(IV)–oxo formation, was observed in the second half of the reaction coordinate, as the rest of the pathway is characterized by O–N bond elongation as unbound N_2 moves away from the cluster. The approximate transition state of the reaction is rather early, with Mn–O and N–O bond lengths of 2.00 Å and 1.39 Å, respectively (Figure 5.3c). From the difference in energy between the initial state and this approximate transition state, the kinetic barrier to N_2O activation in this model cluster was calculated to be approximately 113 kJ/mol. This barrier is comparable to the calculated activation barriers of 167 kJ/mol in the Mn-based trinuclear MOF nodes and 109 kJ/mol in the Mn-substituted polyoxometalate discussed above.[278, 287]

5.4. Conclusions

Herein, we identify features that contribute to strong binding and high uptake of N_2O at Lewis acidic, coordinatively unsaturated metal sites in MOFs. We utilize the M_2(dobdc) series as model systems to facilitate comparisons, as their general structures are related but distinguished by the ligation of the open metal sites. Using the cluster systems to computationally model the oxidation of the M_2(dobdc) series by N_2O, forming M(IV)–oxo species, we find that M–oxo formation is also thermodynamically favorable in Mn_2(dobdc) according to DFT calculations. We thus used the CI-NEB method to map a reaction coordinate for this process and determined an approximate activation barrier of 113 kJ/mol, which is higher than that calculated for Fe_2(dobdc) (94 kJ/mol). These findings suggest that Mn-based MOFs may be promising alternatives to traditionally studied Fe-based materials for N_2O activation. Overall, this work adds to the growing

body of research seeking to identify effective solid-state oxidation catalysts utilizing N_2O, in which Mn-based systems remain relatively understudied. The results reported herein will help to drive the identification and development of other effective MOF-based sorbents to mitigate destructive N_2O emissions.

Chapter 6: Conclusions and Outlook

11.1. Conclusions

In this work, we demonstrated the immense potential of SACs, particularly those incorporating codoping strategies, for optimizing catalytic performance in challenging reactions like the direct methane-to-methanol conversion and ORR. Through a synergistic combination of DFT calculations, VHTS, and ML techniques, we systematically explored the vast chemical space of codoped SAC structures and identified promising candidates exhibiting superior catalytic activity and selectivity.

In the context of direct methane-to-methanol conversion, our investigations highlighted the distinct energetics of SACs compared to TMCs and macrocyclic mimics. We observed that SACs could access metal-ligand bond distances and ligand field strengths distinct from those typically achieved by more flexible homogeneous catalysts, leading to altered reaction energetics. By strategically engineering the coordination environment through codoping in both the first and second coordination spheres, we identified promising SAC candidates along the Pareto frontier of the oxo formation and HAT energetics trade-off. Kinetic analyses further recommended two codoped SACs – an intermediate spin Fe(II) system and a low-spin Ru(II) system – as highly promising for methane-to-methanol catalysis. Our investigations revealed that codoping significantly influences the electronic and geometric properties of SACs by precisely tuning the local coordination environment around the active metal center. This ability to control the dopant type, concentration, and spatial arrangement emerges as a powerful strategy for modulating the electronic structure and catalytic behavior of SACs. Importantly, our findings demonstrate that codoping can disrupt conventional linear free energy relationships and scaling relations typically observed in molecular and heterogeneous catalysts, enabling the decoupling of key reaction steps, and offering new avenues for catalyst optimization.

For the ORR, our VHTS and ML studies identified several codoped SACs with Fe and Ru centers that outperformed conventional catalysts in terms of reaction energetics and catalytic metrics. The ML models trained on the VHTS data exhibited superior predictive accuracy compared to traditional scaling relationships, showcasing the effectiveness of integrating computational screening and machine learning for rational catalyst design and discovery.

In addition, we identify features contributing to strong N_2O binding and uptake at Lewis acidic, coordinatively unsaturated metal sites in MOFs, using the M_2(dobdc) series as model systems. Computational modeling shows M(IV)–oxo formation from N_2O oxidation is thermodynamically favorable for Mn_2(dobdc), with an activation barrier of 113 kJ/mol, higher than Fe_2(dobdc) (94 kJ/mol). This suggests Mn-based MOFs are promising for N_2O activation. Our findings add to research on identifying effective solid-state N_2O oxidation catalysts, where Mn-based systems remain understudied. The results will aid development of MOF-based sorbents to mitigate harmful N_2O emissions.

Overall, this research provides valuable fundamental insights into the factors governing the catalytic behavior of codoped SACs and establishes design principles for tailoring these catalysts for various energy conversion and storage applications. The proposed codoped SAC candidates hold great promise for overcoming the limitations of traditional noble metal catalysts and enabling more sustainable and efficient energy technologies. By harnessing the synergy of VHTS, DFT calculations, and ML techniques, this work paves the way for the rational development of advanced SAC-based catalysts, potentially ushering in a new era of high-performance, cost-effective catalytic systems for a broad range of chemical transformations.

11.2. Outlook

The findings from this doctoral research have opened exciting avenues for further exploring and leveraging the unique properties of SACs, particularly those incorporating codoping strategies. While the computational studies conducted herein have identified several promising codoped SAC candidates with superior catalytic performance for reactions like the direct methane-to-methanol conversion and ORR, experimental validation and characterization of these systems are crucial next steps.

The insights gained from this research regarding the ability of codoping to decouple key reaction steps and transcend conventional scaling relationships can be leveraged to design and optimize SACs for a wide range of other catalytic processes. Exploring codoping strategies in SACs for reactions beyond ORR and methane activation, such as CO_2 reduction, hydrogen evolution, and organic transformations, could lead to the development of highly efficient and sustainable catalytic systems for various energy and chemical applications. Additionally, the integration of VHTS, DFT calculations, and ML techniques demonstrated in this work can be further refined and expanded. The development of more accurate and transferable machine learning models, incorporating advanced featurization techniques and larger training datasets, could enhance the predictive capabilities for SAC catalysts and accelerate the discovery of novel, high-performance systems. Computational studies exploring the influence of different support materials, such as metal-organic frameworks, covalent-organic frameworks, or carbon nanotubes, on the stability and reactivity of codoped SACs could also provide valuable insights for improving the practical implementation of these catalysts in real-world applications.

Finally, the scalable synthesis and manufacturing of codoped SACs remain crucial challenges that must be addressed to realize their full potential. Collaborative efforts between

computational and experimental researchers, as well as industry partners, could lead to the development of cost-effective and environmentally friendly synthesis routes for producing high-quality codoped SAC catalysts on a larger scale. Furthermore, detailed spectroscopic and electrochemical investigations of the most promising codoped SAC candidates would provide valuable insights into their atomic-level structures, oxidation states, and reaction mechanisms under practical operating conditions. Such studies would not only corroborate the computational predictions but also facilitate a deeper understanding of the structure-property relationships governing the exceptional catalytic behavior observed in these systems.

In summary, this doctoral research has laid a solid foundation for the rational design and development of advanced SAC-based catalysts, paving the way for numerous exciting research directions and opportunities. By combining experimental and computational approaches, and fostering interdisciplinary collaborations, the potential of codoped SACs can be fully unlocked, enabling the realization of more sustainable and efficient catalytic systems for a wide range of energy and chemical transformations**.**

Appendix A1

This appendix is blank but kept to maintain appendix numbering.

Appendix A2

Contents

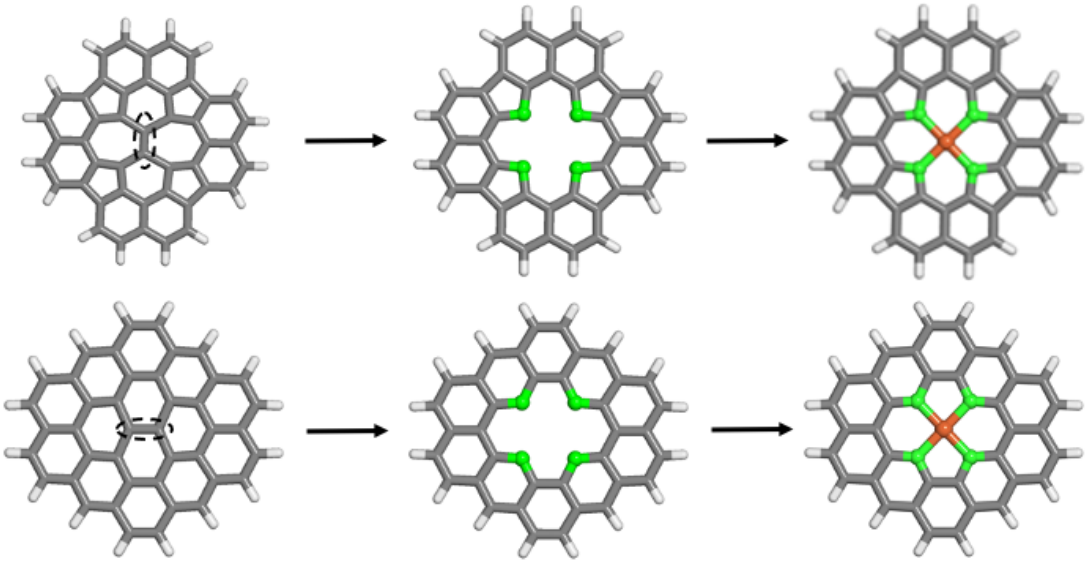

Figure A2.1. Creation of a divacancy in 5- and 6-membered ring graphene flakes (top and bottom respectively). The two carbon atoms annotated with a dashed circle are removed to create a vacancy (left). The four nearest carbon atoms to this region are replaced by dopant atoms (middle). Finally, the Fe atom is embedded in the middle of the divacancy to complete the SAC model (right).

Table S1. Total energies (in Ha) for LS and IS N-doped 5- and 6-membered ring SACs and intermediates.

system	spin state	resting state energy (Ha)	oxo energy (Ha)	hydroxyl energy (Ha)	methanol energy (Ha)
5-membered Fe-N-C	LS	-1874.8439	-1949.9342	-1950.6178	-1990.4720
	IS	-1874.9148	-1949.9961	-1950.6391	-1990.5272
6-membered Fe-N-C	LS	-1721.9736	-1797.0657	-1797.7547	-1837.6396
	IS	-1722.0352	-1797.1170	-1797.7630	-1837.5627

Table A2.2. Spin splitting energy (in kcal/mol) for LS and IS N-doped 5- and 6-membered ring SACs.

system	ΔE_{I-L} spin splitting energy (kcal/mol)			
	resting state	oxo	hydroxyl	methanol
5-membered Fe-N-C	-44.49	-38.87	-13.35	-34.68
6-membered Fe-N-C	-38.63	-32.19	-5.21	-38.63

Table A2.3. Reaction energetics (in kcal/mol) for LS and IS N-doped 5- and 6-membered ring SACs.

system	spin state	ΔE(oxo) (kcal/mol)	ΔE(HAT) (kcal/mol)	ΔE(rebound) (kcal/mol)	ΔE(release) (kcal/mol)
5-membered Fe-N-C	LS	-12.69	-3.42	-39.76	19.02
	IS	-7.07	22.09	-61.09	9.21
6-membered Fe-N-C	LS	-13.83	-6.79	-59.05	42.81
	IS	-7.30	20.17	-72.82	23.17

Table A2.4. Spin states and charges for 5- and 6-membered ring SAC models, 14-membered macrocyclic Fe complexes, and transition-metal complexes with different coordinating atoms (N, O, P and S). For all SAC models, the spin states of other catalytic intermediates are also indicated. Systems that were not explicitly studied in this work are indicated with "--". In all instances, we treat iron as Fe(II) and add it with a net charge of +2.

system	resting state spin state	metal oxo spin state	metal hydroxyl spin state	metal methanol spin state	system charge
5-membered ring SAC					
Fe-N-C	singlet	singlet	doublet	singlet	-2
Fe-O-C	singlet	singlet	doublet	singlet	+2
Fe-P-C	singlet	singlet	doublet	singlet	-2
Fe-S-C	singlet	singlet	doublet	singlet	+2
6-membered ring SAC					
Fe-N-C	singlet	singlet	doublet	singlet	+2
Fe-O-C	singlet	singlet	doublet	singlet	+2
Fe-P-C	singlet	singlet	doublet	singlet	+2
Fe-S-C	singlet	singlet	doublet	singlet	+2
14-membered macrocycle					
Fe-N-C	singlet	--	--	--	+2
Fe-O-C	singlet	--	--	--	+2
Fe-P-C	singlet	--	--	--	+2
Fe-S-C	singlet	--	--	--	+2
TMC					
Fe(pyridine)6	singlet	--	--	--	+2
Fe(4H-pyran)6	singlet	--	--	--	+2
Fe(phosphinine)6	singlet	--	--	--	+2
Fe(4H-thiopyran)6	singlet	--	--	--	+2
Fe(pyrrole)6	singlet	--	--	--	-4
Fe(furan)6	singlet	--	--	--	+2
Fe(phospholide)6	singlet	--	--	--	-4
Fe(thiophene)6	singlet	--	--	--	+2

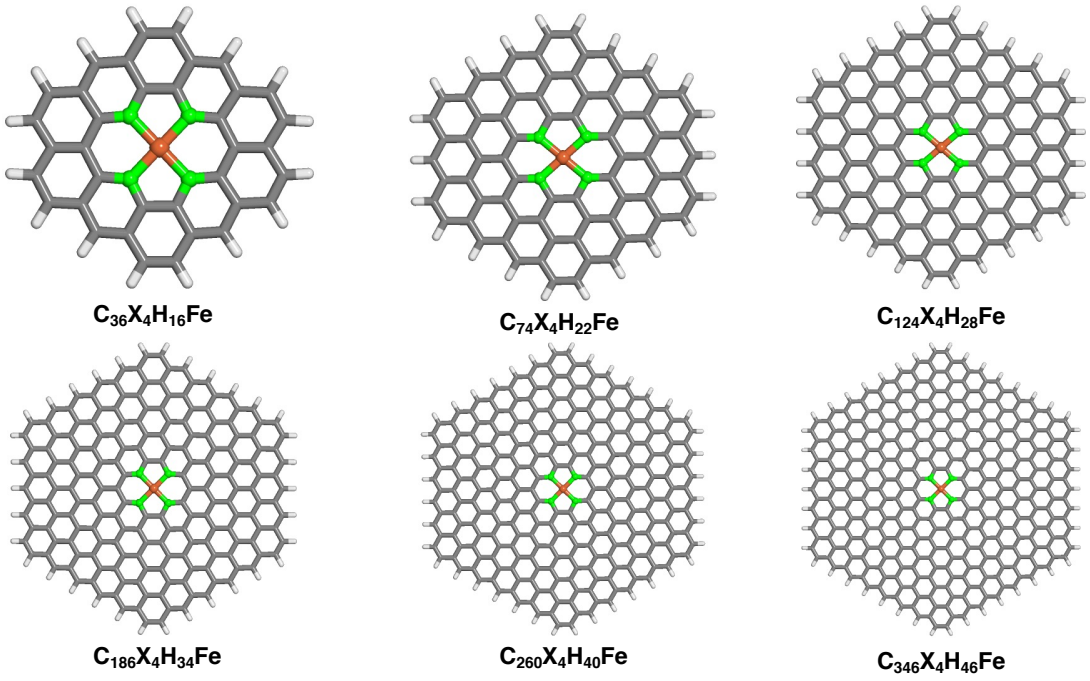

Figure A2.2. Atomic structures of increasingly large SACs with different coordinating atoms shown in green (X = N, O, P or S). The representative structures are shown in ball-and-stick representation colored as follows: Fe in brown, C in gray, and H in white.

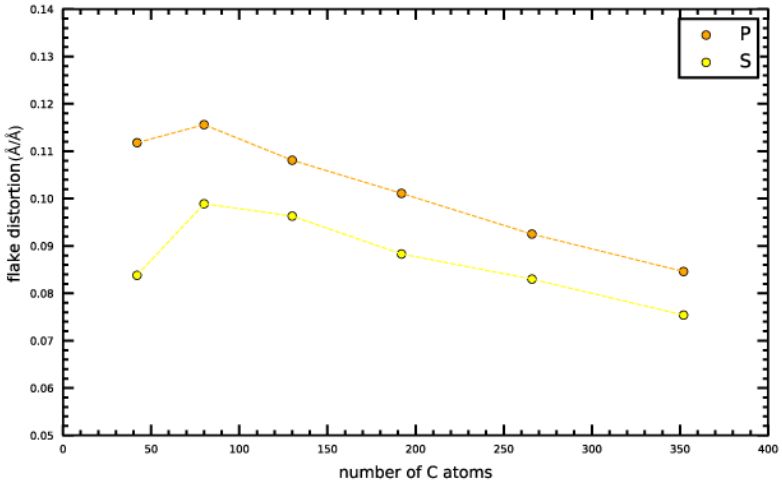

Figure A2.3. Normalized flake distortion of increasingly large P- and S-coordinating SACs with full geometry optimization. Distortion is quantified by measuring the distance of the center of mass from the initial planar SAC geometry after dividing the size of corresponding flake. Here, the number of C atoms refers to all atoms in the flake prior to insertion of the vacancy and placement of the dopants and iron.

Table A2.5. Out-of-plane distortion of increasingly large SACs with P- and S-coordinating atoms for full geometry optimization as quantified by distance of the center of mass from the initial planar SAC geometry. All distances are in units of Å.

system	out-of-plane distortion	out-of-plane distortion
	X=P	X=S
C36X4H16Fe	1.52	1.14
C74X4H22Fe	2.07	1.77
C124X4H28Fe	2.39	2.13
C186X4H34Fe	2.67	2.33
C260X4H40Fe	2.84	2.55
C346X4H46Fe	2.96	2.64

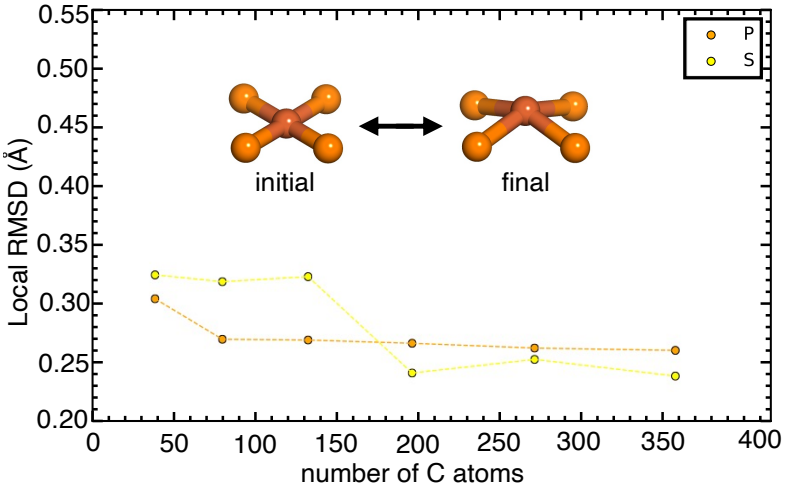

Figure A2.4. Local root-mean-square deviation (RMSD) of the metal and four coordinating atoms of increasingly large P- and S-coordinating SACs as quantified by the difference between the initial planar and the fully optimized distorted structures. Here, the number of C atoms refers to all atoms in the flake prior to insertion of the vacancy and placement of the dopants and iron.

Table A2.6. Average metal–ligand bond lengths of increasingly large SACs with different coordinating atoms (N, O, P and S). All distances are in units of Å.

system	bond length	bond length	bond length	bond length
	X=N	X=O	X=P	X=S
C36X4H16Fe	1.92	1.90	2.15	2.21
C74X4H22Fe	1.90	1.90	2.07	2.10
C124X4H28Fe	1.91	1.89	2.07	2.11
C186X4H34Fe	1.91	1.90	2.07	2.09
C260X4H40Fe	1.88	1.89	2.06	2.10
C346X4H46Fe	1.87	1.90	2.06	2.09

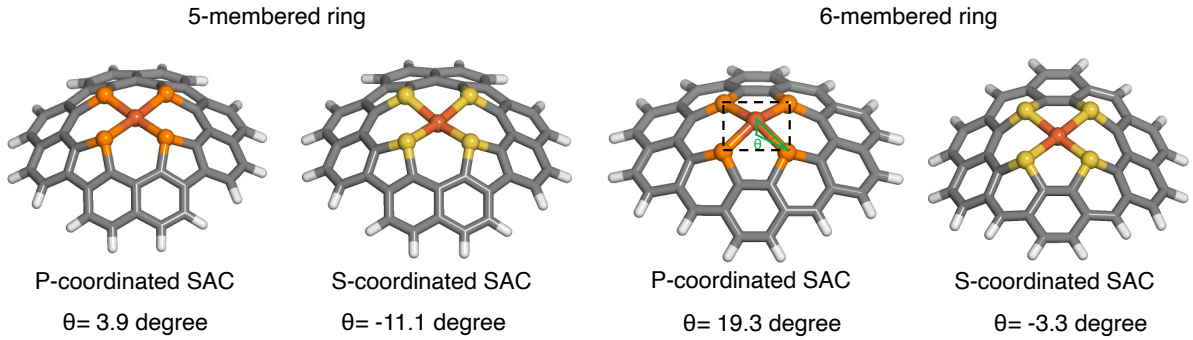

Figure A2.5. The metal dihedral angle, θ, is the dihedral angle between the Fe metal and the plane formed by any 3 of the 4 coordinating atoms. This angle is shown schematically in the P-coordinated 5-membered ring SAC. A negative value for this angle indicates that metal lies below the coordinating atom plane.

Table A2.7. Average metal–ligand bond lengths (BLs, in Å) of 5- and 6-membered SAC models, 14-membered macrocyclic complexes, and mononuclear transition-metal complex analogues with and without constraints out of the plane (i.e., the z-axis, for the 5-membered and 6-memebered SAC only). Results are shown for cases where all coordinating atoms are one of four elements (N, O, P and S). Systems that were not constrained and have no result are indicated as "--".

system	full geometry optimization average M-L BL (Å)	constrained z-axis average M-L BL (Å)
5-membered ring SAC		
Fe-N-C	1.97	1.97
Fe-O-C	1.99	1.99
Fe-P-C	2.19	1.95
Fe-S-C	2.15	1.97
6-membered ring SAC		
Fe-N-C	1.92	1.92
Fe-O-C	1.89	1.89
Fe-P-C	2.15	2.01
Fe-S-C	2.21	1.94
14-membered macrocycle		
Fe-N-C	1.84	--
Fe-O-C	1.87	--
Fe-P-C	2.09	--
Fe-S-C	2.13	--
octahedral transition metal complex		
Fe(pyridine)6	2.11	--
Fe(4H-pyran)6	2.17	--
Fe(phosphinine)6	2.25	--
Fe(4H-thiopyran)6	2.38	--
Fe(pyrrole)6	2.11	--
Fe(furan)6	2.03	--
Fe(phospholide)6	2.33	--
Fe(thiophene)6	2.38	--

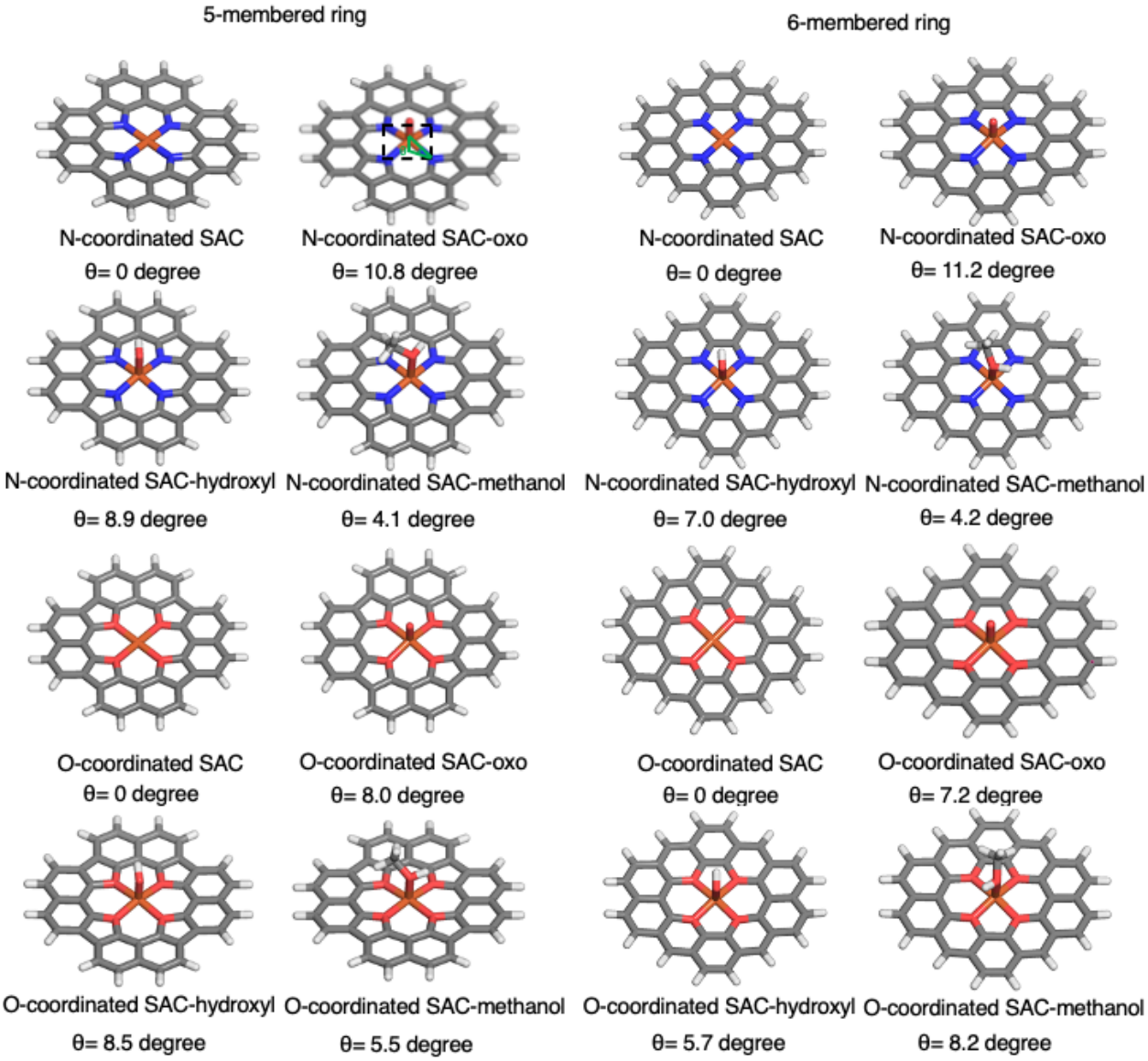

Figure A2.6. The metal dihedral angle, θ (labeled on the N-coordinating 5-membered ring oxo intermediate structure), is the dihedral angle between the Fe metal and the plane formed by 3 coordinating atoms. We annotate this angle for each intermediate (resting state, oxo, hydroxyl, methanol) in the radical rebound mechanism for conversion of methane to methanol.

Table A2.8. The average dopant–dopant distance (in Å) for 5- and 6-membered SAC models with different coordinating atoms (N, O, P and S).

system	dopant-dopant distance (Å)
5-membered ring SAC	
Fe-N-C	2.80
Fe-O-C	2.80
Fe-P-C	3.10
Fe-S-C	3.11
6-membered ring SAC	
Fe-N-C	2.63
Fe-O-C	2.78
Fe-P-C	2.95
Fe-S-C	3.13

Table A2.9. Covalent radii of X bonds (in Å). The low-spin (LS) Fe covalent radius is estimated to be 1.42 Å[290].

X	X radius (Å)
N	0.71
O	0.66
P	1.07
S	1.05

Table A2.10. Relative metal−ligand bond length, d_{rel}(Fe−X), of 5- and 6-membered ring SAC models, 14-membered macrocyclic Fe complexes and mononuclear transition-metal complex analogues with different coordinating atoms (N, O, P and S). All relative bond lengths are unitless because they are the ratios of the bond length to the sum of the covalent radii of the substituent atoms.

system	drel(Fe–X)
5-membered ring SAC	
Fe-N-C	0.93
Fe-O-C	0.95
Fe-P-C	0.88
Fe-S-C	0.87
6-membered ring SAC	
Fe-N-C	0.90
Fe-O-C	0.91
Fe-P-C	0.87
Fe-S-C	0.89
14-membered macrocycle	
Fe-N-C	0.86
Fe-O-C	0.90
Fe-P-C	0.84
Fe-S-C	0.86
octahedral transition metal complex	
Fe(pyridine)6	0.99
Fe(4H-pyran)6	1.04
Fe(phosphinine)6	0.90
Fe(4H-thiopyran)6	0.96
Fe(pyrrole)6	0.99
Fe(furan)6	0.97
Fe(phospholide)6	0.94
Fe(thiophene)6	0.96

Table A2.11. Complexation energies (in eV) of 5- and 6-membered ring SAC models and 14-membered macrocyclic Fe complexes with different coordinating atoms (N, O, P and S) and constraint conditions.

system	full optimization complexation energy (eV)	constrained z-axis complexation energy (eV)	difference between full and constrained (eV)
5-membered ring SAC			
Fe-N-C	-38.08	-38.09	0.01
Fe-O-C	-31.18	-31.18	0.00
Fe-P-C	-33.54	-32.17	-1.37
Fe-S-C	-32.63	-32.03	-0.60
6-membered ring SAC			
Fe-N-C	-37.37	-37.58	0.20
Fe-O-C	-28.60	-28.75	0.14
Fe-P-C	-33.64	-32.10	-1.54
Fe-S-C	-31.39	-29.84	-1.55
14-membered macrocycle			
Fe-N-C	-38.24	--	--
Fe-O-C	-28.10	--	--
Fe-P-C	-33.39	--	--
Fe-S-C	-29.14	--	--

Table A2.12. Comparison of Mulliken spin density on the metal for each intermediate.

system	resting state Mulliken spin density	metal oxo Mulliken spin density	metal hydroxyl Mulliken spin density	metal methanol Mulliken spin density
5-membered ring SAC				
Fe-N-C	0.00	0.00	0.989	0.00
Fe-O-C	0.00	0.00	0.814	0.00
Fe-P-C	0.00	0.00	0.975	0.00
Fe-S-C	0.00	0.00	0.893	0.00
6-membered ring SAC				
Fe-N-C	0.00	0.00	0.952	0.00
Fe-O-C	0.00	0.00	1.034	0.00
Fe-P-C	0.00	0.00	0.955	0.00
Fe-S-C	0.00	0.00	0.986	0.00

Table A2.13. The natural charges and Fe 3*d* orbital populations for 5- and 6-membered SACs with different coordinating atoms (N, O, P and S).

system	natural charge	NBO 3d orbital population
5-membered ring SACs		
Fe-N-C	0.87457	6.74
Fe-O-C	0.98444	6.64
Fe-P-C	0.35333	7.26
Fe-S-C	0.59156	7.07
6-membered ring SACs		
Fe-N-C	1.03059	6.71
Fe-O-C	0.56377	7.05
Fe-P-C	0.36083	7.24
Fe-S-C	0.58992	7.07

Table A2.14. The flake oxidation energy (in eV) (i.e., the energy for oxo formation) for 5- and 6-membered flakes with different coordinating atoms (N, O, P and S) and no metal present. The favorable oxo formation on the P-containing flake is due to formation of a m-oxo that cannot form when a metal is present. All other oxidation energies are less favorable than the equivalent metal-oxo formation.

system	flake oxidation energy (eV)
5-membered ring flakes	
N-C	-0.40
O-C	2.95
P-C	-2.61
S-C	-0.23
6-membered ring flakes	
N-C	0.52
O-C	2.50
P-C	-5.77
S-C	-0.62

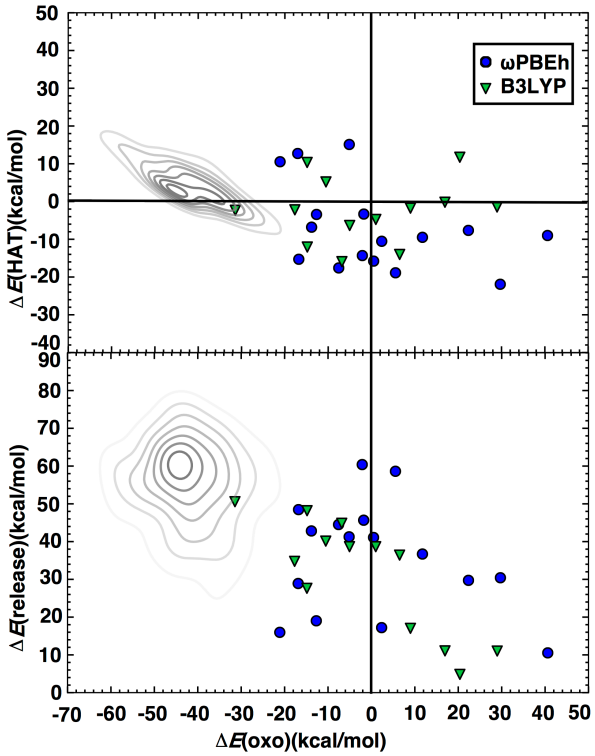

Figure A2.7. ΔE(oxo) vs ΔE(HAT) (top) and ΔE(oxo) vs ΔE(release) (bottom) reaction energies (in kcal/mol) of representative TMCs from prior work[48] computed with B3LYP/LACVP* compared to SAC reaction energies computed with ωPBEh/LACVP*, as reported in the main text, (circles) and B3LYP/LACVP* single-point energies (triangles) on the SAC models. For a subset of O-, P- and S-doped SACs in this work, the B3LYP single-point energy calculations did not converge. The TMCs from prior work are the full LS Fe(II) subset from the square pyramidal constrained (SQ) set of Ref. [48]. The TMC KDEs are colored in gray and shown as contour lines with decreasing saturation in 7 evenly spaced levels. Although a different functional is employed, the energy range sampled on SACs is comparable with changing functional.

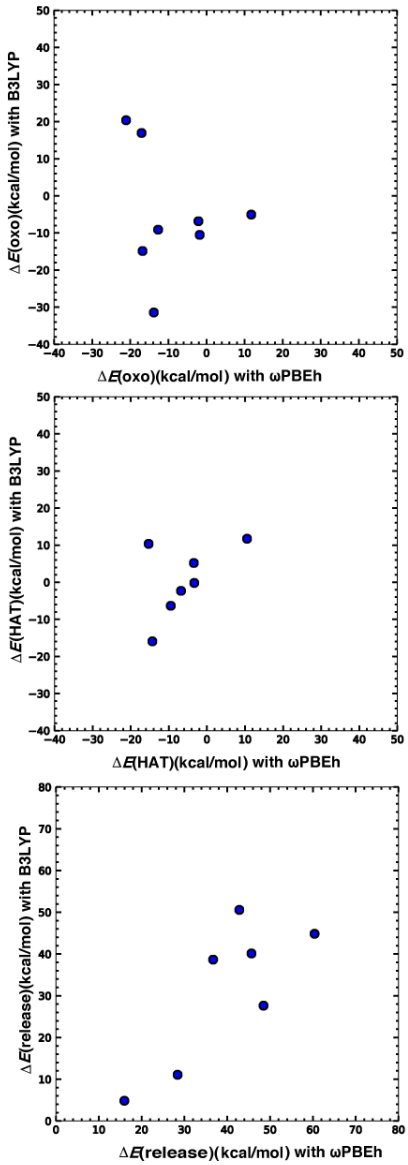

Figure A2.8. Parity plot of SAC reaction energies (ΔE(oxo), ΔE(HAT) and ΔE(release) between the ωPBEh and B3LYP functionals with the LACVP* basis set in kcal/mol. The B3LYP/LACVP* energies are evaluated as single-point energies on the ωPBEh structures.

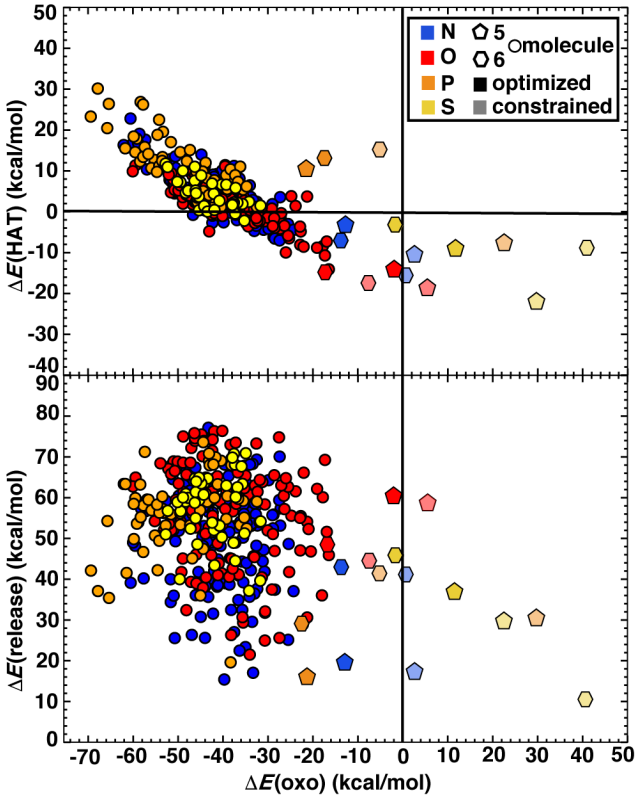

Figure A2.9. ΔE(oxo) vs ΔE(HAT) (top) and ΔE(oxo) vs ΔE(release) (bottom) reaction energies (in kcal/mol) of representative transition-metal complexes (TMCs) from prior work[48] compared to 5- (pentagon symbols) and 6-membered (hexagon symbols) ring SAC systems. Both TMCs and SACs are colored by the metal-coordinating atoms in the ligands, as indicated in inset legend. The TMCs are from the all LS Fe(II) in the square pyramidal constrained (SQ) set in Ref. [48]. For the complexes containing multiple coordinating atom elements, the symbol is colored by the heavier coordinating atom. The SACs are further distinguished by full geometry optimization (opaque) and constrained z-axis optimization (translucent).

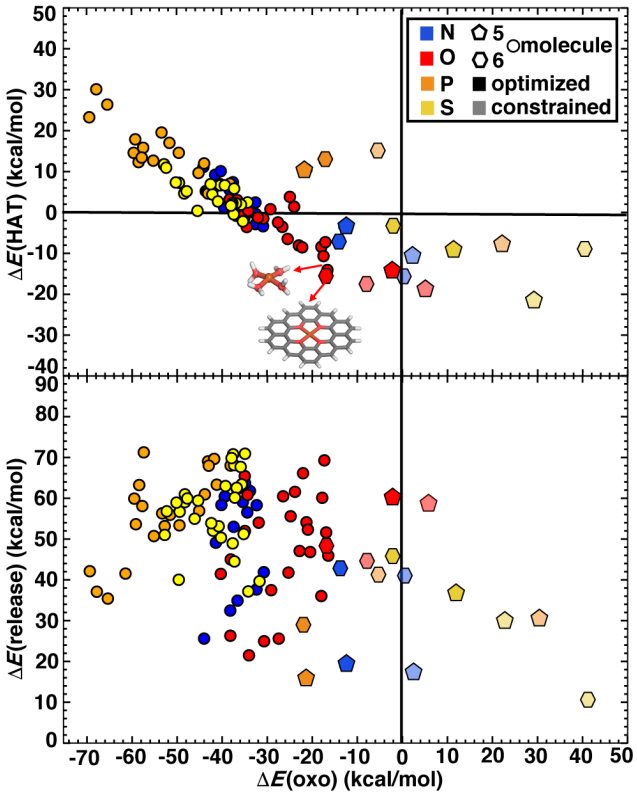

Figure A2.10. ΔE(oxo) vs ΔE(HAT) (top) and ΔE(oxo) vs ΔE(release) (bottom) reaction energies (in kcal/mol) of 80 homoleptic LS Fe(II) molecular complexes from the SQ data set in Ref.[48] relative to 5- (pentagon) and 6-membered (hexagon) ring SAC systems. Both TMCs and SACs are colored by metal-coordinating atoms as indicated in inset legend. The TMCs are from the all LS Fe(II) in the square pyramidal constrained (SQ) set in Ref. [48]. Representative structures of a O-doped 6-membered ring graphene flake SAC with bond length of 1.9 Å and Fe(II)$(OH_2)_4$-oxo with an out-of-plane distortion angle of 10° and bond length of 2.2 Å are shown in inset. The SACs are further distinguished by full geometry optimization (opaque) and constrained z-axis optimization (translucent).

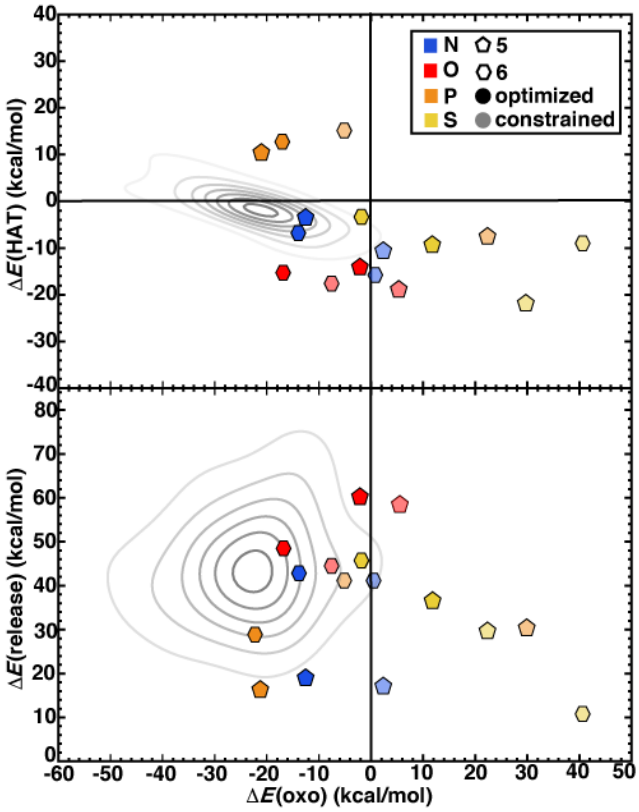

Figure A2.11. ΔE(oxo) vs ΔE(HAT) (top) and ΔE(oxo) vs ΔE(release) (bottom) reaction energies (in kcal/mol) of representative TMCs from prior work[48] compared to 5- (pentagon symbols) and 6-membered (hexagon symbols) ring SAC systems. The SACs are colored by the metal-coordinating atoms in the ligands, as indicated in inset legend. The TMCs are from the all LS Fe(II) in the tetragonal equilibrium (TE) set in Ref. [48]. The TMCs KDEs are colored in gray and shown as contour lines with decreasing saturation in 7 evenly spaced levels. The SACs are distinguished by full geometry optimization (opaque) and constrained z-axis optimization (translucent).

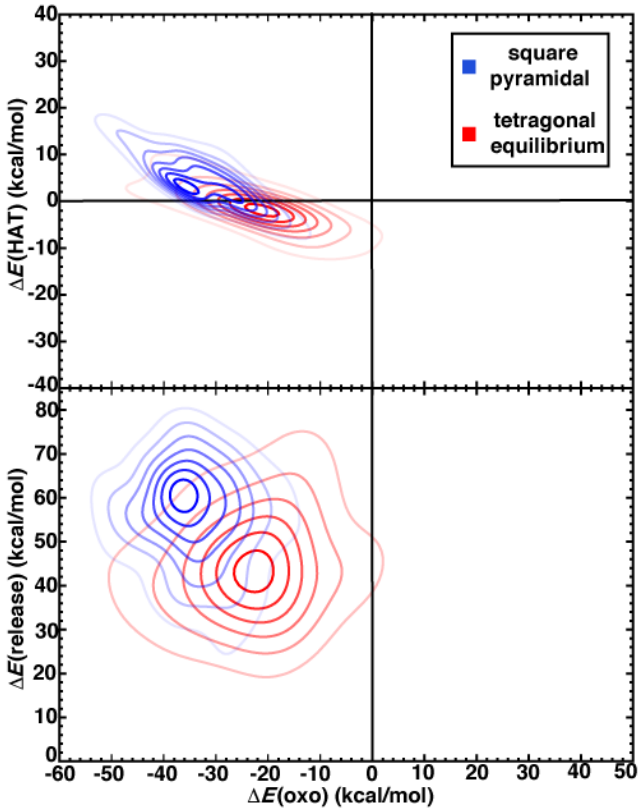

Figure A2.12. ΔE(oxo) vs ΔE(HAT) (top) and ΔE(oxo) vs ΔE(release) (bottom) reaction energies (in kcal/mol) for representative TMCs from prior work[48]. The TMCs are from the all LS Fe(II) in the tetragonal equilibrium (TE) and square pyramidal (SQ) set in Ref. [48]. The TE and SQ TMC KDEs are colored in red and blue, respectively, and shown as contour lines with decreasing saturation in 7 evenly spaced levels.

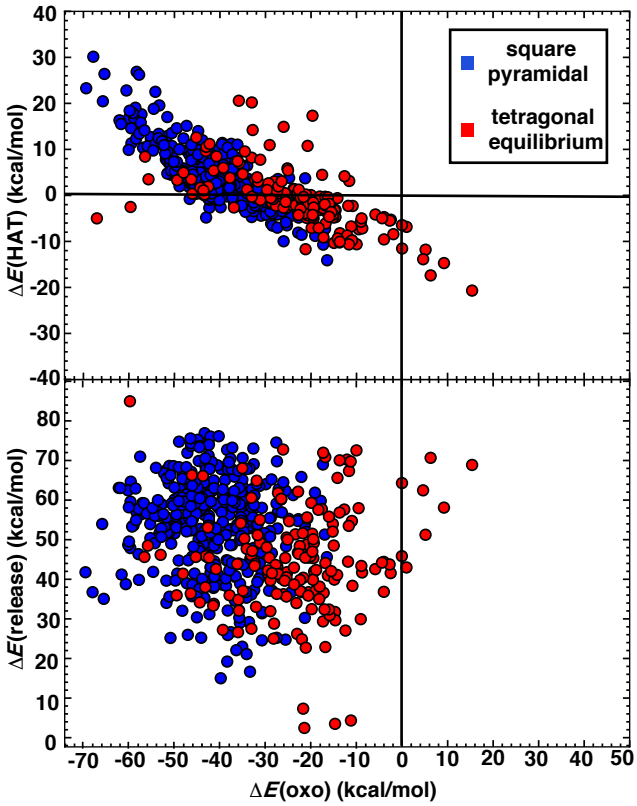

Figure A2.13. ΔE(oxo) vs ΔE(HAT) (top) and ΔE(oxo) vs ΔE(release) (bottom) reaction energies (in kcal/mol) of representative TMCs from prior work[48]. The TMCs are from the all LS Fe(II) in the tetragonal equilibrium (TE) and square pyramidal (SQ) set in Ref. [48]. The TE and SQ TMC scatters are colored in red and blue, respectively. To show structure in the data, the y-axis scale has been slightly truncated in a manner that excludes four points from LS Fe(II) complexes in the TE set (in red) with very high release values.

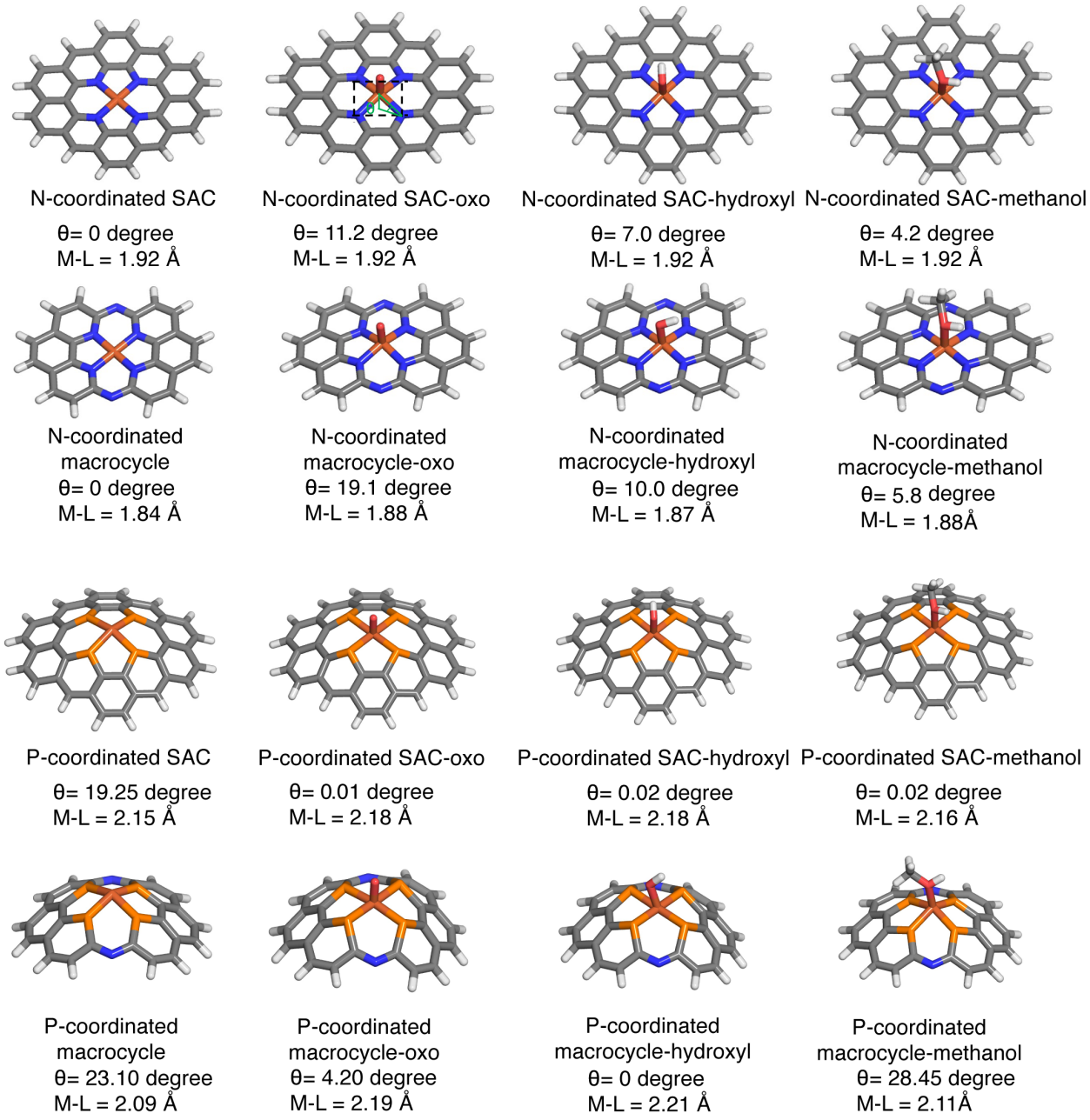

Figure A2.14. The metal dihedral angle, θ (labeled on the the N-coordinating SAC oxo intermediate structure), is the dihedral angle between the Fe metal and the plane formed by 3 coordinating atoms. We report this angle for each intermediate (resting state, oxo, hydroxo, methanol) in the radical rebound mechanism for methane-to-methanol conversion.

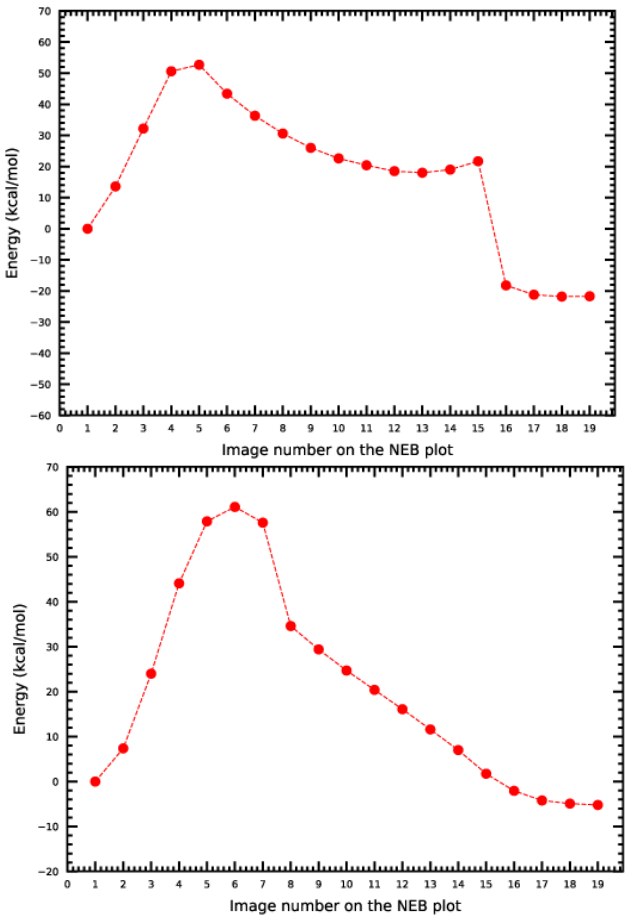

Figure A2.15. The last cycle of Nudged Elastic Band (NEB) in TeraChem (ωPBEh/LACVP*) for oxo formation putative transition states on N-doped 5- and 6-membered ring SACs (top and bottom respectively).

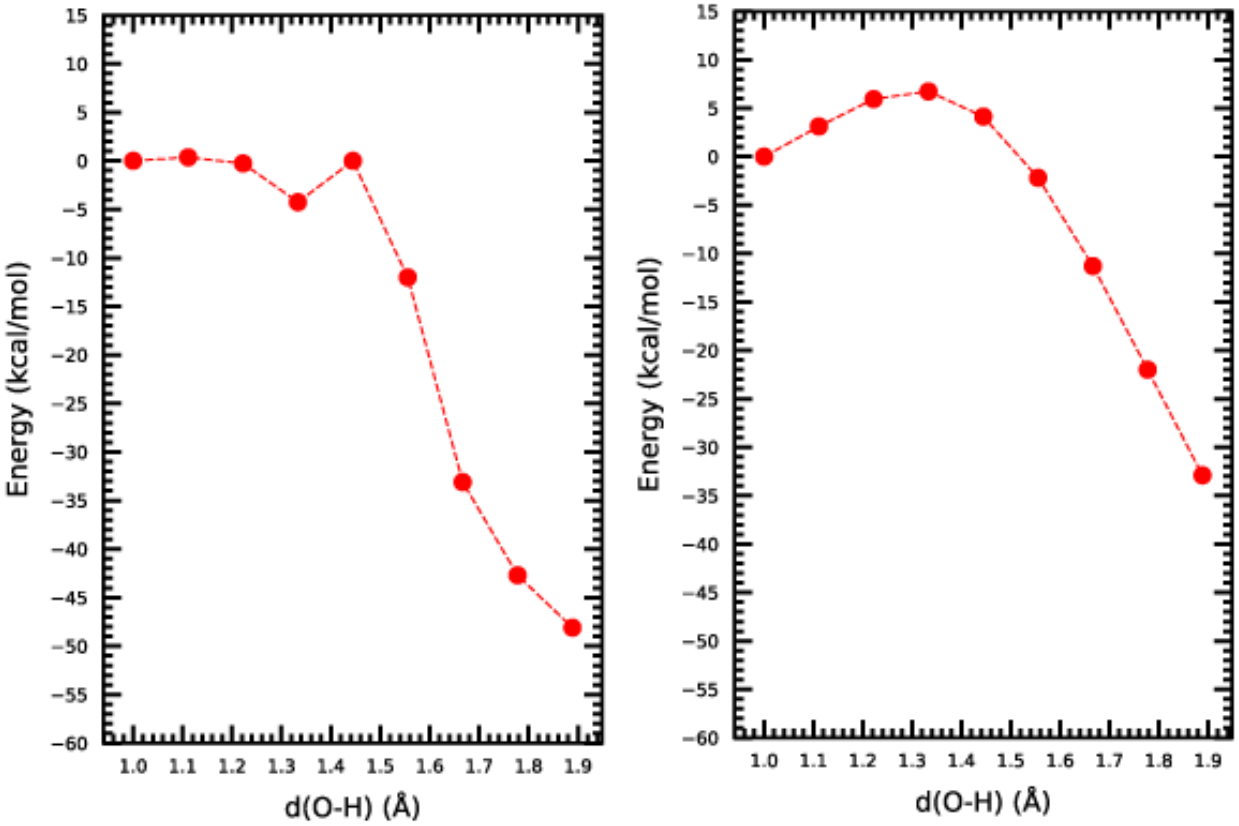

Figure A2.16. The bond length scan between O and H during hydrogen atom transfer (HAT) on N-doped 5- and 6-membered ring SACs (left and right respectively).

Appendix A3

Contents

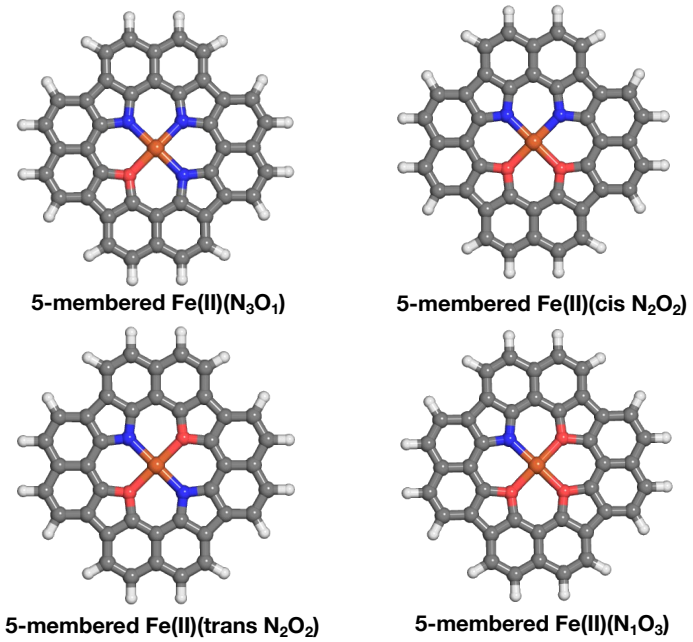

Figure A3.1. Representative structures of 5-membered ring SACs models with N and O codoped in the first coodination shell. The naming scheme for codoping in the first coordination sphere is membered ring size, metal identity, oxidation state, and the identity and number of the dopants in first coordination sphere.The structures are shown in stick representation colored as follows: Fe in brown, nitrogen in blue, oxygen in red, C in gray, and H in white.

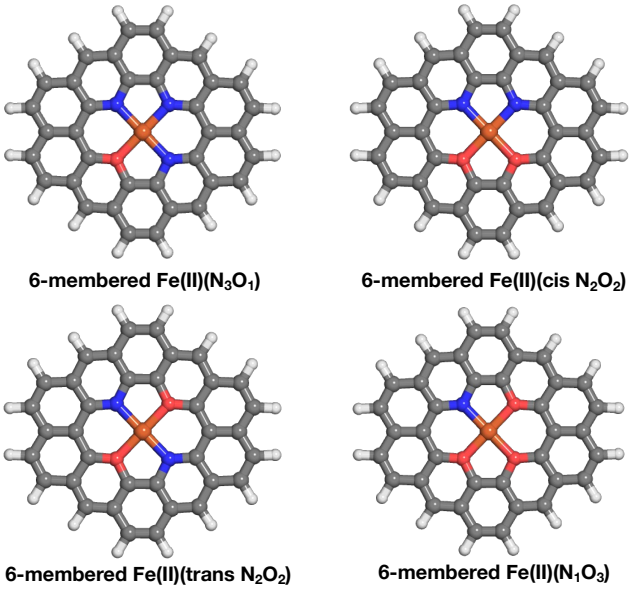

Figure A3.2. Representative structures of 6-membered ring SACs models with N and O codoped in the first coodination shell. The naming scheme for codoping in the first coordination sphere is membered ring size, metal identity, oxidation state, and the identity and number of the dopants in first coordination sphere. The structures are shown in stick representation colored as follows: Fe in brown, nitrogen in blue, oxygen in red, C in gray, and H in white.

Table A3.1. Total energies (in Ha) for LS 6-membered Fe(II)(cis N_2O_2) SAC with NNOO configuration and 6-membered Fe(II)(cis N_2O_2) SAC with NOON configuration and intermediates.

system	resting state energy (Ha)	oxo energy (Ha)	hydroxyl energy (Ha)	methanol energy (Ha)	ΔE(oxo) (kcal/mol)	ΔE(HAT) (kcal/mol)	ΔE(release) (kcal/mol)
LS 6-membered Fe(II)(cis N2O2) SAC with NNOO	-1762.7178	-1837.8262	-1838.5231	-1878.4098	-24.0653	10.8624	-59.1455
LS 6-membered Fe(II)(cis N2O2) SAC with NOON	-1762.7163	-1837.8257	-1838.5212	-1878.4078	-24.6928	11.7409	-58.8317

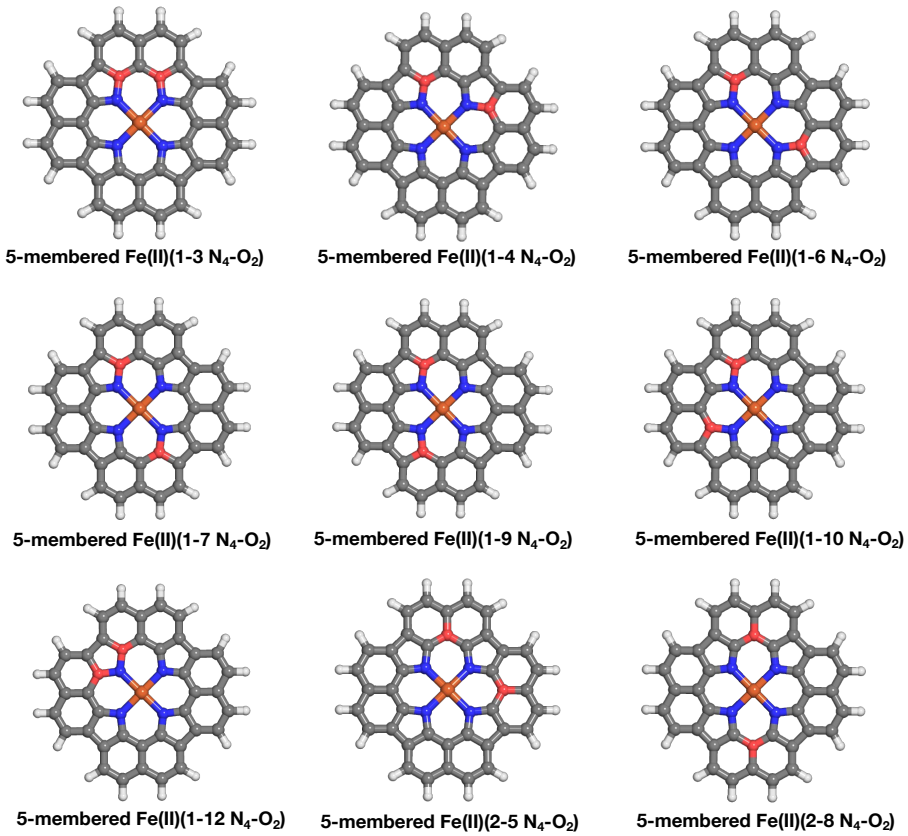

Figure A3.3. Representative structures of the 5-membered ring SACs model with two O dopants in the second coodination shell and 4 N atoms in the first coodination shell. The naming scheme for codoping in both the first and second coordination sphere is member ring size combined with metal identity, oxidation state, positions for dopant in the second coordination sphere, and the identity and number of the dopants in first and second coordination sphere. The structures are shown in stick representation colored as follows: Fe in brown, nitrogen in blue, oxygen in red, C in gray, and H in white.

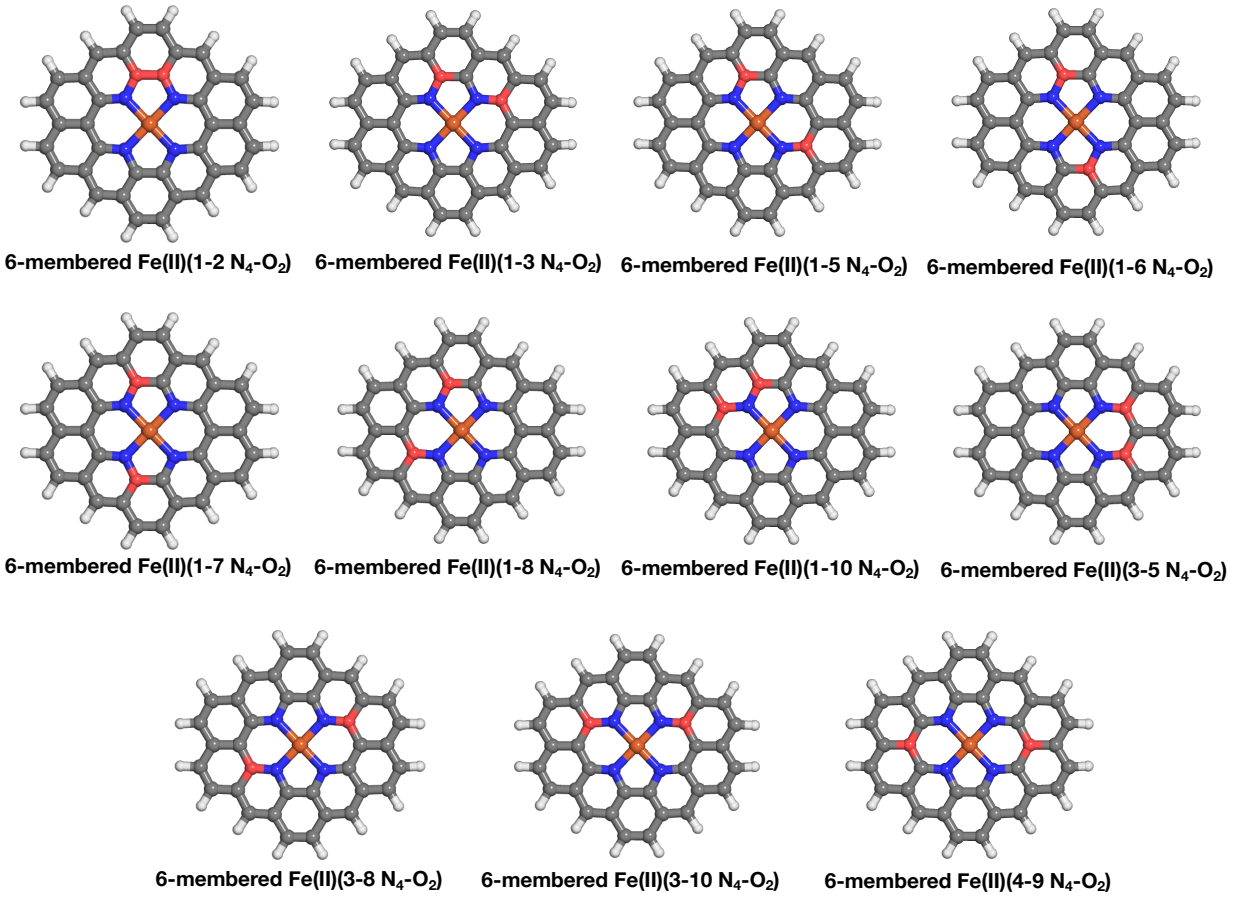

Figure A3.4. Representative structures of the 6-membered ring SACs model with two O dopants in the second coodination shell and 4 N atom in the first coodination shell. The naming scheme for codoping in both the first and second coordination sphere is member ring size combined with metal identity, oxidation state, positions for dopant in the second coordination sphere, and the identity and number of the dopants in first and second coordination sphere. The structures are shown in stick representation colored as follows: Fe in brown, nitrogen in blue, oxygen in red, C in gray, and H in white.

Table A3.2. Spin multiplicity (i.e., 2*S*+1) of each metal, oxidation state, spin state and intermediate.

system	metal oxidation state	spin state	resting state spin state	metal-oxo spin state	metal-hydroxo spin state	metal methanol spin state
Mn	(II)	LS	doublet	doublet	triplet	doublet
		IS	quartet	quartet	quintet	quartet
	(III)	LS	singlet	singlet	doublet	singlet
		IS	triplet	triplet	quartet	triplet
Fe	(II)	LS	singlet	singlet	doublet	singlet
		IS	triplet	triplet	quartet	triplet
	(III)	LS	doublet	doublet	triplet	doublet
		IS	quartet	quartet	quintet	quartet
Co	(II)	LS	doublet	doublet	triplet	doublet
		IS	quartet	quartet	quintet	quartet
	(III)	LS	singlet	singlet	doublet	singlet
		IS	triplet	triplet	quartet	triplet
Ru	(II)	LS	singlet	singlet	doublet	singlet
		IS	triplet	triplet	quartet	triplet
	(III)	LS	doublet	doublet	triplet	doublet
		IS	quartet	quartet	quintet	quartet

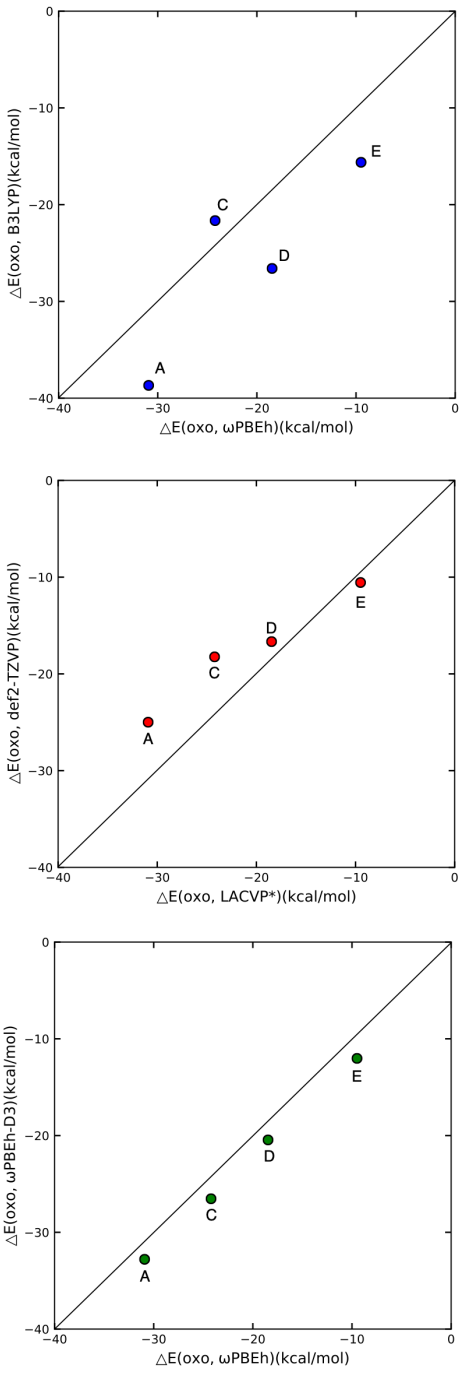

Figure A3.5. Functional sensitivity comparison of ωPBEh and B3LYP functionals (top), basis-set sensitivity comparison of LACVP* and def2-TZVP reaction energies (middle), and empirical D3 dispersion correction sensitivity comparison of ωPBEh and ωPBEh-D3 for ΔE(oxo) (in kcal/mol). All the energies are evaluated as single-point energies on the ωPBEh structures of codoped SACs: **A**: LS 5-membered Mn(III)(O_3P_1) (top left), **C**: IS 6-membered Fe(II)(cis N_2O_2) (bottom left), **D**: LS 5-membered Ru(II)(**14-16** N_4-N_2) (top right), and **E**: LS 6-membered Fe(II)(**14-15** N_4-P_2).

Table A3.3. The charges for 5- and 6-membered ring graphene flake (i.e., without the metal) with different coordinating atom configurations (N, O, P and S) in the first coordination shell.

coordinating atoms	ring types	flake charge
N_3O	5-membered ring	-3
	6-membered ring	1
N_2O_2	5-membered ring	-2
	6-membered ring	0
NO_3	5-membered ring	-1
	6-membered ring	1
N_3P	5-membered ring	-4
	6-membered ring	0
N_2P_2	5-membered ring	-4
	6-membered ring	0
NP_3	5-membered ring	-4
	6-membered ring	0
N_3S	5-membered ring	-3
	6-membered ring	1
N_2S_2	5-membered ring	-2
	6-membered ring	0
NS_3	5-membered ring	-1
	6-membered ring	1
O_3P	5-membered ring	-1
	6-membered ring	1
O_2P_2	5-membered ring	-2
	6-membered ring	0
OP_3	5-membered ring	-3
	6-membered ring	1
O_3S	5-membered ring	0
	6-membered ring	0
O_2S_2	5-membered ring	0
	6-membered ring	0
OS_3	5-membered ring	0
	6-membered ring	0
P_3S	5-membered ring	-3
	6-membered ring	1
P_2S_2	5-membered ring	-2
	6-membered ring	0
PS_3	5-membered ring	-1
	6-membered ring	1

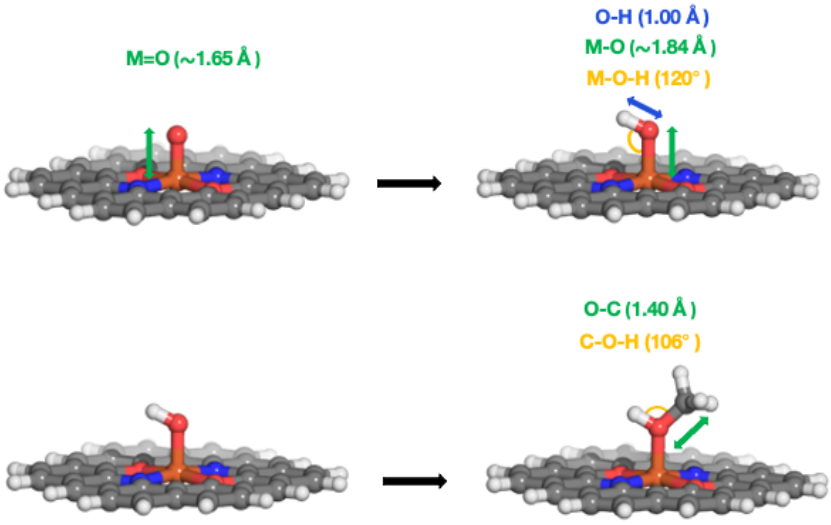

Figure A3.6. Workflow for generating a metal-hydroxo intermediate using the metal-oxo intermediate as a starting point structure (top) and generating a methanol-bound geometry by adding a methyl group to the optimized metal-hydroxo intermediates (bottom). For all metal-oxo intermediates, the M=O bond was placed at 1.65 Å. The initial geometry for all hydroxyl structures were set as follows: the M–O bond was stretched to 1.84 Å, and the hydrogen atom was placed at an M–O–H angle of 120°, 1.00 Å from the oxygen atom. For methanol-bound intermediates, the C–O–H angle was set to 106° in the initial geometry, and the C–O bond was set to 1.4 Å, which are based on the DFT-optimized structure of a methanol molecule. The structures are shown in stick representation colored as follows: Fe in brown, nitrogen in blue, oxygen in red, C in gray, and H in white.

Table A3.4. The number of intermediates that failed to converge during each step of the analysis.

system	total	convergence	bad geometry	spin contamination	spin density deviations	total successful
SACs=oxo	2048	1867	188	280	400	1180
SACs	1180	1180	-	18	20	1154
SACs-OH	1180	896	-	65	106	758
SACs-methanol	758	748	16	9	11	720

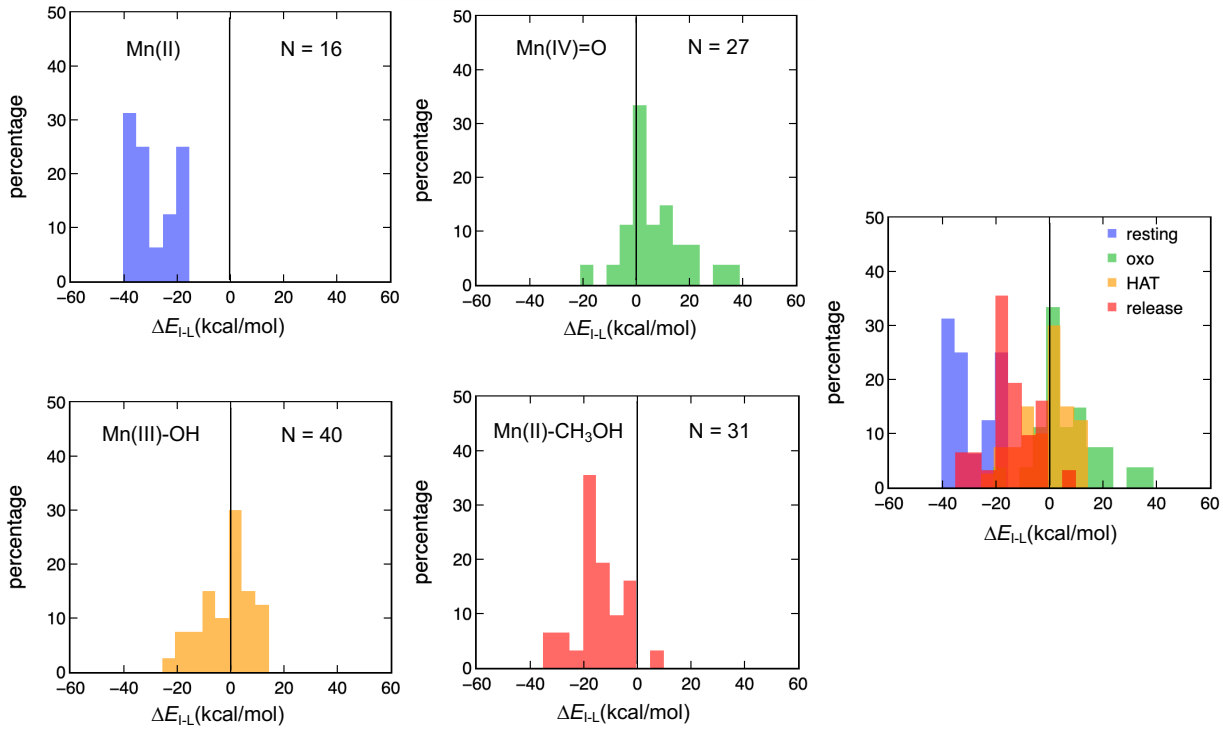

Figure A3.7. Normalized histograms (i.e., by percentage) of spin splitting energies ($\Delta E_{\text{I-L}}$, where L is a doublet and I is a quartet, in kcal/mol) for Mn(II) codoped SACs: the resting state is in blue, metal−oxo in green, metal−hydroxo complex in orange, and methanol-bound intermediate in red. The total number of intermediates used to compute each histogram is indicated in the top right corner of each panel. Zero axes are shown on all plots as solid black lines, with compounds on the left of the line favoring IS states and those on the right of the line favoring LS states. The overlap of the histograms is shown in a single pane at right.

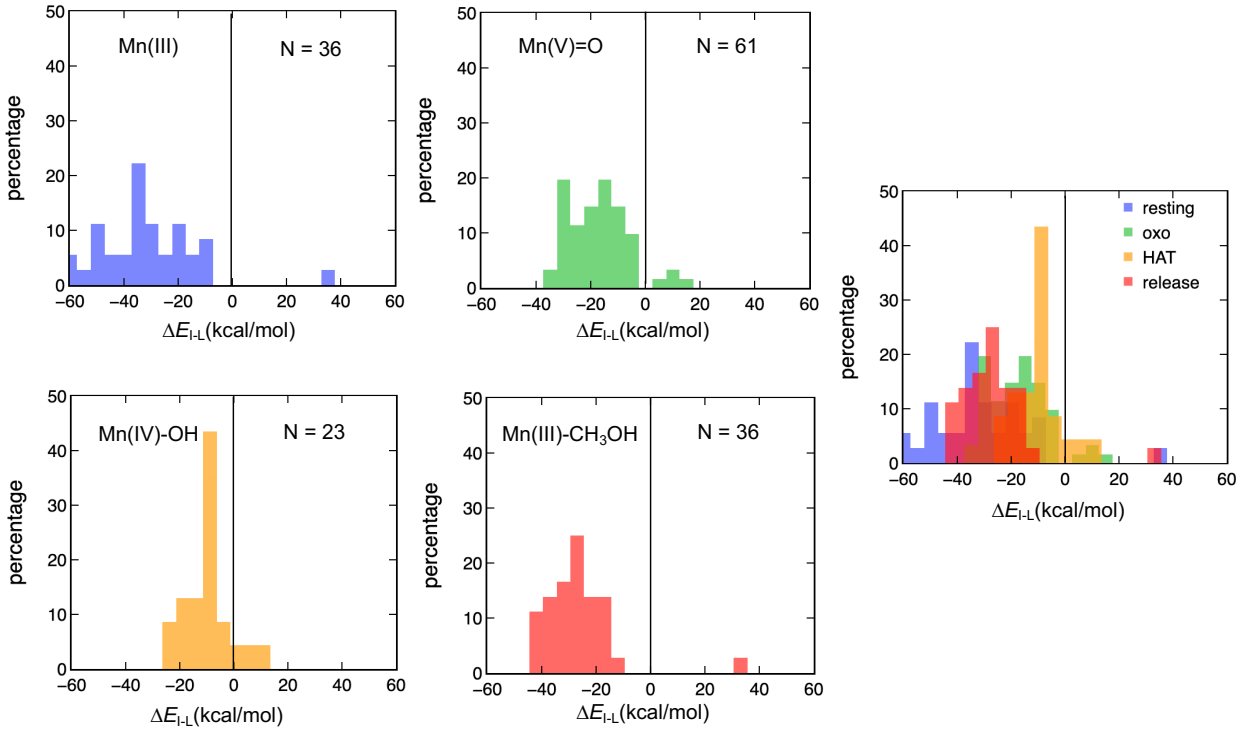

Figure A3.8. Normalized histograms (i.e., by percentage) of spin splitting energies ($\Delta E_{I\text{-}L}$, where L is a singlet and I is a triplet, in kcal/mol) for Mn(III) codoped SACs: the resting state is in blue, metal−oxo in green, metal−hydroxo complex in orange, and methanol-bound intermediate in red. The total number of intermediates used to compute each histogram is indicated in the top right corner of each panel. Zero axes are shown on all plots as solid black lines, with compounds on the left of the line favoring IS states and those on the right of the line favoring LS states. The overlap of the histograms is shown in a single pane at right.

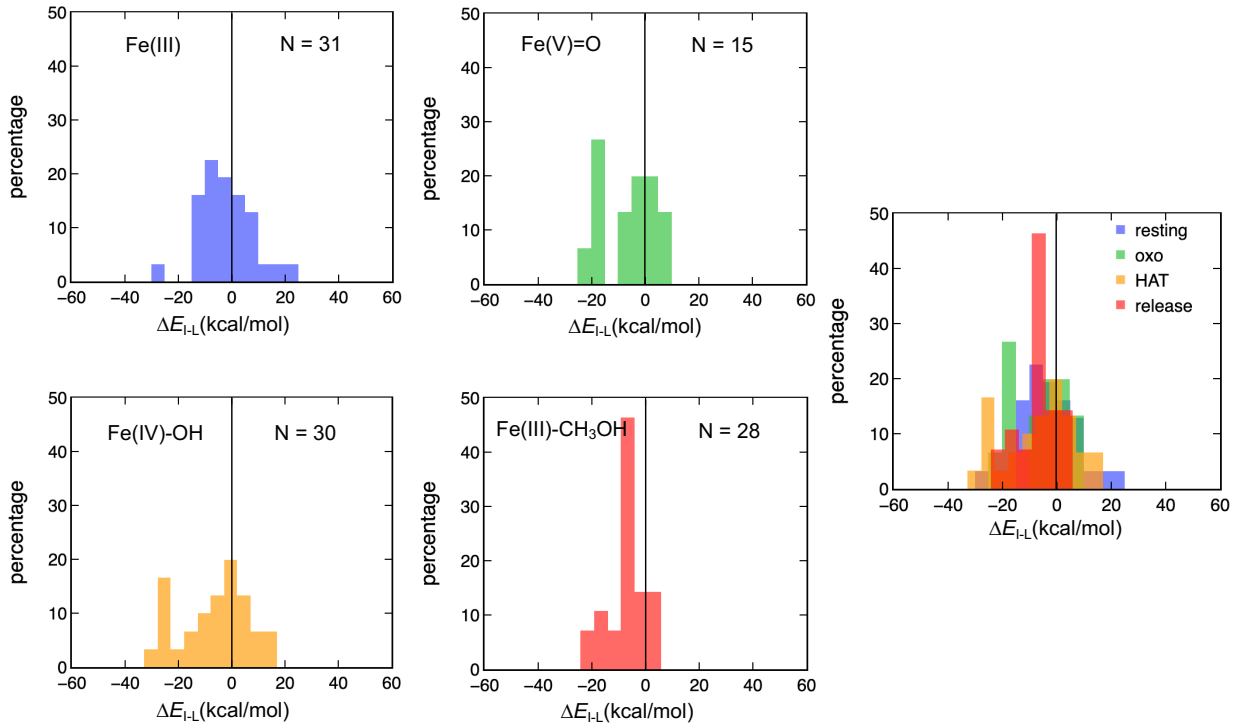

Figure A3.9. Normalized histograms (i.e., by percentage) of spin splitting energies ($\Delta E_{I\text{-}L}$, where L is a doublet and I is a quartet in kcal/mol) for Fe(III) codoped SACs: the resting state is in blue, metal−oxo in green, metal−hydroxo complex in orange, and the methanol-bound intermediate in red. The total number of intermediates used to compute each histogram is indicated in the top right corner of each panel. Zero axes are shown on all plots as solid black lines, with compounds on the left of the line favoring IS states and those on the right of the line favoring LS states. The overlap of the histograms is shown in a single pane at right.

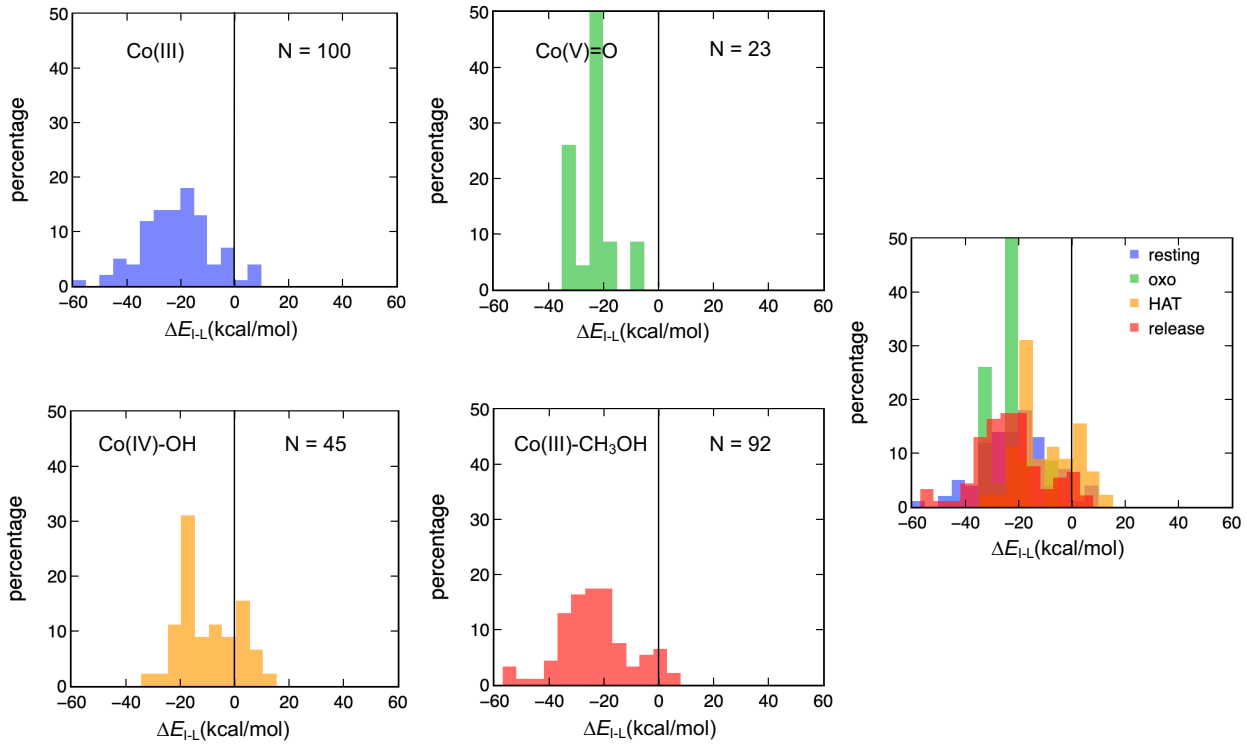

Figure A3.10. Normalized histograms (i.e., by percentage) of spin splitting energies ($\Delta E_{I\text{-}L}$, where L is a singlet and I is a triplet, in kcal/mol) for Co(III) codoped SACs: the resting state is in blue, metal−oxo in green, metal−hydroxo complex in orange, and the methanol-bound intermediate in red. The total number of intermediates used to compute each histogram is indicated in the top right corner of each panel. Zero axes are shown on all plots as solid black lines, with compounds on the left of the line favoring IS states and those on the right of the line favoring LS states. The overlap of the histograms is shown in a single pane at right.

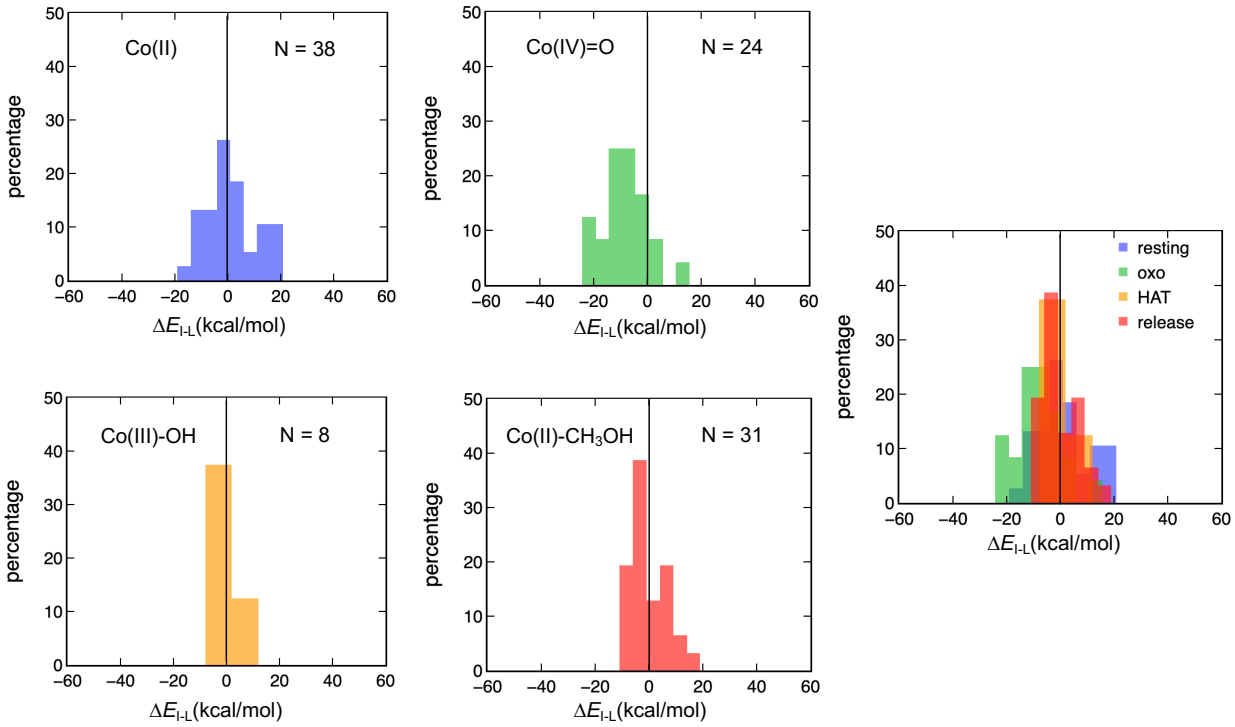

Figure A3.11. Normalized histograms (i.e., by percentage) of spin splitting energies ($\Delta E_{\text{I-L}}$, where L is a doublet and I is a quartet in kcal/mol) for Co(II) codoped SACs: the resting state is in blue, metal−oxo in green, metal−hydroxo complex in orange, and the methanol-bound intermediate in red. The total number of intermediates used to compute each histogram is indicated in the top right corner of each panel. Zero axes are shown on all plots as solid black lines, with compounds on the left of the line favoring IS states and those on the right of the line favoring LS states. The overlap of the histograms is shown in a single pane at right.

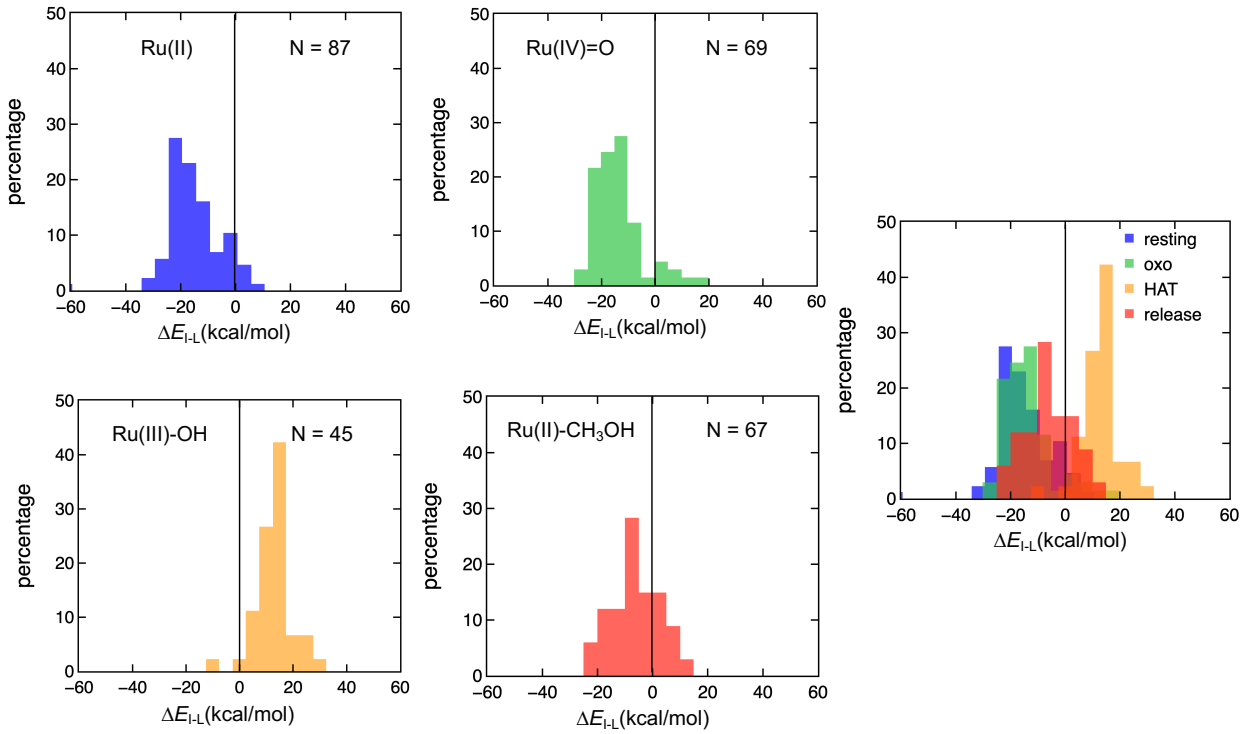

Figure A3.12. Normalized histograms (i.e., by percentage) of spin splitting energies ($\Delta E_{I\text{-}L}$, where L is a singlet and I is a triplet, in kcal/mol) for Ru(II) codoped SACs: the resting state is in blue, metal−oxo in green, metal−hydroxo complex in orange, and the methanol-bound intermediate in red. The total number of intermediates used to compute each histogram is indicated in the top right corner of each panel. Zero axes are shown on all plots as solid black lines, with compounds on the left of the line favoring IS states and those on the right of the line favoring LS states. The overlap of the histograms is shown in a single pane at right.

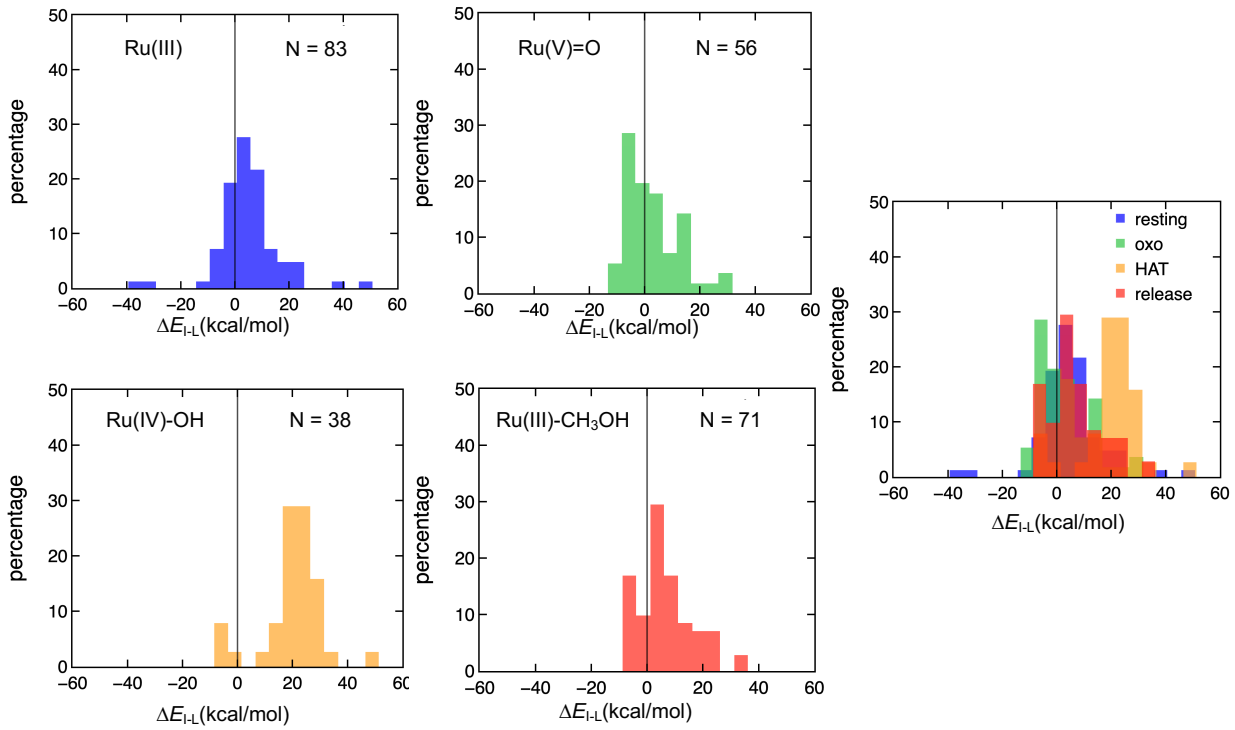

Figure A3.13. Normalized histograms (i.e., by percentage) of spin splitting energies ($\Delta E_{\text{I-L}}$, where L is a doublet and I is a quartet in kcal/mol) for Ru(III) codoped SACs: the resting state is in blue, metal−oxo in green, metal−hydroxo complex in orange, and the methanol-bound intermediate in red. The total number of intermediates used to compute each histogram is indicated in the top right corner of each panel. Zero axes are shown on all plots as solid black lines, with compounds on the left of the line favoring IS states and those on the right of the line favoring LS states. The overlap of the histograms is shown in a single pane at right.

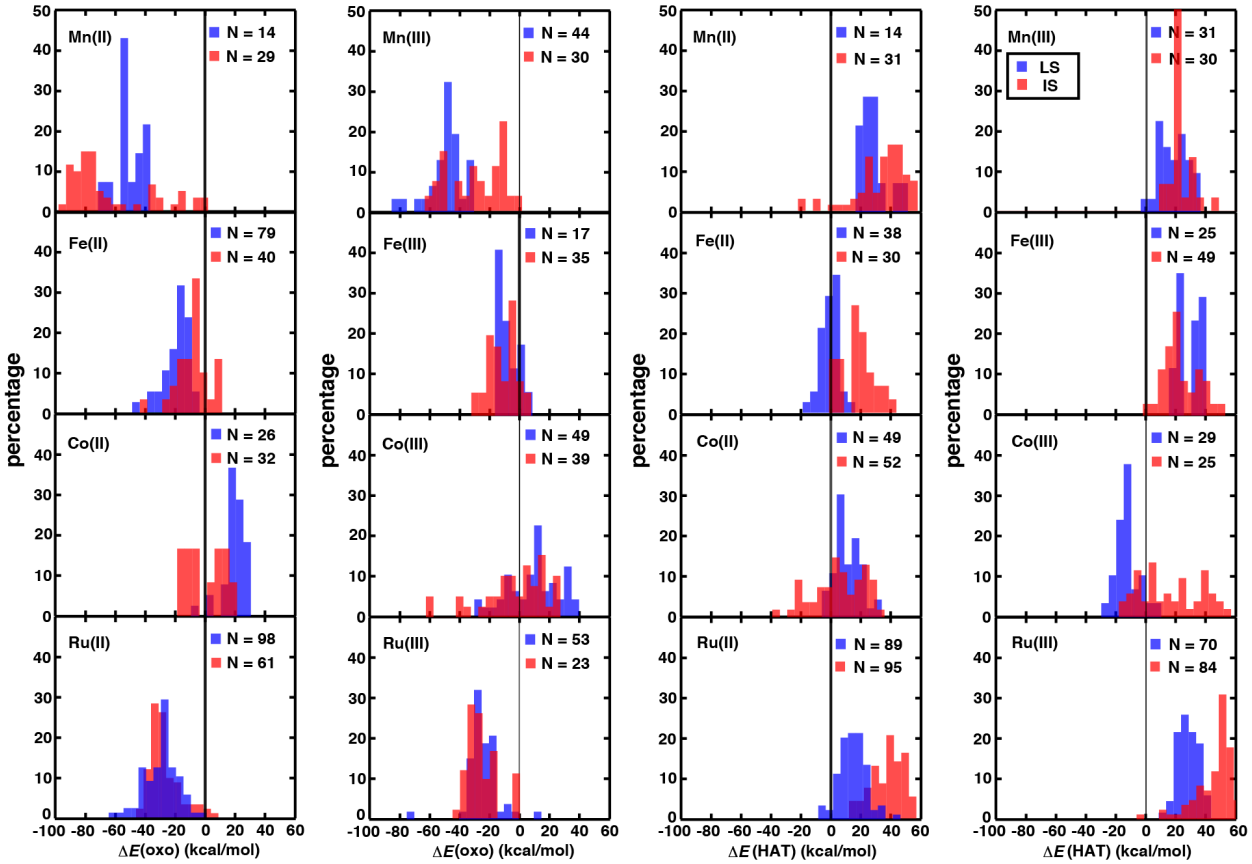

Figure A3.14. Percentage histogram (bin width: 20 kcal/mol) of ΔE(oxo) (left) and ΔE(HAT) (right) of codoped SACs grouped by metal (from top to bottom, Mn(II), Mn(III), Fe(II), Fe(III), Co(II), Co(III), Ru(II), and Ru(III)), colored by spin state (i.e., LS in blue and IS in red). The ΔE(HAT) values are for ferromagnetically coupled hydrogen atom transfer. The total number of intermediates used to compute each histogram is indicated in the top right corner of each panel. The percentage is normalized separately for each spin state. Zero axes are shown on all plots as solid black lines.

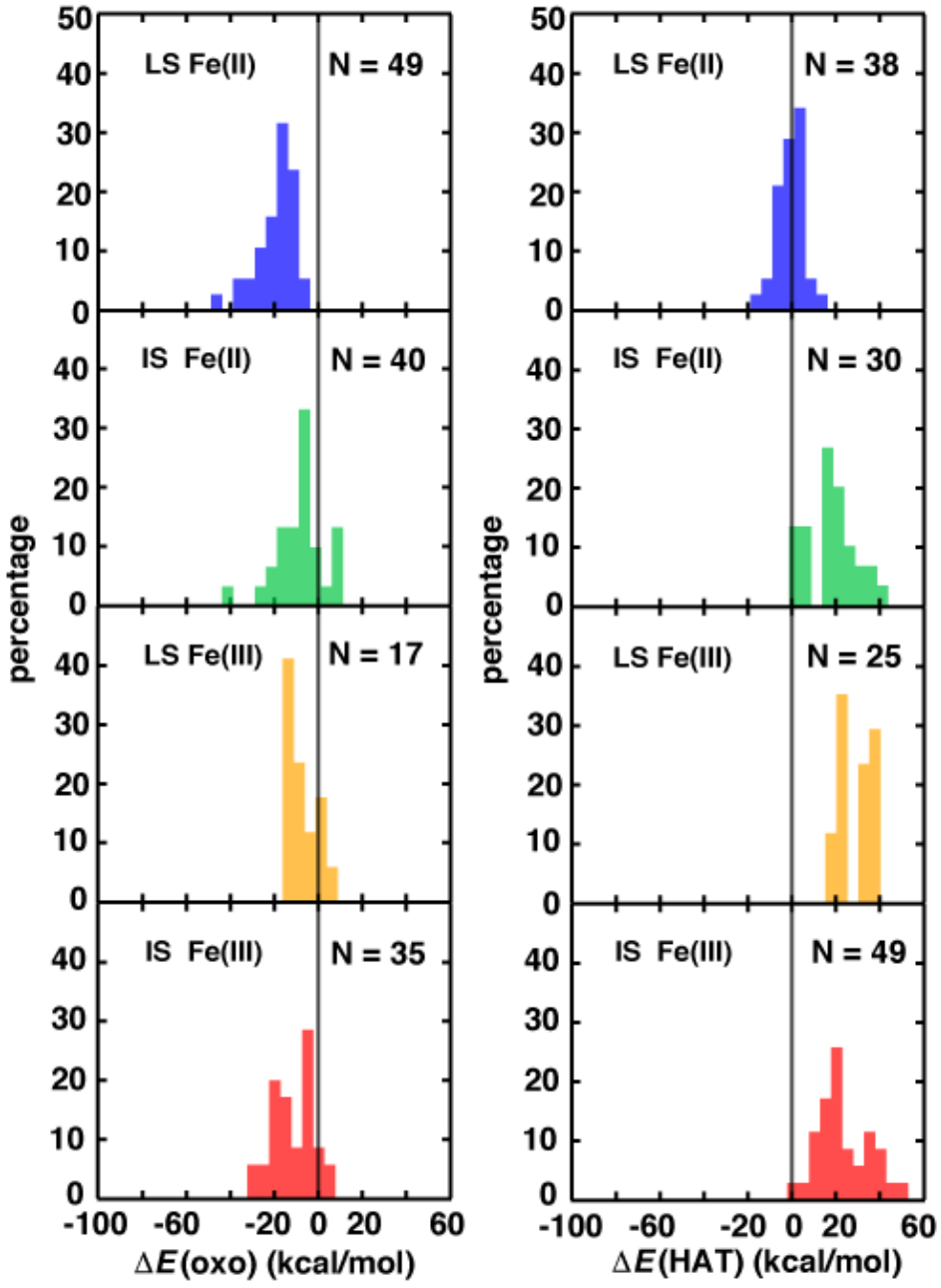

Figure A3.15. Normalized histograms (in percentage) of ΔE(oxo) (left) and ΔE(HAT) (right) (in kcal/mol) of codoped SACs grouped by metal (from top to bottom, LS Fe(II), IS Fe(II), LS Fe(III) and IS Fe(III)). The ΔE(HAT) values are for ferromagnetically-coupled HAT. The total number of intermediates used to compute each histogram is indicated in the top right corner of each panel. Zero axes are shown on all plots as solid black lines.

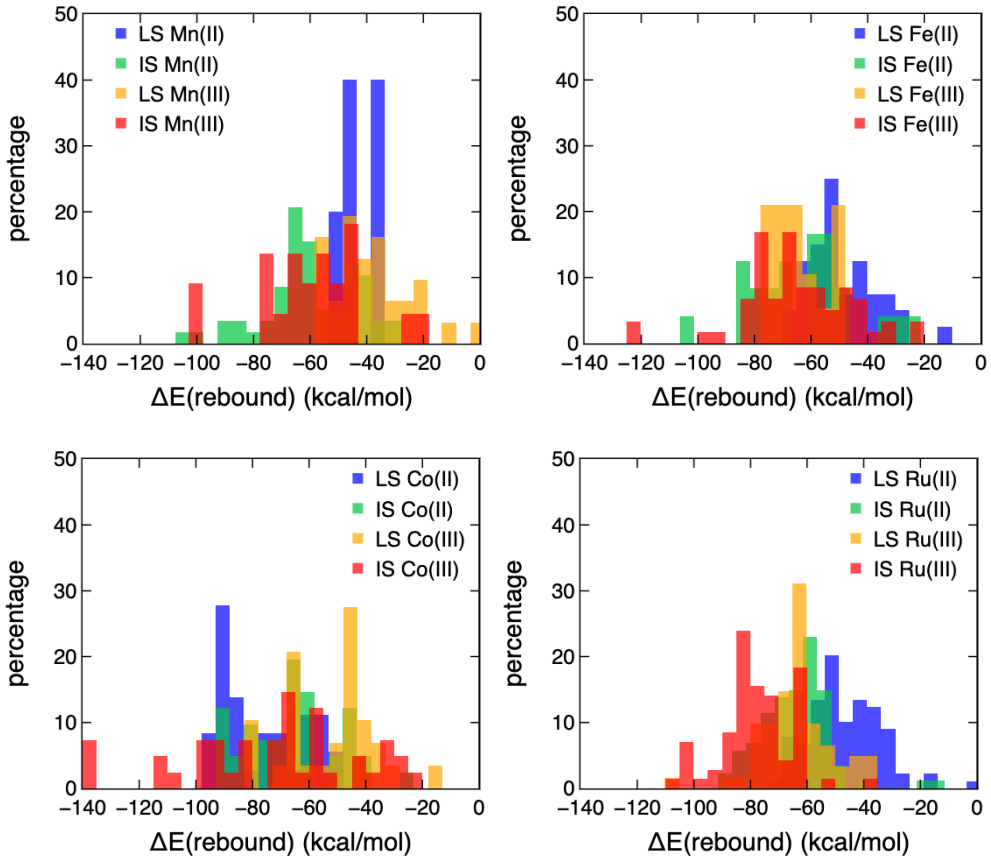

Figure A3.16. Normalized histograms (in percentage) of ΔE(rebound) (in kcal/mol) of codoped SACs grouped by metal (from top left to bottom right, Mn, Fe, Co and Ru): LS M(II) in blue, IS M(II) in green, LS M(III) in orange, and IS M(III) in red.

Table A3.5. Top 10 and bottom 10 ΔE(rebound) energetics (in kcal/mol) of codoped SACs.

Top 10 SAC system	ΔE(rebound)	Bottom 10 SAC system	ΔE(rebound)
LS 6-membered Mn(III)(8-12 N4-N2)	-1.64	IS 6-membered Mn(II)(N3O1)	-107.63
LS 5-membered Ru(II)(14-16 N4-N2)	-1.98	IS 6-membered Ru (III)(cis N2S2)	-110.05
LS 5-membered Mn(III)(6-12 N4-N2)	-10.05	IS 6-membered Co(III)(8-9 N4-N2)	-110.17
LS 5-membered Fe(II)(O1P3)	-13.46	LS 6-membered Ru(III)(6-13 N4-S2)	-110.19
LS 6-membered Co(III) (cis O2P2)	-14.61	IS 6-membered Co(III)(8-13 N4-N2)	-113.96
LS 5-membered Ru(II)(14-15 N4-N2)	-15.11	IS 6-membered Fe(III)(6-12 N4-N2)	-121.23
IS 5-membered Ru(II)(6-12 N4-S2)	-16.34	IS 6-membered Fe(III)(6-7 N4-N2)	-125.11
LS 6-membered Ru(II)(14-15 N4-S2)	-17.43	IS 6-membered Co(III)(6-10 N4-N2)	-135.80
IS 5-membered Mn(III)(6-13 N4-N2)	-19.43	IS 6-membered Co(III)(6-13 N4-N2)	-138.97
LS 6-membered Mn(III)(8-9 N4-N2)	-19.77	IS 6-membered Co(III)(6-8 N4-N2)	-139.93

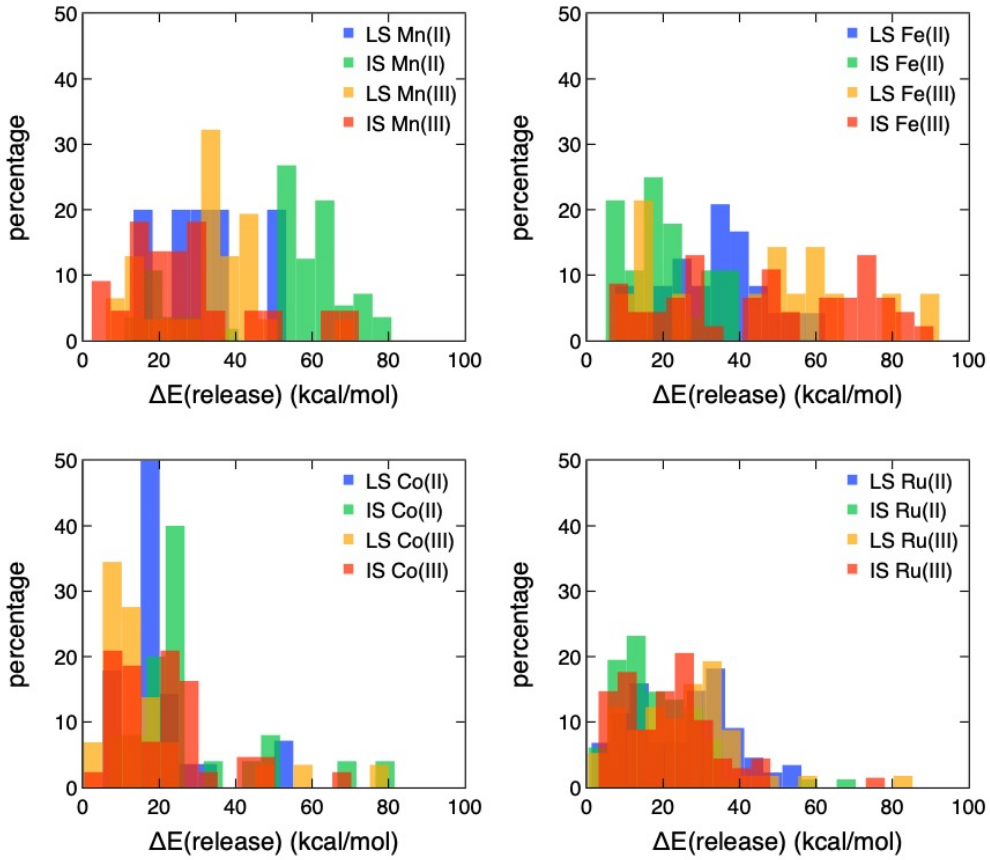

Figure A3.17. Normalized histograms (in percentage) of ΔE(release) (in kcal/mol) of codoped SACs grouped by metal (from top left to bottom right, Mn, Fe, Co and Ru): LS M(II) in blue, IS M(II) in green, LS M(III) in orange, and IS M(III) in red.

Table A3.6. Top 10 and bottom 10 ΔE(release) energetics (in kcal/mol) of codoped SACs.

Top 10 SAC system	ΔE(release)	Bottom 10 SAC system	ΔE(release)
IS 6-membered Fe(III)(O1P3)	89.73	IS 5-membered Ru(III)(14-16 N4-S2)	2.33
IS 5-membered Fe(III)(O1S3)	82.35	LS 5-membered Ru(II)(6-11 N4-N2)	2.26
LS 6-membered Ru(III)(trans O2P2)	82.03	LS 5-membered Ru(III)(6-8 N4-P2)	2.05
IS 6-membered Fe(III)(trans O2S2)	81.20	IS 6-membered Mn(III)(8-12 N4-P2)	2.01
IS 6-membered Mn(III)(P1S3)	79.50	LS 5-membered Ru(III)(trans N2P2)	1.22
IS 6-membered Co(II)(trans O2P2)	79.03	LS 5-membered Ru(II)(P3S1)	1.01
IS 6-membered Fe(II)(cis N2P2)	78.53	IS 6-membered Ru(II)(6-13 N4-N2)	0.42
IS 6-membered Fe(III)(cis O2P2)	78.42	IS 5-membered Ru(II)(6-13 N4-N2)	0.33
IS 6-membered Ru(III)(N3P1)	78.03	IS 5-membered Co(III)(trans N2P2)	0.29
LS 6-membered Fe(III)(cis N2P2)	77.44	LS 6-membered Co(III)(N1S3)	0.13

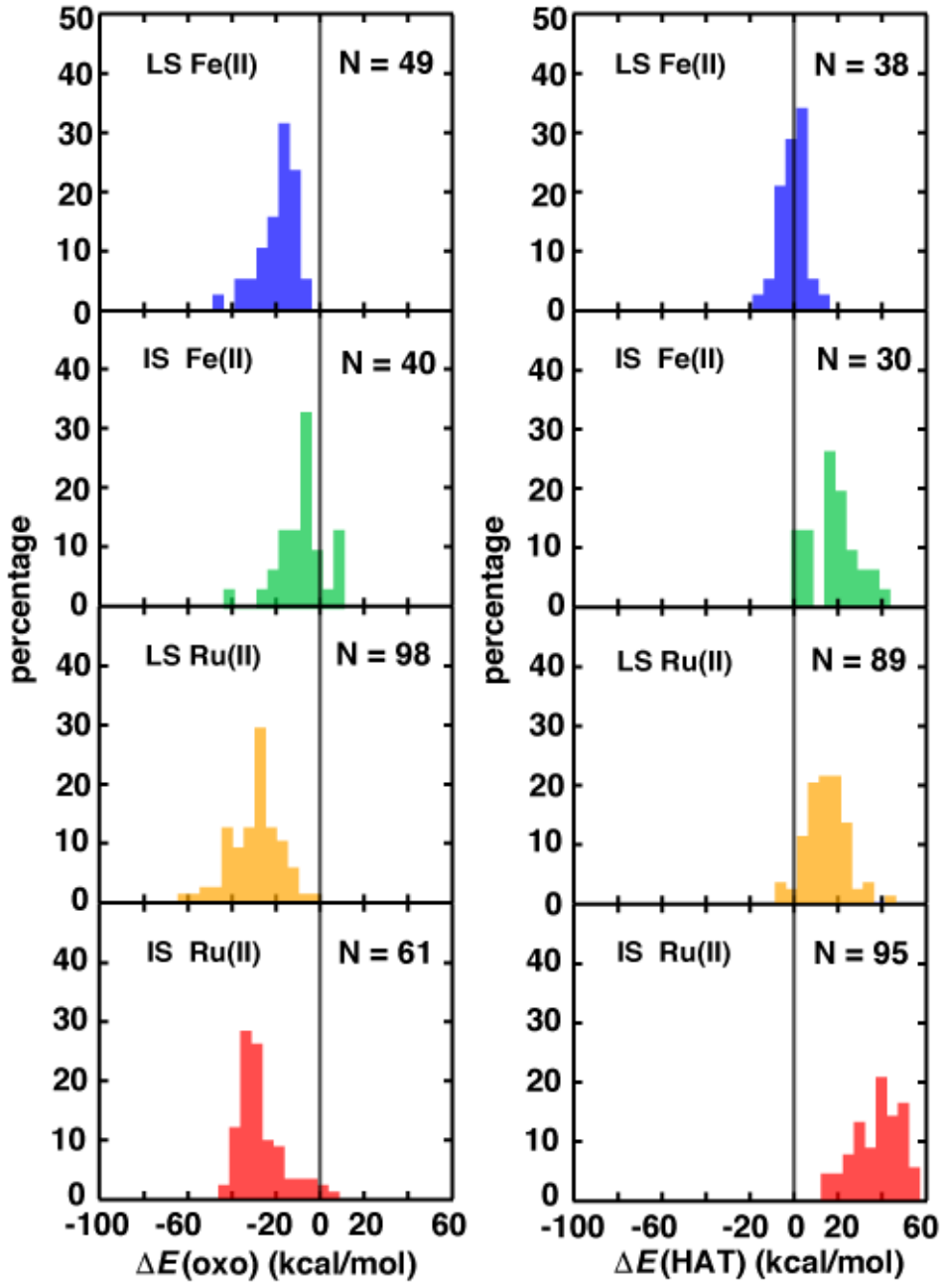

Figure A3.18. Normalized histograms (in percentage) of ΔE(oxo) (left) and ΔE(HAT) (right) (in kcal/mol) of codoped SACs grouped by metal (from top to bottom, LS Fe(II), IS Fe(II), LS Ru(II) and IS Ru(II)). The ΔE(HAT) values are for ferromagnetically coupled HAT. The total number of intermediates used to compute each histogram is indicated in the top right corner of each panel. Zero axes are shown on all plots as solid black lines.

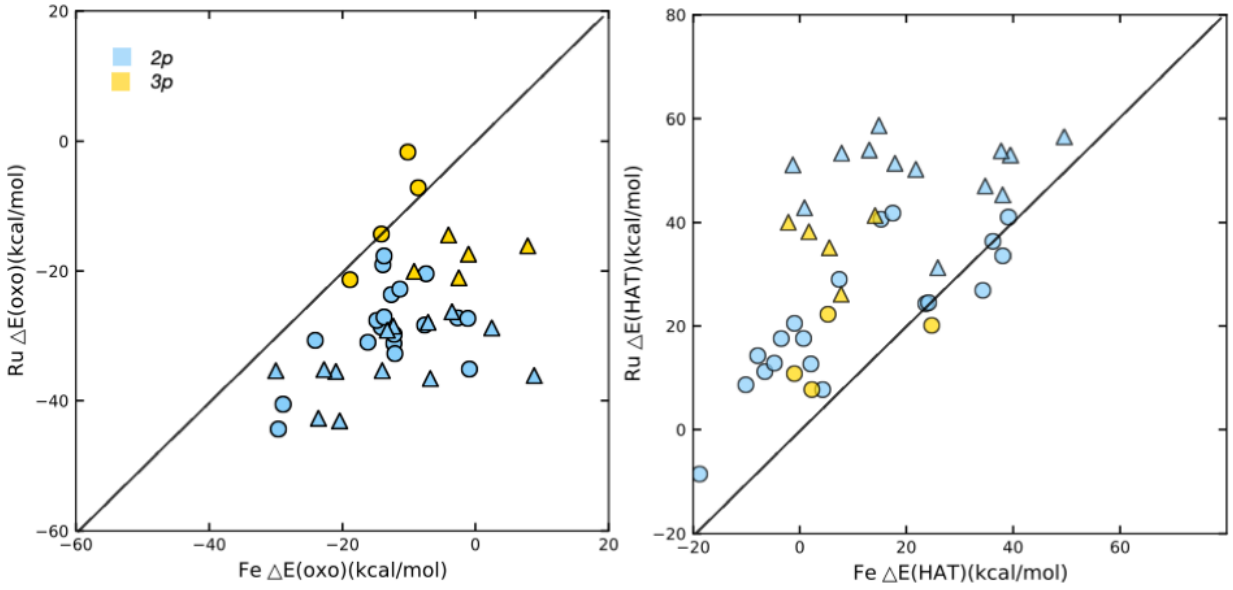

Figure A3.19. Parity plots of ΔE(oxo) (left) and ΔE(HAT) (right) reaction energies (in kcal/mol) between the codoped Fe SACs and Ru SACs under the same flake and oxidation state condition. Data are colored by coordination environment (*2p* in blue and *3p* in yellow) and are distinguished by spin state (LS in circles and IS in triangles).

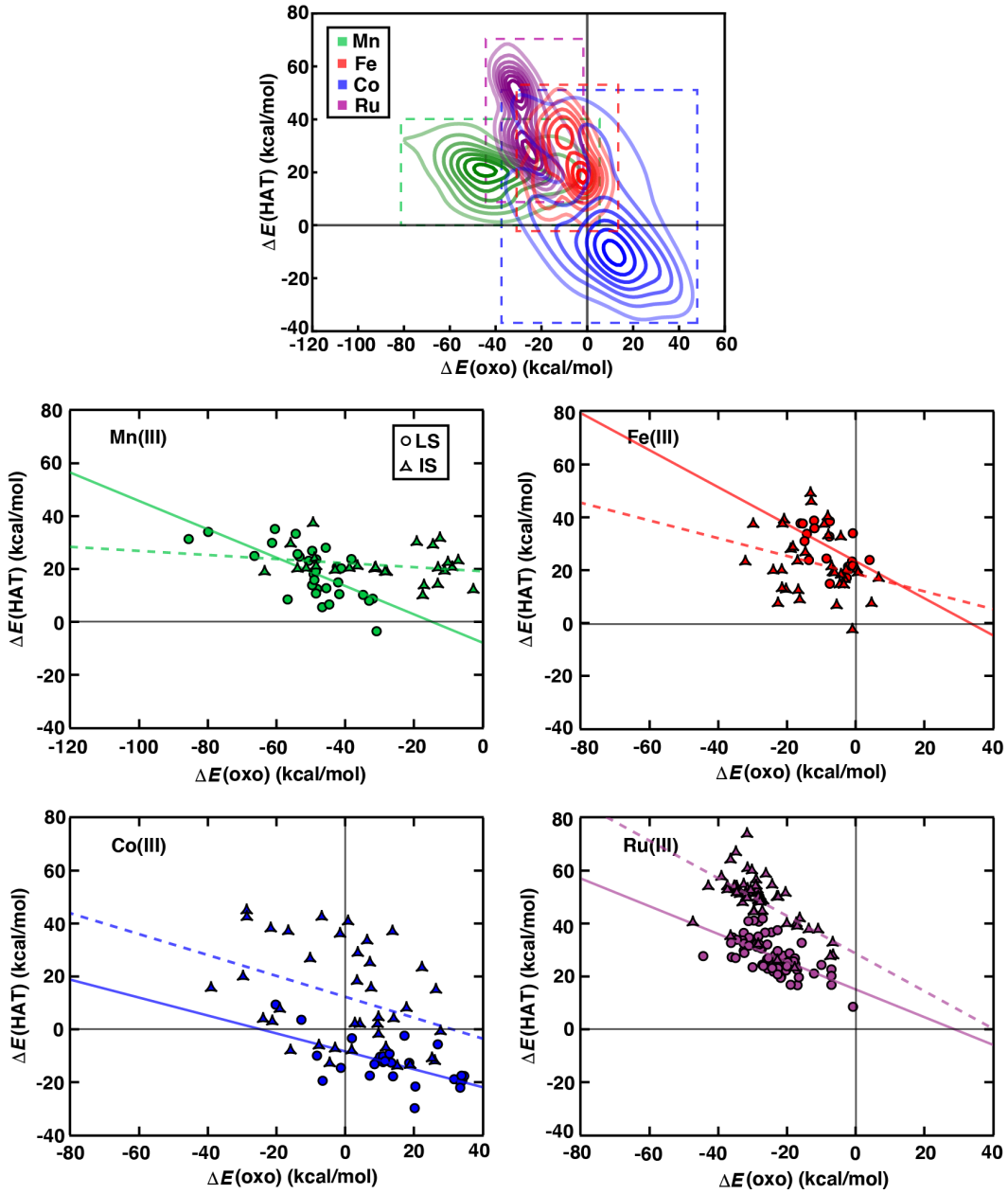

Figure A3.20. ΔE(oxo) vs. ΔE(HAT) reaction energies (in kcal/mol) of codoped M(III) SACs shown as metal-dependent Gaussian kernel density estimates (KDEs, top) and explicit data points for the Mn(III) (middle left), Fe(III) (middle, right), Co(III) (bottom, left), and Ru(III) (bottom, right) panes. The KDEs and explicit data points are colored by metal identities (Mn in green, Fe in red, Co in blue, and Ru in purple). The KDEs of the distributions for the codoped SACs are shown as contour lines with decreasing saturation in 10 evenly spaced levels. Dashed colored outlines in the KDEs correspond to the ranges of ΔE(oxo) and ΔE(HAT) of Mn, Fe, Co and Ru codoped SACs. Explicit data points are distinguished by spin state (LS in circles and IS in triangles) as indicated in the legend. The solid lines are linear fits for the LS codoped SACs and dashed lines are equivalent fits for IS systems. Zero axes are shown on all plots as solid black lines.

Table A3.7. The linear fits (in kcal/mol) and Pearson's r values of ΔE(oxo) vs. ΔE(HAT) reaction energies of codoped SACs.

system	# of data points	linear fit	r value
LS Mn(II) codoped SACs	14	y= -0.17x + 19.10	-0.19
IS Mn(II) codoped SACs	61	y= -0.28x + 17.10	-0.67
LS Fe(II) codoped SACs	38	y= -0.38x - 7.67	-0.53
IS Fe(II) codoped SACs	30	y= -0.49x + 13.96	-0.51
LS Co(II) codoped SACs	26	y= -0.12x + 7.57	-0.08
IS Co(II) codoped SACs	32	y= -0.45x + 8.78	-0.55
LS Ru(II) codoped SACs	89	y= -0.53x - 0.98	-0.64
IS Ru(II) codoped SACs	92	y= -0.59x + 23.07	-0.51
All the data	382	y= -0.38x +11.81	-0.59

Table A3.8. The ΔE(oxo) + ΔE(HAT) (in kcal/mol) of the best-trade-off catalysts (**A**-**F**) across codoped SACs dataset.

system	ΔE(oxo) (in kcal/mol)	ΔE(HAT) (in kcal/mol)	ΔE(oxo) + ΔE(HAT) (in kcal/mol)
A LS 5-membered Mn(III)(O3P1)	-30.79	-3.64	-34.43
B LS 5-membered Fe(II)(6-11 N4-S2)	-27.83	-4.57	-32.40
C IS 6-membered Fe(II)(cis N2O2)	-24.09	-10.12	-34.21
D LS 5-membered Ru(II)(14-16 N4-N2)	-18.34	-7.11	-25.45
E LS 6-membered Fe(II)(14-15 N4-P2)	-9.37	-19.50	-28.87
F LS 6-membered Co(II)-(cis O_2P_2)	-6.60	-19.57	-26.17

Table A3.9. Total energies (in Ha) for LS and IS 5-membered Mn(III)(O_3P_1) SAC and 6-membered Fe(II)(cis N_2O_2) SAC and intermediates.

system	spin state	resting state energy (Ha)	oxo energy (Ha)	hydroxyl energy (Ha)	methanol energy (Ha)
5-membered Mn(III)(O3P1) SAC	LS	-2202.3975	-2277.5167	-2278.2007	-2318.0621
	IS	-2202.4173	-2277.5645	-2278.2625	-2318.0797
6-membered Fe(II)(cis N2O2) SAC	LS	-1762.7177	-1837.8262	-1838.5205	-1878.4098
	IS	-1762.7976	-1837.8774	-1838.5847	-1878.4126

Table A3.10. Spin splitting energy (in kcal/mol) for LS and IS 5-membered Mn(III)(O_3P_1) SAC and 6-membered Fe(II)(cis N_2O_2) SAC and intermediates.

system	ΔEI-L spin splitting energy (kcal/mol)			
	resting state	oxo	hydroxyl	methanol
5-membered Mn(III)(O3P1) SAC	-12.42	-29.99	-38.78	-11.04
6-membered Fe(II)(cis N2O2) SAC	-50.13	-32.12	-40.28	-20.58

Table A3.11. Relative energetics of the catalytic cycle (referenced to the resting state, all in kcal/mol) for the full reaction coordinate of the selected best-performing, codoped SACs.

system	TS oxo	=oxo	TS HAT	-OH	CH3OH	P
A	31.31	-30.79	13.69	-34.43	-78.81	-36.86
LS 5-membered Mn(III)(O3P1)						
C	17.26	-6.08	8.66	-30.63	-45.91	-36.86
IS 6-membered Fe(II)(cis N2O2)						
D	4.01	-18.34	3.22	-25.45	-46.26	-36.86
LS 5-membered Ru(II)(14-16 N4-N2)						
E	26.70	-9.37	29.66	-23.45	-70.71	-36.86
LS 6-membered Fe(II)(14-15 N4-P2)						

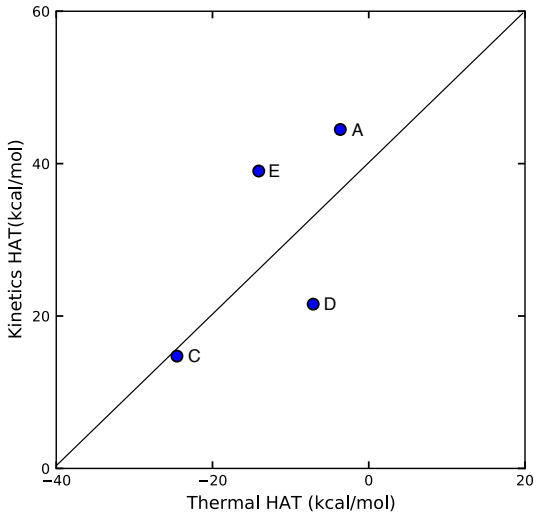

Figure A3.21. Thermodynamic reaction energetics vs. kinetic barriers of HAT step (in kcal/mol) for the selected codoped SACs.

Table A3.12. Relative energies of the TDTS and TDI (referenced to the resting state, all in kcal/mol), the energy span (δE, in kcal/mol), and corresponding turnover frequencies (TOFs, in s^{-1}) for the four selected codoped SACs. Here, the energy span is defined as if TDTS precedes TDI:

$$\delta E = E(TDTS) - E(TDI) + \Delta E_r \rightarrow TOF \approx \frac{k_B T}{h} e^{-\frac{\delta E}{RT}} \qquad (1)$$

Whereas, it's defined as if TDI precedes TDTS:

$$\delta E = E(TDTS) - E(TDI) \rightarrow TOF \approx \frac{k_B T}{h} e^{-\frac{\delta E}{RT}} \qquad (2)$$

ΔE_r is defined as -36.86 kcal/mol for methane to methanol and T is at room temperature 293 K.

system	TDTS	TDI	δE	TOF
A LS 5-membered Mn(III)(O3P1)	31.31	-78.81	73.26	1.11 x 10-42
C IS 6-membered Fe(II)(cis N2O2)	17.26	-45.91	26.31	1.34 x 10-7
D LS 5-membered Ru(II)(14-16 N4-N2)	4.01	-46.26	21.56	4.79 x 10-4
E LS 6-membered Fe(II)(**14-15** N_4-P_2)	26.70	-70.71	60.55	3.49 x 10-33

Appendix A4

Contents

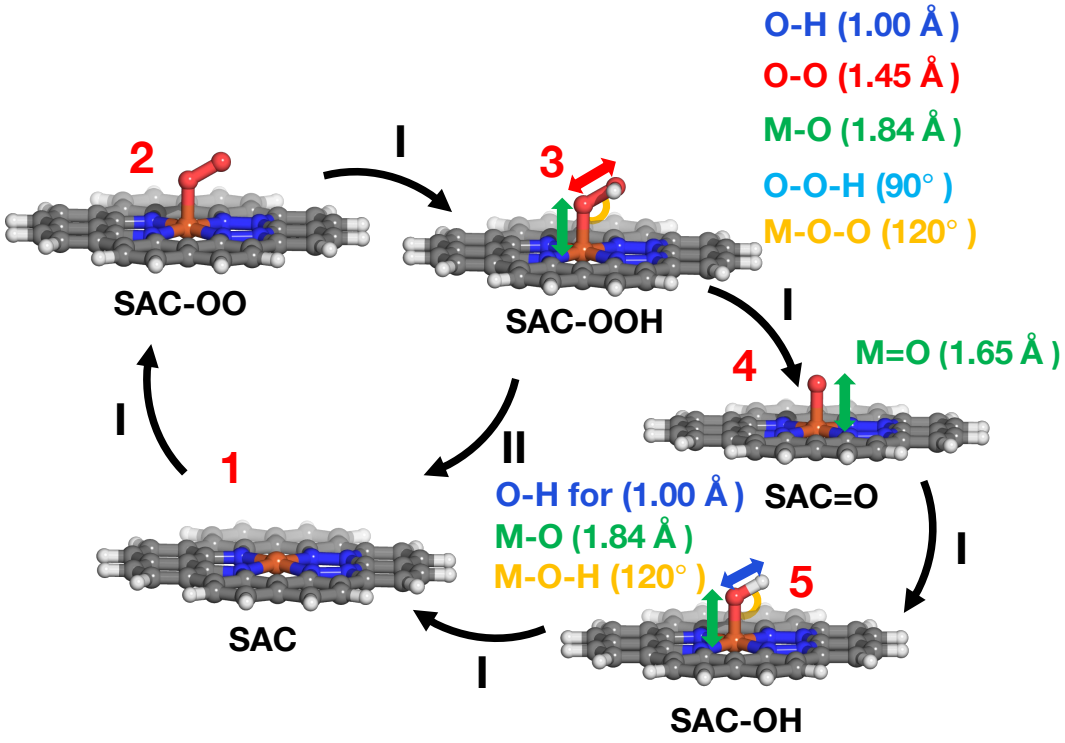

Figure A4.1 Workflow for generating a metal-hydroxo intermediate (**3**) using the optimized metal-oxo intermediate as a starting point structure (**4**) and generating a metal-superhydroxo intermediate (**5**) by adding a hydroxyl group to the optimized metal-oxo intermediates (**4**). For all metal-oxo intermediates, the M=O bond was placed at 1.65 Å. The initial geometry for all hydroxyl structures were set as follows: the M–O bond was stretched to 1.84 Å, and the hydrogen atom was placed at an M–O–H angle of 120° with 1.00 Å from the oxygen atom. For metal-superhydroxo intermediate, the M–O–O angle was set to 120° in the initial geometry, the O–O–H angle was set to 90° in the initial geometry, the M–O bond was set to 1.84 Å, the O–O bond was set to 1.45 Å, and the O–H bond was set to 1.00 Å. The structures are shown in stick representation colored as follows: Fe in brown, nitrogen in blue, oxygen in red, C in gray, and H in white.

Table A4.1 Total number of structures of converged SACs=oxo for LS and IS for both the Fe(II/III) and Ru(II/III) systems. All systems start with 128 distinct initial geometries, as done in prior work[106]. The discarded structures are the result of calculations failing to converge or pass quality checks described in the main text.

spin and oxidation state	number converged	
	Fe	Ru
LS M(II)	128	127
IS M(II)	84	125
LS M(III)	102	123
IS M(III)	98	122

Table 4.2 Spin multiplicity (i.e., 2*S*+1) of each metal, oxidation state, spin state and intermediate.

system	metal oxidation state	spin state	resting state	metal-oxo	metal-hydroxo	metal-superoxo	metal-superhydroxo
Fe	(II)	LS	singlet	singlet	doublet	singlet	doublet
		IS	triplet	triplet	quartet	triplet	quartet
	(III)	LS	doublet	doublet	triplet	doublet	triplet
		IS	quartet	quartet	quintet	quartet	quintet
Ru	(II)	LS	singlet	singlet	doublet	singlet	doublet
		IS	triplet	triplet	quartet	triplet	quartet
	(III)	LS	doublet	doublet	triplet	doublet	triplet
		IS	quartet	quartet	quintet	quartet	quintet

Table 4.3 The linear fits, Pearson's r values and MAE (in kcal/mol) of ΔE(O) vs. ΔE(OOH) and ΔE(O) vs. ΔE(OH) reaction energies of codoped SACs.

system	reaction energies	linear fit	r value	MAE
LS Fe(II) codoped SACs	ΔE(O) vs. ΔE(OOH)	y= 0.38x + 28.06	0.56	5.01
IS Fe(II) codoped SACs		y= 1.00x + 25.37	0.79	6.36
LS Ru(II) codoped SACs		y= 0.53x + 32.12	0.67	6.36
IS Ru(II) codoped SACs		y= 0.36x + 67.96	0.51	6.51
LS Fe(II) codoped SACs	ΔE(O) vs. ΔE(OH)	y= 0.42x – 35.49	0.70	3.76
IS Fe(II) codoped SACs		y= 0.93x – 43.44	0.55	9.41
LS Ru(II) codoped SACs		y= 0.51x – 0.98	0.69	5.12
IS Ru(II) codoped SACs		y= 0.50x – 1.16	0.72	6.78

Appendix A5

Contents

Table A5.1. Spin multiplicity (i.e., 2*S*+1) of the pure metal and Mg-diluted M_2(dobdc) cluster models

	Spin multiplicity	
Metal	**Pure metal**	**Mg-diluted**
Mg	**1**	**-**
Mn	**10**	**4**
Fe	**13**	**5**
Co	**10**	**4**
Ni	**7**	**3**
Cu	**4**	**2**
Zn	**1**	**1**

Table A5.2. DFT-calculated energies of adsorption (ΔE_{ads}) of η^1-N and η^1-O coordination modes of N_2O bound to the open metal site of the pure metal and Mg-diluted M_2(dobdc) cluster models.

	Energy of adsorption (kJ/mol)			
	Pure metal		Mg-diluted	
Metal	**η1-N**	**η1-O**	**η1-N**	**η1-O**
Mg	**-53.4**	**-64.5**	**-**	**-**
Mn	**-69.7**	**-68.4**	**-43.9**	**-48.8**
Fe	**-53.2**	**-53.7**	**-50.0**	**-54.8**
Co	**-53.4**	**-57.7**	**-53.7**	**-58.3**
Ni	**-56.9**	**-62.2**	**-54.4**	**-64.1**
Cu	**-41.7**	**-46.1**	**-47.2**	**-46.7**
Zn	**-49.0**	**-51.9**	**-50.4**	**-53.7**

Table A5.3. Bond angles and bond lengths of N_2O bound to the open metal site of the pure metal and Mg-diluted M_2(dobdc) cluster models in η^1-N and η^1-O coordination modes.

	η1-N		η1-O	
Cluster	**∠M–N2O (°)**	**M–N (Å)**	**∠M–ON2 (°)**	**M–O (Å)**
Mg3	**147.63**	**2.338**	**119.67**	**2.268**
Mn3	**172.10**	**1.949**	**119.53**	**2.285**
MnMg2	**115.67**	**2.515**	**107.33**	**2.519**
Co3	**122.36**	**2.411**	**118.25**	**2.375**
CoMg2	**123.49**	**2.386**	**118.01**	**2.365**
Fe3	**122.61**	**2.409**	**109.45**	**2.409**
FeMg2	**121.45**	**2.469**	**109.11**	**2.432**
Ni3	**122.20**	**2.415**	**117.79**	**2.336**
NiMg2	**131.96**	**2.253**	**118.73**	**2.286**
Cu3	**108.27**	**2.572**	**105.84**	**2.522**
CuMg2	**115.34**	**2.574**	**105.28**	**2.538**
Zn3	**118.16**	**2.546**	**108.23**	**2.453**
ZnMg2	**118.85**	**2.523**	**108.89**	**2.440**

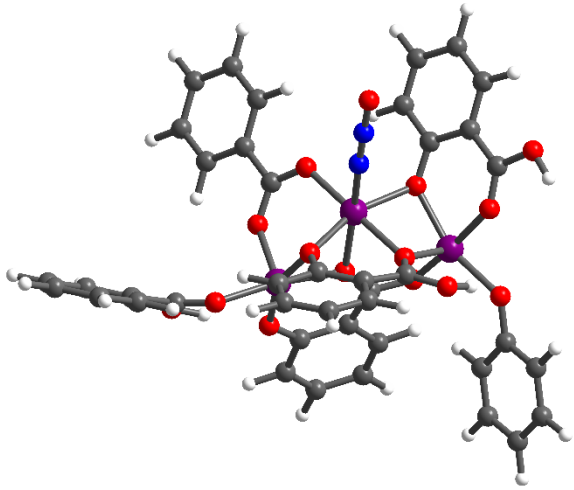

Figure A5.1 DFT-calculated structure of η^1-N coordinated N_2O in the pure metal Mn-based cluster model. Bond lengths: Mn–N (1.95 Å), N–N (1.13 Å), N–O (1.18 Å). ∠M–N_2O = 172.1 °. Purple, blue, gray, red and white spheres represent manganese, nitrogen, carbon, oxygen and hydrogen atoms, respectively.

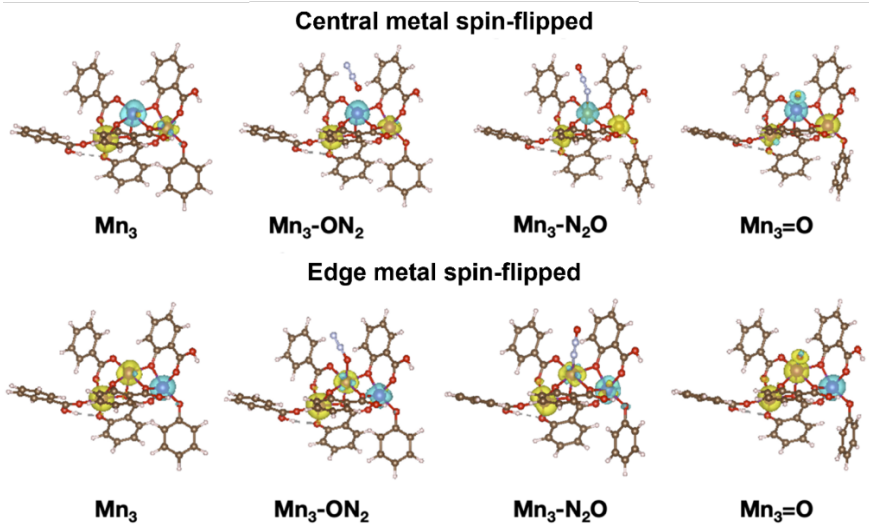

Figure A5.2. Spin densities of the central and edge metal spin-flipped Mn pure metal cluster models and various intermediates. Yellow and light blue isosurfaces represent positive and negative spin densities, respectively. An isosurface value of 0.01 e/bohr^3 is used for all visualizations.

Table A5.4. Broken symmetry DFT-calculated energies of adsorption (ΔE_{ads}) of η^1-N and η^1-O coordination modes of N_2O bound to the open metal site of the open shell pure metal M_2(dobdc) cluster models in central or edge metal spin-flipped configurations.

	Energy of adsorption (kJ/mol)			
	Central Metal		Edge Metal	
Metal	η1-N	η1-O	η1-N	η1-O
Mn	119.3	-252.2	299.9	116.3
Fe	-290.7	-291.2	-53.1	-53.6
Co	-251.2	-255.5	-53.3	-57.7
Ni	-56.8	-62.1	-56.7	-57.1
Cu	-46.9	-46.1	-44.8	-46.1

Table A5.5. DFT-calculated energies of M(IV)–oxo formation (ΔE_f (M–oxo), kJ/mol) in the pure metal and Mg-diluted M_2(dobdc) cluster models.

	M(IV)-oxo formation (kJ/mol)	
Metal	Pure metal	Mg-diluted
Mg	96.7	96.7
Mn	-183.1	-176.1
Fe	-55.5	-52.7
Co	28.5	9.9
Ni	104.2	73.0
Cu	104.6	64.9
Zn	96.8	89.6

Table A5.6. DFT-calculated M–O bond lengths in M(IV)–oxo (Å) pure metal and Mg-diluted M_2(dobdc) cluster models.

	M(IV)–oxo bond length (Å)	
Metal	**Pure metal**	**Mg-diluted**
Mg	**1.929**	**1.929**
Mn	**1.622**	**1.623**
Co	**1.633**	**1.668**
Fe	**1.607**	**1.603**
Ni	**2.414**	**1.840**
Cu	**1.818**	**1.822**
Zn	**1.893**	**1.897**

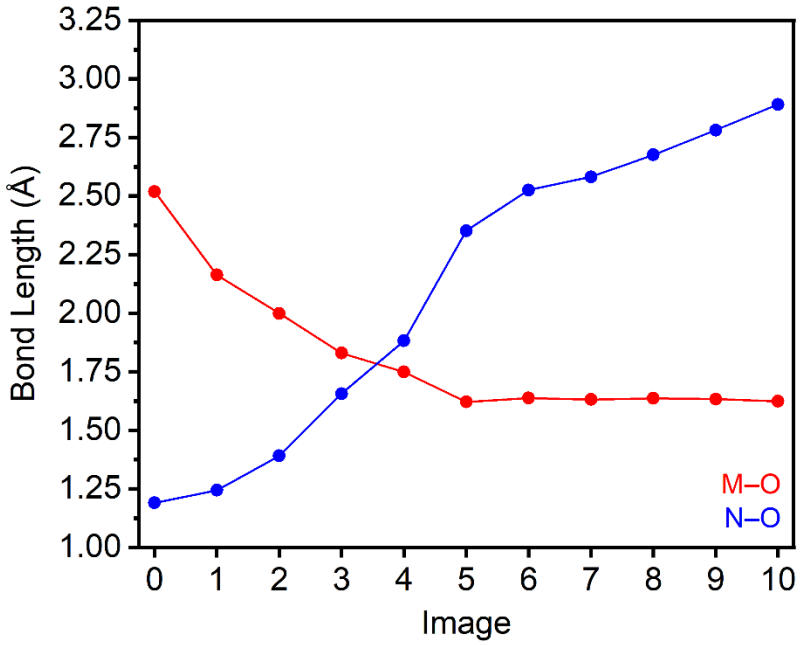

Figure A5.3. Image number vs. bond length of M–O (red) and N–O (blue) bond lengths in the CI-NEB calculated reaction coordinate for the activation of N_2O in the Mg-diluted Mn_2(dobdc) cluster model.

References

(1) Control methane to slow global warming - fast. *Nature* **2021**, *596* (7873), 461-461. DOI: 10.1038/d41586-021-02287-y.
(2) Wuebbles, D. J.; Hayhoe, K. Atmospheric methane and global change. *Earth-Science Reviews* **2002**, *57* (3-4), 177-210. DOI: 10.1016/s0012-8252(01)00062-9.
(3) Nisbet, E. G.; Dlugokencky, E. J.; Bousquet, P. Methane on the Rise-Again. *Science* **2014**, *343* (6170), 493-495. DOI: 10.1126/science.1247828.
(4) Watson, J. D.; Field, L. D.; Ball, G. E. Binding methane to a metal centre. *Nature Chemistry* **2022**, *14* (7), 801-+. DOI: 10.1038/s41557-022-00929-w.
(5) Tomkins, P.; Ranocchiari, M.; van Bokhoven, J. A. Direct Conversion of Methane to Methanol under Mild Conditions over Cu-Zeolites and beyond. *Accounts of Chemical Research* **2017**, *50* (2), 418-425. DOI: 10.1021/acs.accounts.6b00534.
(6) Ravi, M.; Ranocchiari, M.; van Bokhoven, J. A. The Direct Catalytic Oxidation of Methane to Methanol-A Critical Assessment. *Angewandte Chemie-International Edition* **2017**, *56* (52), 16464-16483. DOI: 10.1002/anie.201702550.
(7) Latimer, A. A.; Kakekhani, A.; Kulkarni, A. R.; Norskov, J. K. Direct Methane to Methanol: The Selectivity-Conversion Limit and Design Strategies. *Acs Catalysis* **2018**, *8* (8), 6894-6907. DOI: 10.1021/acscatal.8b00220.
(8) Nandy, A.; Duan, C. R.; Goffinet, C.; Kulik, H. J. New Strategies for Direct Methane-to-Methanol Conversion from Active Learning Exploration of 16 Million Catalysts. *Jacs Au* **2022**, *2* (5), 1200-1213. DOI: 10.1021/jacsau.2c00176.
(9) Price, J. C.; Barr, E. W.; Tirupati, B.; Bollinger, J. M.; Krebs, C. The first direct characterization of a high-valent iron intermediate in the reaction of an alpha-ketoglutarate-dependent dioxygenase: A high-spin Fe(IV) complex in taurine/alpha-ketoglutarate dioxygenase (TauD) from Escherichia coli. *Biochemistry* **2003**, *42* (24), 7497-7508. DOI: 10.1021/bi030011f.
(10) Price, J. C.; Barr, E. W.; Glass, T. E.; Krebs, C.; Bollinger, J. M. Evidence for hydrogen abstraction from C1 of taurine by the high-spin Fe(IV) intermediate detected during oxygen activation by taurine :alpha-ketoglutarate dioxygenase (TauD). *Journal of the American Chemical Society* **2003**, *125* (43), 13008-13009. DOI: 10.1021/ja037400h.
(11) Eichhorn, E.; vanderPloeg, J. R.; Kertesz, M. A.; Leisinger, T. Characterization of alpha-ketoglutarate-dependent taurine dioxygenase from Escherichia coli. *Journal of Biological Chemistry* **1997**, *272* (37), 23031-23036. DOI: 10.1074/jbc.272.37.23031.
(12) Oloo, W. N.; Que, L. Bioinspired Nonheme Iron Catalysts for C-H and C=C Bond Oxidation: Insights into the Nature of the Metal-Based Oxidants. *Accounts of Chemical Research* **2015**, *48* (9), 2612-2621. DOI: 10.1021/acs.accounts.5b00053.
(13) Biswas, A. N.; Puri, M.; Meier, K. K.; Oloo, W. N.; Rohde, G. T.; Bominaar, E. L.; Munck, E.; Que, L. Modeling TauD-J: A High-Spin Nonheme Oxoiron(IV) Complex with High Reactivity toward C-H Bonds. *Journal of the American Chemical Society* **2015**, *137* (7), 2428-2431. DOI: 10.1021/ja511757j.
(14) Que, L.; Tolman, W. B. Biologically inspired oxidation catalysis. *Nature* **2008**, *455* (7211), 333-340. DOI: 10.1038/nature07371.
(15) Periana, R. A.; Taube, D. J.; Gamble, S.; Taube, H.; Satoh, T.; Fujii, H. Platinum catalysts for the high-yield oxidation of methane to a methanol derivative. *Science* **1998**, *280* (5363), 560-564. DOI: 10.1126/science.280.5363.560.

(16) Muehlhofer, M.; Strassner, T.; Herrmann, W. A. New catalyst systems for the catalytic conversion of methane into methanol. *Angewandte Chemie-International Edition* **2002**, *41* (10), 1745-+. DOI: 10.1002/1521-3773(20020517)41:10<1745::aid-anie1745>3.0.co;2-e.
(17) Shilov, A. E.; Shul'pin, G. B. Activation of C-H bonds by metal complexes. *Chemical Reviews* **1997**, *97* (8), 2879-2932. DOI: 10.1021/cr9411886.
(18) Jones, C. J.; Taube, D.; Ziatdinov, V. R.; Periana, R. A.; Nielsen, R. J.; Oxgaard, J.; Goddard, W. A. Selective oxidation of methane to methanol catalyzed, with C-H activation, by homogeneous, cationic gold. *Angewandte Chemie-International Edition* **2004**, *43* (35), 4626-4629. DOI: 10.1002/anie.200461055.
(19) Palkovits, R.; Antonietti, M.; Kuhn, P.; Thomas, A.; Schuth, F. Solid Catalysts for the Selective Low-Temperature Oxidation of Methane to Methanol. *Angewandte Chemie-International Edition* **2009**, *48* (37), 6909-6912. DOI: 10.1002/anie.200902009.
(20) Dinh, K. T.; Sullivan, M. M.; Serna, P.; Meyer, R. J.; Dinca, M.; Roman-Leshkov, Y. Viewpoint on the Partial Oxidation of Methane to Methanol Using Cu- and Fe-Exchanged Zeolites. *Acs Catalysis* **2018**, *8* (9), 8306-8313. DOI: 10.1021/acscatal.8b01180.
(21) Szecsenyi, A.; Li, G. N.; Gascon, J.; Pidko, E. A. Mechanistic Complexity of Methane Oxidation with H2O2 by Single-Site Fe/ZSM-5 Catalyst. *Acs Catalysis* **2018**, *8* (9), 7961-7972. DOI: 10.1021/acscatal.8b01672.
(22) Qiao, B. T.; Wang, A. Q.; Yang, X. F.; Allard, L. F.; Jiang, Z.; Cui, Y. T.; Liu, J. Y.; Li, J.; Zhang, T. Single-atom catalysis of CO oxidation using Pt-1/FeOx. *Nature Chemistry* **2011**, *3* (8), 634-641. DOI: 10.1038/nchem.1095.
(23) Yang, X. F.; Wang, A. Q.; Qiao, B. T.; Li, J.; Liu, J. Y.; Zhang, T. Single-Atom Catalysts: A New Frontier in Heterogeneous Catalysis. *Accounts of Chemical Research* **2013**, *46* (8), 1740-1748. DOI: 10.1021/ar300361m.
(24) O'Connor, N. J.; Jonayat, A. S. M.; Janik, M. J.; Senftle, T. P. Interaction trends between single metal atoms and oxide supports identified with density functional theory and statistical learning. *Nature Catalysis* **2018**, *1* (7), 531-539. DOI: 10.1038/s41929-018-0094-5.
(25) Peters, B.; Scott, S. L. Single atom catalysts on amorphous supports: A quenched disorder perspective. *Journal of Chemical Physics* **2015**, *142* (10), 104708. DOI: 10.1063/1.4914145.
(26) Zhuo, H. Y.; Zhang, X.; Liang, J. X.; Yu, Q.; Xiao, H.; Li, J. Theoretical Understandings of Graphene-based Metal Single-Atom Catalysts: Stability and Catalytic Performance. *Chemical Reviews* **2020**, *120* (21), 12315-12341. DOI: 10.1021/acs.chemrev.0c00818.
(27) Jiang, K.; Siahrostami, S.; Akey, A. J.; Li, Y. B.; Lu, Z. Y.; Lattimer, J.; Hu, Y. F.; Stokes, C.; Gangishetty, M.; Chen, G. X.; et al. Transition-Metal Single Atoms in a Graphene Shell as Active Centers for Highly Efficient Artificial Photosynthesis. *Chem* **2017**, *3* (6), 950-960. DOI: 10.1016/j.chempr.2017.09.014.
(28) Jiang, K.; Siahrostami, S.; Zheng, T. T.; Hu, Y. F.; Hwang, S.; Stavitski, E.; Peng, Y. D.; Dynes, J.; Gangisetty, M.; Su, D.; et al. Isolated Ni single atoms in graphene nanosheets for high-performance CO2 reduction. *Energy & Environmental Science* **2018**, *11* (4), 893-903. DOI: 10.1039/c7ee03245e.
(29) Jia, H. J.; Nandy, A.; Liu, M. J.; Kulik, H. J. Modeling the roles of rigidity and dopants in single-atom methane-to-methanol catalysts. *Journal of Materials Chemistry A* **2022**, *10* (11), 6193-6203. DOI: 10.1039/d1ta08502f.
(30) Liu, F.; Yang, T. H.; Yang, J.; Xu, E.; Bajaj, A.; Kulik, H. J. Bridging the Homogeneous-Heterogeneous Divide: Modeling Spin for Reactivity in Single Atom Catalysis. *Frontiers in Chemistry* **2019**, *7*, 219. DOI: 10.3389/fchem.2019.00219.

(31) Wang, A. Q.; Li, J.; Zhang, T. Heterogeneous single-atom catalysis. *Nature Reviews Chemistry* **2018**, *2* (6), 65-81. DOI: 10.1038/s41570-018-0010-1.
(32) Chen, Y. J.; Ji, S. F.; Wang, Y. G.; Dong, J. C.; Chen, W. X.; Li, Z.; Shen, R. A.; Zheng, L. R.; Zhuang, Z. B.; Wang, D. S.; Li, Y. D. Isolated Single Iron Atoms Anchored on N-Doped Porous Carbon as an Efficient Electrocatalyst for the Oxygen Reduction Reaction. *Angewandte Chemie-International Edition* **2017**, *56* (24), 6937-6941. DOI: 10.1002/anie.201702473.
(33) Cheng, N. C.; Zhang, L.; Doyle-Davis, K.; Sun, X. L. Single-Atom Catalysts: From Design to Application. *Electrochemical Energy Reviews* **2019**, *2* (4), 539-573. DOI: 10.1007/s41918-019-00050-6.
(34) Wei, Z. X.; Zhu, Y. T.; Liu, J. Y.; Zhang, Z. C.; Hu, W. P.; Xu, H.; Feng, Y. Z.; Ma, J. M. Recent advance in single-atom catalysis. *Rare Metals* **2021**, *40* (4), 767-789. DOI: 10.1007/s12598-020-01592-1.
(35) Dzara, M. J.; Artyushkova, K.; Sougrati, M. T.; Ngo, C.; Fitzgerald, M. A.; Serov, A.; Zulevi, B.; Atanassov, P.; Jaouen, F.; Pylypenko, S. Characterizing Complex Gas-Solid Interfaces with in Situ Spectroscopy: Oxygen Adsorption Behavior on Fe-N-C Catalysts. *Journal of Physical Chemistry C* **2020**, *124* (30), 16529-16543. DOI: 10.1021/acs.jpcc.0c05244.
(36) Liu, W. G.; Zhang, L. L.; Liu, X.; Liu, X. Y.; Yang, X. F.; Miao, S.; Wang, W. T.; Wang, A. Q.; Zhang, T. Discriminating Catalytically Active FeNx Species of Atomically Dispersed Fe-N-C Catalyst for Selective Oxidation of the C-H Bond. *Journal of the American Chemical Society* **2017**, *139* (31), 10790-10798. DOI: 10.1021/jacs.7b05130.
(37) Liu, W. G.; Zhang, L. L.; Yan, W. S.; Liu, X. Y.; Yang, X. F.; Miao, S.; Wang, W. T.; Wang, A. Q.; Zhang, T. Single-atom dispersed Co-N-C catalyst: structure identification and performance for hydrogenative coupling of nitroarenes. *Chemical Science* **2016**, *7* (9), 5758-5764. DOI: 10.1039/c6sc02105k.
(38) Zhang, C. H.; Yang, S. Z.; Wu, J. J.; Liu, M. J.; Yazdi, S.; Ren, M. Q.; Sha, J. W.; Zhong, J.; Nie, K. Q.; Jalilov, A. S.; et al. Electrochemical CO2 Reduction with Atomic Iron-Dispersed on Nitrogen-Doped Graphene. *Advanced Energy Materials* **2018**, *8* (19). DOI: 10.1002/aenm.201703487.
(39) Deng, D. H.; Chen, X. Q.; Yu, L.; Wu, X.; Liu, Q. F.; Liu, Y.; Yang, H. X.; Tian, H. F.; Hu, Y. F.; Du, P. P.; et al. A single iron site confined in a graphene matrix for the catalytic oxidation of benzene at room temperature. *Science Advances* **2015**, *1* (11). DOI: 10.1126/sciadv.1500462.
(40) Kramm, U. I.; Abs-Wurmbach, I.; Herrmann-Geppert, I.; Radnik, J.; Fiechter, S.; Bogdanoff, P. Influence of the Electron-Density of FeN4-Centers Towards the Catalytic Activity of Pyrolyzed FeTMPPCl-Based ORR-Electrocatalysts. *Journal of the Electrochemical Society* **2011**, *158* (1), B69-B78. DOI: 10.1149/1.3499621.
(41) Zitolo, A.; Goellner, V.; Armel, V.; Sougrati, M. T.; Mineva, T.; Stievano, L.; Fonda, E.; Jaouen, F. Identification of catalytic sites for oxygen reduction in iron- and nitrogen-doped graphene materials. *Nature Materials* **2015**, *14* (9), 937-+. DOI: 10.1038/nmat4367.
(42) Cui, X. J.; Li, H. B.; Wang, Y.; Hu, Y. L.; Hua, L.; Li, H. Y.; Han, X. W.; Liu, Q. F.; Yang, F.; He, L. M.; et al. Room-Temperature Methane Conversion by Graphene-Confined Single Iron Atoms. *Chem* **2018**, *4* (8), 1902-1910. DOI: 10.1016/j.chempr.2018.05.006.
(43) Yang, L.; Cheng, D. J.; Zeng, X. F.; Wan, X.; Shui, J. L.; Xiang, Z. H.; Cao, D. P. Unveiling the high-activity origin of single-atom iron catalysts for oxygen reduction reaction. *Proc. Natl. Acad. Sci. U. S. A.* **2018**, *115* (26), 6626-6631. DOI: 10.1073/pnas.1800771115.
(44) Mineva, T.; Matanovic, I.; Atanassov, P.; Sougrati, M. T.; Stievano, L.; Clemancey, M.; Kochem, A.; Latour, J. M.; Jaouen, F. Understanding Active Sites in Pyrolyzed Fe-N-C Catalysts

for Fuel Cell Cathodes by Bridging Density Functional Theory Calculations and Fe-57 Mossbauer Spectroscopy. *Acs Catalysis* **2019**, *9* (10), 9359-9371. DOI: 10.1021/acscatal.9b02586.
(45) Li, Y. C.; Liu, X. F.; Zheng, L. R.; Shang, J. X.; Wan, X.; Hu, R. M.; Guo, X.; Hong, S.; Shui, J. L. Preparation of Fe-N-C catalysts with FeNx (x=1, 3, 4) active sites and comparison of their activities for the oxygen reduction reaction and performances in proton exchange membrane fuel cells. *J. Mater. Chem. A* **2019**, *7* (45), 26147-26153. DOI: 10.1039/c9ta08532g.
(46) Liu, F.; Yang, T. H.; Yang, J.; Xu, E.; Bajaj, A.; Kulik, H. J. Bridging the Homogeneous-Heterogeneous Divide: Modeling Spin for Reactivity in Single Atom Catalysis. *Frontiers in Chemistry* **2019**, *7*. DOI: 10.3389/fchem.2019.00219.
(47) Gani, T. Z. H.; Kulik, H. J. Understanding and Breaking Scaling Relations in Single-Site Catalysis: Methane to Methanol Conversion by Fe^{IV}=O. *ACS Catalysis* **2018**, *8*, 975-986.
(48) Nandy, A.; Kulik, H. J. Why Conventional Design Rules for C-H Activation Fail for Open-Shell Transition-Metal Catalysts. *Acs Catalysis* **2020**, *10* (24), 15033-15047. DOI: 10.1021/acscatal.0c04300.
(49) Betley, T. A.; Surendranath, Y.; Childress, M. V.; Alliger, G. E.; Fu, R.; Cummins, C. C.; Nocera, D. G. A Ligand Field Chemistry of Oxygen Generation by the Oxygen-Evolving Complex and Synthetic Active Sites. *Philos. Trans. R. Soc. B* **2008**, *363* (1494), 1293-1303. DOI: 10.1098/rstb.2007.2226.
(50) Kazaryan, A.; Baerends, E. J. Ligand Field Effects and the High Spin–High Reactivity Correlation in the H Abstraction by Non-Heme Iron (IV)–Oxo Complexes: A DFT Frontier Orbital Perspective. *ACS Catal.* **2015**, *5* (3), 1475-1488.
(51) Yuan, K.; Lutzenkirchen-Hecht, D.; Li, L. B.; Shuai, L.; Li, Y. Z.; Cao, R.; Qiu, M.; Zhuang, X. D.; Leung, M. K. H.; Chen, Y. W.; Scherf, U. Boosting Oxygen Reduction of Single Iron Active Sites via Geometric and Electronic Engineering: Nitrogen and Phosphorus Dual Coordination. *Journal of the American Chemical Society* **2020**, *142* (5), 2404-2412. DOI: 10.1021/jacs.9b11852.
(52) Li, X. H.; Yang, X. X.; Liu, L. T.; Zhao, H.; Li, Y. W.; Zhu, H. Y.; Chen, Y. Z.; Guo, S. W.; Liu, Y. N.; Tan, Q.; Wu, G. Chemical Vapor Deposition for N/S-Doped Single Fe Site Catalysts for the Oxygen Reduction in Direct Methanol Fuel Cells. *Acs Catalysis* **2021**, *11* (12), 7450-7459. DOI: 10.1021/acscatal.0c05446.
(53) Shang, H. S.; Zhou, X. Y.; Dong, J. C.; Li, A.; Zhao, X.; Liu, Q. H.; Lin, Y.; Pei, J. J.; Li, Z.; Jiang, Z. L.; et al. Engineering unsymmetrically coordinated Cu-S1N3 single atom sites with enhanced oxygen reduction activity. *Nature Communications* **2020**, *11* (1). DOI: 10.1038/s41467-020-16848-8.
(54) Zhang, J. Q.; Zhao, Y. F.; Chen, C.; Huang, Y. C.; Dong, C. L.; Chen, C. J.; Liu, R. S.; Wang, C. Y.; Yan, K.; Li, Y. D.; Wang, G. X. Tuning the Coordination Environment in Single-Atom Catalysts to Achieve Highly Efficient Oxygen Reduction Reactions. *Journal of the American Chemical Society* **2019**, *141* (51), 20118-20126. DOI: 10.1021/jacs.9b09352.
(55) Lu, B. Z.; Liu, Q. M.; Chen, S. W. Electrocatalysis of Single-Atom Sites: Impacts of Atomic Coordination. *ACS Catal.* **2020**, *10* (14), 7584-7618. DOI: 10.1021/acscatal.0c01950.
(56) Wang, L.; Liu, X. K.; Cao, L. L.; Zhang, W.; Chen, T.; Lin, Y.; Wang, H. J.; Wang, Y.; Yao, T. Active Sites of Single-Atom Iron Catalyst for Electrochemical Hydrogen Evolution. *Journal of Physical Chemistry Letters* **2020**, *11* (16), 6691-6696. DOI: 10.1021/acs.jpclett.0c01943.

(57) Yu, L.; Li, Y. C.; Ruan, Y. F. Dynamic Control of Sacrificial Bond Transformation in the Fe-N-C Single-Atom Catalyst for Molecular Oxygen Reduction. *Angewandte Chemie-International Edition* **2021**, *60* (48), 25296-25301. DOI: 10.1002/anie.202111761.
(58) Marshall-Roth, T.; Libretto, N. J.; Wrobel, A. T.; Anderton, K. J.; Pegis, M. L.; Ricke, N. D.; Van Voorhis, T.; Miller, J. T.; Surendranath, Y. A pyridinic Fe-N-4 macrocycle models the active sites in Fe/N-doped carbon electrocatalysts. *Nat. Commun.* **2020**, *11* (1), 7343. DOI: 10.1038/s41467-020-18969-6.
(59) Adli, N. M.; Shan, W. T.; Hwang, S.; Samarakoon, W.; Karakalos, S.; Li, Y.; Cullen, D. A.; Su, D.; Feng, Z. X.; Wang, G. F.; Wu, G. Engineering Atomically Dispersed FeN4 Active Sites for CO2 Electroreduction. *Angewandte Chemie-International Edition* **2021**, *60* (2), 1022-1032. DOI: 10.1002/anie.202012329.
(60) Jiao, L.; Xu, W. Q.; Zhang, Y.; Wu, Y.; Gu, W. L.; Ge, X. X.; Chen, B. B.; Zhu, C. Z.; Guo, S. J. Boron-doped Fe-N-C single-atom nanozymes specifically boost peroxidase-like activity. *Nano Today* **2020**, *35*. DOI: 10.1016/j.nantod.2020.100971.
(61) Fei, H. L.; Dong, J. C.; Arellano-Jimenez, M. J.; Ye, G. L.; Kim, N. D.; Samuel, E. L. G.; Peng, Z. W.; Zhu, Z.; Qin, F.; Bao, J. M.; et al. Atomic cobalt on nitrogen-doped graphene for hydrogen generation. *Nature Communications* **2015**, *6*. DOI: 10.1038/ncomms9668.
(62) Wang, A.; Zhang, T. Taking cobalt in isolation. *Nature Energy* **2016**, *1*.
(63) Fei, H. L.; Dong, J. C.; Arellano-Jimenez, M. J.; Ye, G. L.; Kim, N. D.; Samuel, E. L. G.; Peng, Z. W.; Zhu, Z.; Qin, F.; Bao, J. M.; et al. Atomic cobalt on nitrogen-doped graphene for hydrogen generation. *Nature Communications* **2015**, *6*, 8668. DOI: 10.1038/ncomms9668.
(64) Wang, A.; Zhang, T. Water splitting: Taking cobalt in isolation. *Nature Energy* **2016**, *1*, 15019.
(65) Xu, H. X.; Cheng, D. J.; Cao, D. P.; Zeng, X. C. A universal principle for a rational design of single-atom electrocatalysts (vol 1, pg 339, 2018). *Nature Catalysis* **2018**, *1* (8), 632-632. DOI: 10.1038/s41929-018-0127-0.
(66) Fung, V.; Hu, G. X.; Wu, Z. L.; Jiang, D. E. Descriptors for Hydrogen Evolution on Single Atom Catalysts in Nitrogen-Doped Graphene. *Journal of Physical Chemistry C* **2020**, *124* (36), 19571-19578. DOI: 10.1021/acs.jpcc.0c04432.
(67) Xi, Y. J.; Heyden, A. Direct Oxidation of Methane to Methanol Enabled by Electronic Atomic Monolayer-Metal Support Interaction. *Acs Catalysis* **2019**, *9* (7), 6073-6079. DOI: 10.1021/acscatal.9b01619.
(68) Hong, S.; Mpourmpakis, G. Mechanistic understanding of methane-to-methanol conversion on graphene-stabilized single-atom iron centers. *Catalysis Science & Technology* **2021**, *11* (19), 6390-6400. DOI: 10.1039/d1cy00826a.
(69) Zhang, L. Z.; Jia, Y.; Gao, G. P.; Yan, X. C.; Chen, N.; Chen, J.; Soo, M. T.; Wood, B.; Yang, D. J.; Du, A. J.; Yao, X. D. Graphene Defects Trap Atomic Ni Species for Hydrogen and Oxygen Evolution Reactions. *Chem* **2018**, *4* (2), 285-297. DOI: 10.1016/j.chempr.2017.12.005.
(70) Sperger, T.; Sanhueza, I. A.; Schoenebeck, F. Computation and Experiment: A Powerful Combination to Understand and Predict Reactivities. *Accounts of Chemical Research* **2016**, *49* (6), 1311-1319. DOI: 10.1021/acs.accounts.6b00068.
(71) Latimer, A. A.; Kulkarni, A. R.; Aljama, H.; Montoya, J. H.; Yoo, J. S.; Tsai, C.; Abild-Pedersen, F.; Studt, F.; Norskov, J. K. Understanding trends in C-H bond activation in heterogeneous catalysis. *Nature Materials* **2017**, *16* (2), 225-229. DOI: 10.1038/nmat4760.
(72) Medford, A. J.; Vojvodic, A.; Hummelshoj, J. S.; Voss, J.; Abild-Pedersen, F.; Studt, F.; Bligaard, T.; Nilsson, A.; Norskov, J. K. From the Sabatier principle to a predictive theory of

transition-metal heterogeneous catalysis. *Journal of Catalysis* **2015**, *328*, 36-42. DOI: 10.1016/j.jcat.2014.12.033.
(73) Abild-Pedersen, F.; Greeley, J.; Studt, F.; Rossmeisl, J.; Munter, T. R.; Moses, P. G.; Skulason, E.; Bligaard, T.; Norskov, J. K. Scaling properties of adsorption energies for hydrogen-containing molecules on transition-metal surfaces. *Physical Review Letters* **2007**, *99* (1). DOI: 10.1103/PhysRevLett.99.016105.
(74) Bligaard, T.; Norskov, J. K.; Dahl, S.; Matthiesen, J.; Christensen, C. H.; Sehested, J. The Bronsted-Evans-Polanyi relation and the volcano curve in heterogeneous catalysis. *Journal of Catalysis* **2004**, *224* (1), 206-217. DOI: 10.1016/j.jcat.2004.02.034.
(75) Yoo, S. H.; Todorova, M.; Wickramaratne, D.; Weston, L.; Van de Walle, C. G.; Neugebauer, J. Finite-size correction for slab supercell calculations of materials with spontaneous polarization. *Npj Computational Materials* **2021**, *7* (1). DOI: 10.1038/s41524-021-00529-1.
(76) Kulik, H. J. Perspective: Treating electron over-delocalization with the DFT plus U method. *Journal of Chemical Physics* **2015**, *142* (24). DOI: 10.1063/1.4922693.
(77) Gaggioli, C. A.; Stoneburner, S. J.; Cramer, C. J.; Gagliardi, L. Beyond Density Functional Theory: The Multiconfigurational Approach To Model Heterogeneous Catalysis. *ACS Catal.* **2019**, *9* (9), 8481-8502. DOI: 10.1021/acscatal.9b01775.
(78) Cramer, C. J.; Truhlar, D. G. Density functional theory for transition metals and transition metal chemistry. *Phys. Chem. Chem. Phys.* **2009**, *11* (46), 10757-10816. DOI: 10.1039/b907148b.
(79) Mori-Sanchez, P.; Cohen, A. J.; Yang, W. T. Localization and delocalization errors in density functional theory and implications for band-gap prediction. *Physical Review Letters* **2008**, *100* (14). DOI: 10.1103/PhysRevLett.100.146401.
(80) Cohen, A. J.; Mori-Sanchez, P.; Yang, W. T. Challenges for Density Functional Theory. *Chemical Reviews* **2012**, *112* (1), 289-320. DOI: 10.1021/cr200107z.
(81) Calborean, A.; Morari, C.; Maldivi, P. Combined Molecular and Periodic DFT Analysis of the Adsorption of Co Macrocycles on Graphene. *J. Comput. Chem.* **2018**, *39* (2), 130-138. DOI: 10.1002/jcc.25093.
(82) Li, J.; Li, X.; Zhai, H. J.; Wang, L. S. Au-20: A tetrahedral cluster. *Science* **2003**, *299* (5608), 864-867. DOI: 10.1126/science.1079879.
(83) Ju, W.; Bagger, A.; Hao, G.-P.; Varela, A. S.; Sinev, I.; Bon, V.; Roldan Cuenya, B.; Kaskel, S.; Rossmeisl, J.; Strasser, P. Understanding activity and selectivity of metal-nitrogen-doped carbon catalysts for electrochemical reduction of CO2. *Nature communications* **2017**, *8* (1), 1-9.
(84) Vijay, S.; Ju, W.; Brückner, S.; Tsang, S.-C.; Strasser, P.; Chan, K. Unified mechanistic understanding of CO2 reduction to CO on transition metal and single atom catalysts. *Nature Catalysis* **2021**, *4* (12), 1024-1031.
(85) Qin, X.; Zhu, S.; Xiao, F.; Zhang, L.; Shao, M. Active sites on heterogeneous single-iron-atom electrocatalysts in CO2 reduction reaction. *ACS Energy Letters* **2019**, *4* (7), 1778-1783.
(86) Vijay, S.; Gauthier, J. A.; Heenen, H. H.; Bukas, V. J.; Kristoffersen, H. H.; Chan, K. Dipole-field interactions determine the CO2 reduction activity of 2D Fe–N–C single-atom catalysts. *ACS Catalysis* **2020**, *10* (14), 7826-7835.
(87) Zhang, C.; Yang, S.; Wu, J.; Liu, M.; Yazdi, S.; Ren, M.; Sha, J.; Zhong, J.; Nie, K.; Jalilov, A. S. Electrochemical CO2 reduction with atomic iron-dispersed on nitrogen-doped graphene. *Advanced Energy Materials* **2018**, *8* (19), 1703487.

(88) Raghavachari, K.; Trucks, G. W.; Pople, J. A.; Head-Gordon, M. A fifth-order perturbation comparison of electron correlation theories. *Chemical Physics Letters* **1989**, *157* (6), 479-483.
(89) Bartlett, R. J.; Musiał, M. Coupled-cluster theory in quantum chemistry. *Reviews of Modern Physics* **2007**, *79* (1), 291.
(90) Sun, Q.; Chan, G. K.-L. Quantum embedding theories. *Accounts of chemical research* **2016**, *49* (12), 2705-2712.
(91) Lei, J.; Zhu, T. Impact of Potential and Active-Site Environment on Single-Iron-Atom-Catalyzed Electrochemical CO2 Reduction from Accurate Quantum Many-Body Simulations. *ACS Catalysis* **2024**, *14* (6), 3933-3942.
(92) Jiao, L.; Yan, H. Y.; Wu, Y.; Gu, W. L.; Zhu, C. Z.; Du, D.; Lin, Y. H. When Nanozymes Meet Single-Atom Catalysis. *Angewandte Chemie-International Edition* **2020**, *59* (7), 2565-2576. DOI: 10.1002/anie.201905645.
(93) Xie, C.; Niu, Z.; Kim, D.; Li, M.; Yang, P. Surface and interface control in nanoparticle catalysis. *Chemical reviews* **2019**, *120* (2), 1184-1249.
(94) Zheng, N.; Stucky, G. D. A general synthetic strategy for oxide-supported metal nanoparticle catalysts. *Journal of the American Chemical Society* **2006**, *128* (44), 14278-14280.
(95) Astruc, D. Introduction: nanoparticles in catalysis. ACS Publications: 2020; Vol. 120, pp 461-463.
(96) Guo, S.; Zhang, S.; Sun, S. Tuning nanoparticle catalysis for the oxygen reduction reaction. *Angewandte Chemie International Edition* **2013**, *52* (33), 8526-8544.
(97) Ma, W.; Wan, H.; Zhang, L. L.; Zheng, J. Y.; Zhou, Z. Single-atom catalysts for electrochemical energy storage and conversion. *Journal of Energy Chemistry* **2021**, *63*, 170-194. DOI: 10.1016/j.jechem.2021.08.041.
(98) Ma, W.; Deng, Z.; Zhang, X. J.; Zhang, Z.; Zhou, Z. Regulating the electronic structure of single-atom catalysts for electrochemical energy conversion. *Journal of Materials Chemistry A* **2023**, *11* (24), 12643-12658. DOI: 10.1039/d3ta00156c.
(99) Zhang, X.; Zhang, Q.; Cui, J.; Yan, J.; Liu, J.; Wu, Y. New insights into the key bifunctional role of sulfur in Fe–N–C single-atom catalysts for ORR/OER. *Nanoscale* **2022**, *14* (8), 3212-3223.
(100) Li, Q.; Chen, W.; Xiao, H.; Gong, Y.; Li, Z.; Zheng, L.; Zheng, X.; Yan, W.; Cheong, W. C.; Shen, R. Fe isolated single atoms on S, N codoped carbon by copolymer pyrolysis strategy for highly efficient oxygen reduction reaction. *Advanced materials* **2018**, *30* (25), 1800588.
(101) Nandy, A.; Zhu, J. Z.; Janet, J. P.; Duan, C. R.; Getman, R. B.; Kulik, H. J. Machine Learning Accelerates the Discovery of Design Rules and Exceptions in Stable Metal-Oxo Intermediate Formation. *Acs Catalysis* **2019**, *9* (9), 8243-8255. DOI: 10.1021/acscatal.9b02165.
(102) Vennelakanti, V.; Nandy, A.; Kulik, H. J. The Effect of Hartree-Fock Exchange on Scaling Relations and Reaction Energetics for C-H Activation Catalysts. *Topics in Catalysis* **2022**, *65* (1-4), 296-311. DOI: 10.1007/s11244-021-01482-5.
(103) Gomez-Bombarelli, R.; Aguilera-Iparraguirre, J.; Hirzel, T. D.; Duvenaud, D.; Maclaurin, D.; Blood-Forsythe, M. A.; Chae, H. S.; Einzinger, M.; Ha, D. G.; Wu, T.; et al. Design of efficient molecular organic light-emitting diodes by a high-throughput virtual screening and experimental approach. *Nature Materials* **2016**, *15* (10), 1120-+. DOI: 10.1038/nmat4717.
(104) Curtarolo, S.; Hart, G. L. W.; Nardelli, M. B.; Mingo, N.; Sanvito, S.; Levy, O. The high-throughput highway to computational materials design. *Nature Materials* **2013**, *12* (3), 191-201. DOI: 10.1038/nmat3568.

(105) Foscato, M.; Jensen, V. R. Automated in Silico Design of Homogeneous Catalysts. *Acs Catalysis* **2020**, *10* (3), 2354-2377. DOI: 10.1021/acscatal.9b04952.
(106) Jia, H.; Duan, C.; Kevlishvili, I.; Nandy, A.; Liu, M.; Kulik, H. J. Computational Discovery of Codoped Single-Atom Catalysts for Methane-to-Methanol Conversion. *ACS Catalysis* **2024**, *14* (5), 2992-3005. DOI: 10.1021/acscatal.3c05506.
(107) Pitt, T. A.; Jia, H.; Azbell, T. J.; Zick, M. E.; Nandy, A.; Kulik, H. J.; Milner, P. J. Benchmarking nitrous oxide adsorption and activation in metal–organic frameworks bearing coordinatively unsaturated metal centers. *Journal of Materials Chemistry C* **2024**.
(108) Janet, J. P.; Ramesh, S.; Duan, C.; Kulik, H. J. Accurate Multiobjective Design in a Space of Millions of Transition Metal Complexes with Neural-Network-Driven Efficient Global Optimization. *Acs Central Science* **2020**, *6* (4), 513-524. DOI: 10.1021/acscentsci.0c00026.
(109) Duan, C. R.; Nandy, A.; Terrones, G. G.; Kastner, D. W.; Kulik, H. J. Active Learning Exploration of Transition-Metal Complexes to Discover Method-Insensitive and Synthetically Accessible Chromophores. *Jacs Au* **2022**. DOI: 10.1021/jacsau.2c00547.
(110) Duan, C. R.; Janet, J. P.; Liu, F.; Nandy, A.; Kulik, H. J. Learning from Failure: Predicting Electronic Structure Calculation Outcomes with Machine Learning Models. *J. Chem. Theory Comput.* **2019**, *15* (4), 2331-2345. DOI: 10.1021/acs.jctc.9b00057.
(111) Duan, C.; Du, Y.; Jia, H.; Kulik, H. J. Accurate transition state generation with an object-aware equivariant elementary reaction diffusion model. *Nature Computational Science* **2023**, *3* (12), 1045-1055.
(112) Ying, Y. R.; Fan, K.; Luo, X.; Qiao, J. L.; Huang, H. T. Unravelling the origin of bifunctional OER/ORR activity for single-atom catalysts supported on C₂N by DFT and machine learning. *Journal of Materials Chemistry A* **2021**, *9* (31), 16860-16867. DOI: 10.1039/d1ta04256d.
(113) Zhao, Z.-J.; Liu, S.; Zha, S.; Cheng, D.; Studt, F.; Henkelman, G.; Gong, J. Theory-guided design of catalytic materials using scaling relationships and reactivity descriptors. *Nature Reviews Materials* **2019**, *4* (12), 792-804.
(114) Kitchin, J. R. Machine learning in catalysis. *Nature Catalysis* **2018**, *1* (4), 230-232.
(115) Ramprasad, R.; Batra, R.; Pilania, G.; Mannodi-Kanakkithodi, A.; Kim, C. Machine learning in materials informatics: recent applications and prospects. *npj Computational Materials* **2017**, *3* (1), 54.
(116) Back, S.; Yoon, J.; Tian, N.; Zhong, W.; Tran, K.; Ulissi, Z. W. Convolutional neural network of atomic surface structures to predict binding energies for high-throughput screening of catalysts. *The journal of physical chemistry letters* **2019**, *10* (15), 4401-4408.
(117) Jinnouchi, R.; Asahi, R. Predicting catalytic activity of nanoparticles by a DFT-aided machine-learning algorithm. *The journal of physical chemistry letters* **2017**, *8* (17), 4279-4283.
(118) Wexler, R. B.; Martirez, J. M. P.; Rappe, A. M. Chemical pressure-driven enhancement of the hydrogen evolving activity of Ni2P from nonmetal surface doping interpreted via machine learning. *Journal of the American Chemical Society* **2018**, *140* (13), 4678-4683.
(119) Jiang, K.; Wang, H. T. Electrocatalysis over Graphene Defect-Coordinated Transition-Metal Single-Atom Catalysts. *Chem* **2018**, *4* (2), 194-195. DOI: 10.1016/j.chempr.2018.01.013.
(120) Shang, H. S.; Zhou, X. Y.; Dong, J. C.; Li, A.; Zhao, X.; Liu, Q. H.; Lin, Y.; Pei, J. J.; Li, Z.; Jiang, Z. L.; et al. Engineering unsymmetrically coordinated Cu-S1N3 single atom sites with enhanced oxygen reduction activity. *Nat. Commun.* **2020**, *11* (1), 3049. DOI: 10.1038/s41467-020-16848-8.

(121) Yoo, S. H.; Todorova, M.; Wickramaratne, D.; Weston, L.; Van de Walle, C. G.; Neugebauer, J. Finite-size correction for slab supercell calculations of materials with spontaneous polarization. *npj Comput. Mater.* **2021**, *7* (1), 58. DOI: 10.1038/s41524-021-00529-1.
(122) Goldsmith, B. R.; Sanderson, E. D.; Bean, D.; Peters, B. Isolated catalyst sites on amorphous supports: A systematic algorithm for understanding heterogeneities in structure and reactivity. *J. Chem. Phys.* **2013**, *138* (20), 204105. DOI: 10.1063/1.4807384.
(123) Kulik, H. J. Perspective: Treating electron over-delocalization with the DFT+U method. *J. Chem. Phys.* **2015**, *142* (24), 240901. DOI: 10.1063/1.4922693.
(124) Patel, A. M.; Ringe, S.; Siahrostami, S.; Bajdich, M.; Norskov, J. K.; Kulkarni, A. R. Theoretical Approaches to Describing the Oxygen Reduction Reaction Activity of Single-Atom Catalysts. *J. Phys. Chem. C* **2018**, *122* (51), 29307-29318. DOI: 10.1021/acs.jpcc.8b09430.
(125) Mori-Sanchez, P.; Cohen, A. J.; Yang, W. T. Localization and delocalization errors in density functional theory and implications for band-gap prediction. *Phys. Rev. Lett.* **2008**, *100* (14), 146401. DOI: 10.1103/PhysRevLett.100.146401.
(126) Moriya, M.; Takahama, R.; Kamoi, K.; Ohyama, J.; Kawashima, S.; Kojima, R.; Okada, M.; Hayakawa, T.; Nabae, Y. Fourteen-Membered Macrocyclic Fe Complexes Inspired by FeN4-Center-Embedded Graphene for Oxygen Reduction Catalysis. *J. Phys. Chem. C* **2020**, *124* (38), 20730-20735. DOI: 10.1021/acs.jpcc.0c05536.
(127) Olah, G. A. Beyond Oil and Gas: the Methanol Economy. *Angewandte Chemie International Edition* **2005**, *44* (18), 2636-2639.
(128) Lunsford, J. H. Catalytic Conversion of Methane to More Useful Chemicals and Fuels: a Challenge for the 21st Century. *Catalysis Today* **2000**, *63* (2), 165-174.
(129) Lan, Z. Z.; Sharada, S. M. Computational strategies to probe CH activation in dioxo-dicopper complexes. *Phys. Chem. Chem. Phys.* **2018**, *20* (40), 25602-25614. DOI: 10.1039/c8cp05096a.
(130) Lan, Z. Z.; Sharada, S. M. Linear free energy relationships for transition metal chemistry: case study of CH activation with copper-oxygen complexes. *Physical Chemistry Chemical Physics* **2020**, *22* (14), 7155-7159. DOI: 10.1039/d0cp01245a.
(131) Liao, P. L.; Getman, R. B.; Snurr, R. Q. Optimizing Open Iron Sites in Metal-Organic Frameworks for Ethane Oxidation: A First-Principles Study. *ACS Appl. Mater. Interfaces* **2017**, *9* (39), 33484-33492. DOI: 10.1021/acsami.7b02195.
(132) Sushkevich, V. L.; Palagin, D.; Ranocchiari, M.; van Bokhoven, J. A. Selective anaerobic oxidation of methane enables direct synthesis of methanol. *Science* **2017**, *356* (6337), 523-+. DOI: 10.1126/science.aam9035.
(133) Jones, C.; Taube, D.; Ziatdinov, V. R.; Periana, R. A.; Nielsen, R. J.; Oxgaard, J.; Goddard, W. A. Selective Oxidation of Methane to Methanol Catalyzed, with C-H Activation, by Homogeneous, Cationic Gold. *Angew. Chem. Int. Ed.* **2004**, *116* (35), 4726-4729.
(134) An, Z. J.; Pan, X. L.; Liu, X. M.; Han, X. W.; Bao, X. H. Combined redox couples for catalytic oxidation of methane by dioxygen at low temperatures. *J. Am. Chem. Soc.* **2006**, *128* (50), 16028-16029. DOI: 10.1021/ja0647912.
(135) Harrath, K.; Yu, X. H.; Xiao, H.; Li, J. The Key Role of Support Surface Hydrogenation in the CH4 to CH3OH Selective Oxidation by a ZrO2-Supported Single-Atom Catalyst. *ACS Catal.* **2019**, *9* (10), 8903-8909. DOI: 10.1021/acscatal.9b02093.

(136) Yuan, J. Y.; Zhang, W. H.; Li, X. X.; Yang, J. L. A high performance catalyst for methane conversion to methanol: graphene supported single atom Co. *Chem. Commun.* **2018**, *54* (18), 2284-2287. DOI: 10.1039/c7cc08713f.
(137) Tan, X.; Tahini, H. A.; Smith, S. C. Defect Engineering in Graphene-Confined Single-Atom Iron Catalysts for Room-Temperature Methane Conversion. *Journal of Physical Chemistry C* **2021**, *125* (23), 12628-12635. DOI: 10.1021/acs.jpcc.1c01806.
(138) Fernandez, M.; Shi, H. Q.; Barnard, A. S. Geometrical features can predict electronic properties of graphene nanoflakes. *Carbon* **2016**, *103*, 142-150. DOI: 10.1016/j.carbon.2016.03.005.
(139) Hanwell, M. D.; Curtis, D. E.; Lonie, D. C.; Vandermeersch, T.; Zurek, E.; Hutchison, G. R. Avogadro: an advanced semantic chemical editor, visualization, and analysis platform. *J. Cheminf.* **2012**, *4*, 17. DOI: 10.1186/1758-2946-4-17.
(140) Ioannidis, E. I.; Gani, T. Z. H.; Kulik, H. J. molSimplify: A toolkit for automating discovery in inorganic chemistry. *Journal of Computational Chemistry* **2016**, *37* (22), 2106-2117. DOI: 10.1002/jcc.24437.
(141) Janet, J. P.; Kulik, H. J. Predicting electronic structure properties of transition metal complexes with neural networks. *Chem. Sci.* **2017**, *8* (7), 5137-5152. DOI: 10.1039/c7sc01247k.
(142) Ufimtsev, I. S.; Martinez, T. J. Quantum Chemistry on Graphical Processing Units. 3. Analytical Energy Gradients, Geometry Optimization, and First Principles Molecular Dynamics. *Journal of Chemical Theory and Computation* **2009**, *5* (10), 2619-2628. DOI: 10.1021/ct9003004.
(143) Rohrdanz, M. A.; Martins, K. M.; Herbert, J. M. A long-range-corrected density functional that performs well for both ground-state properties and time-dependent density functional theory excitation energies, including charge-transfer excited states. *J. Chem. Phys.* **2009**, *130* (5), 054112. DOI: 10.1063/1.3073302.
(144) Hay, P. J.; Wadt, W. R. ABINITIO EFFECTIVE CORE POTENTIALS FOR MOLECULAR CALCULATIONS - POTENTIALS FOR THE TRANSITION-METAL ATOMS SC TO HG. *Journal of Chemical Physics* **1985**, *82* (1), 270-283. DOI: 10.1063/1.448799.
(145) Wadt, W. R.; Hay, P. J. ABINITIO EFFECTIVE CORE POTENTIALS FOR MOLECULAR CALCULATIONS - POTENTIALS FOR MAIN GROUP ELEMENTS NA TO BI. *Journal of Chemical Physics* **1985**, *82* (1), 284-298. DOI: 10.1063/1.448800.
(146) Kulik, H. J.; Zhang, J. Y.; Klinman, J. P.; Martinez, T. J. How Large Should the QM Region Be in QM/MM Calculations? The Case of Catechol O-Methyltransferase. *Journal of Physical Chemistry B* **2016**, *120* (44), 11381-11394. DOI: 10.1021/acs.jpcb.6b07814.
(147) Isborn, C. M.; Luehr, N.; Ufimtsev, I. S.; Martinez, T. J. Excited-State Electronic Structure with Configuration Interaction Singles and Tamm-Dancoff Time-Dependent Density Functional Theory on Graphical Processing Units. *Journal of Chemical Theory and Computation* **2011**, *7* (6), 1814-1823. DOI: 10.1021/ct200030k.
(148) Saunders, V. R.; Hillier, I. H. LEVEL-SHIFTING METHOD FOR CONVERGING CLOSED SHELL HARTREE-FOCK WAVE-FUNCTIONS. *International Journal of Quantum Chemistry* **1973**, *7* (4), 699-705. DOI: 10.1002/qua.560070407.
(149) Wang, L. P.; Song, C. C. Geometry optimization made simple with translation and rotation coordinates. *J. Chem. Phys.* **2016**, *144* (21), 214108. DOI: 10.1063/1.4952956.

(150) Taylor, M. G.; Yang, T.; Lin, S.; Nandy, A.; Janet, J. P.; Duan, C. R.; Kulik, H. J. Seeing Is Believing: Experimental Spin States from Machine Learning Model Structure Predictions. *J. Phys. Chem. A* **2020**, *124* (16), 3286-3299. DOI: 10.1021/acs.jpca.0c01458.
(151) Xu, H.; Cheng, D.; Cao, D.; Zeng, X. C. A universal principle for a rational design of single-atom electrocatalysts. *Nat. Catal.* **2018**, *1* (5), 339-348.
(152) Bühl, M.; Reimann, C.; Pantazis, D. A.; Bredow, T.; Neese, F. Geometries of Third-Row Transition-Metal Complexes from Density-Functional Theory. *J. Chem. Theory Comput.* **2008**, *4* (9), 1449-1459. DOI: 10.1021/ct800172j.
(153) Groves, J. T.; McClusky, G. A. ALIPHATIC HYDROXYLATION VIA OXYGEN REBOUND - OXYGEN-TRANSFER CATALYZED BY IRON. *Journal of the American Chemical Society* **1976**, *98* (3), 859-861. DOI: 10.1021/ja00419a049.
(154) Xiao, D. J.; Bloch, E. D.; Mason, J. A.; Queen, W. L.; Hudson, M. R.; Planas, N.; Borycz, J.; Dzubak, A. L.; Verma, P.; Lee, K.; et al. Oxidation of ethane to ethanol by N2O in a metal-organic framework with coordinatively unsaturated iron(II) sites. *Nature Chemistry* **2014**, *6* (7), 590-595. DOI: 10.1038/nchem.1956.
(155) Barona, M.; Ahn, S.; Morris, W.; Hoover, W.; Notestein, J. M.; Farha, O. K.; Snurr, R. Q. Computational Predictions and Experimental Validation of Alkane Oxidative Dehydrogenation by Fe2M MOF Nodes. *Acs Catalysis* **2020**, *10* (2), 1460-1469. DOI: 10.1021/acscatal.9b03932.
(156) Latimer, A. A.; Kakekhani, A.; Kulkarni, A. R.; Nørskov, J. K. Direct methane to methanol: the selectivity–conversion limit and design strategies. *ACS Catalysis* **2018**, *8* (8), 6894-6907.
(157) Ravi, M.; Ranocchiari, M.; van Bokhoven, J. A. The direct catalytic oxidation of methane to methanol—A critical assessment. *Angewandte Chemie International Edition* **2017**, *56* (52), 16464-16483.
(158) Kumar, P.; Al-Attas, T. A.; Hu, J. G.; Kibria, M. G. Single Atom Catalysts for Selective Methane Oxidation to Oxygenates. *Acs Nano* **2022**, *16* (6), 8557-8618. DOI: 10.1021/acsnano.2c02464.
(159) Luo, L. H.; Luo, J.; Li, H. L.; Ren, F. N.; Zhang, Y. F.; Liu, A. D.; Li, W. X.; Zeng, J. Water enables mild oxidation of methane to methanol on gold single-atom catalysts. *Nature Communications* **2021**, *12* (1). DOI: 10.1038/s41467-021-21482-z.
(160) Wang, S. M.; Xin, Y.; Yuan, J. Y.; Wang, L. B.; Zhang, W. H. Direct conversion of methane to methanol on boron nitride-supported copper single atoms. *Nanoscale* **2022**, *14* (14), 5447-5453. DOI: 10.1039/d1nr08466f.
(161) Huang, E. R.; Liu, P. Theoretical Perspective of Promoting Direct Methane-to-Methanol Conversion at Complex Metal Oxide-Metal Interfaces. *Journal of Physical Chemistry Letters* **2023**, *14* (29), 6556-6563. DOI: 10.1021/acs.jpclett.3c01525.
(162) Marshall-Roth, T.; Libretto, N. J.; Wrobel, A. T.; Anderton, K. J.; Pegis, M. L.; Ricke, N. D.; Voorhis, T. V.; Miller, J. T.; Surendranath, Y. A pyridinic Fe-N4 macrocycle models the active sites in Fe/N-doped carbon electrocatalysts. *Nature communications* **2020**, *11* (1), 5283.
(163) Li, J. J.; Zhang, Y. M.; Zhang, X. H.; Huang, J. Z.; Han, J. C.; Zhang, Z. H.; Han, X. J.; Xu, P.; Song, B. S, N Dual-Doped Graphene-like Carbon Nanosheets as Efficient Oxygen Reduction Reaction Electrocatalysts. *Acs Applied Materials & Interfaces* **2017**, *9* (1), 398-405. DOI: 10.1021/acsami.6b12547.
(164) Gao, Y.; Cai, Z. W.; Wu, X. C.; Lv, Z. L.; Wu, P.; Cai, C. X. Graphdiyne-Supported Single-Atom-Sized Fe Catalysts for the Oxygen Reduction Reaction: DFT Predictions and

Experimental Validations. *Acs Catalysis* **2018**, *8* (11), 10364-10374. DOI: 10.1021/acscatal.8b02360.
(165) Kraushofer, F.; Parkinson, G. S. Single-Atom Catalysis: Insights from Model Systems. *Chemical Reviews* **2022**, *122* (18), 14911-14939. DOI: 10.1021/acs.chemrev.2c00259.
(166) Patniboon, T.; Hansen, H. A. Acid-Stable and Active M-N-C Catalysts for the Oxygen Reduction Reaction: The Role of Local Structure. *Acs Catalysis* **2021**, *11* (21), 13102-13118. DOI: 10.1021/acscatal.1c02941.
(167) Goldsmith, B. R.; Sanderson, E. D.; Bean, D.; Peters, B. Isolated catalyst sites on amorphous supports: A systematic algorithm for understanding heterogeneities in structure and reactivity. *Journal of Chemical Physics* **2013**, *138* (20). DOI: 10.1063/1.4807384.
(168) Ren, C. J.; Jiang, Q. Y.; Lin, W.; Zhang, Y. F.; Huang, S. P.; Ding, K. N. Density Functional Theory Study of Single-Atom V, Nb, and Ta Catalysts on Graphene and Carbon Nitride for Selective Nitrogen Reduction. *Acs Applied Nano Materials* **2020**, *3* (6), 5149-5159. DOI: 10.1021/acsanm.0c00512.
(169) Zhao, K. Y.; Shen, Q. K.; Tao, Y.; Li, J. R.; Wang, M. L.; Li, C.; Xu, B. J. Atomically Dispersed N/O-Coordinated Cobalt Catalyst Enables Aerobic Oxygenation of Olefins under Ambient Conditions. *Acs Catalysis* **2023**, *13* (19), 12591-12600. DOI: 10.1021/acscatal.3c03209.
(170) Sun, H.; Wang, M. F.; Du, X. C.; Jiao, Y.; Liu, S. S.; Qian, T.; Yan, Y. C.; Liu, C.; Liao, M.; Zhang, Q. H.; et al. Modulating the d-band center of boron doped single-atom sites to boost the oxygen reduction reaction. *Journal of Materials Chemistry A* **2019**, *7* (36), 20952-20957. DOI: 10.1039/c9ta06949f.
(171) Rohrdanz, M. A.; Martins, K. M.; Herbert, J. M. A long-range-corrected density functional that performs well for both ground-state properties and time-dependent density functional theory excitation energies, including charge-transfer excited states. *Journal of Chemical Physics* **2009**, *130* (5). DOI: 10.1063/1.3073302.
(172) Wang, L. P.; Song, C. C. Geometry optimization made simple with translation and rotation coordinates. *Journal of Chemical Physics* **2016**, *144* (21). DOI: 10.1063/1.4952956.
(173) O'Boyle, N. M.; Banck, M.; James, C. A.; Morley, C.; Vandermeersch, T.; Hutchison, G. R. Open Babel: An open chemical toolbox. *Journal of Cheminformatics* **2011**, *3*. DOI: 10.1186/1758-2946-3-33.
(174) Nandy, A.; Duan, C. R.; Janet, J. P.; Gugler, S.; Kulik, H. J. Strategies and Software for Machine Learning Accelerated Discovery in Transition Metal Chemistry. *Industrial & Engineering Chemistry Research* **2018**, *57* (42), 13973-13986. DOI: 10.1021/acs.iecr.8b04015.
(175) Neese, F. Software update: The ORCA program system-Version 5.0. *Wiley Interdisciplinary Reviews-Computational Molecular Science* **2022**, *12* (5). DOI: 10.1002/wcms.1606.
(176) Larson, V. A.; Battistella, B.; Ray, K.; Lehnert, N.; Nam, W. Iron and manganese oxo complexes, oxo wall and beyond. *Nature Reviews Chemistry* **2020**, *4* (8), 404-419. DOI: 10.1038/s41570-020-0197-9.
(177) Cao, L. L.; Luo, Q. Q.; Chen, J. J.; Wang, L.; Lin, Y.; Wang, H. J.; Liu, X. K.; Shen, X. Y.; Zhang, W.; Liu, W.; et al. Dynamic oxygen adsorption on single-atomic Ruthenium catalyst with high performance for acidic oxygen evolution reaction. *Nature Communications* **2019**, *10*. DOI: 10.1038/s41467-019-12886-z.
(178) Harper, D. R.; Kulik, H. J. Computational Scaling Relationships Predict Experimental Activity and Rate-Limiting Behavior in Homogeneous Water Oxidation. *Inorganic Chemistry* **2022**, *61* (4), 2186-2197. DOI: 10.1021/acs.inorgchem.1c03376.

(179) Jalama, K. Carbon dioxide hydrogenation over nickel-, ruthenium-, and copper-based catalysts: Review of kinetics and mechanism. *Catalysis Reviews-Science and Engineering* **2017**, *59* (2), 95-164. DOI: 10.1080/01614940.2017.1316172.
(180) Ayers, P. W. An elementary derivation of the hard/soft-acid/base principle. *Journal of Chemical Physics* **2005**, *122* (14). DOI: 10.1063/1.1897374.
(181) Ayers, P. W.; Parr, R. G.; Pearson, R. G. Elucidating the hard/soft acid/base principle: A perspective based on half-reactions. *Journal of Chemical Physics* **2006**, *124* (19). DOI: 10.1063/1.2196882.
(182) Gani, T. Z. H.; Kulik, H. J. Understanding and Breaking Scaling Relations in Single-Site Catalysis: Methane to Methanol Conversion by Fe-IV=O. *Acs Catalysis* **2018**, *8* (2), 975-986. DOI: 10.1021/acscatal.7b03597.
(183) Rosen, A. S.; Notestein, J. M.; Snurr, R. Q. Structure-Activity Relationships That Identify Metal-Organic Framework Catalysts for Methane Activation. *Acs Catalysis* **2019**, *9* (4), 3576-3587. DOI: 10.1021/acscatal.8b05178.
(184) van Santen, R. A.; Neurock, M.; Shetty, S. G. Reactivity Theory of Transition-Metal Surfaces: A Bronsted-Evans-Polanyi Linear Activation Energy-Free-Energy Analysis. *Chemical Reviews* **2010**, *110* (4), 2005-2048. DOI: 10.1021/cr9001808.
(185) Simons, M. C.; Vitillo, J. G.; Babucci, M.; Hoffman, A. S.; Boubnov, A.; Beauvais, M. L.; Chen, Z. H. Y.; Cramer, C. J.; Chapman, K. W.; Bare, S. R.; et al. Structure, Dynamics, and Reactivity for Light Alkane Oxidation of Fe(II) Sites Situated in the Nodes of a Metal-Organic Framework. *Journal of the American Chemical Society* **2019**, *141* (45), 18142-18151. DOI: 10.1021/jacs.9b08686.
(186) Vitillo, J. G.; Bhan, A.; Cramer, C. J.; Lu, C. C.; Gagliardi, L. Quantum Chemical Characterization of Structural Single Fe(II) Sites in MIL-Type Metal-Organic Frameworks for the Oxidation of Methane to Methanol and Ethane to Ethanol. *Acs Catalysis* **2019**, *9* (4), 2870-2879. DOI: 10.1021/acscatal.8b04813.
(187) Debe, M. K. Electrocatalyst approaches and challenges for automotive fuel cells. *Nature* **2012**, *486* (7401), 43-51.
(188) Cheng, F.; Chen, J. Metal–air batteries: from oxygen reduction electrochemistry to cathode catalysts. *Chemical Society Reviews* **2012**, *41* (6), 2172-2192.
(189) Cao, R.; Lee, J. S.; Liu, M.; Cho, J. Recent progress in non-precious catalysts for metal-air batteries. *Advanced Energy Materials* **2012**, *2* (7), 816-829.
(190) Wang, X.; Li, Z.; Qu, Y.; Yuan, T.; Wang, W.; Wu, Y.; Li, Y. Review of metal catalysts for oxygen reduction reaction: from nanoscale engineering to atomic design. *Chem* **2019**, *5* (6), 1486-1511.
(191) Stephens, I. E.; Bondarenko, A. S.; Grønbjerg, U.; Rossmeisl, J.; Chorkendorff, I. Understanding the electrocatalysis of oxygen reduction on platinum and its alloys. *Energy & Environmental Science* **2012**, *5* (5), 6744-6762.
(192) Nie, Y.; Li, L.; Wei, Z. Recent advancements in Pt and Pt-free catalysts for oxygen reduction reaction. *Chemical Society Reviews* **2015**, *44* (8), 2168-2201.
(193) Wu, J.; Yang, H. Platinum-based oxygen reduction electrocatalysts. *Accounts of chemical research* **2013**, *46* (8), 1848-1857.
(194) Jung, N.; Chung, D. Y.; Ryu, J.; Yoo, S. J.; Sung, Y.-E. Pt-based nanoarchitecture and catalyst design for fuel cell applications. *Nano Today* **2014**, *9* (4), 433-456.

(195) Sui, S.; Wang, X.; Zhou, X.; Su, Y.; Riffat, S.; Liu, C.-j. A comprehensive review of Pt electrocatalysts for the oxygen reduction reaction: Nanostructure, activity, mechanism and carbon support in PEM fuel cells. *Journal of Materials Chemistry A* **2017**, *5* (5), 1808-1825.
(196) Stamenkovic, V. R.; Fowler, B.; Mun, B. S.; Wang, G.; Ross, P. N.; Lucas, C. A.; Markovic, N. M. Improved oxygen reduction activity on Pt3Ni (111) via increased surface site availability. *science* **2007**, *315* (5811), 493-497.
(197) Zhang, Z.; Sun, J.; Wang, F.; Dai, L. Efficient oxygen reduction reaction (ORR) catalysts based on single iron atoms dispersed on a hierarchically structured porous carbon framework. *Angewandte Chemie* **2018**, *130* (29), 9176-9181.
(198) Chen, Z.; Higgins, D.; Yu, A.; Zhang, L.; Zhang, J. A review on non-precious metal electrocatalysts for PEM fuel cells. *Energy & Environmental Science* **2011**, *4* (9), 3167-3192.
(199) Yang, L.; Cheng, D.; Xu, H.; Zeng, X.; Wan, X.; Shui, J.; Xiang, Z.; Cao, D. Unveiling the high-activity origin of single-atom iron catalysts for oxygen reduction reaction. *Proceedings of the National Academy of Sciences* **2018**, *115* (26), 6626-6631.
(200) Xu, H.; Cheng, D.; Cao, D.; Zeng, X. C. Revisiting the universal principle for the rational design of single-atom electrocatalysts. *Nature Catalysis* **2024**, *7* (2), 207-218.
(201) Kulkarni, A.; Siahrostami, S.; Patel, A.; Nørskov, J. K. Understanding catalytic activity trends in the oxygen reduction reaction. *Chemical reviews* **2018**, *118* (5), 2302-2312.
(202) Fu, C.; Luo, L.; Yang, L.; Shen, S.; Wei, G.; Zhang, J. Breaking the scaling relationship of ORR on carbon-based single-atom catalysts through building a local collaborative structure. *Catalysis Science & Technology* **2021**, *11* (23), 7764-7772.
(203) Zhu, G.; Liu, F.; Wang, Y.; Wei, Z.; Wang, W. Systematic exploration of N, C coordination effects on the ORR performance of Mn–N x doped graphene catalysts based on DFT calculations. *Physical Chemistry Chemical Physics* **2019**, *21* (24), 12826-12836.
(204) Nørskov, J. K.; Rossmeisl, J.; Logadottir, A.; Lindqvist, L.; Kitchin, J. R.; Bligaard, T.; Jonsson, H. Origin of the overpotential for oxygen reduction at a fuel-cell cathode. *The Journal of Physical Chemistry B* **2004**, *108* (46), 17886-17892.
(205) Ge, X.; Sumboja, A.; Wuu, D.; An, T.; Li, B.; Goh, F. T.; Hor, T. A.; Zong, Y.; Liu, Z. Oxygen reduction in alkaline media: from mechanisms to recent advances of catalysts. *Acs Catalysis* **2015**, *5* (8), 4643-4667.
(206) Strmcnik, D.; Kodama, K.; Van der Vliet, D.; Greeley, J.; Stamenkovic, V. R.; Marković, N. The role of non-covalent interactions in electrocatalytic fuel-cell reactions on platinum. *Nature chemistry* **2009**, *1* (6), 466-472.
(207) Stamenkovic, V. R.; Strmcnik, D.; Lopes, P. P.; Markovic, N. M. Energy and fuels from electrochemical interfaces. *Nature materials* **2017**, *16* (1), 57-69.
(208) Guo, X.; Lin, S.; Gu, J.; Zhang, S.; Chen, Z.; Huang, S. Simultaneously achieving high activity and selectivity toward two-electron O2 electroreduction: the power of single-atom catalysts. *Acs Catalysis* **2019**, *9* (12), 11042-11054.
(209) Dai, L.; Xue, Y.; Qu, L.; Choi, H.-J.; Baek, J.-B. Metal-free catalysts for oxygen reduction reaction. *Chemical reviews* **2015**, *115* (11), 4823-4892.
(210) Greeley, J.; Stephens, I.; Bondarenko, A.; Johansson, T. P.; Hansen, H. A.; Jaramillo, T.; Rossmeisl, J.; Chorkendorff, I.; Nørskov, J. K. Alloys of platinum and early transition metals as oxygen reduction electrocatalysts. *Nature chemistry* **2009**, *1* (7), 552-556.
(211) Su, H.-Y.; Gorlin, Y.; Man, I. C.; Calle-Vallejo, F.; Nørskov, J. K.; Jaramillo, T. F.; Rossmeisl, J. Identifying active surface phases for metal oxide electrocatalysts: a study of

manganese oxide bi-functional catalysts for oxygen reduction and water oxidation catalysis. *Physical Chemistry Chemical Physics* **2012**, *14* (40), 14010-14022.
(212) Suntivich, J.; Gasteiger, H. A.; Yabuuchi, N.; Nakanishi, H.; Goodenough, J. B.; Shao-Horn, Y. Design principles for oxygen-reduction activity on perovskite oxide catalysts for fuel cells and metal–air batteries. *Nature chemistry* **2011**, *3* (7), 546-550.
(213) Tritsaris, G. A.; Nørskov, J. K.; Rossmeisl, J. Trends in oxygen reduction and methanol activation on transition metal chalcogenides. *Electrochimica acta* **2011**, *56* (27), 9783-9788.
(214) Seifitokaldani, A.; Savadogo, O.; Perrier, M. Density functional theory (DFT) computation of the oxygen reduction reaction (ORR) on titanium nitride (TiN) surface. *Electrochimica Acta* **2014**, *141*, 25-32.
(215) Janet, J. P.; Kulik, H. J. Resolving transition metal chemical space: Feature selection for machine learning and structure–property relationships. *The Journal of Physical Chemistry A* **2017**, *121* (46), 8939-8954.
(216) Duan, C.; Nandy, A.; Adamji, H.; Roman-Leshkov, Y.; Kulik, H. J. Machine learning models predict calculation outcomes with the transferability necessary for computational catalysis. *Journal of Chemical Theory and Computation* **2022**, *18* (7), 4282-4292.
(217) Moosavi, S. M.; Nandy, A.; Jablonka, K. M.; Ongari, D.; Janet, J. P.; Boyd, P. G.; Lee, Y.; Smit, B.; Kulik, H. J. Understanding the diversity of the metal-organic framework ecosystem. *Nature communications* **2020**, *11* (1), 1-10.
(218) Adamji, H.; Nandy, A.; Kevlishvili, I.; Román-Leshkov, Y.; Kulik, H. J. Computational Discovery of Stable Metal–Organic Frameworks for Methane-to-Methanol Catalysis. *Journal of the American Chemical Society* **2023**, *145* (26), 14365-14378.
(219) Nandy, A.; Duan, C.; Kulik, H. J. Using machine learning and data mining to leverage community knowledge for the engineering of stable metal–organic frameworks. *Journal of the American Chemical Society* **2021**, *143* (42), 17535-17547.
(220) Davidson, E. A.; Winiwarter, W. Urgent abatement of industrial sources of nitrous oxide. *Nature Climate Change* **2023**, *13* (7), 599-601.
(221) Masson-Delmotte, V. Climate change 2021: the physical science basis: Working Group I contribution to the sixth assessment report of the Intergovernmental Panel on Climate Change. *(No Title)* **2021**.
(222) Tian, H.; Xu, R.; Canadell, J. G.; Thompson, R. L.; Winiwarter, W.; Suntharalingam, P.; Davidson, E. A.; Ciais, P.; Jackson, R. B.; Janssens-Maenhout, G. A comprehensive quantification of global nitrous oxide sources and sinks. *Nature* **2020**, *586* (7828), 248-256.
(223) Ravishankara, A.; Daniel, J. S.; Portmann, R. W. Nitrous oxide (N2O): the dominant ozone-depleting substance emitted in the 21st century. *science* **2009**, *326* (5949), 123-125.
(224) Hassan, M. U.; Aamer, M.; Mahmood, A.; Awan, M. I.; Barbanti, L.; Seleiman, M. F.; Bakhsh, G.; Alkharabsheh, H. M.; Babur, E.; Shao, J. Management strategies to mitigate N2O emissions in agriculture. *Life* **2022**, *12* (3), 439.
(225) Gu, B.; Zhang, X.; Lam, S. K.; Yu, Y.; Van Grinsven, H. J.; Zhang, S.; Wang, X.; Bodirsky, B. L.; Wang, S.; Duan, J. Cost-effective mitigation of nitrogen pollution from global croplands. *Nature* **2023**, *613* (7942), 77-84.
(226) Li, L.; Xu, J.; Hu, J.; Han, J. Reducing nitrous oxide emissions to mitigate climate change and protect the ozone layer. *Environmental science & technology* **2014**, *48* (9), 5290-5297.
(227) Ding, M.; Flaig, R. W.; Jiang, H.-L.; Yaghi, O. M. Carbon capture and conversion using metal–organic frameworks and MOF-based materials. *Chemical Society Reviews* **2019**, *48* (10), 2783-2828.

(228) Firooz, S. K.; Armstrong, D. W. Metal-organic frameworks in separations: A review. *Analytica Chimica Acta* **2022**, *1234*, 340208.
(229) Bavykina, A.; Kolobov, N.; Khan, I. S.; Bau, J. A.; Ramirez, A.; Gascon, J. Metal–organic frameworks in heterogeneous catalysis: recent progress, new trends, and future perspectives. *Chemical reviews* **2020**, *120* (16), 8468-8535.
(230) Furukawa, H.; Cordova, K. E.; O'Keeffe, M.; Yaghi, O. M. The chemistry and applications of metal-organic frameworks. *Science* **2013**, *341* (6149), 1230444.
(231) Queen, W. L.; Hudson, M. R.; Bloch, E. D.; Mason, J. A.; Gonzalez, M. I.; Lee, J. S.; Gygi, D.; Howe, J. D.; Lee, K.; Darwish, T. A. Comprehensive study of carbon dioxide adsorption in the metal–organic frameworks M 2 (dobdc)(M= Mg, Mn, Fe, Co, Ni, Cu, Zn). *Chemical Science* **2014**, *5* (12), 4569-4581.
(232) He, Y.; Zhou, W.; Qian, G.; Chen, B. Methane storage in metal–organic frameworks. *Chemical Society Reviews* **2014**, *43* (16), 5657-5678.
(233) Lin, Y.; Kong, C.; Chen, L. Amine-functionalized metal–organic frameworks: structure, synthesis and applications. *RSC advances* **2016**, *6* (39), 32598-32614.
(234) Sharifzadeh, Z.; Morsali, A. Amine-functionalized metal-organic frameworks: from synthetic design to scrutiny in application. *Coordination Chemistry Reviews* **2022**, *459*, 214445.
(235) Zick, M. E.; Cho, D.; Ling, J.; Milner, P. J. Carbon Capture Beyond Amines: CO2 Sorption at Nucleophilic Oxygen Sites in Materials. *ChemNanoMat* **2023**, *9* (1), e202200436.
(236) Li, J.; Han, X.; Zhang, X.; Sheveleva, A. M.; Cheng, Y.; Tuna, F.; McInnes, E. J.; McCormick McPherson, L. J.; Teat, S. J.; Daemen, L. L. Capture of nitrogen dioxide and conversion to nitric acid in a porous metal–organic framework. *Nature chemistry* **2019**, *11* (12), 1085-1090.
(237) Zhang, X.; Chen, W.; Shi, W.; Cheng, P. Highly selective sorption of CO 2 and N 2 O and strong gas-framework interactions in a nickel (ii) organic material. *Journal of materials chemistry A* **2016**, *4* (41), 16198-16204.
(238) Denysenko, D.; Jelic, J.; Magdysyuk, O. V.; Reuter, K.; Volkmer, D. Elucidating Lewis acidity of metal sites in MFU-4l metal-organic frameworks: N2O and CO2 adsorption in MFU-4l, CuI-MFU-4l and Li-MFU-4l. *Microporous and Mesoporous Materials* **2015**, *216*, 146-150.
(239) Yang, J.; Du, B.; Liu, J.; Krishna, R.; Zhang, F.; Zhou, W.; Wang, Y.; Li, J.; Chen, B. MIL-100Cr with open Cr sites for a record N 2 O capture. *Chemical communications* **2018**, *54* (100), 14061-14064.
(240) Ma, L.; Zhang, F.; Li, K.; Zhang, Y.; Song, Z.; Wang, L.; Yang, J.; Li, J. Improved N2O capture performance of chromium terephthalate MIL-101 via substituent engineering. *Journal of Solid State Chemistry* **2022**, *309*, 122951.
(241) Wang, L.; Zhang, F.; Yang, J.; Li, L.; Li, J. The efficient separation of N 2 O/CO 2 using unsaturated Fe 2+ sites in MIL-100Fe. *Chemical Communications* **2021**, *57* (54), 6636-6639.
(242) Saha, D.; Bao, Z.; Jia, F.; Deng, S. Adsorption of CO2, CH4, N2O, and N2 on MOF-5, MOF-177, and zeolite 5A. *Environmental science & technology* **2010**, *44* (5), 1820-1826.
(243) Wang, L.; Li, Y.; Wang, Y.; Yang, J.; Li, L.; Li, J. Research on CO2-N2O separation using flexible metal organic frameworks. *Separation and Purification Technology* **2020**, *251*, 117311.
(244) Azbell, T. J.; Pitt, T. A.; Bollmeyer, M. M.; Cong, C.; Lancaster, K. M.; Milner, P. J. Ionothermal Synthesis of Metal-Organic Frameworks Using Low-Melting Metal Salt Precursors. *Angewandte Chemie* **2023**, *135* (17), e202218252.

(245) Rieth, A. J.; Tulchinsky, Y.; Dincă, M. High and reversible ammonia uptake in mesoporous azolate metal–organic frameworks with open Mn, Co, and Ni sites. *Journal of the American Chemical Society* **2016**, *138* (30), 9401-9404.
(246) Caskey, S. R.; Wong-Foy, A. G.; Matzger, A. J. Dramatic tuning of carbon dioxide uptake via metal substitution in a coordination polymer with cylindrical pores. *Journal of the American Chemical Society* **2008**, *130* (33), 10870-10871.
(247) Bloch, E. D.; Murray, L. J.; Queen, W. L.; Chavan, S.; Maximoff, S. N.; Bigi, J. P.; Krishna, R.; Peterson, V. K.; Grandjean, F.; Long, G. J. Selective binding of O2 over N2 in a redox–active metal–organic framework with open iron (II) coordination sites. *Journal of the American Chemical Society* **2011**, *133* (37), 14814-14822.
(248) Severin, K. Synthetic chemistry with nitrous oxide. *Chemical Society Reviews* **2015**, *44* (17), 6375-6386.
(249) Parmon, V.; Panov, G.; Uriarte, A.; Noskov, A. Nitrous oxide in oxidation chemistry and catalysis: application and production. *Catalysis Today* **2005**, *100* (1-2), 115-131.
(250) Le Vaillant, F.; Mateos Calbet, A.; González-Pelayo, S.; Reijerse, E. J.; Ni, S.; Busch, J.; Cornella, J. Catalytic synthesis of phenols with nitrous oxide. *Nature* **2022**, *604* (7907), 677-683.
(251) Bols, M. L.; Snyder, B. E.; Rhoda, H. M.; Cnudde, P.; Fayad, G.; Schoonheydt, R. A.; Van Speybroeck, V.; Solomon, E. I.; Sels, B. F. Coordination and activation of nitrous oxide by iron zeolites. *Nature Catalysis* **2021**, *4* (4), 332-340.
(252) Simons, M. C.; Prinslow, S. D.; Babucci, M.; Hoffman, A. S.; Hong, J.; Vitillo, J. G.; Bare, S. R.; Gates, B. C.; Lu, C. C.; Gagliardi, L. Beyond radical rebound: Methane oxidation to methanol catalyzed by iron species in metal–organic framework nodes. *Journal of the American Chemical Society* **2021**, *143* (31), 12165-12174.
(253) Barona, M.; Ahn, S.; Morris, W.; Hoover, W.; Notestein, J. M.; Farha, O. K.; Snurr, R. Q. Computational predictions and experimental validation of alkane oxidative dehydrogenation by fe2m mof nodes. *Acs Catalysis* **2019**, *10* (2), 1460-1469.
(254) Xiao, D. J.; Bloch, E. D.; Mason, J. A.; Queen, W. L.; Hudson, M. R.; Planas, N.; Borycz, J.; Dzubak, A. L.; Verma, P.; Lee, K. Oxidation of ethane to ethanol by N2O in a metal–organic framework with coordinatively unsaturated iron (II) sites. *Nature chemistry* **2014**, *6* (7), 590-595.
(255) Tofoni, A.; Tavani, F.; Vandone, M.; Braglia, L.; Borfecchia, E.; Ghigna, P.; Stoian, D. C.; Grell, T.; Stolfi, S.; Colombo, V. Full Spectroscopic Characterization of the Molecular Oxygen-Based Methane to Methanol Conversion over Open Fe (II) Sites in a Metal–Organic Framework. *Journal of the American Chemical Society* **2023**, *145* (38), 21040-21052.
(256) Verma, P.; Vogiatzis, K. D.; Planas, N.; Borycz, J.; Xiao, D. J.; Long, J. R.; Gagliardi, L.; Truhlar, D. G. Mechanism of oxidation of ethane to ethanol at Iron (IV)–oxo sites in magnesium-diluted Fe2 (dobdc). *Journal of the American Chemical Society* **2015**, *137* (17), 5770-5781.
(257) Suh, B. L.; Kim, J. Ligand Insertion in MOF-74 as Effective Design for Oxidation of Ethane to Ethanol. *The Journal of Physical Chemistry C* **2018**, *122* (40), 23078-23083.
(258) Costas, M.; Mehn, M. P.; Jensen, M. P.; Que, L. Dioxygen activation at mononuclear nonheme iron active sites: enzymes, models, and intermediates. *Chemical reviews* **2004**, *104* (2), 939-986.
(259) Wallar, B. J.; Lipscomb, J. D. Dioxygen activation by enzymes containing binuclear non-heme iron clusters. *Chemical Reviews* **1996**, *96* (7), 2625-2658.
(260) Neese, F. The ORCA program system. *Wiley Interdisciplinary Reviews-Computational Molecular Science* **2012**, *2* (1), 73-78. DOI: 10.1002/wcms.81.

(261) Becke, A. D. DENSITY-FUNCTIONAL THERMOCHEMISTRY .3. THE ROLE OF EXACT EXCHANGE. *Journal of Chemical Physics* **1993**, *98* (7), 5648-5652. DOI: 10.1063/1.464913.
(262) Grimme, S.; Antony, J.; Ehrlich, S.; Krieg, H. A consistent and accurate ab initio parametrization of density functional dispersion correction (DFT-D) for the 94 elements H-Pu. *Journal of Chemical Physics* **2010**, *132* (15). DOI: 10.1063/1.3382344.
(263) Grimme, S.; Ehrlich, S.; Goerigk, L. Effect of the Damping Function in Dispersion Corrected Density Functional Theory. *Journal of Computational Chemistry* **2011**, *32* (7), 1456-1465. DOI: 10.1002/jcc.21759.
(264) van Lenthe, E.; Ehlers, A.; Baerends, E. J. Geometry optimizations in the zero order regular approximation for relativistic effects. *Journal of Chemical Physics* **1999**, *110* (18), 8943-8953. DOI: 10.1063/1.478813.
(265) Weigend, F.; Ahlrichs, R. Balanced basis sets of split valence, triple zeta valence and quadruple zeta valence quality for H to Rn: Design and assessment of accuracy. *Physical Chemistry Chemical Physics* **2005**, *7* (18), 3297-3305. DOI: 10.1039/b508541a.
(266) Neese, F.; Wennmohs, F.; Hansen, A.; Becker, U. Efficient, approximate and parallel Hartree-Fock and hybrid DFT calculations. A 'chain-of-spheres' algorithm for the Hartree-Fock exchange. *Chemical Physics* **2009**, *356* (1-3), 98-109. DOI: 10.1016/j.chemphys.2008.10.036.
(267) Neese, F. Definition of corresponding orbitals and the diradical character in broken symmetry DFT calculations on spin coupled systems. *Journal of Physics and Chemistry of Solids* **2004**, *65* (4), 781-785. DOI: 10.1016/j.jpcs.2003.11.015.
(268) Henkelman, G.; Uberuaga, B. P.; Jónsson, H. A climbing image nudged elastic band method for finding saddle points and minimum energy paths. *Journal of Chemical Physics* **2000**, *113* (22), 9901-9904. DOI: 10.1063/1.1329672.
(269) Borycz, J.; Paier, J.; Verma, P.; Darago, L. E.; Xiao, D. J.; Truhlar, D. G.; Long, J. R.; Gagliardi, L. Structural and Electronic Effects on the Properties of Fe2 (dobdc) upon Oxidation with N2O. *Inorganic chemistry* **2016**, *55* (10), 4924-4934.
(270) Zhuravlev, V.; Malinowski, P. J. A Stable Crystalline Copper (I)–N2O Complex Stabilized as the Salt of a Weakly Coordinating Anion. *Angewandte Chemie* **2018**, *130* (36), 11871-11874.
(271) Mokhtarzadeh, C. C.; Chan, C.; Moore, C. E.; Rheingold, A. L.; Figueroa, J. S. Side-on coordination of nitrous oxide to a mononuclear cobalt center. *Journal of the American Chemical Society* **2019**, *141* (38), 15003-15007.
(272) Piro, N. A.; Lichterman, M. F.; Harman, W. H.; Chang, C. J. A structurally characterized nitrous oxide complex of vanadium. *Journal of the American Chemical Society* **2011**, *133* (7), 2108-2111.
(273) Pamplin, C. B.; Ma, E. S.; Safari, N.; Rettig, S. J.; James, B. R. The nitrous oxide complex, RuCl2 (η1-N2O)(P− N)(PPh3)(P− N=[o-(N, N-dimethylamino) phenyl] diphenylphosphine); low temperature conversion of N2O to N2 and O2. *Journal of the American Chemical Society* **2001**, *123* (35), 8596-8597.
(274) Paulat, F.; Kuschel, T.; Näther, C.; Praneeth, V.; Sander, O.; Lehnert, N. Spectroscopic properties and electronic structure of pentammineruthenium (II) dinitrogen oxide and corresponding nitrosyl complexes: binding mode of N2O and reactivity. *Inorganic chemistry* **2004**, *43* (22), 6979-6994.
(275) Puerta Lombardi, B. M.; Gendy, C.; Gelfand, B. S.; Bernard, G. M.; Wasylishen, R. E.; Tuononen, H. M.; Roesler, R. Side-on Coordination in Isostructural Nitrous Oxide and Carbon

Dioxide Complexes of Nickel. *Angewandte Chemie International Edition* **2021**, *60* (13), 7077-7081.
(276) Gyton, M. R.; Leforestier, B.; Chaplin, A. B. Rhodium (I) Pincer Complexes of Nitrous Oxide. *Angewandte Chemie International Edition* **2019**, *58* (43), 15295-15298.
(277) Ketrat, S.; Maihom, T.; Wannakao, S.; Probst, M.; Nokbin, S.; Limtrakul, J. Coordinatively unsaturated metal–organic frameworks M3 (btc) 2 (M= Cr, Fe, Co, Ni, Cu, and Zn) catalyzing the oxidation of CO by N2O: Insight from DFT calculations. *Inorganic chemistry* **2017**, *56* (22), 14005-14012.
(278) Barona, M.; Snurr, R. Q. Exploring the tunability of trimetallic MOF nodes for partial oxidation of methane to methanol. *ACS applied materials & interfaces* **2020**, *12* (25), 28217-28231.
(279) Yu, D.; Yazaydin, A. O.; Lane, J. R.; Dietzel, P. D.; Snurr, R. Q. A combined experimental and quantum chemical study of CO 2 adsorption in the metal–organic framework CPO-27 with different metals. *Chemical Science* **2013**, *4* (9), 3544-3556.
(280) Zhang, Q.; Li, B.; Chen, L. First-principles study of microporous magnets M-MOF-74 (M= Ni, Co, Fe, Mn): the role of metal centers. *Inorganic chemistry* **2013**, *52* (16), 9356-9362.
(281) Bloch, E. D.; Queen, W. L.; Krishna, R.; Zadrozny, J. M.; Brown, C. M.; Long, J. R. Hydrocarbon separations in a metal-organic framework with open iron (II) coordination sites. *science* **2012**, *335* (6076), 1606-1610.
(282) Vogiatzis, K. D.; Haldoupis, E.; Xiao, D. J.; Long, J. R.; Siepmann, J. I.; Gagliardi, L. Accelerated computational analysis of metal–organic frameworks for oxidation catalysis. *The Journal of Physical Chemistry C* **2016**, *120* (33), 18707-18712.
(283) Vitillo, J. G.; Lu, C. C.; Cramer, C. J.; Bhan, A.; Gagliardi, L. Influence of First and Second Coordination Environment on Structural Fe (II) Sites in MIL-101 for C–H Bond Activation in Methane. *ACS Catalysis* **2020**, *11* (2), 579-589.
(284) Yamashita, T.; Vannice, A. N2O decomposition over manganese oxides. *Journal of Catalysis* **1996**, *161* (1), 254-262.
(285) Ross, R. A.; Fairbridge, C. Oxidation of 1-butene by nitrous oxide over manganese (III) and related transition metal oxides. *Canadian journal of chemistry* **1984**, *62* (8), 1483-1486.
(286) Ben-Daniel, R.; Weiner, L.; Neumann, R. Activation of nitrous oxide and selective epoxidation of alkenes catalyzed by the manganese-substituted polyoxometalate,[MnIII2ZnW (Zn2W9O34) 2] 10. *Journal of the American Chemical Society* **2002**, *124* (30), 8788-8789.
(287) Jiang, M.-X.; Liu, C.-G. New insight into the catalytic cycle about epoxidation of alkenes by N2O over a Mn–substituted Keggin-type polyoxometalate. *Journal of Molecular Graphics and Modelling* **2017**, *73*, 8-17.
(288) Li, Y.; Armor, J. N. Catalytic decomposition of nitrous oxide on metal exchanged zeolites. *Applied Catalysis B: Environmental* **1992**, *1* (3), L21-L29.
(289) Campa, M. C.; Indovina, V.; Pietrogiacomi, D. The selective catalytic reduction of N2O with CH4 on Na-MOR and Na-MFI exchanged with copper, cobalt or manganese. *Applied Catalysis B: Environmental* **2012**, *111*, 90-95.
(290) Cordero, B.; Gomez, V.; Platero-Prats, A. E.; Reves, M.; Echeverria, J.; Cremades, E.; Barragan, F.; Alvarez, S. Covalent radii revisited. *Dalton Transactions* **2008**, (21), 2832-2838. DOI: 10.1039/b801115j.